GE Astro Space Division
PO Box 800
Princeton, NJ 08540

Definition and Preliminary Design of the

LAWS

Laser Atmospheric Wind Sounder

PHASE II
FINAL REPORT VOLUME II

Date: 9/30/92

Contract Number: NAS8-37589

GE Astro Space
Hughes Danbury
STI Optronics

TABLE OF CONTENTS

LIST OF FIGURES

LIST OF TABLES

ACKNOWLEDGEMENTS

The Laser Atmospheric Wind Sounder (LAWS) program was conducted by GE Astro-Space Division, with the dedicated support of Hughes Danbury Optical Systems, Danbury, CT (optical subsystem), and STI Optronics, Bellevue, WA, (laser subsystem). Lassen Research, Manton, CA (receiver subsystem) and Simpson Weather Associates, Charlottesville, VA (mission requirements) also participated in a supporting role.

This study was completed through the efforts of many individuals at GE Astro-Space Division, HDOS, STI, Lassen and SWA, and with the cooperation and guidance of those at NASA Marshall Space Flight Center, and the LAWS Science Team. I would like to thank all who contributed to the success of this project. In particular, I would like to acknowledge the following:

NASA Marshall Space Flight Center	Dick Beranek, Bob Jayroe', Randy Bagget, Jim Bilbro, Rex Geveden, Mike Kavaya, Gary Spiers
LAWS Science Team Leader	Wayman Baker
Hughes Danbury	Alan Wissinger, Dick Calef, Steve Donley, Mike Krim, Bob Noll,
STI Optronics	Rhidian Lawrence, Pauline DeHart, Terry DeHart, J.J. Ewing, Charles Fisher, Pat Jones, Steve Moody
Lassen Research	Bob Lee
Simpson Weather Associates	Dave Emmitt
GE Astro Space	Kent Anderson, Tom Bluesteen, Mike DiOrio, Nancy Gaston, Dave Kenyon, Ed Kuhar, George McWilliams, Keith Moore, Ed Pruett, Peck Sohn, Jeff Sroga, John Weaver

Lastly, I would like to thank my predecessor, Bob Vitz who, by his foresight in reassembling the Windsat team and leadership and dedication through most of the program, was largely responsible for its successful completion.

John C. Petheram
LAWS Program Manager

LIST OF ACRONYMS

BDU	Bus Data Unit
BSR	Bus Select Relay
CEI	Contract End Item
CW	Continuous Wave
DR	Data Requirement
EOS	Earth Observing System
EOSDIS	EOS Data and Information System
GFE	Government Furnished Equipment
GIIS	General Instrument Interface Specification
ICD	Interface Control Document
IF	Intermediate Frequency
LAWS	Laser Atmospheric Wind Sounder
LIDAR	Light Detection And Ranging
LOS	Line Of Sight
MCT	Mercury Cadmium Telluride
MSFC	Marshall Space Flight Center
PPS	Portable Platform Simulator, Pulses Per Second
RF	Radio Frequency
RPM	Revolutions Per Minute
SNR	Signal to Noise Ratio
SOW	Statement Of Work
TBD	To Be Determined
TBR	To Be Revised
TBS	To Be Supplied
TDRSS	Tracking and Data Relay Satellite System

1.0 INTRODUCTION

This document is Volume II of the LAWS Phase II Final Study Report and describes the definition and preliminary design of the LAWS instrument, together with details of the laser breadboard program conducted during the last 18 months of the program. Volume I of the Phase II Final Study Report is an Executive Summary and Volume III contains a cost estimate and schedule for the Phase C/D instrument procurement.

1.1 Mission Objectives

Accurate knowledge of winds is critical to our understanding of the earth's climate and to our ability to predict climate change. Winds are a fundamental component of highly non-linear interactions between oceans, land surfaces and the atmosphere. Interactions at these interfaces are the focus of much climate change research.

Although wind information is critical for advancing our understanding, currently most of our description of atmospheric motion is obtained indirectly - i.e., derived from observations of temperature and moisture through geostrophic relationships. Direct measurement of winds over the globe is limited to land-based rawinsonde surface stations and a few ship/aircraft reports. Cloud track winds using satellite imagery are calculated but must be used with great care.

The LAWS mission objective, therefore, is to provide diurnal and global direct observations of winds - an observation that will incrementally enhance our knowledge of the earth's climate and physical processes responsible for its change.

To meet mission objectives, the LAWS instrument and data processors are being optimized to provide a product that is best suited for assimilation into global climate models, regional scale models and numerical weather prediction models. Given that there are constraints on the operation of an active sensor (e.g., power, laser life time, thermal control), the LAWS design must take into consideration:

that the value of LAWS observations will be measured in terms of incremental impact on man's knowledge.

that LAWS winds will be weighted to other wind observations, both direct and indirect.

that LAWS must give priority to taking observations where there currently are no or incomplete wind observations.

that LAWS should provide enhanced resolution of ageostrophic winds over regions of the globe (e.g., tropics, oceans) not observed by other instruments.

that LAWS should also provide a minimum set of observations, unbiased in space and time, for long term climate analysis.

The system design reported herein has assumed a given power, weight and volume allowance for the LAWS instrument. As the study progressed these numbers changed and it is likely that they will change again in the future. With this in mind the GE team has incorporated flexibility into the system design to allow LAWS to be configured for a range of launch vehicles and programmed to achieve the most science for whatever spacecraft resources are eventually made available.

1.2 Study Objectives

The LAWS contract was managed by the NASA Marshall Space Flight Center and performed in two phases beginning March 27, 1989 and ending September 30, 1992.

The objective of phase I of the LAWS study was to define and perform a preliminary design for the LAWS instrument. The definition phase consisted of identifying realistic concepts for LAWS and analyzing them in sufficient detail to be able to choose the most promising one for the LAWS application. System and subsystem configurations were then developed for the chosen concept. The concept and subsequent configuration were to be compatible with two prospective platforms- the Japanese Polar Orbiting Platform (JPOP) and as an attached payload on the Space Station Freedom.

After a thorough and objective concept selection process, we chose a heterodyne detection Doppler lidar using a CO_2 laser transmitter operating at 9.1 μm over a 2.1 μm solid state system. The choice of the CO_2 approach over solid-state reflects the advanced state of development of CO_2 lasers, its maturity in ground-based systems and the eased subsystem requirements associated with the longer wavelength.

The CO_2 lidar concept was then analyzed in detail to arrive at a configuration for the instrument and its major subsystems. Our approach throughout the configuration design was to take a systems perspective and trade requirements between subsystems, wherever possible, to arrive at configurations which made maximum use of existing, proven technology or relatively

straightforward extensions to existing technology to reduce risk and cost. At the conclusion of Phase I we arrived at a configuration for LAWS which meets the performance requirements, yet which is less complex than previous designs of space-based wind sensors (e.g. Windsat), employs lightweight technologies to meet its weight goal (<800 kg) and sufficiently flexible to offer various operational scenarios with power requirements from about 2 kW to 3 kW. The Phase I Final Report was released in March 1990.

The 21-month Phase II began in October 1990. The requirement to accommodate LAWS as an attached payload on Space Station Freedom was deleted and the orbit altitude for the Japanese polar orbiting platform was changed from 824 km to 705 km. The power allocated to LAWS was reduced to 2.2 kW from 3 kW. Subsequently the availability of a Japanese Polar Orbiting Platform was called into question and LAWS accommodation studies were continued using a conceptual, ATLAS-launched platform supplied by MSFC. In March 1991 a modification to the original contract was funded to provide a LAWS laser breadboard which could demonstrate all the performance requirements of the LAWS laser. Also funded as part of the same contract extension was a lifetest demonstration using an existing laser at STI. The breadboard extension was an eighteen month effort and the period of performance was therefore extended to September 30, 1992.

1.3 Highlights of the Phase II Design

The Phase II design configured for the MSFC supplied bus is shown in Figure 1-1. The main interface between the instrument and platform is a graphite-epoxy optical bench which maintains the strict alignment tolerances between the laser and optical subsystems. Support subsystem components and electronics boxes are mounted to the side of the optical bench on platform provided cold-plates. Laser heat is rejected via heat exchangers mated to cold plates under the optical bench. This configuration minimizes the amount of instrument structure yet allows LAWS to be integrated and tested prior to integration with the platform. The configuration is easily adaptable to other platforms and launch vehicles. The major subsystems draw on existing technology or heritage where possible and all have been subject to risk retirement activities during the 4 years of the LAWS program.

The phase II **laser** design (shown in the figure) is based on lasers which have demonstrated that they can meet the requirements of operational Doppler lidars. The NOAA Doppler system, which uses an STI supplied laser, has been operating since the early '80's. A ground-based , mobile system constructed at GE during the LAWS program uses a 2-J laser based on the NOAA design but with upgrades to improve the beam quality and efficiency. The upgrades resulted in an intrinsic efficiency of 6.3% for the GE laser. The goal of the LAWS phase II design

is for a wallplug efficiency of 6%. CORA (MIT-Lincoln Laboratory) is the largest Doppler lidar in existence and uses an STI supplied 200-J laser of similar (although physically much larger) design to the NOAA and GE devices.

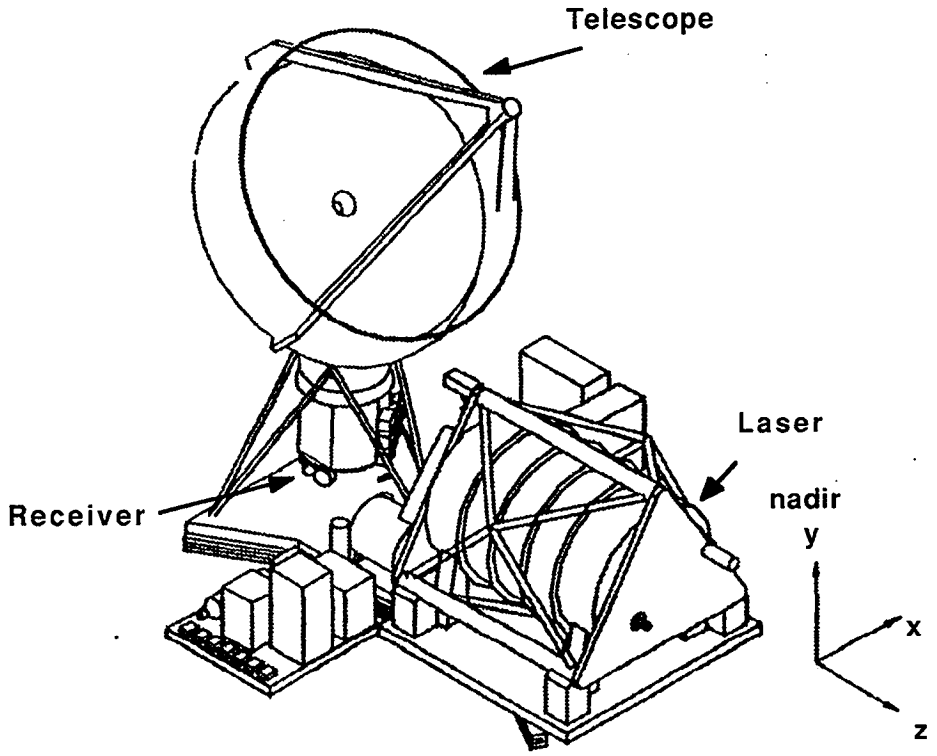

Figure 1-1 LAWS Instrument Configuration

At the beginning of the LAWS program it was recognized that the biggest challenge to CO_2 lasers was achieving the life requirement of 10^9 pulses. The demonstration in May 1992 of 10^8 pulses from the LAWS life-testbed laser at STI has shown that there are no unforeseen barriers to achieving long-life. The data generated by this important demonstration will be invaluable in designing the LAWS phase C/D laser.

The design of the LAWS **optical system** has been facilitated throughout by HDOS-developed code which predicts the impact on system SNR in terms of optical parameters such as despace and decenter. Also the error budget allocations for the pointing and control subsystem have been substantiated by measurement (e.g. the bearing runout was measured for a typical LAWS-type bearing) or by data available from other programs.

The optical system largely determines the LAWS envelope. The fact that it is compact allows us to package LAWS very efficiently and we were not only able to show LAWS configurations in the Atlas vehicle as required, but also in a Delta vehicle, with no compromise on performance.

The **receiver subsystem** uses a HgCdTe detector in the focal plane of the optical subsystem which must operate at a bandwidth in excess of 1 GHz (due to the motion of the spacecraft). GE investment in HgCdTe detectors and coplanar waveguides over the course of the LAWS Study has resulted in an increase in quantum efficiency of about 3 dB at the high bandwidths required.

Finally, the GE team investment, which developed extensive, detailed computer models to predict the performance of the LAWS system and subsystems, provides an infrastructure and basis from which to investigate alternate configurations and proceed with phase C/D system design.

2.0 SYSTEMS ENGINEERING

This section discusses the system requirements for the LAWS instrument and then the derived subsystem requirements, in particular the optics, laser and receiver. The system error budgets are also detailed in this section. The analysis of the performance of LAWS, which has been used to derive system and subsystem requirements, is detailed in a separate section, section 5.0.

2.1 System Level Requirements

The top-level science requirements for LAWS remained the same throughout both Phase I and Phase II of the Study. They are:– velocity accuracy: ±1 m/s (high backscatter), ±5 m/s (low backscatter); horizontal resolution: 100 km x 100 km; vertical resolution: 1 km; life: 5 years or 10^9 shots. The dynamic range of velocities changed from ±100 m/s to ±150 m/s during Phase II.

2.1.1 Performance Requirements

System trades were performed in both Phases I and II (using existing performance model codes) to define ranges of possible values of the major LAWS parameters: laser energy, telescope aperture, laser repetition rate, laser pulse length, scan nadir angle and scan rate. A maturing understanding of the signal-to-noise-ratio (SNR) and coverage required to achieve the desired velocity accuracy, then constrained the values of those parameters to a certain range, for a given set of spacecraft resources. The statement of work (SOW) was amended as the Study progressed to reflect this new understanding. Figure 2.1-1 shows, at its center, the derived instrument requirements as they eventually appeared in the SOW for Phase II, with their relationship to the top-level science requirements around the outside.

The requirement for wind velocity estimation specifies a standard deviation of less than 1 m/s in areas of high backscatter (high beta (β)), and a standard deviation of less than 5 m/s in low backscatter regions (low β). A derived requirement is that the instrument contribution to the velocity estimation must be less than 1 m/s. The velocity estimation requirement leads to the following laser derived requirements: pulse length between 2.5 and 3.5 μsec, a wavelength of 9.11 microns (achievable using the oxygen-18 isotope), and a minimum energy provided of 15 Joules/pulse in the far field[1].

[1]The term far-field is often confusing. It is most useful to the laser designers who must specify a wavefront which their laser must produce to ensure a maximum heterodyne mixing efficiency. The performance codes used during this Study determine the mixing efficiency by propagating the laser wavefront through the optical subsystem to the

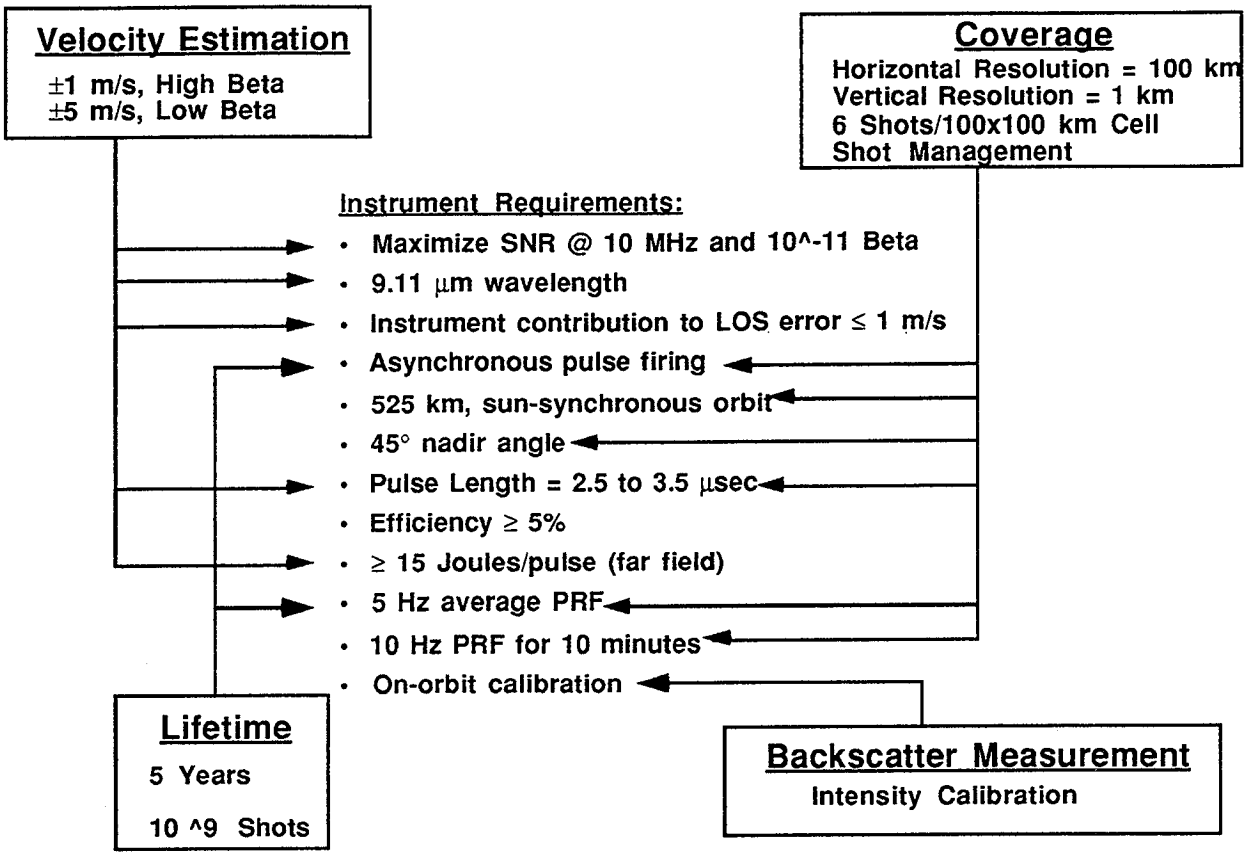

Figure 2.1-1 Science and Instrument Requirements

The requirements for coverage include: horizontal resolution of 100 km, vertical resolution of 1 km, shot density of 6 shots per 100 km x 100 km cell area, and shot management capability. These coverage requirements and the specified 525 km sun-synchronous orbit drive the following instrument requirements: asynchronous pulse firing, 45-degree nadir angle, pulse length between 2.5 and 3.5 μsec (mentioned previously), and 5-Hz average pulse repetition frequency. The so-called Survey Mode of the LAWS instrument will provide the required six shots (three shot pairs) in each 100 km x 100 km cell area. The maximum shot rate for the Survey Mode is approximately

---

atmosphere ("the far-field") while at the same time virtually propagating the local oscillator field back through the same optical subsystem. The mixing efficiency is then calculated as the overlap of the 2 wavefronts in the "far-field." The laser codes which are used to predict the laser performance and evaluate competing designs are defined in terms of this "far-field" energy, i.e. the quoted "useful" energy is the energy in the far field and the laser wallplug efficiency is predicted on the basis of the useful energy.

8 Hz (see section 5.1 for a more complete discussion of coverage and shot placement algorithms). The design also includes a high-repetition rate mode, with a 10 Hz average shot rate. This mode which will be used predominantly over the Tropics and perhaps other regions where ageostrophic conditions may be expected, will occur for periods under ten minutes.

Additional requirements for the instrument include: maximize the system signal-to-noise ratio (SNR) for a β of 10^{-11} (1/m-sr) and a noise equivalent bandwidth of 10 MHz. The weight requirement for LAWS is 800 kg, and the power available is 2.2 kW. The laser efficiency must be greater than 5%. The instrument life requirement is 5 years, and 10^9 shots.

The instrument specification has been developed based on the top-level science and instrument requirements given in the SOW and discussed above. The main parameters specified were: laser pulse energy, telescope aperture, scan rotation rate, and the maximum laser repetition rate. The laser pulse length, asynchronous operation, and nadir scan angle are given in the SOW, and were defined previously. The relationship of the derived design parameter, the value, and the driving requirement are summarized in Table 2.1-1.

Table 2.1-1 Top Level Instrument Specifications

Parameter	Value	Driver
Useful Pulse Energy	15 Joules	Performance, Power, Weight
Optics Aperture	1.5 meters	Size, Weight
Pulse Length	3 μsec	Laser Efficiency
Scan Rotation Rate	12 RPM	Various
Scan Nadir Angle	45 degrees	Coverage, SNR
Laser Repetition Rate	Asynchronous, up to 20 Hz	Coverage

The laser pulse energy at the exit pupil of the laser is a total of 19 Joules; however approximately 1.5 J falls outside of the 10 MHz bandwidth (the so-called gain-switch spike). The transition to the far-field (see earlier discussion) results in a so-called useful pulse energy of 15 Joules[2]. The telescope aperture is 1.5 m in diameter which is derived from the system size, weight and performance requirements. The laser pulse repetition rate is asynchronous, with a maximum

[2]N.B., 15 J is a specification used only by STI since their laser codes are defined in terms of the far-field pulse energy. The performance model uses 17.5 J (the energy within 10 MHz); the transition to the far-field being accounted for by the mixing efficiency factor.

burst rate of 20 Hz, equivalent to a minimum interval of 50 msec between pulses. The duration that the instrument can be operated in a particular mode (Survey Mode, High Repetition Rate Mode or Burst Mode) is a function of the power available from the EOS Platform and the heat removal capacity of the laser fluid loop. The scan rotation rate is 12 RPM. This rate is selected to maximize the along-track resolution (the cross-track resolution is controlled by the pulse firing rate), while maintaining the necessary requirements for the residual lag angle compensation mirror.

2.1.2 Interface Requirements

The LAWS external interface requirements are specified by the EOS Program. These requirements are imposed for the EOS Platform (in this case the conceptual, MSFC-provided platform), launch vehicle, TDRSS, and EOSDIS interfaces. The LAWS launch vehicle interface requirements are coordinated through the EOS Program. The remaining EOS Program interface requirements are outlined below.

The design of the interfaces between the EOS Platform and the LAWS are in accordance with the requirements and constraints imposed by the General Instrument Interface Specification (GIIS). The specific interface requirements for accommodation of the LAWS on the EOS Platform will be defined herein, and will be referenced and/or transferred from this document into the LAWS ICD with the EOS Platform as the LAWS design matures, during Phase C/D of the program. The general requirements specified in the GIIS shall be consistent with and traceable to the detailed requirements specified herein and in the LAWS ICD with the EOS Platform. Section 3.0 of this Final Report provides details of design requirements which have been driven by the need to comply with the GIIS.

The TDRSS scheduled contact times shall be coordinated through the EOS Program. In accordance with EOS Program requirements, two orbits of data shall be stored. The LAWS instrument generates an orbit average of 270 Gigabits of data, (based on a 1.5 Mbps data acquisition rate over a 90 minute orbit period). The required TDRSS contact time per orbit is dependent upon the on-board data storage capability. The TDRSS contact time is TBD, pending further analysis.

The preliminary LAWS data system requirements are specified in the "LAWS Data System Preliminary Requirements," LAWS Data System Study Team, Document No. TBS. The data path from the LAWS to the EOSDIS is included in the document. The restrictions imposed by the User Segment shall be reflected in the LAWS-EOSDIS data flow scenario.

2.2 Specification and Subsystem Trees

The LAWS Specification and Subsystem Trees are shown in Figures 2.2-1 and 2.2-2, respectively. The Specification Tree identifies the requirements flow from the EOS Program documentation, including the Performance Assurance Requirements and General Instrument Interface Specification, to the LAWS documents. The existing LAWS documents include GE-TBD DR-10, the Contract End Item Specification, GE-TBD DR-9, the Interface Requirements Document, and GE-TBD DR-7, Systems Engineering and Integration Requirements. The Subsystem Tree identifies the 3 major LAWS subsystems (Laser, Optics and Receiver), in addition to all of the support subsystems. Each subsystem is segmented into assemblies, where appropriate. The Subsystem Tree identifies hardware assemblies at the level required for the generation of top-level subsystem and component performance specifications.

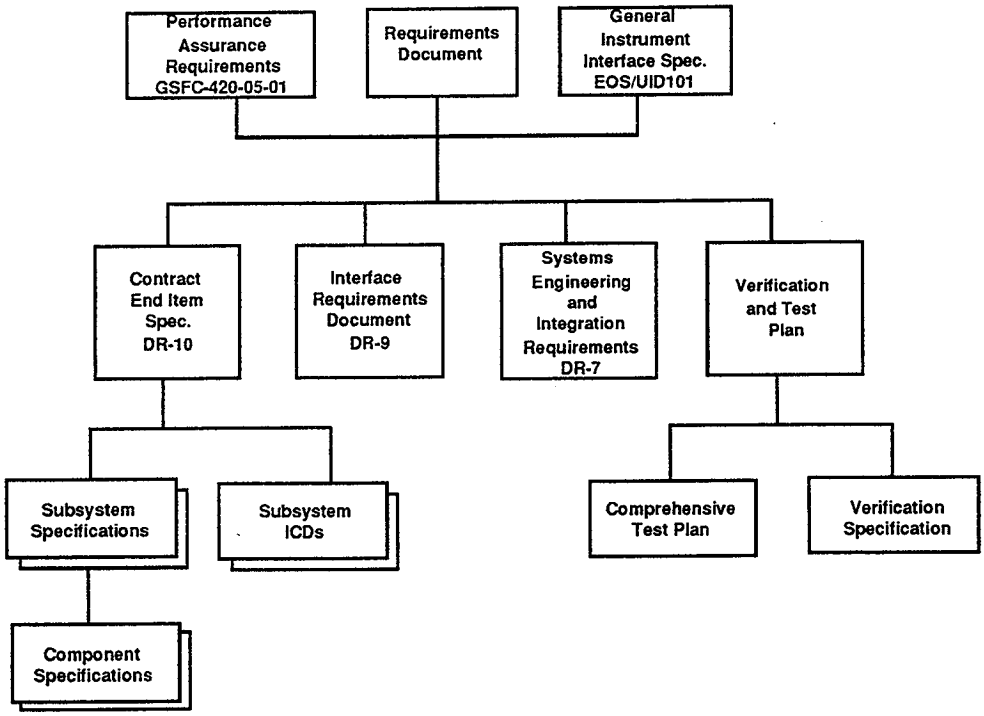

Figure 2.2-1 Laws Specification Tree

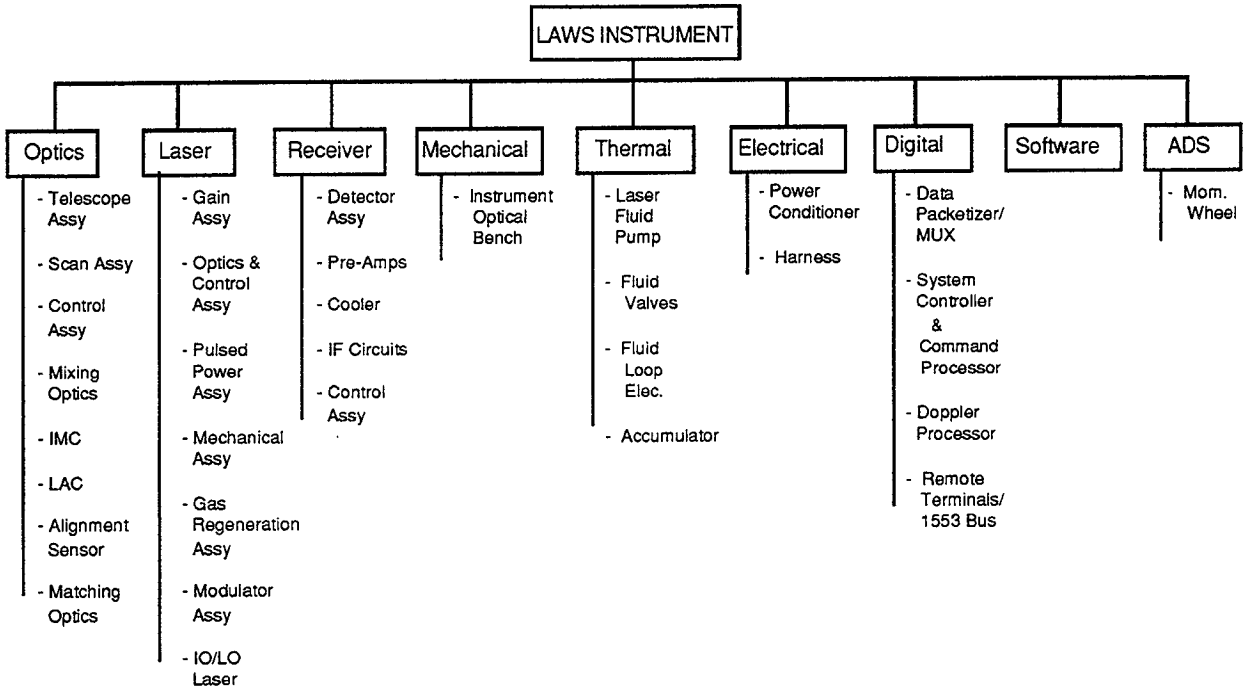

Figure 2.2-2 LAWS Subsystem Tree

2.3 Subsystem Level Requirements

2.3.1 Performance Requirements

The top-level performance requirements for the 3 major subsystems are given in Tables 2.3-1 to 2.3-3 Further details are available in GE-TBD DR-10 "Preliminary CEI Specifications."

Table 2.3-1 Optical Subsystem Requirements

OPTICAL SUBSYSTEM	
Telescope Aperture	1.5 meters
Nadir Angle	Fixed at 45°
Rotation Rate	12 RPM
Lag Angle Compensation	Support Asynchronous PRF
Laser Feedback (Narcissus)	< 0.01%
Boresight Stability During Round Trip Time	1.5 μrad (1 sigma, per axis)
Other	No Internal Focal Points

Table 2.3-2 LaserSubsystem Requirements

LASER SUBSYSTEM	
Pulse Energy	> 15 Joules in Far Field
Pulse Repetition Frequency	Asynchronous, Commandable to 20 Hz
Pulse Length	3 μsec
Wavelength	9.11 μm
Chirp	< 200 kHz over 3 μsec
Beam Quality	< 1.1 x Diffraction Limited
Beam Jitter (Shot to Shot at Laser Exit)	< 25 μrad
Wallplug Efficiency	> 5%
Lifetime	10^9 Shots

Table 2.3-3 Receiver Subsystem Requirements

RECEIVER SUBSYSTEM	
Detection Method	Heterodyne
Detector	5-Element HgCdTe
Bandwidth	1.2 GHz
Quantum Efficiency	40% at Maximum Bandwidth
Dynamic Range	60 dB
Calibration	On-Board Intensity and Velocity Calibration

2.3.2 Subsystem Interface Requirements

The LAWS subsystems and the inter-subsystem and platform interfaces are depicted in Figure 2.3-1. Intra-subsystem interfaces are also indicated. Interface details are given in GE-TBD DR-9 "Interface Requirements Document."

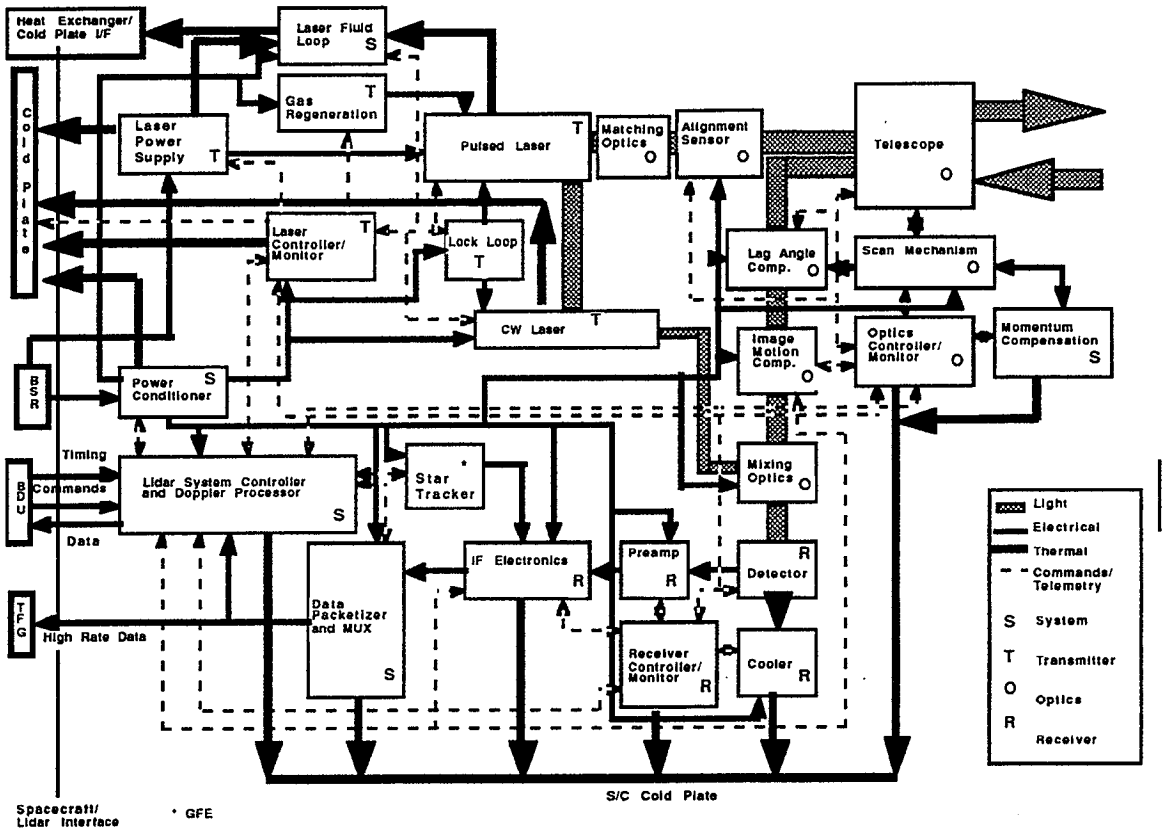

Figure 2.3-1 System Functional Block Diagram

2.4 System Error Budget

This section presents the error budgets, associated requirements allocations, and supporting error analyses. The LAWS instrument, in conjunction with Ground-Segment algorithms, will provide measurements of Doppler frequency, from which line-of-sight (LOS) wind-velocity components are derived, which in turn are used to compute horizontal wind vectors. The top-level data flow is indicated in Figure 2.4-1.

The scope of this section is limited to the portions of the error budget that impact the instrument performance requirements. The only instrument-determined parameter that affects the accuracy of the horizontal inversion process will be the horizontal spatial distribution of measurements, determined by the laser inter-pulse time interval and the telescope scan rate. The derivation of requirements for these parameters, and the analysis of the horizontal inversion accuracy, were not part of this Study.

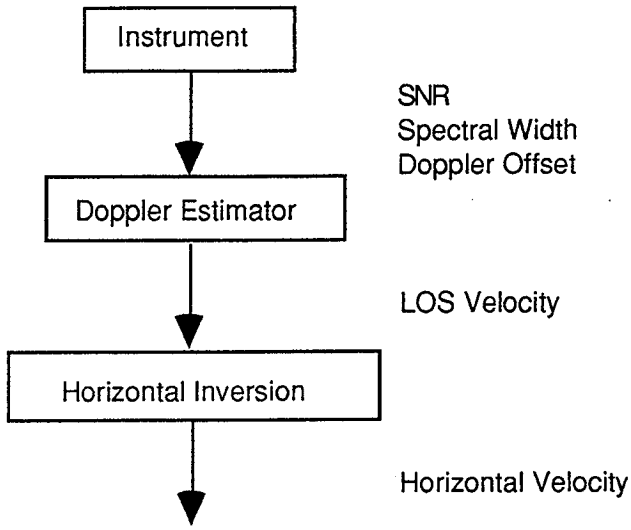

Figure 2.4-1 Top-Level Data Flow

The specified instrument LOS velocity accuracy requirement is 1.0 m/s one-sigma, from a single pulse return, over a 1 km altitude interval. As shown in the allocated error budget in Figure 2.4-2, the two major categories of error sources contributing to the LOS velocity measurement are: 1) LOS Doppler estimation error, and 2) Doppler offset (subtraction) error. The overall LOS Doppler estimation accuracy and reliability are dependent upon the Doppler Estimator as well as the instrument performance, and therefore cannot be specified solely as an instrument requirement. Section 2.4.5 discusses some of the issues pertaining to estimator performance and SNR requirements. The remainder of this section, however, addresses only the spaceborne instrument contributions to the error budget, assuming the estimator random measurement uncertainty is determined by the received signal spectral spread.

A distinction is made between three temporal scales: 1) random errors (pulse-to-pulse), 2) systematic errors (over several scans), and 3) long-term errors (over several orbits). The Doppler estimation component is random from pulse-to-pulse, while the Doppler offset is partly random, and partly systematic over several scan periods. Returns from ground observations may be used to correct for the long-term errors, and the time interval defined as "long-term" is sufficient to reduce the correction residuals to a negligible contributor. Therefore, the only significant error budget contributors are "random" and "systematic". Since suitable ground observation opportunities may not occur on every orbit, variations that occur over one orbit must be included in the "systematic" category.

The systematic error represents a more serious performance-limiting factor than the random error, because it is not reducible by averaging multiple pulse returns from a horizontal grid, and it

is therefore weighted more heavily in the overall budget. The allocated requirement proposed here is that the sum of the one-sigma random error and the two-sigma systematic error be less than 1.0 m/sec. Figure 2.4-2 shows the error budget allocated from this requirement. A bottom-up prediction of achievable performance is shown in Figure 2.4-3.

The signal-to-noise ratio (SNR) will affect the reliability, but not the accuracy of the Doppler Estimator, and is therefore independently budgeted. There is no definite SNR requirement, so the design guideline is to achieve a maximum "practical" SNR.

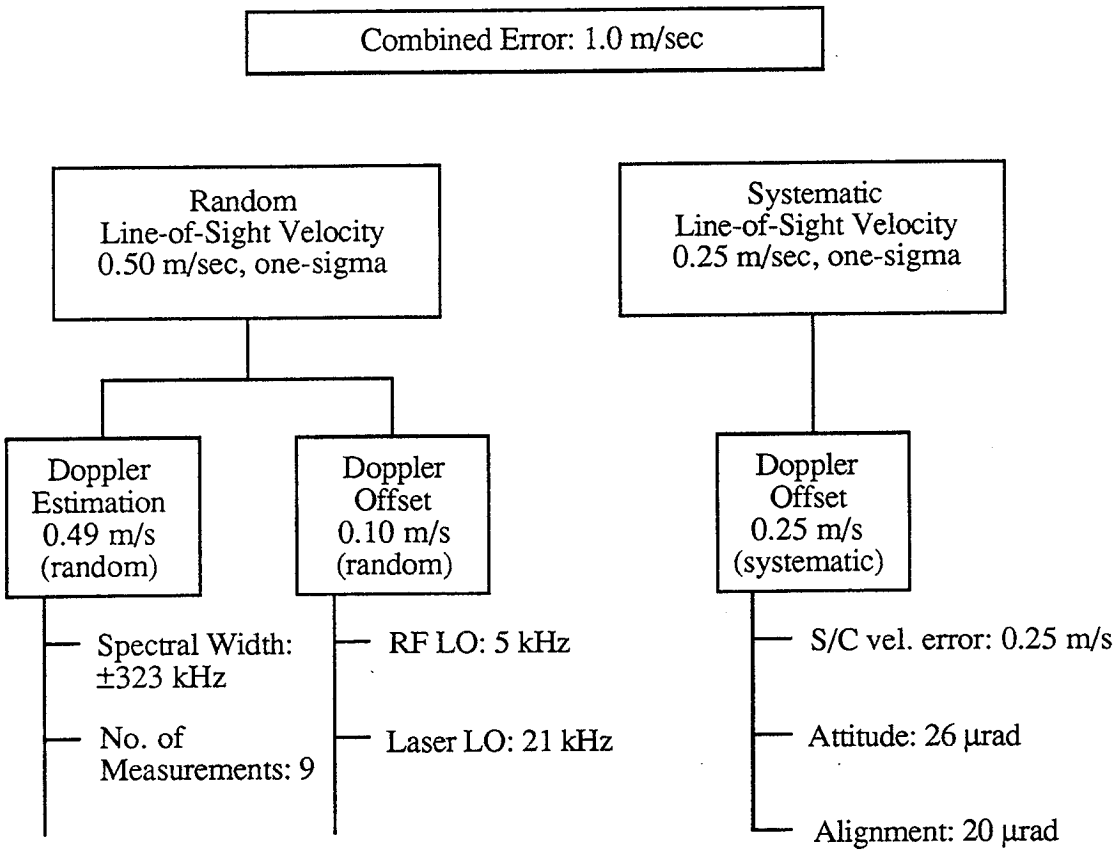

Figure 2.4-2. LOS Velocity Error Budget Allocation

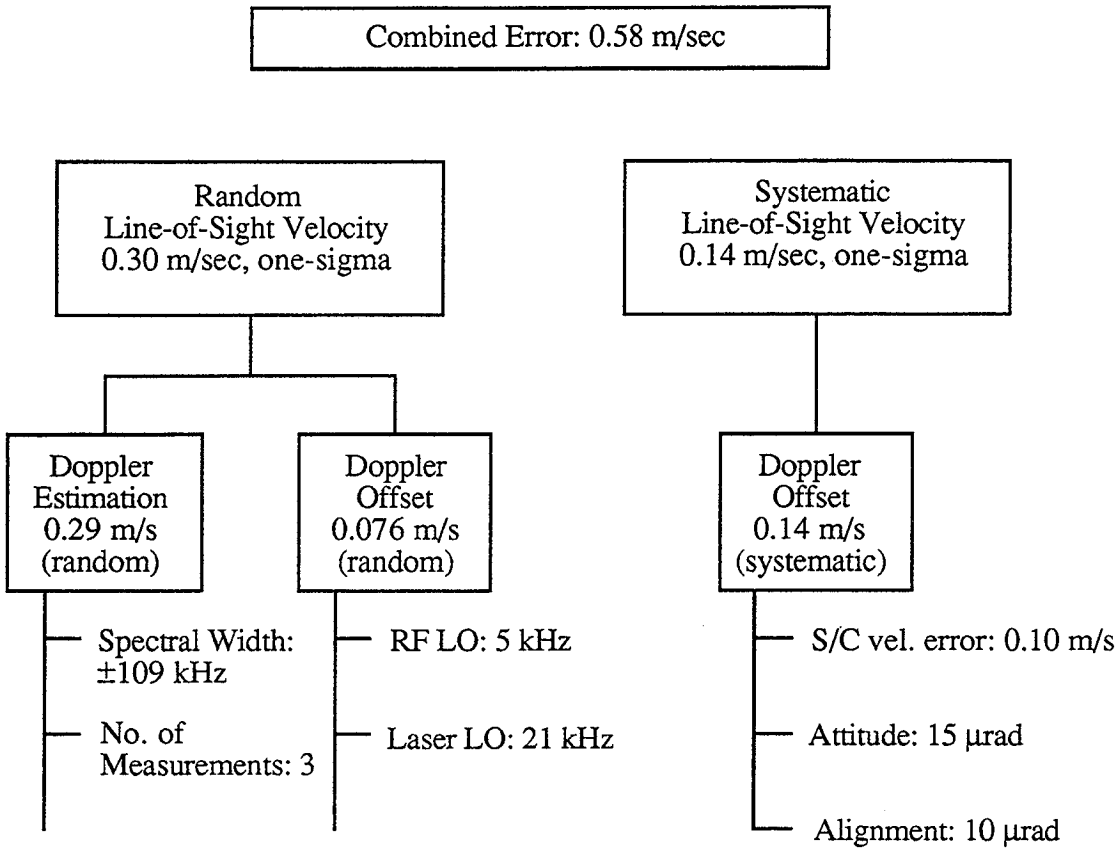

Figure 2.4-3 Predicted Error Budget

2.4.1 Doppler Estimation

Assuming adequate SNR for reliable Estimator operation, the resulting estimation accuracy will be given by:

$$\sigma_{los} = (\lambda/2)\ \sigma_f / \sqrt{N}$$

where

σ_f = standard deviation of the received signal spectrum

N = equivalent number of independent samples over the 1km altitude interval.

The predicted spectral width budget, excluding atmospheric effects, is shown in Figure 2.4-4, based on analyses of the laser chirp and the pulse transform spectrum. Only the portion of the laser pulse that contributes to a narrow-band Doppler signal is considered; the initial gain switched spike has a wide bandwidth that only contributes to a noise floor in the spectrum, and is therefore excluded from this portion of the analysis. The laser pulse spectrum and pulse width are shown in

Figure 2.4-5. The computed chirp spectrum, based on modeling by STI, is ± 75 kHz standard deviation, and the transform contribution is ± 80 kHz, giving an RSS spectral standard deviation of σ_f = 109 kHz.

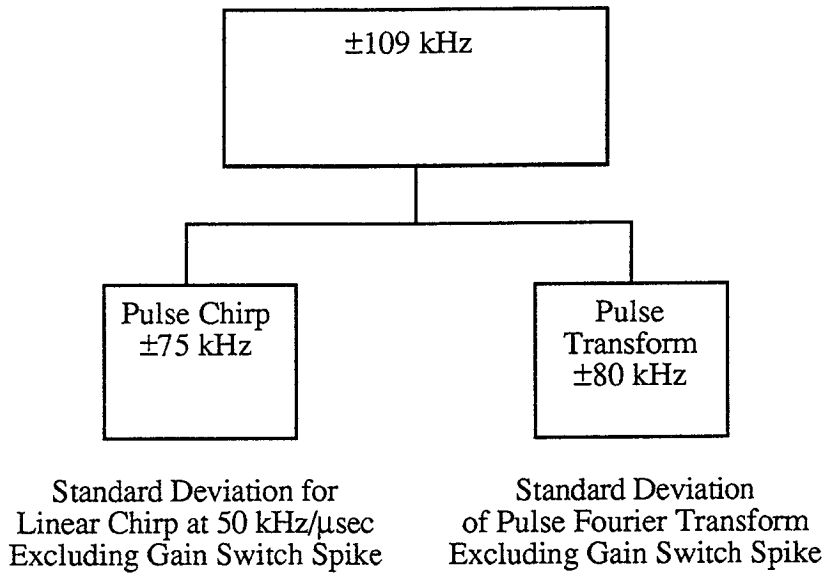

Figure 2.4-4 Spectral Width Budget

If N independent measurements are made during the 1 km altitude interval, the resulting Doppler estimation variance will be reduced by 1/N. For the LAWS viewing geometry (525 km altitude and 45° nadir angle) the time interval corresponding to 1 km altitude is T = 10.364 μsec. For continuous sampling of a signal, the resulting sample mean will have a variance given by

$$\sigma_s^2 = (2\,\sigma_x^2 / T^2) \int (T - \tau)\, \rho(\tau)\, d\tau$$

where

T = integration time

$\rho(\tau)$ = normalized auto correlation function

The variance reduction factor, $N = \sigma_x^2/\sigma_s^2$, achievable by sampling over the given time interval, can be described as the equivalent number of independent samples. Based on this analysis, 3.0 independent samples are available. This means that if three or more estimates are made over the 1 km interval, the variance of the average will be reduced by 1/3. The resulting Doppler estimation error is

$$(\lambda/2)\sigma_f/\sqrt{N} = 0.29 \text{ m/s}$$

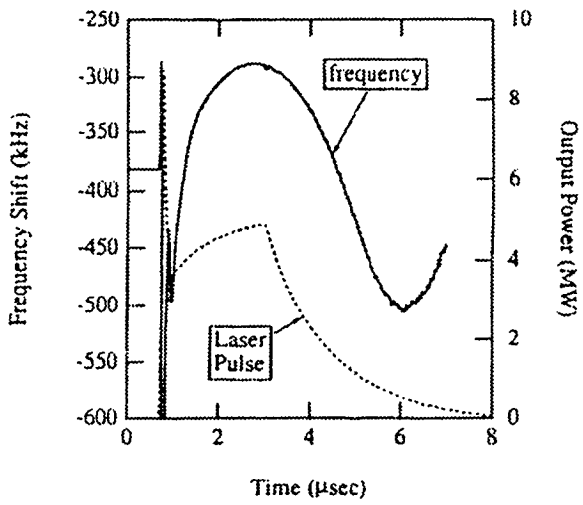

Figure 2.4-5 Laser Pulse Chirp

2.4.2 Doppler Offset

The LOS wind velocity will be determined by subtracting a Doppler offset, F_{DO}, from the measured Doppler:

$$V_{los} = (\lambda/2)\,[F_D - F_{DO}],$$

The offset is computed from :

$$F_{DO} = (2/\lambda)\,[v_e - v_s] \bullet r$$

where

v_e	=	Earth surface velocity
v_s	=	Spacecraft velocity = 7599 m/s
r	=	LOS unit vector.

The velocity offset error, in terms of uncertainties in the components of v_S and r, is:

$$(\lambda/2)\Delta F_{DO} = \Sigma\,[\Delta v_{si}\, r_i + \Delta r_i\, v_{si}]$$

where

i	=	index for x,y,z components.

In the spacecraft reference frame, the velocity is nominally along the x-axis, and therefore $\Delta v_{sx} >> \Delta v_{sy,z}$. The resulting simplified expression is:

$$\Delta v = (\lambda/2)\Delta F_{DO} = \Delta v_s \cos\psi \sin\phi + v_s(\Delta p \cos\phi + \Delta y \sin\psi \sin\phi)$$

where

ψ	=	scan angle, relative to velocity vector,
ϕ	=	cone angle, relative to spin axis
Δp, Δy	=	pitch and yaw angle errors.

If the velocity knowledge error is small enough that the total error is dominated by angle uncertainty, then the maximum occurs when viewing cross track ($\psi = 90°$):

$$\Delta v = v_s(\Delta p \cos\phi + \Delta y \sin\phi)$$

The resulting rms LOS velocity error, for random independent pitch and yaw uncertainties, with equal variances, and for $\phi = 45°$, will be

$$\sigma_v = v_s \sigma_a,$$

where

σ_a	=	pitch and yaw angle standard deviations.

Allocating 0.25 m/sec for the one-sigma systematic error in LOS velocity offset, the resulting angle knowledge requirement is

$$\sigma_a < 32.9 \text{ } \mu\text{radians}$$

The maximum contribution for spacecraft velocity uncertainty occurs at $\psi = 0°$, for which

$$\sigma_v = \sqrt{(\sigma_{vsc}^2 + v_{sc}^2\sigma_p^2)/2}$$

To meet the same allocation ($\sigma_v < 0.25$ m/sec) then requires a spacecraft velocity uncertainty $\sigma_{vsc} <$ 0.25 m/sec.

2.4.2.1 Ground Return Corrections

Ground return signals, used for correcting long-term systematic errors, will have a LOS velocity measurement:

$$v_g = v_s[\cos\psi \sin\phi + \Delta p \cos\phi] + \Delta v_s \cos\psi \sin\phi + V_{lo},$$

where

V_{lo} is the effect of LO frequency error.

The sum of measurements at $\psi = 0°$ and $\psi = 180°$ (fore and aft) will be

$$v_g(0) + v_g(180) = 2(v_s \Delta p \cos\phi + V_{lo}),$$

giving a measurement of the combined effect of Δp and V_{lo}. The difference between the measurements at these locations is $v_g(0) - v_g(180) = 2(v_s + \Delta v_s)\sin\phi$, indicating the spacecraft velocity error. Yaw errors are corrected by noting the scan angle positions for maximum and minimum frequencies ($\psi = 0°$ and $\psi = 180°$).

2.4.2.2 Attitude Determination

The requirements allocated for instrument attitude determination (per axis, one-sigma) are:

1. Star Tracker random error: 13 μradians
2. Star Tracker systematic error: 26 μradians
3. Physical alignment between star tracker and LAWS boresight: 20 μradians

The expected performance from ASTRA-2 star trackers, operating in a gyroless, multiple-star mapping mode, is 10 μradians random error and 15. μradians systematic.

2.4.2.3 Spacecraft Velocity

The allocated requirement for spacecraft velocity knowledge is 0.25 m/s, one-sigma. The predicted 6-channel GPS receiver performance is < .10 m/s.

2.4.3 Pointing Jitter

Heterodyne detection efficiency is degraded by any relative misalignment between the transmit beam and the receiver optical boresight. The SNR budget allows an allocation of 1.5 μradian residual random jitter. This is a one-sigma error, per axis, that is independent from pulse to pulse. The design uses two control systems (shown in Figures 2.4-6 and 2.4-7) to provide corrections for attaining this performance: 1) an Image Motion Compensation (IMC) feedback loop; and 2) a Lag Angle Compensation (LAC) feed-forward system. In each case, there are three categories of error sources, as shown in the budget in Figure 2.4-8: 1) angle measurement errors;

2) control system residual errors; and 3) uncorrected effects (unsensed errors). The IMC system corrects for variations that occur during the transmit-receive interval (5. msec); the LAC for errors that are independent shot-to-shot. Pointing error sources that have longer decorrelation times are correctable by computing the long-term average signal levels from the four outer elements of the receiver detector.

A diode laser mounted on the telescope structure provides an object-space alignment-measurement source, that is detected by an angle-measurement sensor (the "boresight monitor") on the optical bench. A pair of Angle Displacement Sensors (ADS), mounted near the diode laser, provide a measurement of high-frequency inertial jitter. Signals from the boresight monitor and the ADS are then applied to the IMC mirror to stabilize the receive boresight. The measurement errors listed in Figure 2.4-8 include both sensor noise and gain calibration uncertainties. The portions of the optical paths that contribute to "uncorrected effects" are identified in the following analysis.

The alignment errors considered in this budget are:

1. Inertial orientation of the instrument, considered as a rigid body
2. Bending of the optical bench, between the receiver detector and the scan assembly.
3. Bending of the receive optical boresight due to misaligned optical bench components.
4. Laser boresight jitter
5. Scan bearing assembly jitter
6. Bending of telescope metering structure and secondary mirror mount
7. Difference between boresight-monitor detector axes and receiver detector axes.

The reference frames used in the jitter analysis, shown in Figure 2.4-9, define the physical alignment of the receiver detector boresight ($x_1y_1z_1$), the optical bench interface to the scan bearing ($x_2y_2z_2$), the telescope primary mirror ($x_3y_3z_3$), and the alignment source ADS inertial sensor ($x_4y_4z_4$). The figure also shows the optical boresights of the receive beam (v_r) and the transmit beam (v_t) at the optical bench-to-scan assembly interface. The angles used in the analysis are defined below:

θ_i = Orientation of $(x_1y_1z_1)$ relative to inertial

θ_r = Orientation of v_r relative to $(x_1y_1z_1)$

θ_{bs} = Orientation of v_r relative to boresight sensor

θ_L = Orientation of v_t relative to $(x_1y_1z_1)$

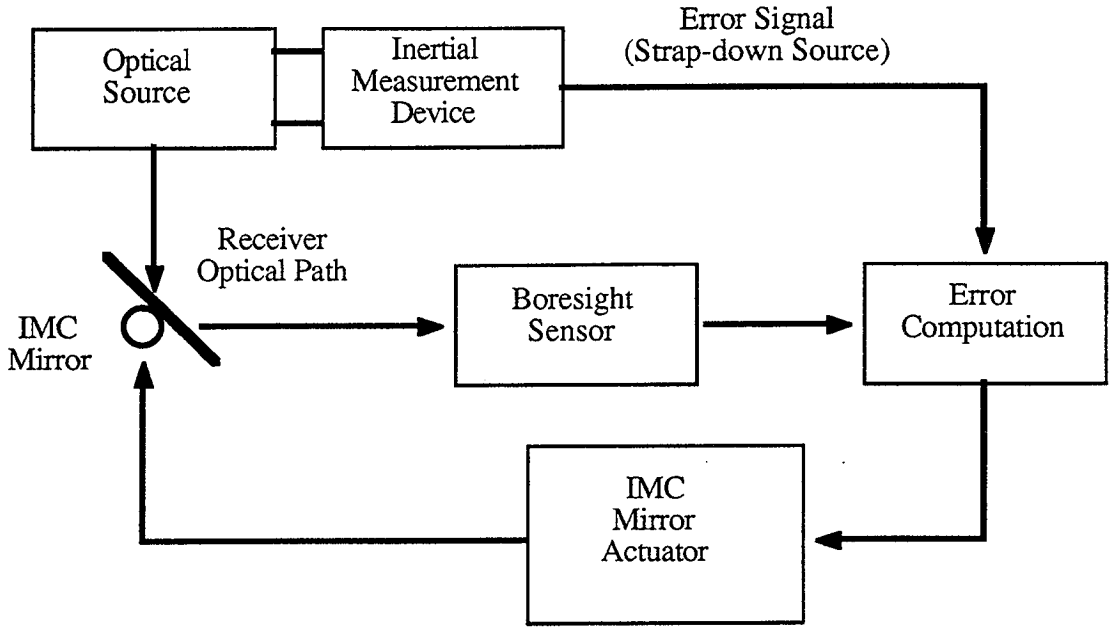

Figure 2.4-6 IMC Control System

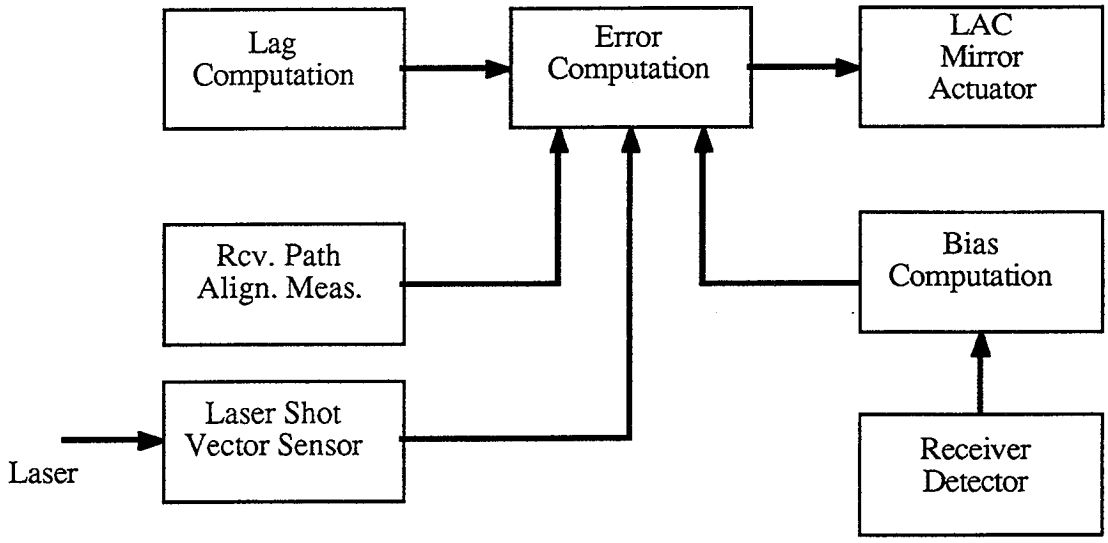

Figure 2.4-7 LAC Control System

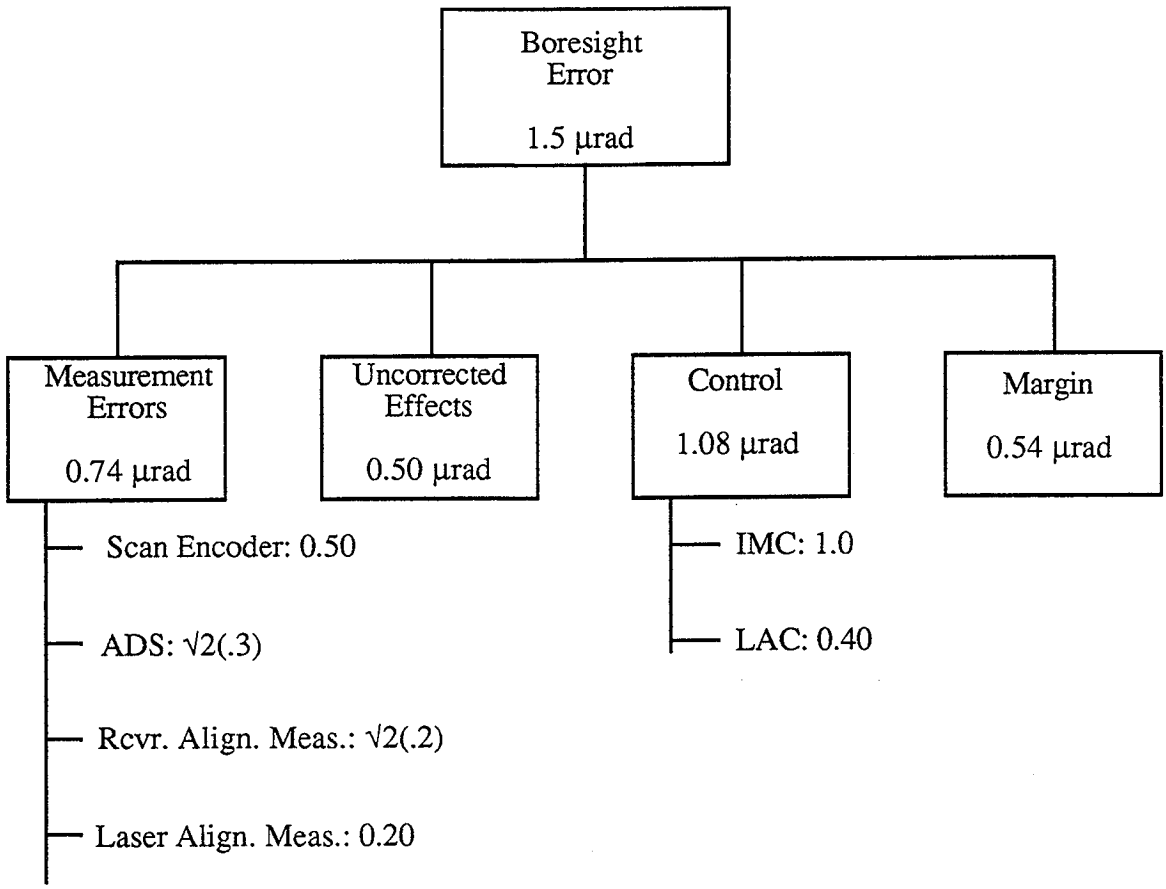

Figure 2.4-8 Pointing Jitter Budget

θ_b	=	Orientation of $(x_2y_2z_2)$ relative to $(x_1y_1z_1)$
θ_{pm}	=	Orientation of $(x_3y_3z_3)$ relative to $(x_2y_2z_2)$
$\theta_{pbr}, \theta_{pbt}$	=	Orientation of $(x_3y_3z_3)$ relative to v_r, and v_t
θ_{sm}	=	Orientation of the telescope secondary boresight, relative to $(x_3y_3z_3)$
θ_{ms}	=	Orientation of $(x_4y_4z_4)$ relative to $(x_3y_3z_3)$
θ_j	=	Orientation of alignment source boresight relative to $(x_4y_4z_4)$
M	=	Telescope magnification

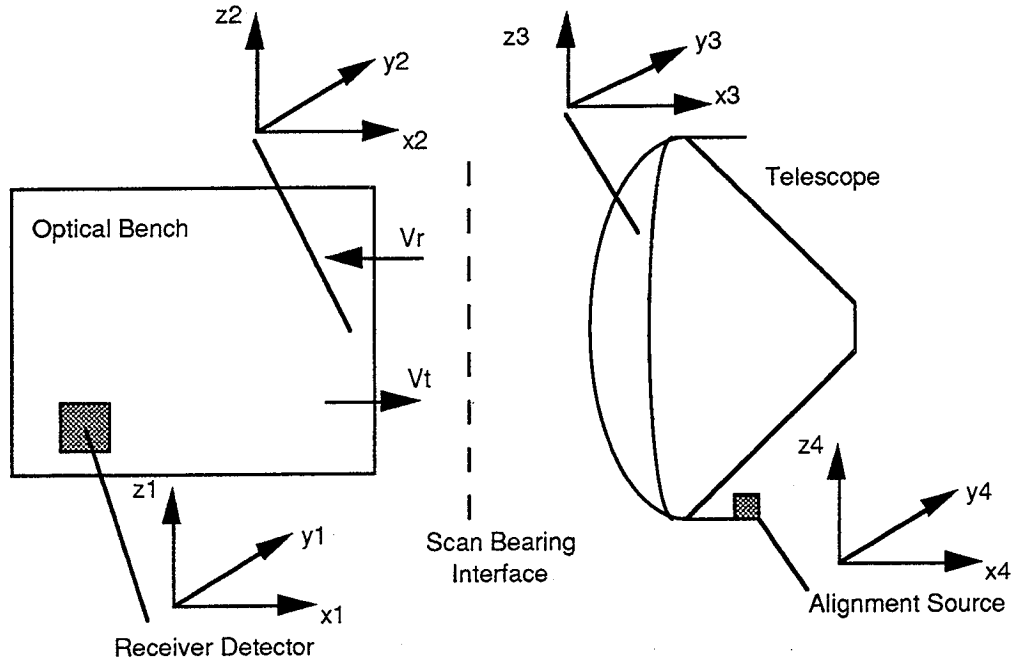

Figure 2.4-9 Reference Frames

The transmit beam boresight angle, in object space, relative to the inertial frame at t=0, is:

$$\theta_1 = \theta_i(0) + \theta_L + [(M-1)/M]\theta_{pbt} - \theta_{sm}(0)/M$$
$$= \theta_i(0) + \theta_L/M + [(M-1)/M]\,[\theta_{pm}(0) + \theta_b(0)] - \theta_{sm}(0)/M$$

Similarly, the receive boresight angle, at time $t = \tau$, is given by :

$$\theta_2 = \theta_i(\tau) + \theta_r(\tau)/M + [(M-1)/M]\,[\theta_{pm}(\tau) + \theta_b(\tau)] - \theta_{sm}(\tau)/M$$

The transmit-to-receive error, without applying any IMC correction, is then:

$$\Delta\theta = \theta_2 - \theta_1$$

The inertial measurement performed on the telescope structure, at the alignment-laser source, is:

$$M_{ir} = \theta_i(t) + \theta_b(t) + \theta_{pm}(t) + \theta_{ms}(t) + \varepsilon_{ir}$$

where e_{ir} is the inertial measurement error (ADS). The open-loop measurement by the boresight detector is given by:

$$M_{bs} = \theta_j + \theta_{ms} + \theta_f + (\theta_{sm} + \theta_{pm} + \theta_b - \theta_r + \theta_{bs})/M + \varepsilon_{bs}$$

where θ_f represents a possible error contribution due to telescope defocus, (i.e. measuring alignment with partial aperture illumination) and ε_{bs} is the boresight sensor error. Applying this correction to the IMC mirror results in a residual receive-time error, allocated to the IMC system:

$$\begin{aligned} E_{imc} &= \theta_2 + M_{bs}(\tau) - M_{ir}(\tau) \\ &= \theta_{bs}(\tau)/M + \theta_f(\tau) + \theta_j(\tau) + \varepsilon_{ir}(\tau) + \varepsilon_{bs}(\tau) \end{aligned}$$

Similarly, application of transmit-time correction to the LAC results in the following LAC system error:

$$E_{lac} = \theta_1 + M_{bs}(0) - M_{ir}(0) + M_{svs} + \varepsilon_{se}$$

where M_{svs} is the shot-vector sensor measurement of laser beam alignment:

$$M_{svs} = [\theta_{pm}(0) + \theta_b(0) - \theta_L]/M + \varepsilon_{svs}$$

and ε_{se} is the contribution from scan encoder measurement error. Substitution then gives:

$$\begin{aligned} E_{lac} = [\theta_{pm}(0) + \theta_b(0) - \theta_r(0) + \theta_{bs}(0)]/M + \theta_f(0) + \theta_j(0) + \varepsilon_{ir}(0) \\ + \varepsilon_{bs}(0) + \varepsilon_{svs} + \varepsilon_{se} \end{aligned}$$

The relative receive-to-transmit residual error is then:

$$\begin{aligned} E = E_{imc} - E_{lac} = \{[\theta_r(0) - \theta_{pm}(0) - \theta_b(0)]/M\} \\ + \{[\theta_{bs}(\tau) - \theta_{bs}(0)]/M + \theta_f(\tau) - \theta_f(0) + \theta_j(\tau) - \theta_j(0)\} \\ + \{\varepsilon_{ir}(\tau) - \varepsilon_{ir}(0) + \varepsilon_{bs}(\tau) - \varepsilon_{bs}(0) - \varepsilon_{svs} - \varepsilon_{se}\} \end{aligned}$$

The first term includes the error due to an unwanted "correction" for receive path bending at the transmit time, and a portion of the laser beam alignment measurement. Both of these are pulse-to-pulse independent errors. The second term includes high-frequency components of uncorrected

errors, which decorrelate over the transmit-receive interval (t = 5. msec). The third term includes the error contributions from the measuring devices (ADS, boresight sensor, shot-vector sensor, and scan encoder).

The closed-loop boresight measurement, for zero control error, will be:

$$M_{ir} = \theta_i + \theta_{pm} + \theta_b + \theta_{ms} + \varepsilon_{ir}$$

This indicates the dynamic range over which the boresight monitor detector is required to operate.

2.4.4 Heterodyne Efficiency

The heterodyne efficiency is determined by the following parameters:

Pointing jitter
Wavefront phase errors
Laser output profile
Beam truncation

The effects of pointing jitter were simulated, assuming that the pointing error along each axis is an independent Gaussian process, with equal variances. The resulting efficiency degradations are shown in Figure 2.4-10 as a function of per-axis one-sigma pointing errors.

2.4.5 Doppler Estimator

Doppler estimation accuracy is dependent upon the particular estimator algorithm employed, and generally must be determined by simulation. As a benchmark, an analytical expression may be used for the expected lower bound. The expression used here is the Cramer-Rao bound derived by Zrnic [1,2] for the case of a Gaussian signal spectrum and additive white Gaussian noise over the Nyquist frequency band:

$$\sigma_v^2 = (\sqrt{\pi})\lambda^2 W^3 / (F_S \cdot M \cdot SNR^2)$$

w	=	spectral width of the signal, Hz (Gaussian one-sigma)
F_S	=	sampling rate, Hz
M	=	no. of samples
SNR	=	wideband signal-to-noise ratio.

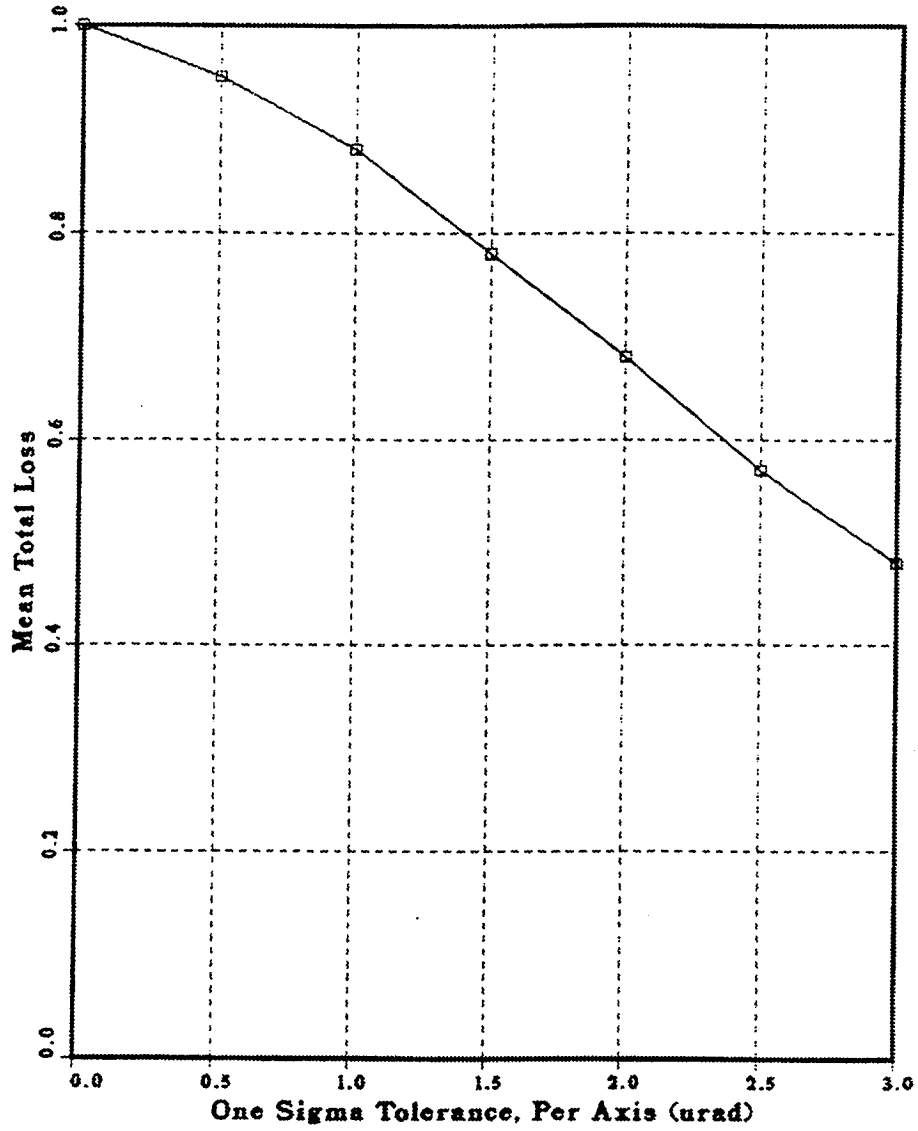

Figure 2.4-10 Degradation Due to Pointing Jitter

This equation is an approximation valid for high noise, for $w << F_S$, and asymptotic for large M. For the radar case, considered by Zrnic, M is the number of pulses processed (since the pulse rate is greater than the Doppler frequency). For Lidar, however, M is the number of digitized samples within one range bin of a single pulse return: $M = F_S \cdot \tau_d$, where τ_d is the decorrelation time of the transmitted pulse. The noise bandwidth assumed in the derivation of the equation was equal to the sampling frequency. The narrow-band noise bandwidth, matched to the signal spectrum, is $B = (\sqrt{2\pi})w$, giving a narrow-band signal-to-noise ratio:

$$SNR_n = SNR \cdot F_S / ((\sqrt{2\pi})\, w)$$

Substituting for M, and using the narrow-band SNR, then gives:

$$\sigma_v^2 = \lambda^2 w / (2(\sqrt{\pi})\tau_d \cdot M \cdot SNR_n^2) \qquad (1)$$

When n_m independent measurements are made to obtain an average over an altitude interval, the variance will be reduced to σ_v^2/n_m. For an altitude interval of 1 km, and 225 m range bins, n_m = 6. Figure 2.4-11 shows this velocity error bound, for w = 204 kHz, and τ_d = 1.5 μsec.

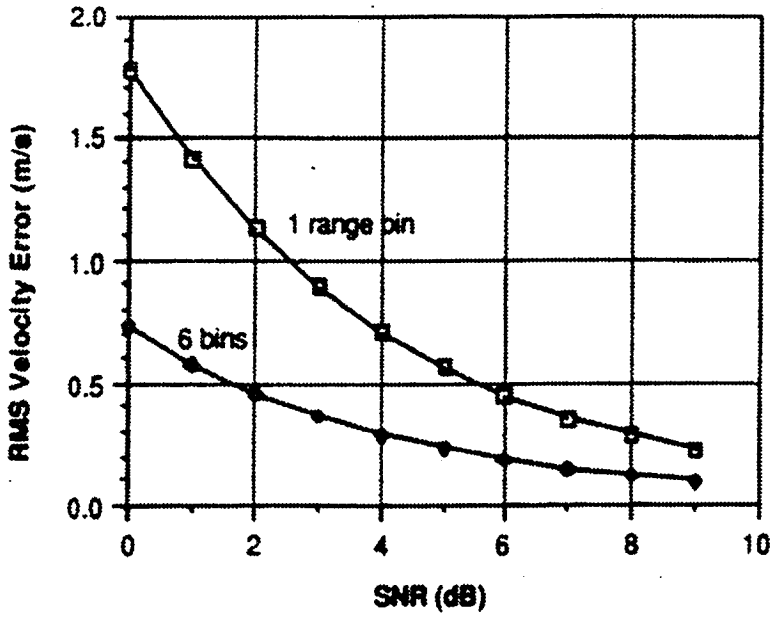

Figure 2.4-11 Cramer-Rao Bound

A more realistic assessment of Doppler estimation accuracy requires analysis and/or simulation of particular estimator algorithms. Anderson [3] has performed simulations to determine the performance of various types of estimators, and has reported the results as the percentage of estimates within a 1 m/sec error bound, which is a more appropriate performance measure in this case than the standard deviation of estimation error. The plot in Figure 2.4-12 shows his predicted performance for the Capon estimator (the best estimator considered), as a function of wide-band SNR. This analysis was performed for a 72-sample measurement, ±1 m/s signal bandwidth, and ±25 m/s processing bandwidth; the narrow-band SNR is 14 dB greater than the wide-band SNR

shown in the plot. Anderson reported that the performance of this algorithm can be improved 1 dB by processing overlapping data blocks. He also considered a "Block Filter Bank" (BFB) algorithm, which showed about 2.5 dB poorer performance than the Capon estimator.

An analysis was performed on an estimation procedure similar to the BFB, to determine its performance for the case of 16 frequency channels per measurement, and 6 measurements during a 1 km altitude interval. The estimation procedure assumed is simply the selection of the spectral channel that has the highest level. The probability of false alarm (i.e. the selection of a noise-only channel) is shown in Figure 2.4-13 as a function of narrow-band SNR. A detection criterion is employed that requires the selection of the same channel m out of n times, where n is the number of measurements in the altitude interval. The two curves are for 2 out of 6 (applicable to a 1 km altitude interval) and 3 out of 10 (1.6 km interval). Similarly, Figure 2.4-14 shows the probability of detecting the true signal. Anderson's study [3] indicated that the Capon Estimator can be expected to perform about 3.5 dB better than the BFB estimator, which suggests that a narrow-band SNR = 1 dB may provide adequate probabilistic performance.

References

[1] Dusan Zrnic, "Estimation of Spectral Moments for Weather Echoes," IEEE Trans. Geosc. Electr., Vol. GE-I 7, pp 113-128, Oct 1979.

[2] Pravas Mahapatra and Dusan Zrnic, "Practical Algorithms for Mean Velocity Estimation in Pulse Doppler Weather Radars Using a Small Number of Samples," lEEE Trans. Geosc. & Rem. Sens, Vol GE-21, pp 491-501, Oct 1983.

[3] John R. Anderson, "An Initial Study of the Use of High Performance Signal Processing Algorithms for the LAWS Instrument," Final Report for UAB Contract #SUB89-21 8,1989.

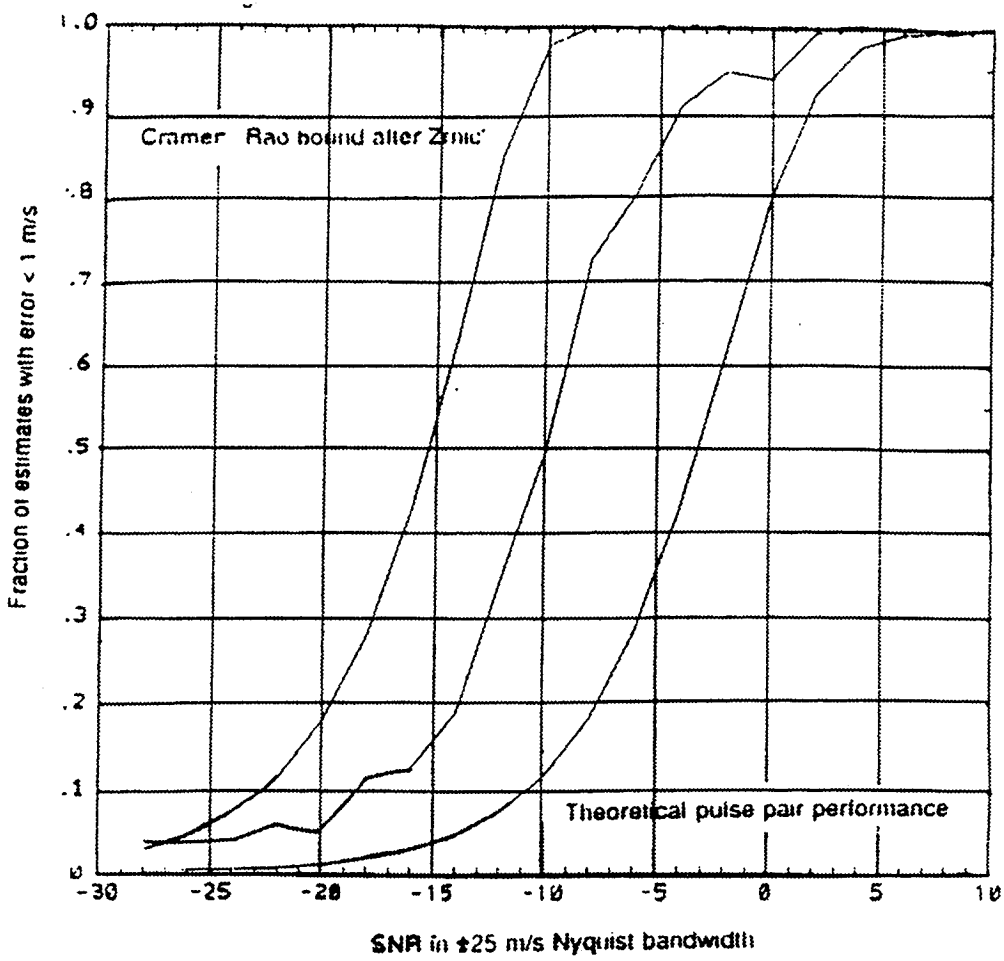

Figure 2.4-12 Capon Estimator Performance

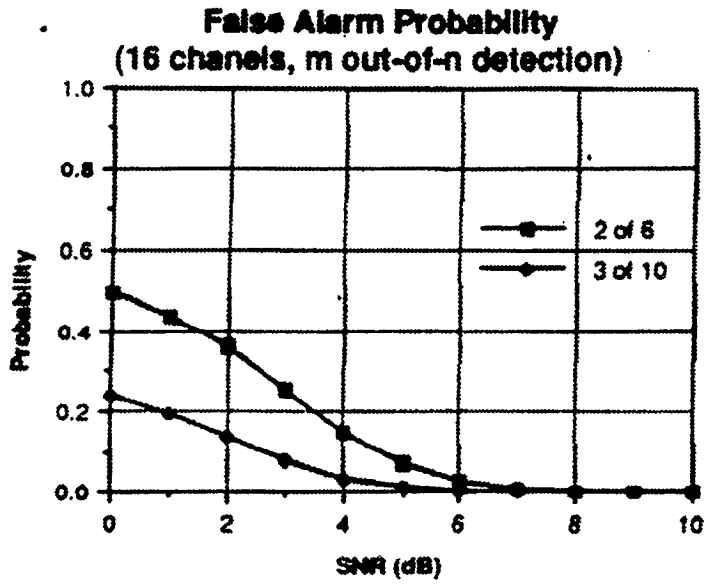

Figure 2.4-13 Estimator False Alarm Probability

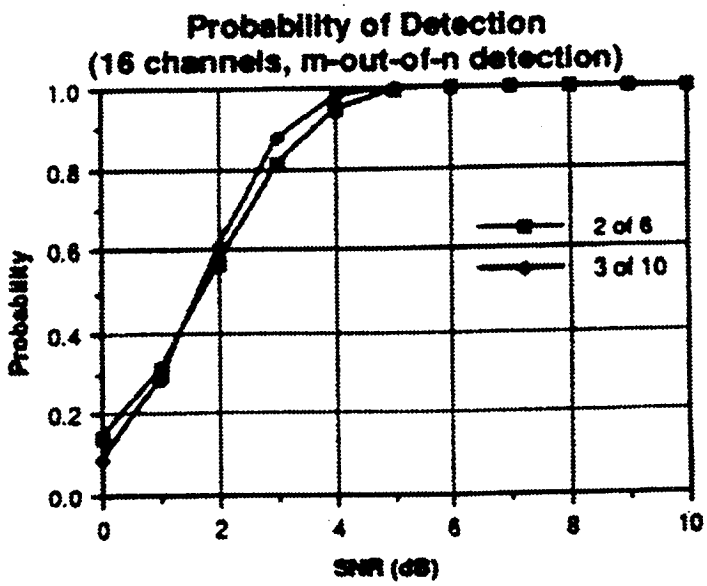

Figure 2.4-14 Estimator Detection Probability

2.5 Mission Operations

Figure 2.5-1 shows the LAWS mission timeline with mission phases on the left of the diagram and operational modes on the right. Specific mission events and their estimated times of occurance are shown in the middle of the diagram. The mission phases include: pre-launch, launch and ascent, orbit acquisition initialization, orbit trimming, operational initialization, normal operations and disposal. For each of these phases there are specific operational modes which are detailed in the next section. This mission timeline is based on the GIIS with the exception that an ATLAS IIAS launch vehicle has been assumed.

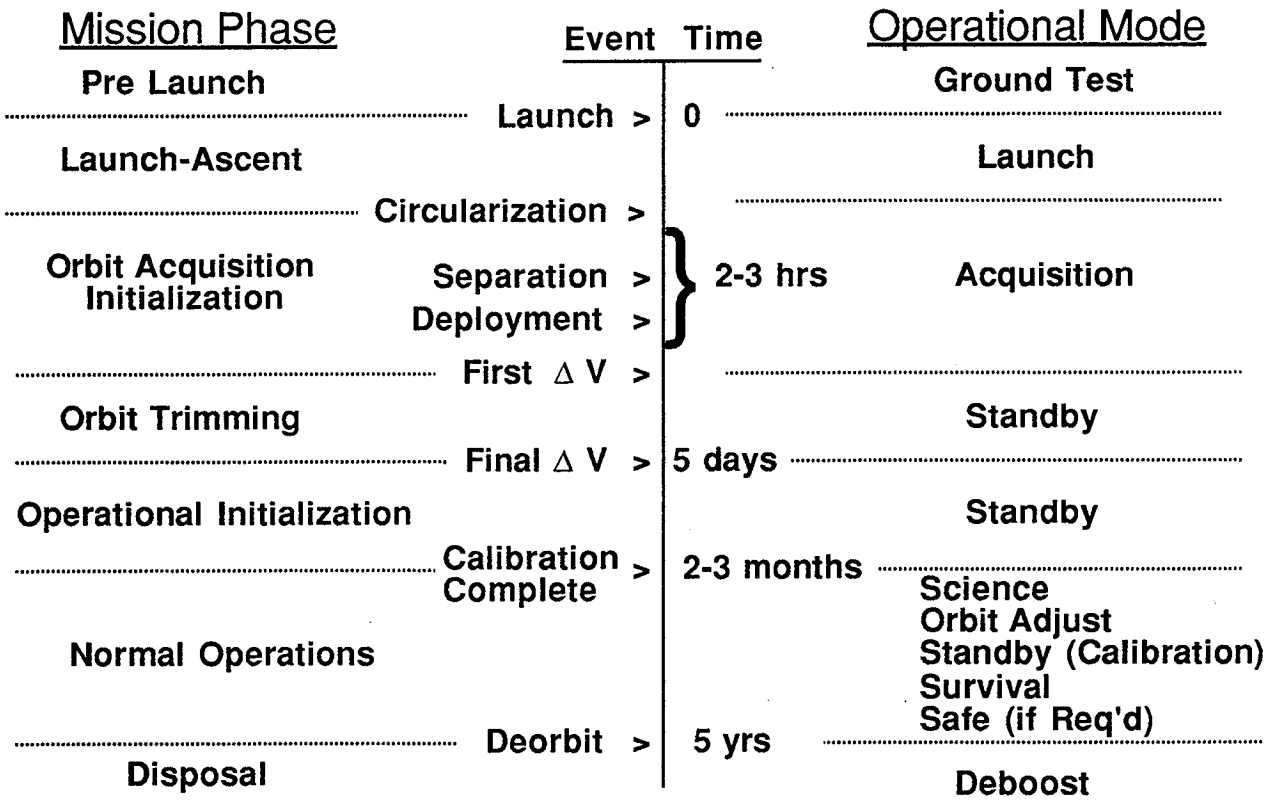

Figure 2.5-1 LAWS Mission Timeline

The pre-launch phase starts with the commencement of final countdown and ends with the separation of the T minus 0 umbilical. During this phase the instrument is connected to the ground support equipment and ground tests are performed to ensure flight readiness.

The launch and ascent phase starts with the disconnect of the T minus 0 umbilical and ends with the Atlas Centaur orbit circularization burn. The orbit aquisition initialization phase includes separation of the platform from the Atlas Centaur upper stage and deployment of the Platform

subsystems such as antennas and solar arrays. The instrument is in the acquisition mode during this phase.

The orbit trimming phase involves delta-v manuevers to place the Platform in the desired orbit (i.e. the 6 PM sun-synchronous orbit). The instrument is maintained in the standby mode during this phase. The operational initialization phase begins when the platform has reached the correct orbit and ends with commencement of normal operations. During this phase the Platform and LAWS instrument perform complete checkout and calibration functions.

The normal operations phase begins after the instrument is fully calibrated and system performance is completely verified. During this phase the Platfrom provides full resources to the instrument while in science mode and reduced resources during occasional orbit adjust and calibration modes. Survival and safe modes will also be included in this mission phase if required.

The final mission phase is the disposal phase after completion of the useful instrument and/or Platform life. Each mission phase comprises one or more operational modes. These modes are defined by the minimum functional and performance capabilities required to support the given mission phase. Detailed modes within the ground test, start-up, operational (or science) and stand-by modes will be identified during the LAWS Phase C/D program.

The ground test mode refers to the period after which the instrument and platform have been integrated into the launch vehicle and does not apply to the ground integration and test phase of the program. During this mode the platform receives power from the launch vehicle umbilical. Only survival heaters and essential low rate commands and telemetry are supported during this phase.

During the launch mode the platform batteries supply only survival heater power and the instrument is essentially off. During the acqusition mode the platform provides survival heater power and only essential low rate commands and telemetry are supported. It is during this phase that the platform establishes a telemetry link, deploys solar arrays and attains a stable attitude.

The standby mode is a non-science mode and occurs during orbit trimming and operational initialization. This mode includes complete instrument checkout, verification and calibration which will include occasional laser firing, operation of the receiver Stirling cryocooler, operation of the laser cooling loop and teslescope scanning. The high rate data link, however, may not be available.

The Science mode is the only mode which supports continuous laser firing and high data rate interfaces. During orbit adjust mode the science is not supported and most of the instrument systems including the telescope scanning, laser power supply and laser cooling loop will be off. Depending on the duration of this orbit adjust, the power to the receiver Stirling cryocooler will most probably remain on. This orbit adjust includes reboost and possibly out of plane manuevers.

During survival mode the platform provides only sufficient power for heaters and low rate commands and telemetry, all other non-essential instrument power will be off. During safe mode only survival heater power is supplied and there is no command and telemetry link between the instrument and platform. In addition, during safe mode, the Platform Control Processor (PCP) and Bus Data Unit (BDU) are off. The deboost mode provides the same platform resources (survival heaters and low rate data and telemetry) as the survival mode.

2.6 Reliability Analyses

The results of the Reliability Analysis include identification of the following system elements as potential single-point failures:

a. Laser Subsystem elements including: gain module fan, segmented electrode, catalytic monolith, photodetector, mirror actuator, and acoustic-optic modulator

b. Pressure boundary elements such as quick disconnects, valve packings and seats, seals and gaskets

c. Deployment mechanisms including: contamination cover, derotator launch lock "W" band, laser gain module launch lock separation nuts, laser supply gas tank isolation pyro valve (if laser gas supply required). These mechanisms are expected to have redundant pyro actuators. The single-point failure concern is in regard to mechanical elements such as springs, linkages, and other moving elements.

The feasibility of incorporating redundant Stirling Engine pairs within the LAWS weight budget was assessed. The failure rate of the engine used was .7327 per million hours (based on some TRW reliability calculations). Redundant engine pairs can be accommodated within the weight budget and were therefore included in the LAWS design.

The probability of success, P_S, for the LAWS design at five years is 0.9336, as a result of the preliminary Reliability Analysis. This value exceeds the required P_S at five years of 0.90 for critical measurements of Facility Instruments specified per NASA GSFC direction. The P_S values at five years for the LAWS subsystems are listed in Table 2.6-1.

Table 2.6-1 Probability of Success Estimates

Subsystem	P_S at Five Years
Optical	0.9811
Laser	0.9645
Receiver	0.9955
Thermal	0.9971
Electrical	0.9999
Digital	0.9941

The deployment mechanisms have a P_S value at 48 hours (initial on-orbit operating duration) of 0.9997. The single point failure requirement is addressed in the individual subsystem design description sections to follow. The requirements are derived from the Instrument PAR.

As a result of Reliability Analyses performed, the following recommendations have been incorporated into the system design:

1. Incorporation of redundant Sterling Engine pairs

2. Incorporation of redundant pyro-actuated valves for the pressure relief valve, fill valve and pressure transducer/controller in the gas refill system of the Laser Subsystem (note, a gas refill system is currently not part of the LAWS baseline). Leak detection provisions are recommended if the gas fill is required.

3. Incorporation of a 2-for-1 redundancy for the IF channels dedicated to each of the two redundant photodetectors in the Receiver Subsystem.

2.7 Risk Assessment

The specific subsystem components which were viewed as high risk are outlined in Table 2.7-1 along with the risk retirement plan. Note that this plan was drawn up at the beginning of Phase II and reflected the thinking regarding Phase B extension activities at that time. However, because of the successful IR & D and breadboard programs it is anticipated (at the time of writing) that Phase B extension activities will only be concerned with further lifetest demonstrations.

More information on the Laser Breadboard Program is contained in Section 6.0.

Table 2.7-1 Risk Reduction Plan

Risk Item	GE/STI/HDOS IR&D	Laser Breadboard	Extended Phase B	Other
Laser Subsystem				
Pulse Power	x	x	x	x[1]
Prionizer Discharge	x	x	x	
Catalyst Development		x	x	x[2]
Chirp	x	x	x	
Efficiency	x	x	x	
Flow Loop Uniformity		x	x	
Resonator Design		x	x	
Beam Jitter		x	x	
Asynchronous Operation			x	
Optics Contamination			x	
Alignment			x	
Laser Gas Chemistry	x	x	x	
IO/LO Laser			x	
Component Development	x	x	x	
Receiver				
Detector Quantum Eff.	x		x	x[3]
Detector Reliability	x		x	
Stirling Cooler				x[4]
Optical Subsystem				
Scan Bearing	x		x	x[5]
Polarization Sensitivity			x	
System				
System Modeling	x			
System Issues	x		x	
Laser Fluid Pumps				x[6]

1: Various DoD programs
2: LaRC, UoP efforts
3: Potential DoD programs
4: GSFC/EOS development
5: Flown on many Hughes satellites
6: Flown on shuttle

3.0 PRELIMINARY DESIGN

3.1 System Functional Description

The LAWS System block diagram, detailing the subsystems and internal and external data flow interfaces, is shown in Figure 3.1-1. Some of the instrument/Platform interfaces, such as the Bus Data Unit (BDU) for data and the Bus Select Relay (BSR) for power are provided as GFE to the LAWS instrument contractor for integration with the instrument. The Transfer Frame Generator (TFG, also assumed GFE) is the interface between the instrument high-rate science data and the Platform. The laser fluid loop interfaces with the Platform at a heat exchanger, which is mated to a Platform coldplate, in accordance with the GIIS. The LAWS instrument is functionally partitioned into the following subsystems: optical, laser, receiver, mechanical, thermal, electrical, digital, and attitude determination which are discussed in the following sections. .

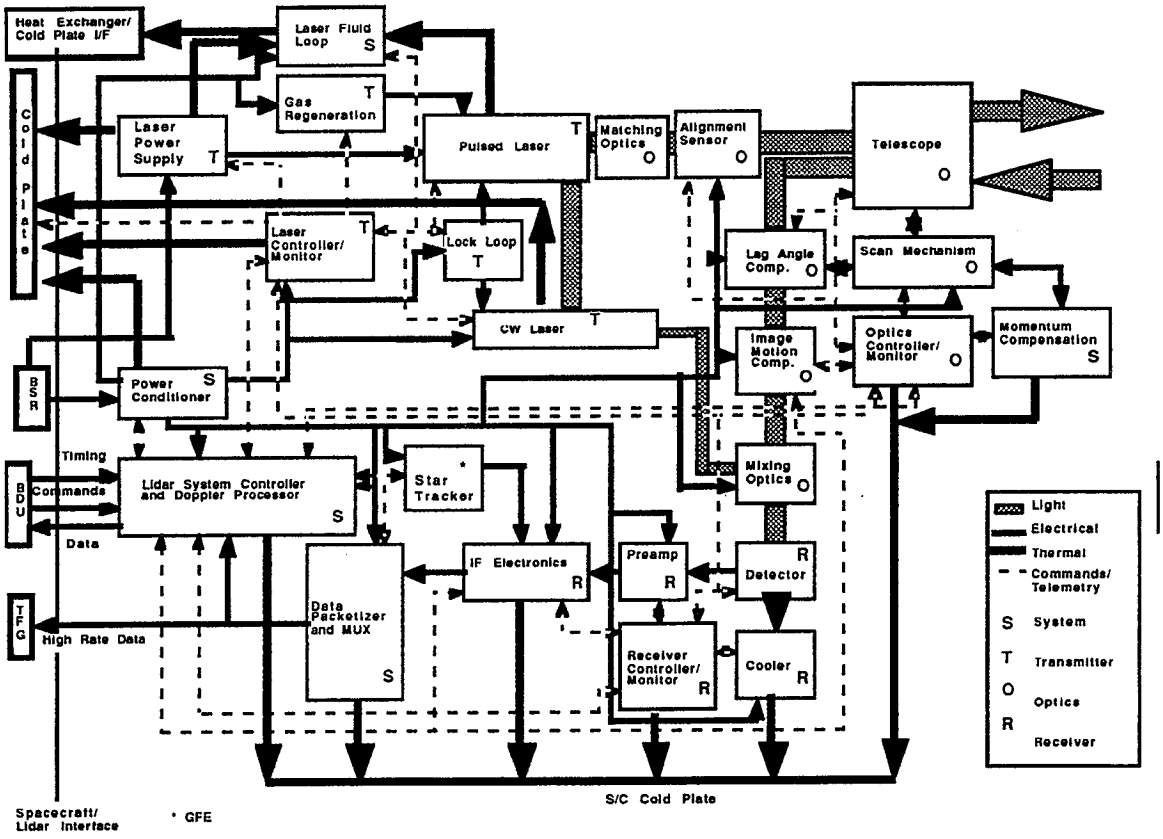

Figure 3.1-1 System Functional Block Diagram

3.2 Optical Subsystem

3.2.1 Optical Subsystem Performance Requirements

The requirements shown in Table 3.2-1 below are the system-derived parameters that the Optical Subsystem must meet to fulfill the LAWS mission objectives. In all cases, our recommended baseline configuration is able to meet the minimum requirements, and to approach the goals listed here.

The discussion that follows justifies the various requirements and identifies their source.

Table 3.2-1 Optical Subsystem Performance Requirements

Parameter	Value/Comments
Telescope Aperture	1.5 meters
Nadir Angle	Fixed at 45°
Rotation Rate	12 rpm
Weight	<350 Kg. (goal 300 Kg)
Polarization	Linear to Detector Signal and LO
T/R Switch and Lag Angle Comp.	Support Asynchronous Laser prf
Laser Feedback (Narcissus)	<0.01%
Boresight Stability During Round Trip	1.5 μradian (1σ, per axis)
Power	<250 W (Avg.)
Other	No Internal Focal Points
	Ground System Test

The telescope aperture diameter requirement is set by the energy-aperture product required to achieve the LAWS SNR.

The scan or nadir angle is fixed at a 45° angle according to the decision by the science working group.

The polarization requirement, based on the need for high heterodyne efficiency, will be met by the incorporation of very high efficiency reflective coatings and by compensating for phase shifts at the various coatings (particularly at the dichroic beamsplitters) to avoid elliptical polarization.

The requirement for the Transmit/Receive function to be asynchronous arises out of the need to conserve laser shots. Managing the timing of the shots to place them only in portions of the scan azimuth where favorable components of the wind velocity can be measured will increase laser

lifetime appreciably. As we show later, our recommended optical configuration accomplishes asynchronous operation, and eliminates the T/R switch entirely.

Our baseline configuration contains a single receiver detector sized to the diffraction image spot size. Another preliminary requirement placed on the Optical Subsystem is to stabilize the image to within 10% of its diameter on a root-mean-squared basis *per axis*, which, for the 1.5m aperture operating at 9.11 μm, is 10% of 15μradians, or 1.5 μradians.

The limit on the backscatter to the laser arises from the need to prevent the pulling of the laser frequency by the presence of an (unintended) external cavity formed by the telescope optics. Our studies show that we can meet the 0.01% requirement.

The weight allocation for the Optical Subsystem is 350 Kg., with a 300 Kg. goal. The allocation is for all of the components of the subsystem, including telescope, scan bearing, mixing optics, image motion compensation (IMC) assembly and electronics, and folding optics and structure.

The list of requirements in Table 3.2.-2 is derived from the Optical Subsystem Performance Requirements or from the error budgets that govern the subsystem performance.

Table 3.2-2 Optical Subsystem Derived Requirements

Telescope	**Requirement**	**Source of Requirement**
- Field of View	< 0.27°	Lag Angle
- Magnification	33x	Beam Truncation
- Wavefront error	l/20 λ rms @ λ = 9.11μm	< Diffraction Limit
- Barrel length	1.5 m, f/1 primary mirror	Shroud Diameter
Beam Stabilization	Accommodate image motion disturbances (as listed below)	
-External Disturbances	~180μradian	Lag angle, pitch rate and random spacecraft attitude jitter
- Laser Beam Jitter	~1μradian	Predicted laser performance

The field of view requirement is derived from the lag angle, which is in turn determined by the scan rate, cone angle, and platform altitude. For the 525 km nominal altitude, 12 RPM scan rate, and 45° cone angle, the lag angle will be 0.27° (full field). The altitude is expected to vary by ±3% due to the non-sphericity of the Earth. Since the lag angle is proportional to the time after laser pulse is transmitted, we allow for minor variations in altitude by increasing the range of the

lag angle compensator, and for major changes (as might result from a change in orbital altitude) by changing the scan rate.

The Optical Subsystem is required to stabilize the image on the detector in the face of a number of disturbances. The spacecraft itself will jitter an appreciable fraction of the 1.5μradians requirement. The laser beam will jitter in direction from shot to shot by ~1μradian (TBR). And there will be image motions caused by errors in the Optical Subsystem itself that must be compensated. The runout of the scan bearing is an example of such an error. The derived requirements chart lists the expected magnitude of the larger disturbances. The error budget sets the requirements for individual components of the Optical Subsystem and the image motion compensation configuration.

In the next section, we describe in detail the Optical Subsystem functions that are necessary to meet these requirements.

3.2.2 Optical Subsystem Functional Description

The overall function of the LAWS Optical Subsystem is to expand the laser beam and direct it toward the atmosphere in a conical scan, to receive the backscattered radiation, compensate for the lag angle and any jitter, mix the received, stabilized beam with the local oscillator, then focus the combined beams on the receiver detector. In addition, the optical sub system functions include certain diagnostic and correction operations which are detailed in the following paragraphs

The Optical Subsystem consists of: Telescope, Scan Drive, Derotator, Lag Angle Compensation, Image Motion Compensation, Mixing Optics, Shutter, Hartmann Wavefront Sensor, Boresight Reference and Source, Pointing Control Electronics, Power and Thermal Control Electronics, and Matching Optics. The Optical Subsystem Block Diagram is shown in Figure 3.2.2-1. Functional descriptions of each of the subsystem elements is provided below. Referenced (parenthetical) numbers refer to the subsystem elements as shown in Figure 3.2-1.

1. <u>Telescope:</u>

The LAWS Telescope is an afocal, two mirror, confocal parabola system which serves both as the transmitter laser beam expander and as the receiver collecting telescope. The present baseline Telescope magnification is 33x. The Telescope is scanned in azimuth around the NADIR axis at 12 RPM by the Scan Drive (see No. 2, Figure 3.2-1) and is mounted to the Scan Drive at a fixed 45° angle from NADIR, resulting in a conical scan with an included cone angle of 90°. The Primary Mirror (PM) is 1.5 m diameter, has an f/No. of 1.0 and contains two holes, off–set on either side of center, to provide for penetration of the transmit and receive beams. The angular

separation between the transmit and receive beams results from the continuous azimuth motion, the time delay between transmit pulse and reflected "echo", and the magnification of the Telescope.

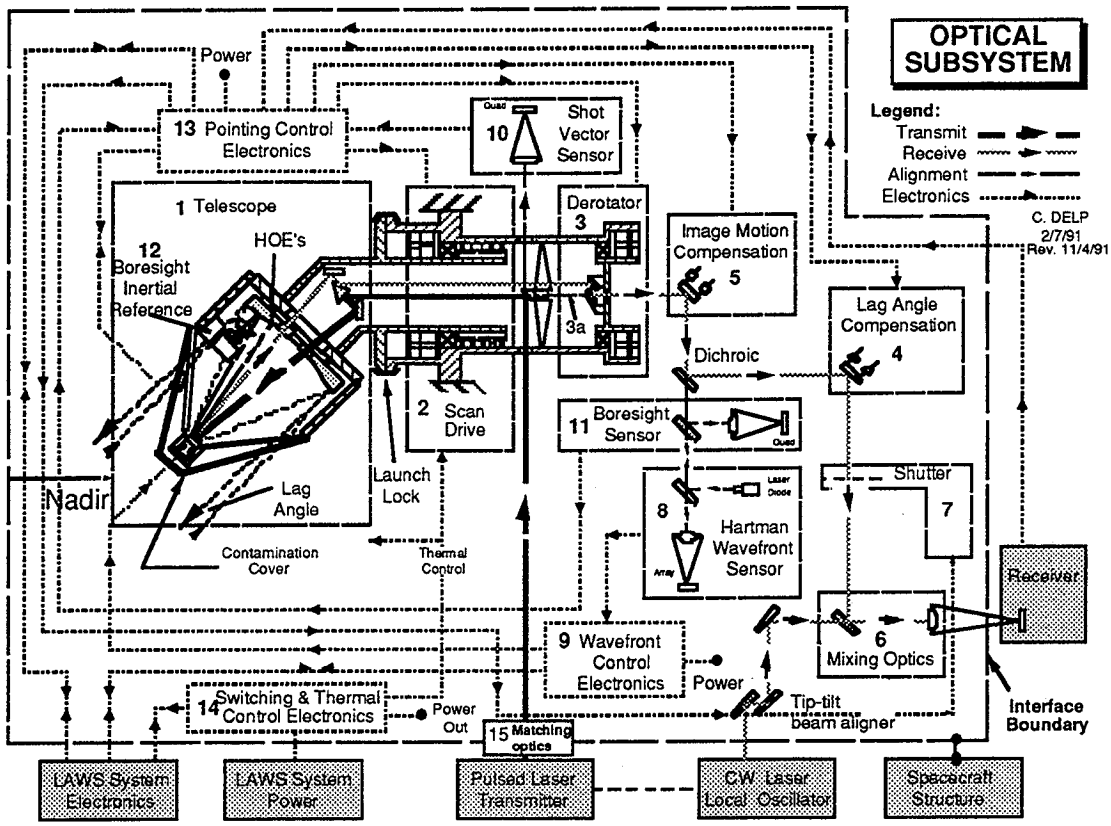

Figure 3.2-1 Optical Subsystem Block Diagram

A structural bulkhead behind the PM forms the Telescope structural backbone to which the PM, Secondary Mirror (SM) metering structure and the Telescope mounting structure are attached. Fold mirrors are mounted behind the bulkhead to relay the transmit and receive beams between the Telescope SM and the bore of the Scan Drive. The SM is supported by a spider from the forward end of the metering structure and mounted on actuators to provide on–orbit alignment adjustment capability. Encoders are included in the SM adjustment mechanism to provide position feedback to the control system. A removable aperture cover protects the optics during ground and launch operations.

2. Scan Drive:

The Scan Drive is the rotating interface between the scanning Telescope and the fixed elements of the LAWS instrument. The drive is based on Hughes Space and Communications

Group's spaceflight proven Bearing and Power Transfer Assembly (BAPTA) technology and contains scan bearings, redundant drive torque motors, redundant rotary incremental position encoders and the slip rings and brushes necessary to transfer all electrical power and signals across the rotating interface. The encoders provide 20 bit resolution azimuth position data to the scan drive controller and includes zero position index sensing. A hollow bore is provided through the drive to allow the transmit and receive beams to be relayed through the center.

A Launch Lock is provided at the interface between the Scan Drive outer housing (non–rotating) and the Telescope mounting structure (rotating) to restrain the telescope during ground and launch operations. The Launch Lock consists of a "W-clamp" band with redundant release devices spaced on opposite sides of the clamp and retraction springs to clear the band away from the clamp flanges after it is released.

3. Derotator:

The transmit beam is relayed through the scan drive so that it is coincident with the drive axis. The receive beam is relayed through the drive parallel to, but off–set from, the drive axis to provide beam path separation. Consequently, the receive beam orbits around the transmit beam (scan axis) as the telescope rotates. The Derotator serves to maintain beam path separation while eliminating receive beam motion. The transmit beam enters the Derotator radially through a hole in the fixed outer housing and is folded down the scan drive by a fold flat mounted on the drive axis. This flat is supported by a spider mounted to the fixed outer Derotator housing. The receive beam bypasses the transmit fold flat and is folded onto the scan axis by a rotating "periscope" mounted immediately above the transmit fold flat spider. The receive beam then exits the Derotator coincident with the scan axis and therefore with no translational motion. Derotator periscope rotation must be synchronized to telescope rotation by the drive controller, therefore the Derotator includes scan bearings, drive torque motors and position encoders to provide the necessary closed loop control functions.

4. Lag Angle Compensation:

The nominal lag angle between transmit and receive beams, representing the round trip pulse flight time between spacecraft and atmosphere, is built into the telescope. However, the receive beam pulse dwell, representing the time delay between the echoes at the top and bottom of the atmosphere, is ~200 microseconds. In addition, the spacecraft rotates once per orbit to keep the scan axis coincident with NADIR. Therefore, since the telescope is rotating at different rates about two axes during the return pulse, the lag angle changes that occur during the pulse must be compensated to maintain the alignment of the return image on the receiver detector. The Lag Angle

Compensator (LAC) is a momentum compensated, two axis steering mirror which has the primary function of low bandwidth compensation for lag angle shift. The mirror is driven by the Pointing Controller in a repeating pattern so that the scan timing and vector keep the image centered on the detector during the receive pulse. Since the lag angle shift is systematic and deterministic, the control profile is calculated open loop, based on the spacecraft clock and state vectors and on the Scan Drive position encoder data.

The transmitter laser jitters from shot to shot. Therefore, the vector of the outgoing transmit laser pulse must be measured by the Shot Vector Sensor (see No. 10, Figure 3.2-1) and reported to the Pointing Controller, which biases the LAC mirror during the pulse flight time so that the echo is centered on the detector upon its return.

Another function that must also be provided by the LAC subsystem is an alignment bias off–set, that can be used to compensate for systematic misalignment of the image. The off–set bias vector is calculated by the Pointing Controller, based on image position data from the receiver.

5. Image Motion Compensation:

In addition to systematic lag angle shift, there are also sources of random image motion that must be compensated to maintain alignment of the image on the detector during the return pulse. These include transmit laser shot vector jitter, image jitter caused by vibrations of the optics in the beam path and telescope pointing errors caused by spacecraft motion, scan bearing noise, and errors in the Scan Drive control system. The Image Motion Compensator (IMC) is a momentum compensated, two axis, high speed steering mirror which has the primary function of high bandwidth removal of jitter from the receive image bundle. This is accomplished by vectorally adding the error signals reported by several different sensors and driving the IMC mirror to null the composite error. Image bundle jitter and the various telescope pointing errors are all sensed by the Boresight Alignment Sensor (see No. 11 below) and reported to the Pointing Controller, which drives the IMC mirror in real time to remove the jitter.

6. Mixing Optics:

The Mixing Optics function to heterodyne (mix) the beam of a stable local oscillator with the receive beam and then to image the combined beams onto the receiver detector, where the resulting RF beat frequency is detected. The beat frequency results from Doppler shift between the transmit and receive beams, caused by the sum of the spacecraft and wind velocity vector components which are parallel to the laser beam vector. The mixing is accomplished by a beam combiner with a high reflected to transmitted ratio. The receive beam, which contains a very

limited number of photons, utilizes the efficient reflective path, while the local oscillator, with ample photons, utilizes the less efficient transmissive path.

7. Shutter:

When the transmit laser is fired, a small percentage of the energy is scattered off the primary and secondary mirrors and finds its way back through the receive beam path to the receiver focal plane. Preliminary indications are that the backscattered energy that reaches the receiver may be sufficient to damage the detector or as a minimum, affect its performance. Therefore, a Shutter is provided that is capable of first blocking the receive beam path to the detector during the 3 microsecond transmit pulse and then completely clearing the beam path during the 3.79 milliseconds (minimum) before the echo pulse returns.

There are several possible techniques to implement the shutter function. The most obvious is a mechanical interrupter (i.e., a slotted rotary wheel or similar device) located as close as possible to the focal plane where the image bundle is small. Another technique is to use one of the compensation steering mirrors (most appropriately implemented by the LAC mirror) to slew the image off the detector during the transmit pulse and then reestablish alignment during the echo time. This technique eliminates the need for an additional servo controlled mechanical device with critical variable timing requirements and potential loss–of–mission failure modes.

8. Hartmann Wavefront Sensor:

The Hartmann Wavefront Sensor (HWS) measures wavefront tilt, coma and astigmatism caused by telescope misalignment. Wavefront aberrations are determined by sampling wavefront tilt from four widely spaced subaperture on the PM. A laser diode source in the HWS is collimated and injected into the receive beam path toward the PM where the SM expands the beam, flooding the PM. Four Holographic Optical Elements (HOEs) redirect a small portion of the beam back through the receive path where it is imaged onto a matrix detector. The spacing and symmetry of the spots from the HOEs is indicative of specific aberrations and therefore the alignment of the telescope. This data is supplied to the Wavefront Control Electronics (see No. 9 below) which commands the SM actuators to realign the system.

9. Wavefront Control Electronics:

The Wavefront Control Electronics (WCE) accepts commands from the LAWS System electronics and power from the Power and Thermal Control Electronics (see No. 14 below) and reports Wavefront Control Subsystem status and data back to the LAWS System electronics.

The WCE reads the data from the Hartmann Wavefront Sensor detector and determines the centroid location of each HOE spot. Based on the spacing and symmetry of the spot centroids, the WCE calculates what misalignments are present in the telescope and what SM motions are required to correct the misalignments. The WCE then performs the transformations necessary to determine the direction and magnitude of SM actuator motions required to realign the telescope. Using this data and position feedback from the SM position encoders, the WCE drives the SM actuators to the correct position and reports position and status data back to the LAWS System electronics.

10. Shot Vector Sensor:

The vector of the outgoing beam from the carbon dioxide transmit laser varies or jitters from shot to shot by as much as one (TBR) microradians. This results in a random angular off–set of both the transmit beam and the subsequent receive beam from the nominal boresight of the telescope. Without compensation for transmit laser jitter, the resultant image jitter can be as much as 75% (TBR) of the airy disk diameter. It is not feasible to correct transmit beam jitter during the 3 microsecond transmit pulse. However, by measuring the vector of the transmit beam, the LAC mirror can be biased during the echo time to align the image onto the detector. The Shot Vector Sensor is provided to measure the jitter of the transmit laser and to send the jitter data to the Pointing Control Electronics (see No. 12 below) which commands the LAC mirror to the correct compensating bias. Photons are split from the main transmit beam by the fold flat (transmissive path) at the scan axis in the derotator and directed to the Shot Vector Sensor. The Shot Vector Sensor contains filters as required to reduce the beam energy to safe levels, optics to image the beam onto the detector and a pyroelectric quad cell detector to measure the relative position of the image, from which the shot vector can be determined.

11. Boresight Alignment Sensor:

The boresight of the telescope is measured and controlled in real time to compensate for random image motion caused by the composite effects of vibrations of the spacecraft, scan bearing, individual optical elements and other sources. The instantaneous boresight over a bandwidth of 500 Hz is determined by directing a collimated reference beam from the telescope aperture back through the receive path to the Boresight Alignment Sensor. In addition, an angular displacement sensor (ADS) mounted in close proximity to the collimated source. The ADS provides sensing of telescope motions relative to inertial space. The conbination of sensors detects boresight vibrations and misalignments and sends the data to the boresight alignment servo system in the Pointing Control Electronics (see No. 12 below) which commands the IMC mirror to steer the receive beam back to nominal boresight.

12. Boresight Reference and Source:

The boresight reference beam is generated in image space by an laser diode source (wavelength ≈ 0.9 micrometers) mounted in a collimating lens. This assembly is fixed at half the collimating lens' focal length from a retro–flat in the Boresight Inertial Reference. Light from the laser diode is reflected from the retro–flat, collimated by the lens and directed toward the PM, creating a reference beam that moves in image space, in response to telescope vibrations. A redundant set of angular displacement sensores (ADS) are mounted on the structure close to the boresight reference beam source. The ADS senses angular displacements of the telescope at frequencies above 2 Hz. The output signals of the ADS are summed at the boresight sensor electronics to provide an inertially-referenced boresight error. Any off–set of this reference beam detected by the Boresight Alignment Sensor and the ADS represents a perturbation from nominal boresight by the optical train. A dichroic beam dump is mounted between the PM and the Boresight Inertial Reference to protect the LED source from the transmit laser.

13. Pointing Control Electronics:

The Pointing Control Electronics (PCE) accepts commands from the LAWS System electronics and power from the Power and Thermal Control Electronics (see No. 14 below) and reports Pointing Control Subsystem status and data back to the LAWS System electronics. The PCE performs a number of inter–related functions with the ultimate goal of keeping the image centered on the detector to within 5% of the image diameter. These functions are:

a. Scan Drive Rate and Position Control: Scan rate commands and spacecraft clock data are supplied to the PCE by the LAWS System electronics. Using position feedback generated by the scan drive zero index and encoder, the scan drive servo electronics drives the scan torque motor at the commanded rate and reports Scan Drive status and azimuth position error (relative to spacecraft coordinates) back to the LAWS System electronics.

b. Derotator Synchronization: Derotator rotation must be synchronized to Scan Drive rotation. Using position feedback generated by both Scan Drive and Derotator zero indexes and encoders, the derotator servo electronics drives the derotator torque motor to slave derotator position with telescope azimuth position and reports derotator status and position error (relative to azimuth position) back to the LAWS System electronics.

c. Boresight Reference Source Control: The PCE powers and controls the boresight reference source and provides reference source status back to the spacecraft electronics.

d. Image Motion Compensation: The PCE contains the IMC servo electronics. Using the Boresight Alignment Sensor error signal and angular position feedback from the ADS, the IMC

electronics drive the IMC mirror to null the boresight alignment error signal and reports IMC status and position errors back to the LAWS System electronics.

e. Lag Angle Compensation: The PCE consolidates scan rate data, spacecraft clock and state vector data and systematic image/detector off–set data and drives the LAC mirror to center and stabilize the image on the receiver detector during the echo pulse. Using scan rate feedback from the scan drive, timing and state vector data from the LAWS System electronics, image off–set data from the receiver and position feedback from the LAC mirror encoders, the servo electronics in the PCE calculate the optimum mirror scan profile, slopes and off–set biases and drive the mirror to minimize image motion and position errors.

14. Power and Thermal Control Electronics:

The Power and Thermal Control Electronics (P&TCE) accepts commands from the LAWS System electronics and power from the LAWS System power bus, switches and distributes power to all telescope electronic and thermal control subsystems, provides circuit protection and provides power and thermal status back to the LAWS System electronics. In addition, the P&TCE contains the temperature transducer signal conditioning and multiplexing required for all telescope subsystem temperature measurements. Voltage regulation/power conditioning is provided by the spacecraft power distribution systems.

15. Matching Optics:

The Matching optics provides an intermediate stage of optical magnification to match properly the outgoing laser beam size and the secondary mirror size. The beam will be truncated at the secondary mirror in such a way as to optimize the overall signal-to- noise ratio. The magnification ratio will most likely be in the range of 1.4x to 1.6x. A reflective, non-imaging magnifier will be used. The matching optics will be designed after the characteristics of the laser are completely established.

Section 3.2.3, which follows, describes and quantifies the performance characteristics of the Optical Subsystem with regard to signal-to-noise and the effects of alignment, focus, beam shape, etc. on system signal-to-noise.

3.2.3 Performance Characteristics

The baseline optical configuration that provides the functions described in the previous section is shown below in Figure 3.2-2, showing the optics "hanging in air". Many analyses and trade studies were performed in arriving at this configuration. These analyses and trades are

summarized in Section 3.2.4. The preliminary design of the structure, bearings and the various control and diagnostic functions is covered in Section 3.2.5.

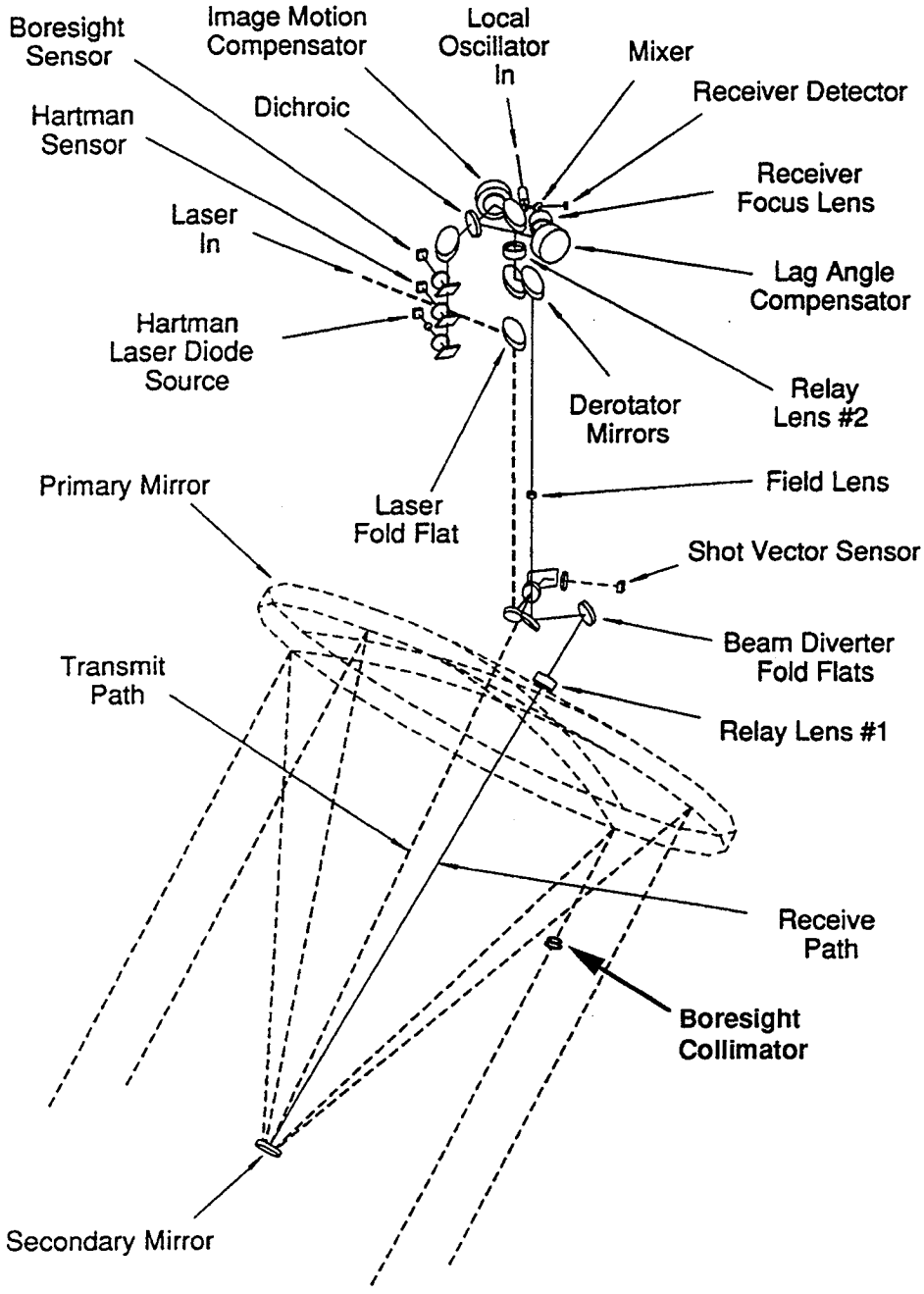

Figure 3.2-2 Optical Subsystem Schematic

3.2.3.1 Signal-to-Noise Ratio (SNR) Analysis

The LAWS Optical Subsystem has been modeled using a Hughes-developed code to determine the Optical Subsystem performance, and to support the Optical Subsystem error budgeting. The following provides the results of this modeling.

The LAWS computer models are based on the optical heterodyne theorem implemented in a local oscillator back propagation mode. Laser light is propagated through the transmitting telescope to a target plane. In addition the local oscillator field distribution integrated over the detector is back propagated to the target plane. The overlap integral of the transmitted intensity and the back propagated local oscillator beam form a measure of the heterodyne efficiency of the process. The back propagated local oscillator method is a computational aid in accounting for the received scattered signal from the target. It is *not* an approximation.

The analysis results and discussion presented in this section are divided into four parts: telescope performance and alignment, local oscillator alignment, miscellaneous analysis and a description of analysis that is yet needed.

TELESCOPE PERFORMANCE AND ALIGNMENT

Typical laser profiles for the CO_2 laser have been obtained from our LAWS teammate STI. The phase of the profile was primarily focus which was removed from the beam assuming that the laser as interfaced to the telescope would be optically corrected. The optical subsystem which would perform this correction should also be used to size the laser beam and optimally fit the beam into the transmitting aperture. Analysis has shown that the optimal fit of the beam into the aperture requires clipping some of the laser profile. In fact the optimum clipping depends upon the profile shape and is likely to have to be adjusted as part of the overall optical alignment of the laser to the telescope. The analysis displayed in Figure 3.2-3 uses two laser profiles, one from a gain loaded cavity model and one from a passive cavity model. These models produced a 12% difference in beam clipping to produce the optimum beam size when mixed with a Gaussian local oscillator to estimate heterodyne efficiency. In all the analysis presented here the passive cavity laser profile was used as a baseline so that degradations in performance are measured relative to this baseline. The baseline system for analysis also assumes a single Airy disk-sized detector.

FOCUS MISALIGNMENT

Figure 3.2.3-3 shows the dependence of efficiency on the focus of the telescope. Note that efficiency does not peak at the telescope focus. The small shift in focus is due to the target distance of 525km. not being in the far field. Thus the optimum telescope focus is shifted by a small amount as shown. Additional focus or spherical aberration in the laser will cause differing amounts of shift and thereby different optimal focus positions. The important point here is the very

sensitive nature of efficiency to optical focus alignment be it telescope or laser. In addition the 5% difference between the gain loaded and passive case shows the sensitivity of efficiency to the type of laser profile.

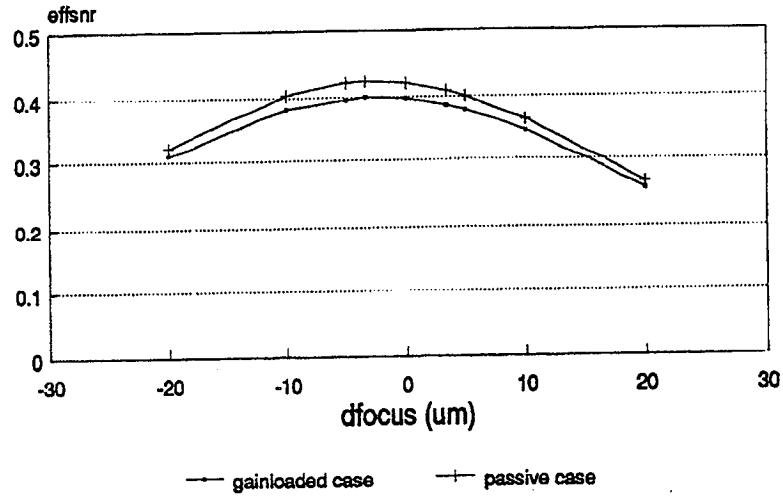

Figure 3.2-3 SNR Degradation Due to Telescope Defocus

TILT MISALIGNMENT

The misalignment described here is a displacement of the received image relative to the detector position assuming a perfectly aligned local oscillator. The analysis further assumes that the tilt in the telescope pupil is present on transmission and not on reception (aberrations on reception are accounted for by back propagating the local oscillator through the telescope). Note, if the telescope had a fixed tilt for both transmission and reception the image and local oscillator would be aligned on the detector but the scattering observed would be from a displaced point on the target. In general a tilt of the primary mirror produces other off axis aberrations beside tilt and these have been included in the analysis. However, for very small tilts the other aberrations are almost negligible. Figure 3.2-4 shows the result using a Gaussian local oscillator (LO) in two LO configurations. The first configuration is where the LO amplitude is clipped at its e^{-2} point in the pupil and the second configuration corresponds to a plane wave illumination on the detector. For each curve the detector size was adjusted to maximize the efficiency. The key points of Figure 3.2-4 are the basic sensitivity to primary mirror tilt and the magnitude of the degradation produced by using a plane wave LO. A more optimum LO configuration is described later on in this section.

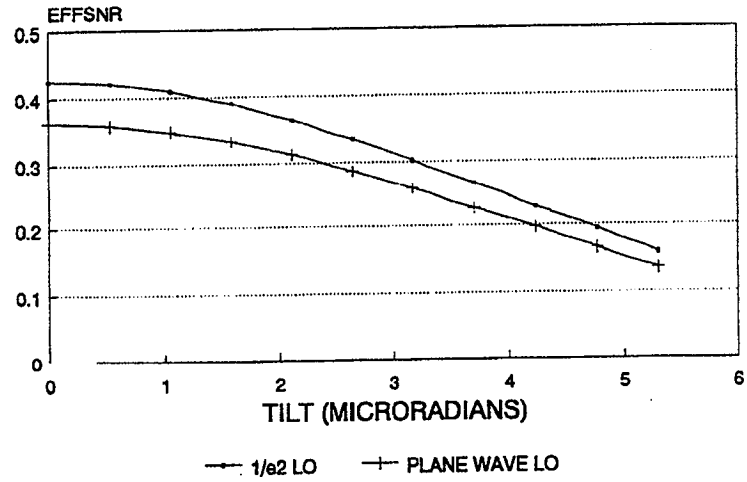

Figure 3.2-4 SNR Degradation Due to Primary Mirror Tilt

DECENTER MISALIGNMENT

Figure 3.2-5 shows the degradation in performance when the telescope primary mirror and secondary mirror are decentered. The decentered aberrations are contained in both the transmitted and received beams and as such are treated in the model in both the transmission to the target and the back propagated local oscillator.

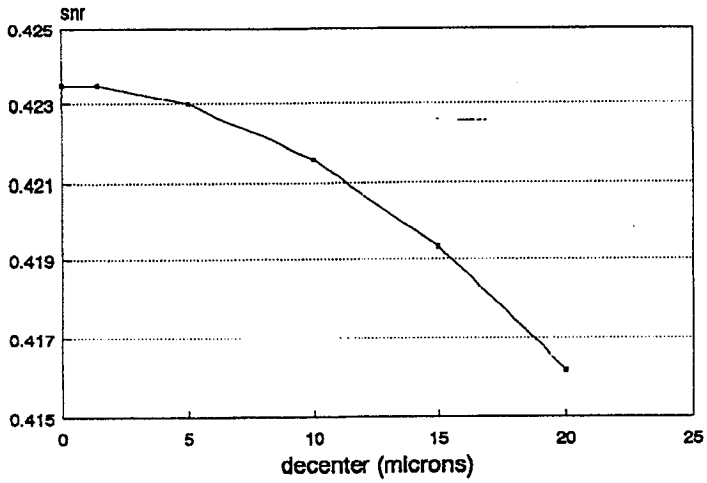

Figure 3.2-5 SNR Degradation Due to Telescope Decenter

LOCAL OSCILLATOR MISALIGNMENT

In this section some elementary analysis of LO misalignment issues are discussed. In Figure 3.2-6 the effect of the receive beam displacement (tilt) is evaluated for a plane wave LO and variable detector size.

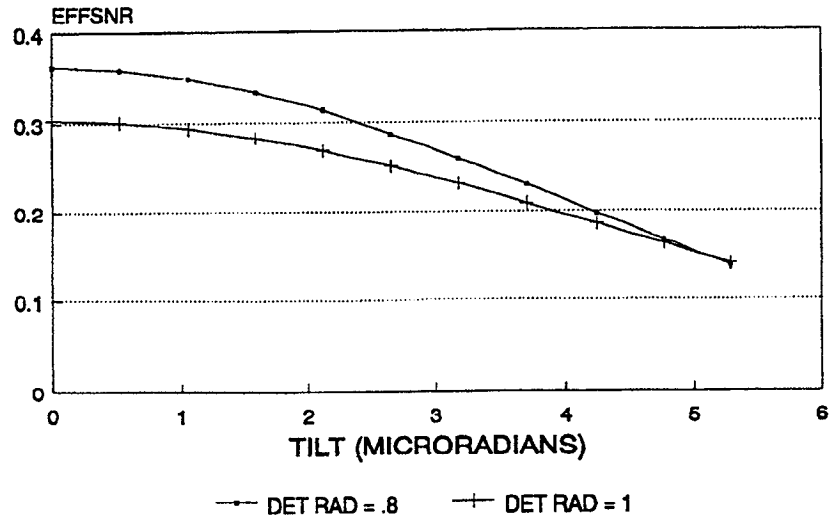

Figure 3.2-6 Effect of Detector Size on Primary Mirror Tilt for a Plane Wave LO

The figure shows that the efficiency is higher for a detector size of order .8 Airy disks which is close to optimum for a plane wave LO. However as shown in Figure 3.2-7 the plane wave LO is degraded some what from the e^{-2} focused LO.

A key question at this point is the degradation of a misaligned focused LO compared to the best plane wave performance. Figure 3.2-7 shows the efficiency vs. focused LO tilt measured in the LO pupil for 3 LO f-numbers. The best performance occurs when the LO f-number matches the telescope f-number. The main message of Figure 3.2-7 is that the LO has to be tilted by a large amount before the degradation matches that for the best plane wave LO. This suggests that a focused LO provides superior performance to a plane wave LO system. The optical design of the LO optics should therefore concentrate on a focused LO instead of a plane wave design.

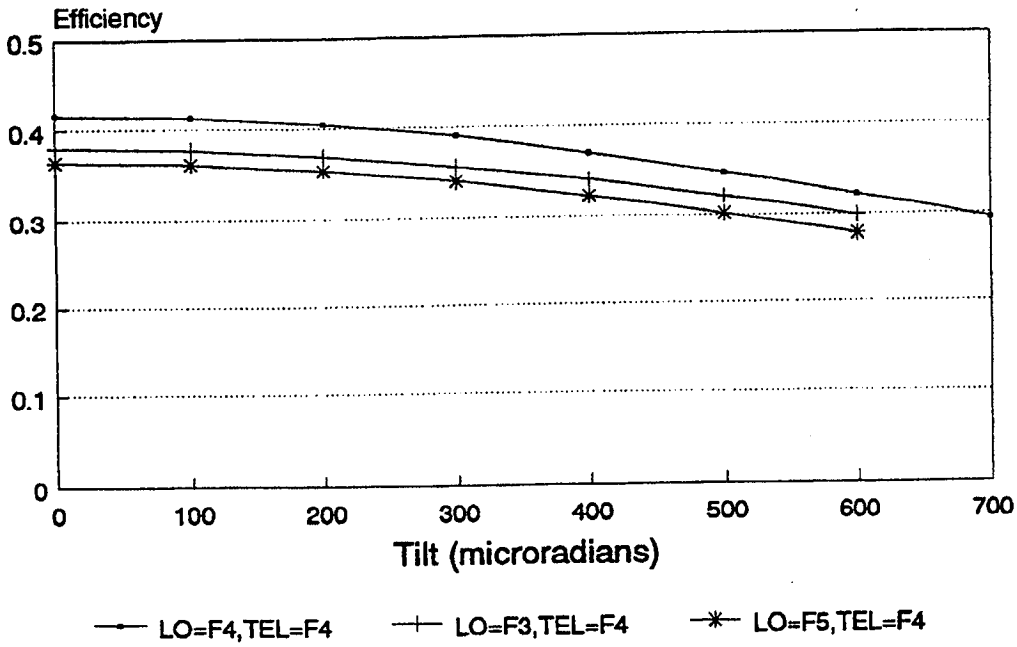

Figure 3.2-7 Effect of LO Tilts for Varying Shaped LO Beams.

MISCELLANEOUS ANALYSIS

Figure 3.2-8 shows the far fields produced after transmission through the telescope for the graded reflector and scraper mirror resonator configurations. The graphs are plotted so that the volume under the radially symmetric profiles represents the total energy reaching the target plane. The curves show that the graded reflector configuration produces more energy in the far field core then the scraper configuration. Figure 3.2-9 shows the degradation in efficiency when the laser has either a quarter wave or half wave of astigmatism. The graph is plotted as a function of LO defocus which shows that defocusing the LO can only correct the effect of astigmatism in the laser to a minor extent.

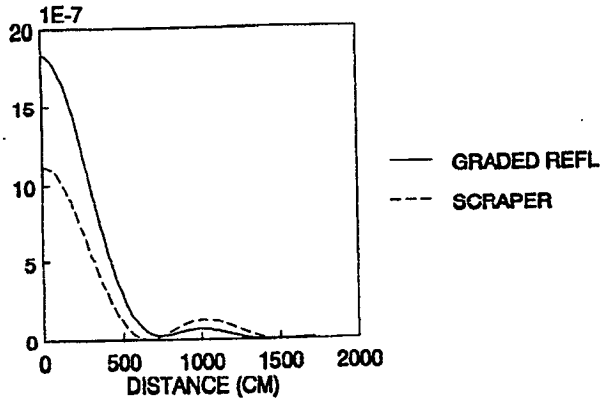

Figure 3.2-8 Laser Resonator Far Fields.

CONCLUSIONS

The performance characteristics described in this section have led to a rational errror budget and optical tolerances that are documented elsewhere in the LAWS Phase 2 DR's. The analysis also provided the inputs for the overall system performance prediction calculations.

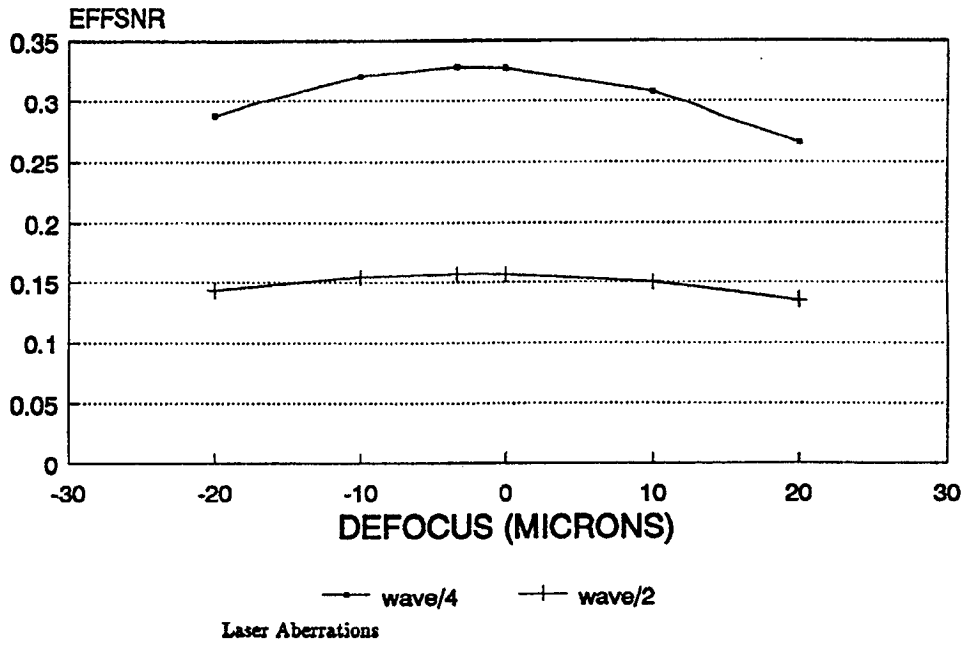

Figure 3.2-9 Degradation of SNR Due to Astigmatism in the Laser Beam.

3.2.3.2 Lag Angle Compensation

The so-called "lag angle" is inherent in any spaceborne scanning lidar system. It is also important in systems where the scanning causes a significant pointing error during the laser interrogating pulse echo time. In a heterodyne lidar system, the lag angle, if uncompensated, will significantly reduce the signal-to-noise ratio.

What is "Lag Angle"?

Lag angle is the apparent change in direction to the laser-illuminated spot in the atmosphere relative to the transmitted line of sight angle during the laser pulse round trip time. It occurs in all nadir-oriented, orbiting systems whether fixed or scanning. Let's take the case of a non-scanning lidar first.

Why should there be any lag angle when the system is not scanning?

It occurs as the space-borne lidar system rotates continuously to remain aligned with the Earth, as in a nadir-oriented system. The spacecraft and lidar must pitch in order to remain oriented to nadir; therefore the line of sight rotates during the laser pulse round-trip time and during the pulse reception time. A numerical example will make this effect clear.

During a single orbital revolution, the spacecraft rotates 2π radians. The rotation rate is 2π radian per orbital period. For an altitude of 525 km, the orbital period will be about 88 minutes. The pitch rate is then 1190 μrad per second. During a pulse round trip time of ~5 ms, the spacecraft will rotate 6 μrad. This is equal to the lag angle. For a system whose beam spread is 15 μrad, an uncorrected lag angle of this magnitude is unacceptable. Note that the lag angle change during pulse reception (stretched due to reflection from the layers of the atmosphere) may be as high as 0.23 μrad. If we budget a total error of 1.5 μrad (10% of the beam spread) to the lag angle, the 0.23 μrad lag angle error is comparable to other error contributors in the error budget.

The lag angle due to pitching is separable into a fixed component and a time-varying component. The fixed component can be compensated in the optical design since it is merely the equivalent to a fixed position in the field of the telescope. The dynamic correction is required to compensate for the variation in field angle during the time the stretched pulse is being received. Note that the lag angle due to pitching will occur only in the plane of the orbit, which is not the case in a scanning system.

Let us now go on to the case of a scanning lidar system in Earth orbit.

The angular scan rate, given by ω, in radians per second, is defined as the rotation rate around the scan axis (not necessarily about nadir). Since light propagates in inertial space (not affected by transmitter motions after pulse transmission), the source of the backscattered light is the part of the atmosphere that is illuminated by the pulse. As seen from the reference frame of the transmitter telescope, this point will move continuously in the field of view in the direction tangentially away from the direction of the scan.

Figure 3.2-10 illustrates the geometry during the scan. In this example, the scan axis coincides with nadir, but the lag angle geometry is not affected if there is an angle between the two. However, the placement of the laser shots on the atmosphere (or ground) will be a function of the magnitude of the angle between the scan axis and nadir.

The lag angle is the angle subtended by $r(t) \cdot \omega \cdot t_e$ at the slant range $L(t)$,

where ω is the scan rate (radians per second)

t_e is the echo time (seconds) corresponding to the slant range $L(t)$

$r(t)$ is the instantaneous perpendicular radius from the scan axis to the range-gated scatterer

Defining the lag angle explicitly, we have

$$\text{Lag Angle} = r(t) \cdot \omega \cdot t_e / L(t)$$

$r(t)$ is simply the sine component of the slant range: $r(t) = L(t)\sin\phi$. Substituting for $r(t)$ and simplifying, we have

$$\boxed{\text{Lag Angle} = \sin\phi \cdot \omega \cdot t_e}$$

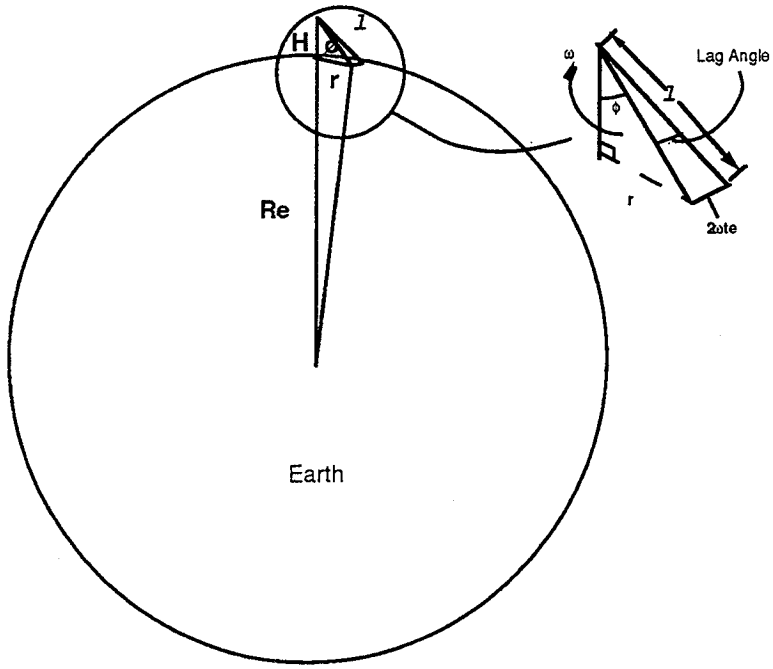

Figure 3.2-10 Computation of Lag Angle for Scanning System

Note that the lag angle is only a function of time (given a fixed angle relative to nadir and a constant scan rate); it is a *not* a function of altitude, although the echo time corresponding to an echo from a ground *will* be a function of altitude, H. If there is a variation in altitude, the *range* of the lag angle compensation must be large enough to accommodate the maximum variation in echo time. We can accomplish this by increasing the size of the fixed lag angle mirrors, and designing the lag angle compensation control to have sufficient range to cover all possible values of lag angle, to 3σ or maybe even to 5σ.

How can we compute the echo time and its variation as a function of altitude?

The echo time, t_e, is merely the slant range to the target of interest (a layer of the atmosphere or the ground) divided by the speed of light, c. Referring again to Figure 1 and for the moment assuming that the scan axis is coincident with nadir, we can write the expression for the slant range, $L(t)$, as

$$L(t) = (H(t) + R_e)\cos\phi - \sqrt{(H(t) + R_e)^2 \cos^2\phi - H(t)(H(t) + 2R_e)}$$

Dividing by the speed of light, c, we have

$$t_e = L(t)/c$$

As an example, let us compute the variation in lag angle for an oblate Earth, where the altitude may vary by 40 km. Taking a nominal altitude of 525 km and allowing a variation due to oblateness of ± 20km, we obtain the graphs shown in Figure 3.2-11.

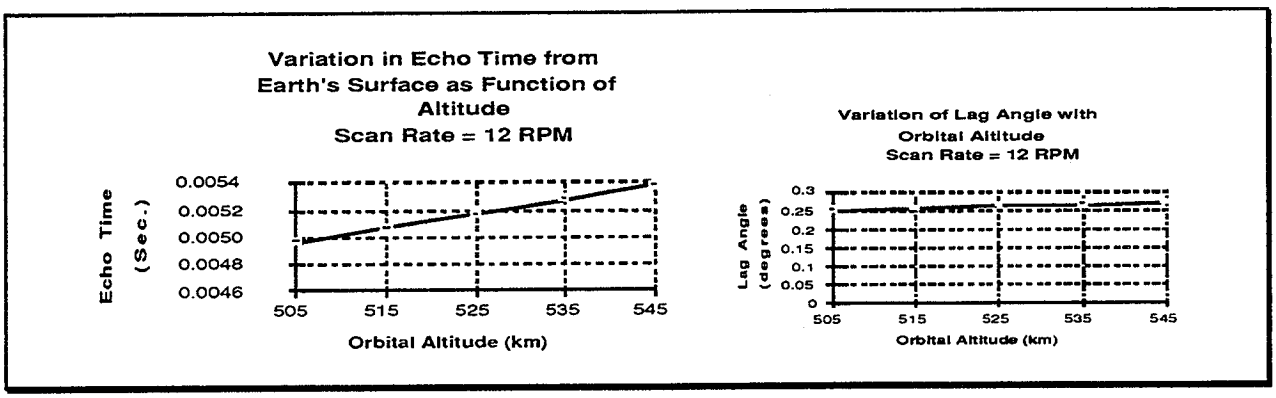

Figure 3.2-11 Trend of echo time and lag angle with variation in orbital altitude.

These curves are essentially linear for the cases considered. Although the variation in both lag angle and echo time when compared to the nominal altitude is only about ±4%, the Earth's oblateness is comparable to the thickness of the atmosphere (20km). Either the scan rate must be varied ±4 % in synchronism with the oblateness function or the range of the lag angle compensator must be doubled in order to cover the thickness of the atmosphere and the range of variation cause by the Earth's oblateness.

There is, however, another effect that can cause a variation of the lag angle. If the scan axis does not coincide with the nadir axis, the line of sight will describe an ellipse on the Earth's surface (neglecting the spacecraft motion). The slant range and lag angle will vary around each scan.

The geometry and mathematics for this situation is not straight-forward, but through a series of approximations, we derived a relationship between the angle between the spin axis and nadir, ε, and the total variation in lag angle, ΔLA, over a single scan revolution. The relationship is (good for small ε)

$$\Delta LA = LA(\phi_o + \varepsilon) - LA(\phi_o - \varepsilon) = 4 \times LA(\phi_o) \cdot \varepsilon$$

where ϕ_o is the nominal scan angle relative to nadir.

Expressing $\Delta LA/LA(\phi_o)$ as a fraction and evaluating for $\varepsilon = 1$ milliradian, we compute

$$\Delta LA/LA(\phi_o) = 0.0017\ \%$$

The ranging to the ground will vary by about 0.3 Km for every milliradian error between the spin axis and nadir. The corresponding echo time will vary by 1 μsecond. We expect the nadir error to be less than a milliradian, and conclude that a few percent of added lag angle compensation will be adequate to provide margin for both of the effects discussed above.

3.2.4 Optical Subsystem Analysis and Trades

This section documents the key optical design trades that were completed during the Phase 2 Study.

3.2.4.1 Optical Design Trades

The LAWS trade study began by trading telescope design forms that could accommodate a 1.5 meter diameter aperture and a 33.33X demagnification. The WINDSAT optical design form was scaled up and used as a starting point. The WINDSAT design form is a three- mirror afocal design with a field bias of 0.5° to get the exit pupil away from the prime focus of the telescope. The magnification of the system is too high to fold the beam out at the prime focus and keep the obscuration at the prime focus small. Two other conventional telescope designs were traded against the WINDSAT form. The first was a two- mirror telescope with a refractive element in place of the tertiary mirror of the WINDSAT design. This design eliminates the need for the field bias and is viable since we are operating at a single wavelength of 9.11 μm. The third design form is a simple confocal parabola configuration.

A system-level requirement is for a design that can be tested in air instead of vacuum. The amount of energy in the high power laser used in the LAWS instrument will cause air breakdown if brought to a focus anywhere in the transmitted path. The confocal parabola design avoids this

problem. Other design forms—such as eccentric pupil designs and off-axis designs—were not considered due to the complexity of the mirrors, alignment costs and the large 1.5 meter aperture required.

The confocal parabola design is an elegant yet simple means of meeting the LAWS requirements. The transmit and receive paths can be designed independently to meet the desired configuration of each path. The transmit path can use the telescope only, thus avoiding an internal focus. An accessible pupil is desired in the return path for a LAC (lag angle compensator). The LAC when located at a pupil will facilitate correction of angular beam errors without beam walk. If the LAC is not located at an exit pupil, a two-mirror active system would be needed to perform this correction. Relay optics were added in the receive path to relay the beam with a 1—to—1 magnification through focus. A field lens was then placed near the internal focus to image the exit pupil of the telescope (located behind the secondary mirror) to a convenient location for the LAC in the mechanical structure.

The confocal parabola design was chosen early in the program as the baseline candidate for LAWS. A trade study of F/1 versus F/1.5 confocal parabolas was conducted. Layouts for each design were prepared. The F/1 design is obviously more compact than the F/1.5 design and is desirable from a packaging viewpoint. Sensitivities for each design were tabulated. The F/l design is more sensitive to changes in the system. A final trade of each design versus lag angle was also completed. At the beginning of the LAWS study it had not been determined whether a fixed or variable lag angle was required. For a variable lag angle, two active fold mirrors would be required to fold the beam from the telescope to the optical axis of the rest of the system. The other effects are an increased residual aberration due to the field curvature of the confocal parabolas and a larger hole in the primary mirror. The obscurations do not grow to be very large for the lag angles considered (up to $\pm$ 0.3°). The residual aberration is larger for the F/l design as the lag angle is increased. Both designs, however, have a small residual aberration at the baseline lag angle. The F/1 design was chosen to be the baseline design because of packaging requirements.

A trade study of different magnifications for the secondary mirror of the confocal parabola telescope was completed. Three telescope magnifications were used; 20X, 33X and 48X. The 20X design would put less magnification in the telescope and more in the relay optics. The exit beam size of 45 mm or smaller is about what is needed to have reasonably sized optics through the rest of the system. The 48X magnification was studied to see if a smaller beam (31 mm) could be used. The sensitivities of the three telescopes were expressed in terms of Zernike polynomials. The despace sensitivities for the three cases are a function of the primary mirror and thus are the same value for each case. Decentering the secondary mirror introduces the same amount of tilt in the wavefront independent of the power of the secondary mirror. The focus term for the decenter

cases increases with magnification producing total wavefront errors for decenter that slightly increase with magnification of the secondary mirror. Tilting the secondary mirror causes the sensitivities to decrease with magnification. This arises from the fact that the secondary mirror focal length gets shorter as the magnification increases. Tilting the secondary mirror can be thought of as an equivalent decenter of the mirror. The shorter the "lever arm" (focal length), the smaller the equivalent decenter on the mirror will be. Secondary mirror despace and decenter angular sensitivities increase as the power of the secondary mirror increases and as such increase with magnification. Secondary mirror tilt causes angular boresight errors that are independent of the power of the secondary mirror.

The last part of the analysis concerning the tradeoff of secondary mirror magnification investigates the range of lag angles expected in the receive path. The primary and secondary mirrors of the LAWS confocal parabola telescope have been adjusted to give the smallest design residual at the transmit and receive field points, $\pm 0.11°$. The receive path sensitivities include a misalignment of the beam to the expected receive path of $\pm 0.005°$ about a $0.11°$ semi-field angle. This causes an increase in the wavefront error. The wavefront error due to the change in field position increases as the magnification of the secondary mirror increases. This sensitivity is for the telescope only. The LAC will take out the angular boresight error leaving the residual wavefront aberration only.

Surface figure errors were computed for the primary and secondary mirrors. The primary mirror is the same for all three cases and exhibits the same effect on the telescope wavefront. The secondary mirror figure error is greater as the magnification of the secondary mirror increases.

The trade studies leading to the design for the local oscillator path are described below. The maximum signal is obtained when the profile of the local oscillator beam exactly matches the profile of the receive beam and they are aligned to be collinear. This can simply be accomplished by designing a lens that has the same F/# as the receive path. The trade study was to compare a focussed LO with a plane wave (flooded) LO beam at the detector plane. The plane wave LO would ease alignment tolerances for the local oscillator. HDOS's proprietary performance modeling code was applied to calculate the loss in signal to determine the sensitivities of not matching the receive beam profile. The exit pupil diameter is 350 μm for both cases and the wavefront curvature is flat. Another approach to flood the detector plane with the LO is to use a combination of a lens to bring the laser to a focus and a field lens to locate the exit pupil on the detector. The exit pupil in this case is 850 μm in diameter and the wavefront has a long radius of curvature.

The receive path has an F/4 lens to focus the beam onto the detector. A beam splitter is used to insert the LO beam in the receive path. The receive beam reflects off the beam splitter to preserve

as much of the signal as possible. Any of the three scenarios for the LO design can be used with this layout as long as there is enough back working distance for the beam splitter and the detector package.

The requirements for the LAWS optical design for the Phase 2 study are shown below in Table 3.2-3. The LAWS optical design for the transmit path consists of the F/1 confocal parabolas and a Galilean beam expander. The laser beam used in the transmit paths will be truncated and have an effect on the transmitted wavefront unless the outside diameters (OD) of all of the lenses can be 2X larger than the clear apertures (see Siegman). This is not possible for the primary mirror.

Table 3.2-3 Optical Design Requirements

Requirement	Value
Aperture Diameter	1.5 m
Lag Angle	±0.132°
Altitude	525 km
Fixed Lag Angle (Not Variable)	
Laser Beam Diameter	6 cm
Laser Truncation	0.8 x $1/\varepsilon^2$ of PM Diameter
Laser Back Reflection	≤0.01%
Laser Wavelength	9.11 μm
No Thru-Focus in Transmit Path	
Accessible Pupil for LAC in Receive Path	

To maximize the SNR of the receiver, it is necessary to calculate the optimum truncation of the transmitted wavefront by specifying the size of the transmitted beam relative to the OD of the primary mirror. This is usually done be specifying the beam truncation relative to the $1/\varepsilon^2$ intensity points for a Gaussian beam. The HDOS Modeling code was used to complete this calculation for the actual laser profiles we have for LAWS. The current specification is 0.8 times the $1/\varepsilon^2$ diameter. The final profile of the laser will probably not be available until after the fabrication process for the telescope mirrors has started. The Galilean beam expander will be used to adjust the output laser beam size for maximum SNR.

The LAWS optical design for the receive path is shown in Figure 3.2-12. The 1.5 meter aperture is demagnified with a 33.33X confocal parabola telescope to 45 mm.

A pair of identical relay lenses is used to bring the receive path through focus with a 1-to-1 magnification. A field lens is placed near the focus to image the exit pupil of the telescope to an

accessible pupil at the LAC. An F/4 doublet is designed to image the receive path onto the detector. Table 3.2-4 contains a description of the receiver relay optics.

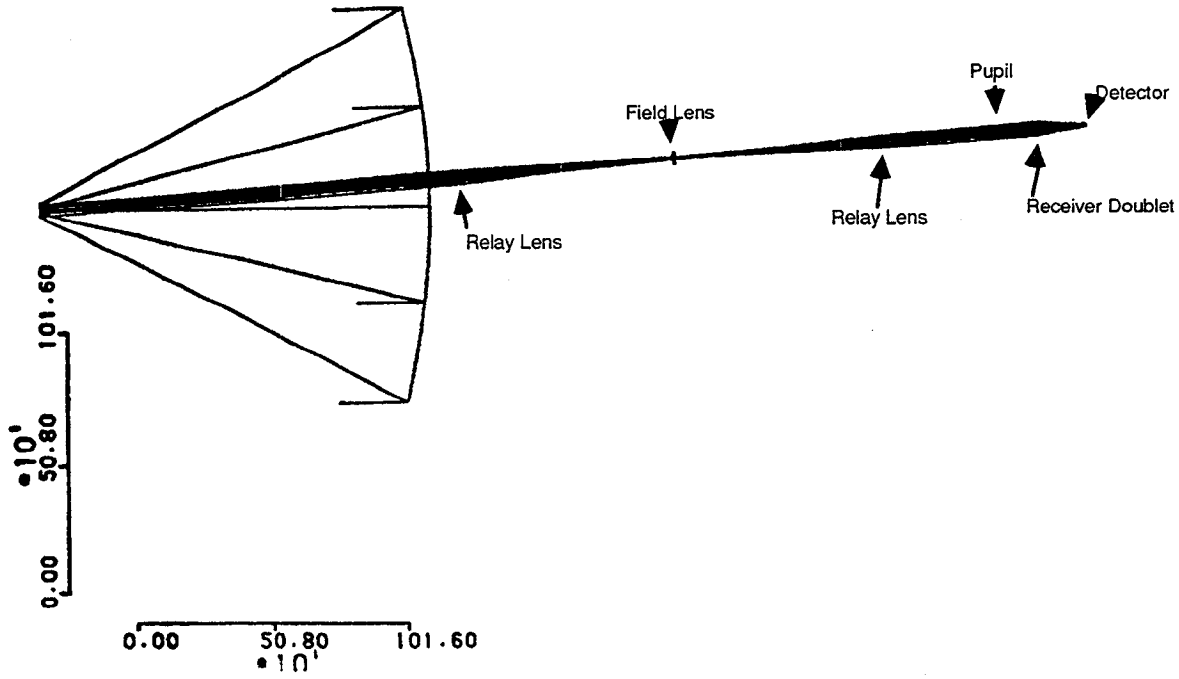

Figure 3.2-12 Receive Path Optical Design

A schematic illustrating the final concept for the local oscillator design is shown in Figure 3.2-13.

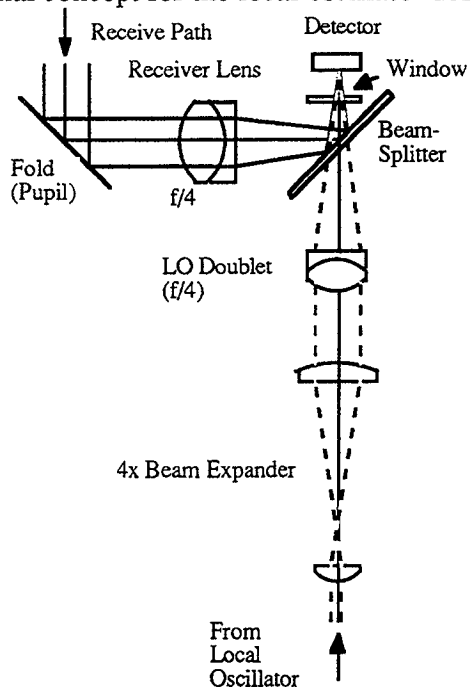

Figure 3..2-13 LO Path Schematic

There are three possibilities for the design of the LO optics as mentioned previously. The first is simply a doublet with the same F/# as the receiver doublet. The other two designs are variations of a pupil relay; one is a beam expander and the other is a focusing lens with a field lens. HDOS completed a SNR trade study for the three possibilities and found that flooding the detector plane with the LO pupil relay (with either design) causes a drop in SNR that is too large. The maximimum SNR is obtained by using a doublet with the same F/# as the receiver optics. The laser that was chosen for the LO has a 6-mm diameter output beam. A back working distance of 3.75 inches is required between the last lens in the LO design and the detector to fit the detector package and beam splitter in the optical path. For an F/4 image, the beam diameter entering the LO doublet has to be about an inch. A 4X beam expander is needed between the laser and the doublet to expand the L0 beam from 6 to 24 mm.

Table 3.2-4 Laws Receiver Lenses

Relay Lenses—2 Plano-Convex	
Glass	ZnSe
Radius	1172.8611mm
Thickness	7.0mm
Clear Aperture	45.0mm ϕ
Field Lens—1Plano-Convex	
Glass	ZnSe
Radius	2649.5000mm
Thickness	7.0mm
Clear Aperture	~10.0mm ϕ
Receiver Air Space Doublet—1	
First Lens	BiConvex
R_1	212.3863mm
R2	401.4874mm
Thickness	7.0mm
Glass	ZnSe
Clear Aperture	45.0mm ϕ
Second Lens	Plano-Concave
Radius	295.7615mm
Thickness	3.0mm
Glass	ZnSe
Clear Aperture	45.0mm ϕ

SUMMARY

The LAWS optical design for the Phase 2 study is complete. The data from the trade studies are available to make decisions concerning the optical design once a launch vehicle is chosen for the LAWS payload. The confocal parabola approach is a simple means of satisfying the requirements for LAWS and at the same time provides the flexibility to tailor the transmit and receive optical paths to meet the desired configurations of each.

3.2.4.2 Polarization Analysis

In order to achieve a maximal SNR from the LAWS optical system, the polarization state of the received signal and the LO must match at the detector plane. In addition, the two beams must be in phase (or nearly so). Although the high-power transmit beam is linearly polarized, and little change in the polarization state is expected from reflection in the atmosphere sample (Ref. 1), the metal-coated LAWS mirrors and transfer optics in the optical system will generally introduce a differential polarization phase change, introducing ellipticity in the polarization state at the detector. The differential effects on polarization of reflections from metal-coated mirrors are well known (see for example Ref. 2, ¶25.10) and the degree of ellipticity is deterministic and can be computed using the methods described below, given the optical index parameters of all of the coatings (reflective and anti-reflective) in the system and the angles of incidence for each of the surfaces.

It is important to bear in mind that our LAWS coating designs offer very high reflectivity values (i.e. 99.9+%). The reflectivity is the average of those for the p- and s-states. It is obvious, then, that the amplitudes of the two polarizations states will not differ by more than a fraction of a percent. Therefore, the coating design specifications must be aimed at controlling the relative *phase* of the two polarization components.

Complicating the polarization behavior in the LAWS system is the conical scan geometry, necessitating a combination of rotating and non-rotating optics in the optical system.

The net effect of propagating a beam through a series of optics, some of which are rotating is that the plane of incidence, and hence the polarization state, subsequently rotates at all additional surfaces.

Operators of ground-based Lidar have noticed variations in SNR as a function of scan angle, even though precautions were taken to minimize differential polarization effects (Ref. 3). In the NOAA windvan lidar, the outgoing beam is circularly polarized using a Fresnel rhomb (Ref. 4). The receive beam is intended to be linearly polarized by the same rhomb. Evidently, the changing angle of incidence on the scan mirrors is introducing differential polarization *phase* effects that have not been predicted.

The problem we must solve for LAWS is to create a design that corrects for the changing polarization phase, or modifies the LO polarization state so that optimal mixing with the receive beam is achieved. Since the polarization problem is deterministic, a solution can be reached, although many specific details of the design must wait upon the complete detailed design (including coating design) of all of the optical elements in the system.

Preliminary Model

The LAWS optical design is complex, involving twenty-five surfaces, including dichroics. For this preliminary design analysis, a simplified optical geometry was deduced from a set of system drawings (Fig 3.-12) for the polarization ray trace. A ray trace of this system for four principal rays at orthogonal rotation states of the primary mirror was performed "by hand" and these results were used in subsequent analyses.

In addition to these traces, the static system was characterized by determining the output polarization for a sequence of rotated input polarization states at the interface between rotating and non-rotating optics (see Fig 3.2-12).

Coatings for the various reflecting and transmitting surfaces were undefined prior to this study, and specifications for the performance of the various coating types were only roughly determined. Based on these approximate design goals, "text-book" coating designs were developed for the reflective and dichroic coatings required in the receiving optical design. No anti-reflective coatings were included on transmitting surfaces, as these are not expected to have a dramatic effect on the polarization behavior of the system. The coatings applied to each surface are summarized in Table 3.2-5. It should be strongly noted that the coating designs have not been optimized either for throughput or polarization concerns, as such optimization are highly dependent on the exact nature of the optical design—particularly with regard to angles of incidence at the various surfaces.

Analysis Method Outline

A complete and detailed description of the polarization and throughput ray trace algorithm can be obtained by reviewing references 1,5,6. The present discussion is meant to provide an overview to establish a general familiarity with the fundamentals of the technique.

Table 3.2-5 Summary of Coating Designs

Surface #	Description	Coating
1	Source Fold Flat #1	Enhanced Gold Reflector
2	Source Fold Flat #2	Enhanced Gold Reflector
3	Source Fold Flat #3	Enhanced Gold Reflector
4	Secondary Mirror	Enhanced Gold Reflector
5	Primary Mirror	Enhanced Aluminum Reflector
6	Atmosphere	Uncoated
7	Primary Mirror	Enhanced Aluminum Reflector
8	Secondary Mirror	Enhanced Gold Reflector
9	Relay Lens #1	Uncoated
10	Relay Lens #2	Uncoated
11	Beam Diverter #1	Enhanced Gold Reflector
12	Beam Diverter #2	Enhanced Gold Reflector
13	Field Lens front	Uncoated
14	Field Lens rear	Uncoated
15	DeRotator #1	Enhanced Gold Reflector
16	DeRotator #2	Enhanced Gold Reflector
17	Air/Relay Lens #2	Uncoated
18	Relay Lens #2/Air	Uncoated
19	Fold Flat	Enhanced Gold Reflector
20	Image Motion Compensator	Enhanced Gold Reflector
21	Dichroic	Dichroic Beamsplitter
22	Lag Angle Compensator	Enhanced Gold Reflector
23	Air/Receiver Focus Lens	Uncoated
24	Receiver Focus Lens/Air	Uncoated
25	Mixer	Enhanced Gold Reflector
26	Air/Dewar Window	Uncoated
27	Dewar Window/Air	Uncoated
28	Detector	Uncoated

Both the system throughput and polarization effects of an optical system can be characterized by a 2x2 complex-valued Jones matrix, M, of the system considered as a single device. This matrix is the product of the Jones matrices of each of the optical surfaces encountered by the propagating ray between the source and detector. J_0 is the input polarization state

$$T=Tr(M\bullet J_0\bullet M^{\dagger})$$

$$P=\sqrt{1-\frac{4\left|M\bullet J_0\bullet M^{\dagger}\right|}{Tr(M\bullet J_0\bullet M^{\dagger})}}$$

$$M=\begin{bmatrix}\tau_s & 0\\ 0 & \tau_p\end{bmatrix}$$

$$M=\prod_{i=1}^{N}M_i$$

Each surface Jones matrix M_i is of the form

$$M_i=D_i\bullet R_i=\begin{bmatrix}\tau^i_s & 0\\ 0 & \tau^i_p\end{bmatrix}\bullet\begin{bmatrix}\cos\psi & \sin\psi\\ -\sin\psi & \cos\psi\end{bmatrix}$$

where, D_i is the device matrix for the surface containing the complex-amplitude throughput for the TE and TM (s- and p-state polarization) modes, and R_i is a rotation matrix to transform the polarization coordinate system appropriately as the direction of propagation changes through the system (i.e.. after reflective surfaces at non-normal incidence angles).

At each optical surface, the elements of the rotation matrix are determined by:

$$\hat{s}\bullet\hat{s}'=\cos\psi$$
$$\hat{s}'\sin\theta=\hat{n}\times\hat{r}$$

where:

r = direction of reflected/transmitted ray

n = direction of surface normal

q = angle of incidence

The complex throughput amplitudes τ_s and τ_p are determined from an optical interference coating analysis algorithm (Ref. 2) which computes a 2x2 complex-valued characteristic matrix S for the film system as a product of characteristic matrices S_i for each film layer, based on material optical constants, film thickness and angle of incidence. From the film system characteristic matrix S the complex transmitted or reflected amplitude is determined after scaling for the bounding entrance and substrate media indices.

$$S=\prod_{i=1}^{m} S_i=\begin{bmatrix} s_{11} & s_{12} \\ s_{21} & s_{22} \end{bmatrix}$$

This analysis method has been implemented in a C software package, POLAR, which allows interactive construction of optical coatings for a given optical system. POLAR accepts as input a ray trace file containing directional cosine data for the propagating ray and surface normal at each optical surface in the system, and previously generated coating design files. This asset permits both throughput and polarization analyses to be performed between any two optical surfaces in the system over arbitrary wavelengths and input polarization states. This latter feature in particular allows specification of a rotating linear (or other) polarization state to be specified at any given location in the optical system. Output data may include throughput, polarization Jones matrix and/or degree of polarization.

POLAR has been cross-checked for polarization and throughput calculations against an earlier FORTRAN polarization ray trace package, MUCOAT, which in turn has been checked against commercially available packages.

Results

Figure 3.2-14 shows the results of calculations of the polarization state transmitted to the detector plane at 9.11 μm wavelength along the principal ray at four primary mirror positions. Both the rotation and elliptical behavior of the polarization state is clearly evident. Due to the symmetry of the rays chosen, only two unique patterns are shown. It should be noted that the degree of ellipticity and angle of rotation indicated are strong functions of the optical system geometry, and hence should NOT be considered as a quantitative result.

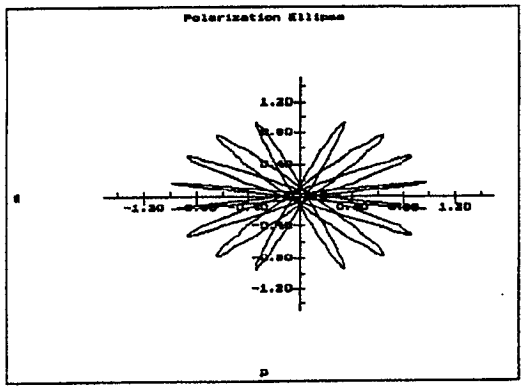

Figure 3.2-14 Simulation of Polarization State at Detector for Linearly Polarized Received Beam

Figure 3.2-15 shows the results of calculations in which the effect of optical system rotation was simulated by introducing a linear rotating polarization state at the interface . Here the full qualitative behavior expected for the LAWS system is shown: there are two polarization eigenstates in which linear polarization states are preserved, and significant degradation at intermediate rotation angles.

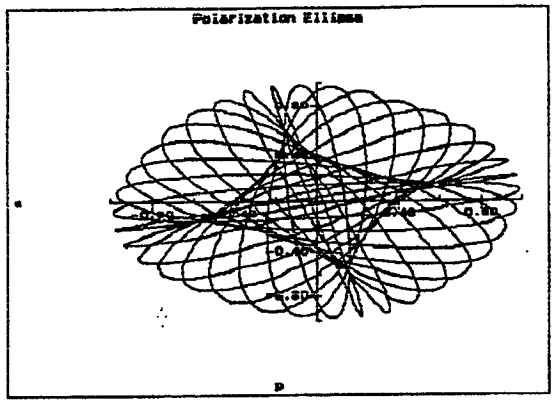

Figure 3.2-15 Qualitative Simulation of Polarization State at Detector, 10° Scan Increments

Discussion

Polarization analysis of the LAWS receiving optics demonstrates two problems needing resolution: the polarization state at the detector plane rotates with the primary optic rotation, and the degree of ellipticity in the polarization state varies within this rotation, between two eigenstates. Solution of these issues requires that the detector plane polarization be stabilized and linearized.

An intuitive approach to the stabilization problem is to force the polarization state to be circular when the transition from rotating to stationary optics occurs. The inherent symmetry in the

polarization state under this approach will result in a stable polarization azimuth. Figure 3.2-16 shows the results of calculations in which a rotating circularly polarized state was introduced at the rotating/stable interface. Rotation of the polarization ellipse has been greatly suppressed, though significant variation in ellipticity and some "rocking" in the azimuth angle remains. During the detailed design phase of the program, minimization of these effects will be achieved through fine-tuning of the optical coatings throughout the system.

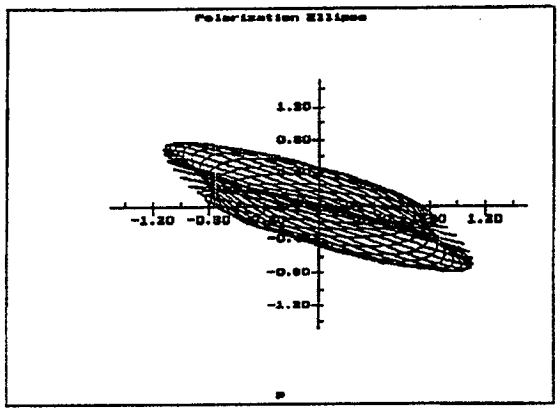

Figure 3.2-16 Effect of Circularly Polarizing Beam at Rotating Interface

To achieve a circularly polarized state at the transition between rotating and stationary optics from an input linear state, a phase retarding reflective coating represents the simplest solution. Such a coating could feasibly be placed on any small reflecting optic in the rotating segment of the system. A second, significantly higher risk, option is the incorporation of a Fresnel rhomb or possibly a quarter wave plate within this section of the system. This may be undesirable from a cost and weight viewpoint and would degrade system throughput by introducing two additional surfaces.

The use of the circular polarization approach to the polarization stabilization problem requires a second rhomb or phase-changing coating to reintroduce linear polarization prior to arrival at the detector plane. This coating may be applied to any reflecting surface in the stationary optical subsystem. We have successfully designed and fabricated high efficiency polarizing beamsplitters for operation at 10.6 μm. We are confident that a similar design approach will provide overall system efficiency figures at the levels stated elsewhere in this report.

An alternative approach is to operate on the LO beam to make it circularly polarized, then mix it with the circularly-polarized receive beam. Since the receive and the LO beams will be at different frequencies and the desired beat frequency (due to the Doppler shift) may or may not

occur when the polarization of the two beams is in phase, this approach may be problematical. In any event, it deserves some consideration during the detail design phase of the program.

Recommendations

Additional efforts on the characterization and control of polarization effects in the LAWS optical system require two major detail design efforts: a complete definition of the geometry of the system in the form of exhaustive ray trace and coating design data, and the determination of acceptable polarization and throughput performance at the detector plane. Ray traces are necessary for a set of primary rotation angles and off-axis positions. Off-axis traces are particularly important if there is appreciable asymmetry in any subsection of the optical design.

As such data become available, a full polarization characterization and design effort will be necessary to finalize the coating designs applied to surfaces throughout the system, particularly to develop appropriate phase retardation and linearization coatings to stabilize the polarization rotation behavior.

References

1. Gross et. al., Applied Optics , Vol. 23, p2518 (1984)
2. Jenkins and White, Fundamentals of Optics, McGraw-Hill, New York, 1976
3 M. J. Post, Private Communication
4. M. J. Post, R.A. Richter, R. M. Hardesty, T. R. Lawrence, F. F. Hall, Jr., "National Oceanic and Atmospheric Administration's (NOAA) pulsed, coherent, infrared Doppler lidar—characteristics and data", Physics and Technology of Coherent Infrared Radar, SPIE Vol. 300 (1981)
5. Waluschka,E. Optical Engineering, Vol. 28 #2 p86
6. Thelen, A. Design of Optical Interference Coatings, McGraw-Hill, New York, 1989
7. HDOS Engineering Notebook #1005, A. Turner

3.2.5 Optical Subsystem Preliminary Design

The optical subsystem design forms the bridge between the laser and the receiver, as well as providing the scan function of the system.

3.2.5.1 Mechanical Configuration

The preliminary configuration design that evolved through the Phase 2 study effort is shown isometrically in Figure 3.2-17.

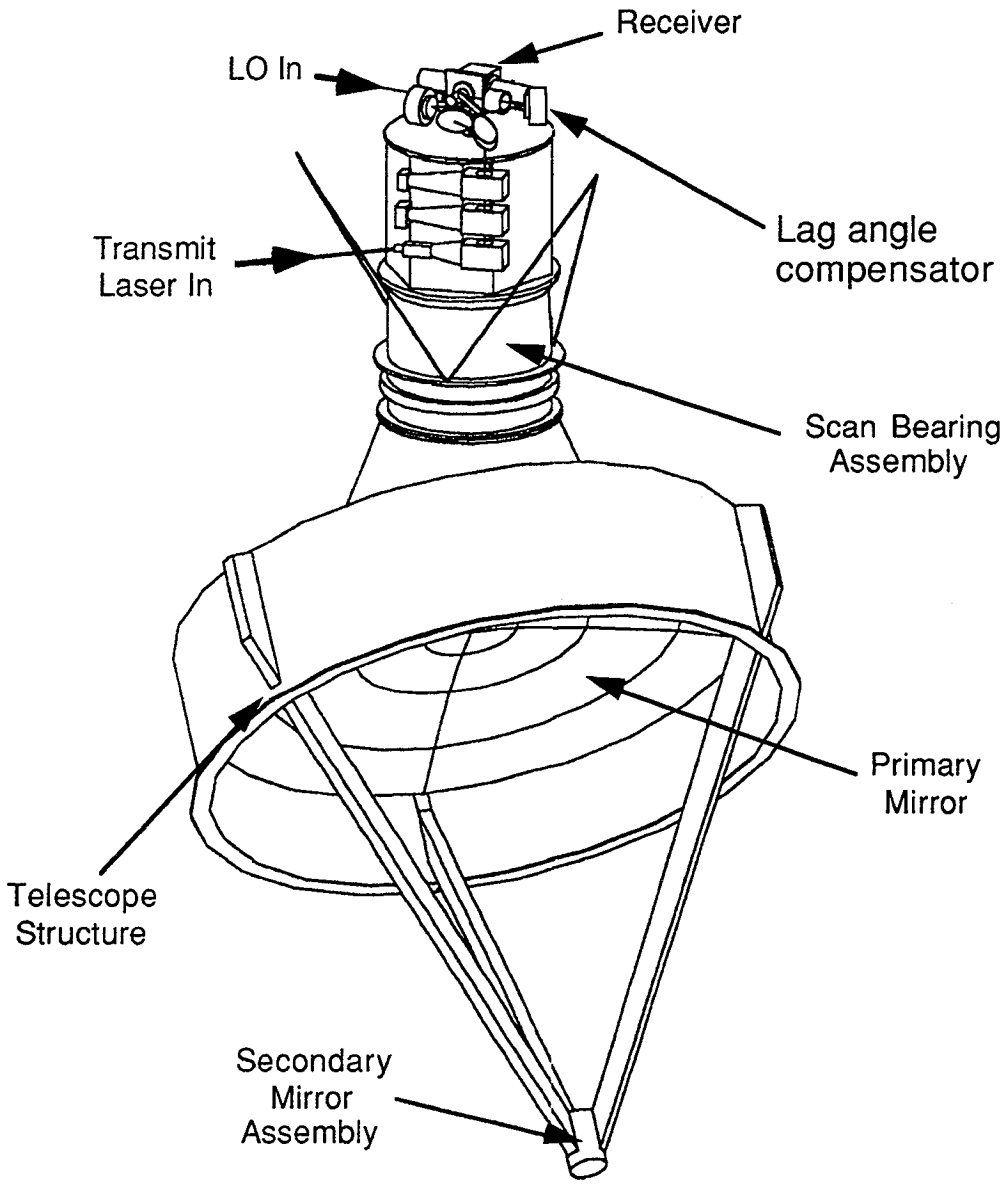

Figure 3.2-17 Optical Subsystem Baseline Design

The basic configuration resembles an RF radar system. Most optical telescopes require a tube or baffle system to prevent the Sun from heating and deforming the primary mirror. Because of the orbit geometry of LAWS and its seasonal variation, a tube baffle would need to be ~12 feet long. For a scanned telescope, such a lengthy baffle would be unworkable.

A thermal design analysis performed at HDOS showed that the temperature of a primary mirror made of ultra-low expansion glass will remain within allowable bounds if the mirror coating is an overcoated aluminum. Therefore, an unbaffled design was adopted.

The heart of the design is an adaptation of the Hughes Aircraft bearing and power transfer assembly (BAPTA), developed for use on their line of commercial communications satellites. Over a hundred of these assemblies have been launched and successfully operated for mission lifetimes averaging over eleven years. Approximately 80% of the existing HS A10 design is incorporated in the LAWS configuration. A detailed illustration of the LAWS BAPTA is provided later in this section.

The locations of the outgoing laser beam and the local oscillator beam are indicated on the drawing. The receiver, along with its cooler, is mounted on the "top hat" optical bench at the position indicated.

The major dimensions of the Optical Subsystem are shown in Figure 3.2-18

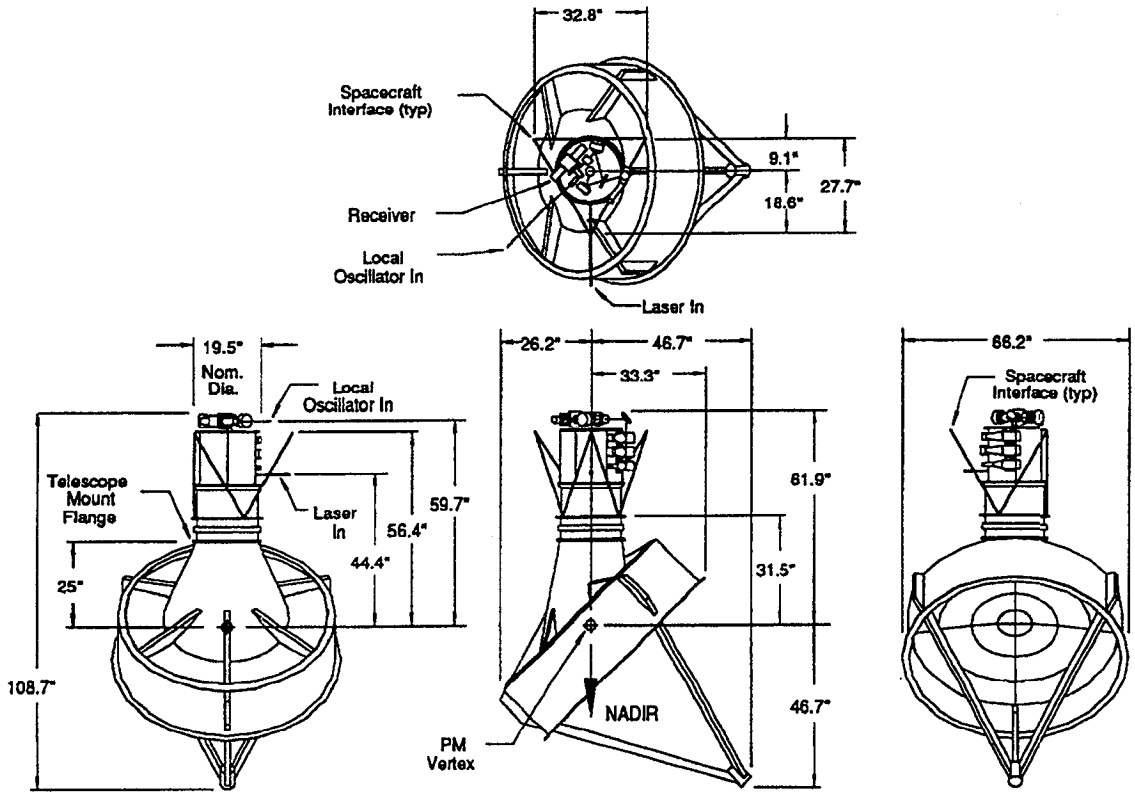

Figure 3.2-18 Dimensions of the Optical Subsystem

3.2.5.1 Scan Bearing Design

Figure 3.2-19 shows a cross section of the Scan Bearing/Derotator/Optical Bench Assembly configuration. The scan bearing design is one of the most significant accomplishments of the Phase 2 Optical Subsystem effort.

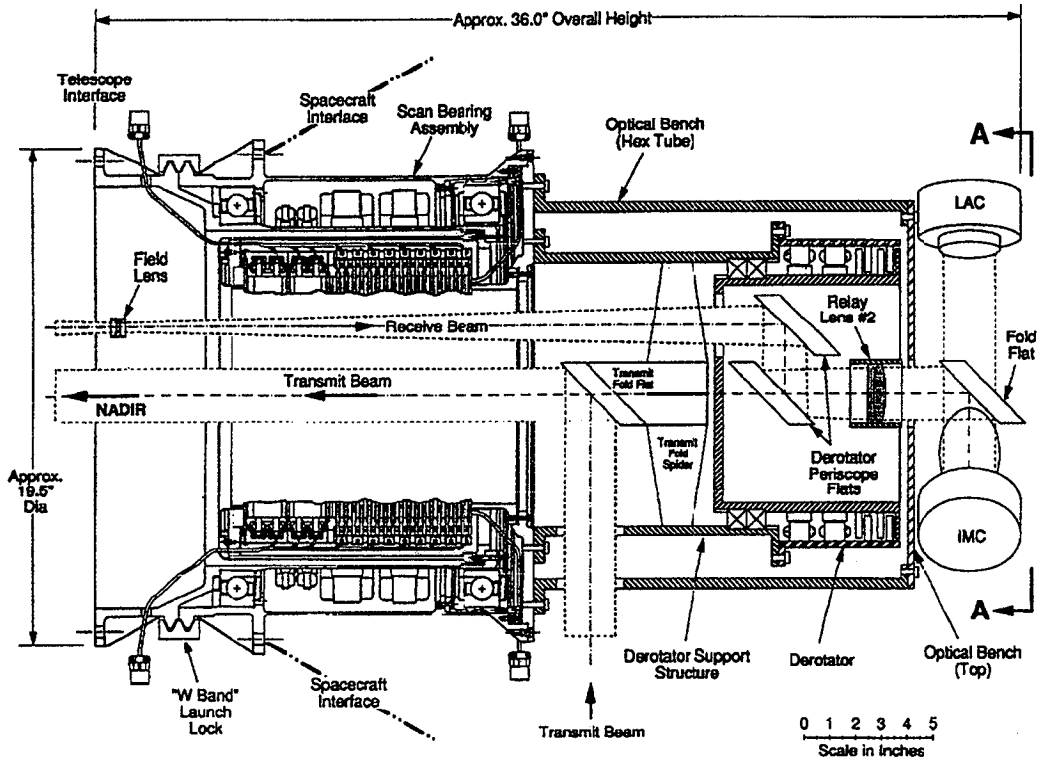

Figure 3.2-19 Scan Bearing/Derotator/Optical Bench Assembly Configuration.

The core Scan Bearing Assembly on the left side of the illustration is a derivative design of the Hughes space-proven HS A-10 BAPTA (Bearing and Power Transfer Assembly). The HS A10 BAPTA meets the power, signal, and run-out requirements of LAWS. The HS A-10 design has been modified to provide a hollow bore through the shaft for the transmit and receive beams. It includes the bearings, motors, encoders and sliprings required to perform the conical scan and to transfer utilities across the rotating interface to the telescope. Electrical functional redundancy is provided to preclude single-point failures. An integral flange on the outer housing near the left hand bearing provides a hard point for attachment of the telescope assembly. Between the two flanges is a "W" band clamp launch lock which prevents rotation of the telescope during launch, unloads the bearings, and provides a by-pass launch load path around the bearings.

Mounted on the top of the BAPTA (shown inside the Optical Bench on the right side of the chart) is the derotator assembly. The rotating part of this assembly is electronically synchronized to the rotation of the telescope and contains a "periscope" which diverts the orbiting beam onto the scan axis to eliminate beam motion. The derotator contains electro-mechanical components similar to the BAPTA, except it has no sliprings. Again, electrical function redundancy is provided. Attached to the inside of the Derotator Support Structure is a spider-supported fold flat. The transmit laser beam enters laterally through a port in the side of the derotator and is folded down the scan axis toward the telescope by this flat.

Also attached to the top of the BAPTA and surrounding the derotator is the Optical Bench. This structure provides metering, support and mounting provisions for the subsequent receive path optics, the Receiver and cooler Assembly, and the Optical Subsystem diagnostic optics. This design is illustrated in Figure 3.2-20 below. The "Tip-tilt" assembly is used for aligning the LO beam to the receiver.

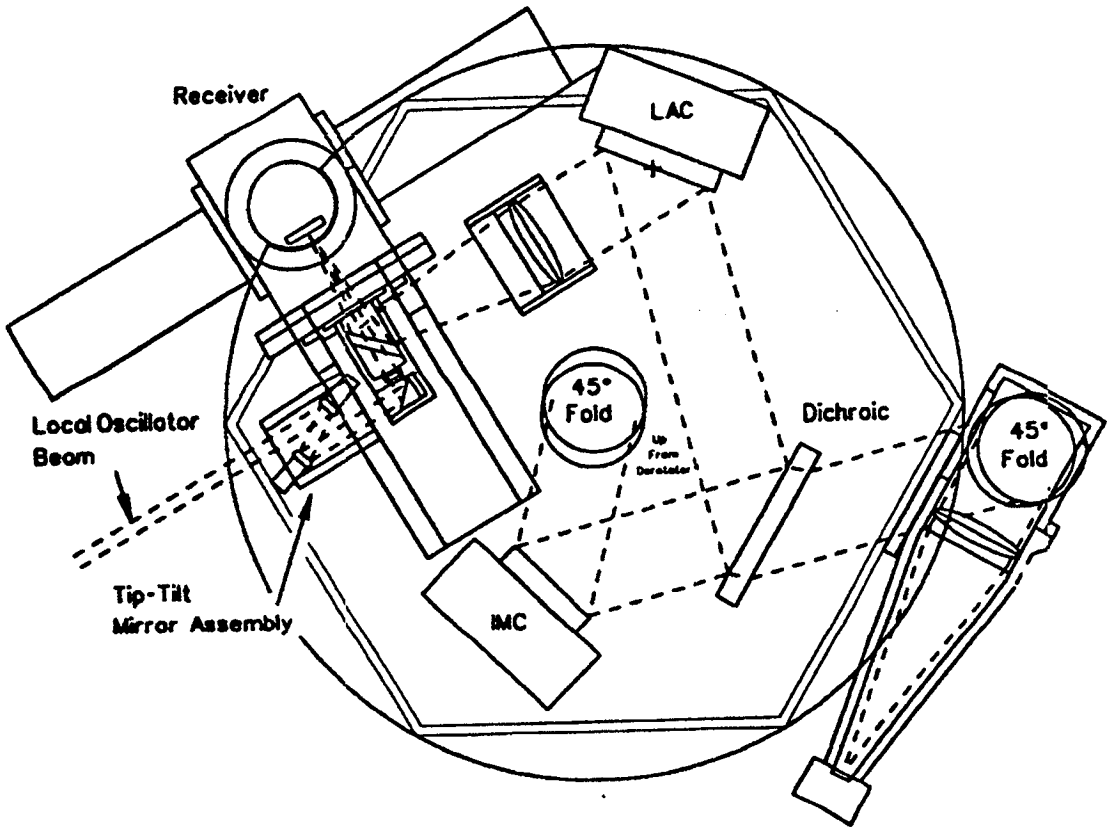

Figure 3.2-20 Top View of Optical Bench showing Lag Angle Compensator, Receiver, and Diagnostics Arrangement.

Hughes Aircraft's Space and Communications group has gained significant experience in designing and producing bearing and power transfer assemblies for their line of spinning communications satellites. Hughes Danbury is able to bring this technology to the LAWS program. Although the LAWS requirements will result in a program specific design, the performance requirements are within the envelope of this proven technology. 80% of the existing design will be incorporated in the LAWS design. Therefor, the risk level associated with the scan bearing is considerably reduced.

The BAPTA design incorporates the full range of motor, encoder and slip ring redundancies, assuring a reliable design, confirmed by successful flight experience. A comprehensive specification for the supporting electronics has been prepared to facilitate the cost estimates for LAWS.

3.2.5.3 Lag Angle Compensator Design

For the lag compensation system, a feedback control loop was designed and feedforward acceleration and deceleration profiles developed. The performance of the system was evaluated for a range of system parameter values and it was shown that the requirements can be met. The details are described in the following paragraphs.

In the LAWS system, when the backscattered laser pulse arrives, its length is about 0.2 ms. Since the telescope is rotating, its image on the detector will move unless a beam steering mirror is used to hold it stationary. Here we address the problem of the control of such a beam steering mirror.

Parameters

A range of telescope rotational velocities were investigated. For system elevation a few values were also tried. We list (Table 3.2-6) the parameters chosen and some that are system constraint values.

The main requirement is that the RMS angle error referred to the object space be less than 0.35 μR. In addition the mirror dynamic range is desirable to be small. The control bandwidth should also be as small as possible.

Control Concept

Large steps in reference command of feedback systems result in excessive actuator torque requirements. In such cases, if possible, computed feedforward torque and other loop variables such as position and velocity are of immense help. For the present problem, we are going to use

feedforward signals. Fig 3.2-21 shows a block diagram of the control concept for one axis. A position loop is closed using a local sensor. Computed torque and position reference signals are used for the feedforward control.

Table 3.2-6 Lag Angle Compensator Control Loop Parameters

Parameter	Value
Elevation	450 km, 525 km
Scan angle	45 °
Telescope rpm	6 - 12
Magnification	33
Pulse return time	4.4044 ms, 5.173 ms
Mirror speed needed	1.2218 * (Tel rpm) R/s
Mirror moment of inertia	0.00017 in lb s^2
Flexure resonance	50 Hz
Mount moment of inertia	0.0017 in lb s^2
Mount resonance	2000 Hz
Actuator reaction into mount	5 %
Damping coefficient	0.005
Computational delay	1 ms minimum
Peak torque	2.7 in lb

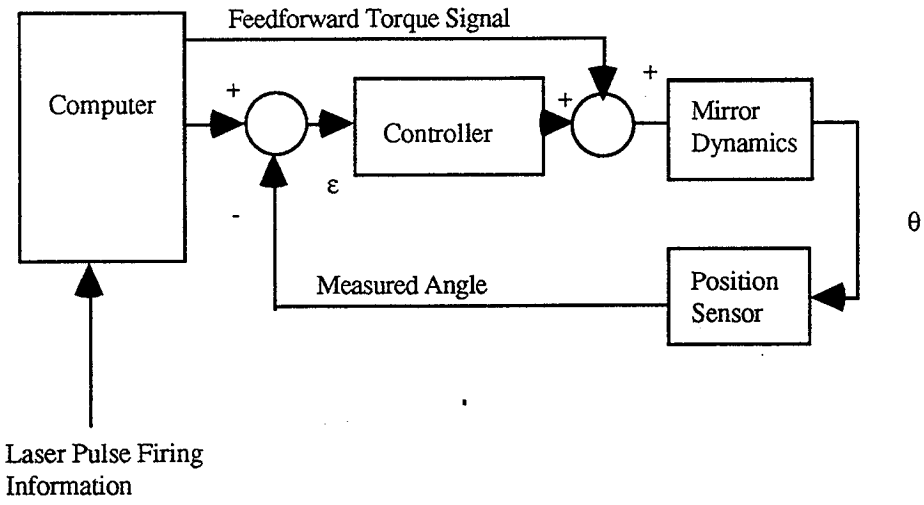

Figure 3.2-21 Lag Angle Combined Feedforward/Feedback Control Concept

Fig 3.2-22 shows further details of feedforward acceleration. A single pulse consisting of two half cycle raised cosine sections and a constant acceleration region is used to bring the mirror to the desired angular velocity at the desired instant. The fraction of the total time used by one raised cosine section is denoted by ß. This fraction can range from 0 to 0.5. A small value indicates fast rise and a larger value, slower rise to the peak acceleration. A smaller ß will require a smaller peak acceleration while a larger value will result in a lower peak jerk magnitude. For the simulation results given here, a ß of 0.1 was used.

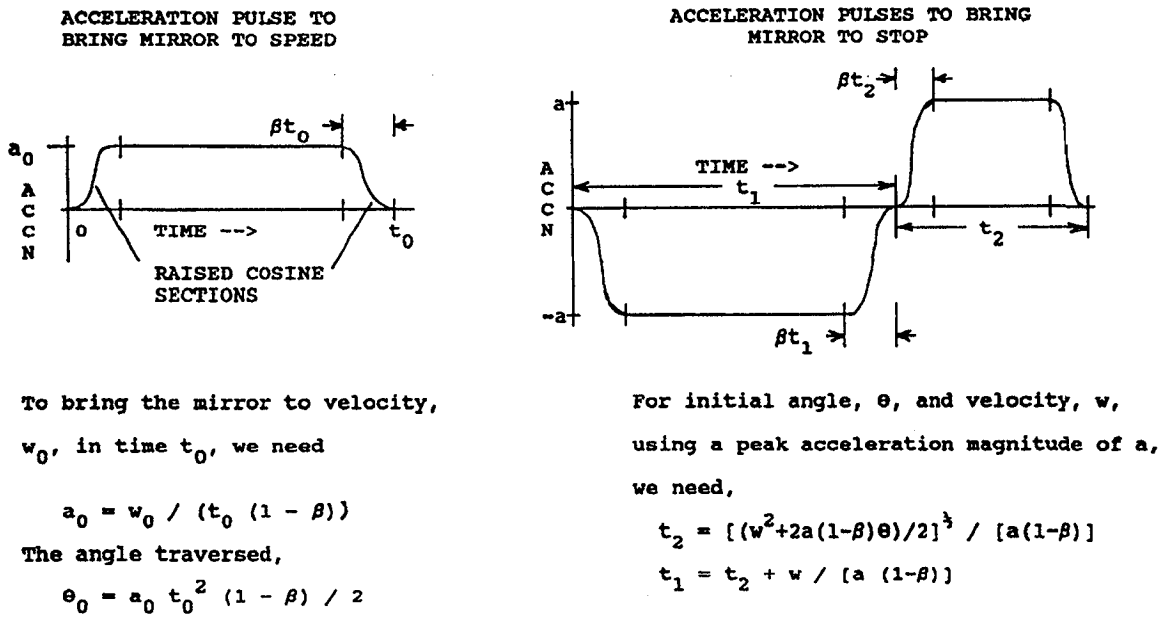

Figure 3.2-22 Feedforward Acceleration and Stopping (Fly Back) Profiles

For a given ß and the pulse duration, the peak acceleration is the only variable to be chosen and thus both angular velocity and angle traversed cannot be independently chosen. This matters more in the stopping strategy where both angle and the angular velocity must be brought to the reference null values. In this case, a combination of a negative and a positive pulse is used. The relations for the two pulse durations are given in the figure.

A position profile computed from the acceleration profiles shown will form the reference to the feedback control loop. In addition torque signals proportional to the accelerations will be added to the torque given by the controller. In this scheme, the difference between the assumed inertial mirror and the real mirror on flexure will be taken care of by the feedback loop. If desired a feedforward torque profile closer to the total needed can be computed.

Loop Design

Fig 3.2-23 shows the dynamic model used for the mirror system. A control system was designed for the model shown.

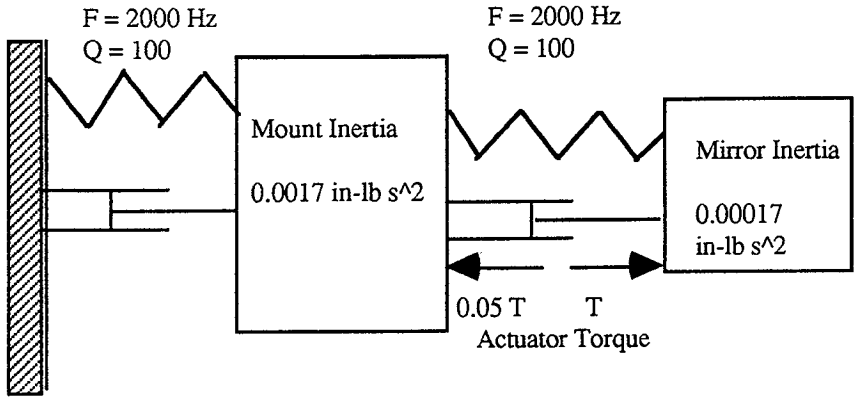

Figure 3.2-23 Mirror and Mount Dynamic Model

The control parameters are shown in Table 3.2-7 below. Excellent gain and phase margins were achieved.

Table 3.2-7 Control Loop Parameters

Parameter	Value
Type	1
Bandwidth (Open Loop Unity Gn X-Over)	500 Hz
Lead-Lag Network	158/1580 Hz
Proportional-Integral Breakpoint Freq	100 Hz
Gain	3.234E5 in-lb/Radian
Phase Margin	43°
Gain Margin	Lower 7.78 Higher > 100

The above is a synopsis of significant analysis and control system simulations performed during the course of the Study. Further details are available in the LAWS Data requirements documents.

Conclusion

A control system design has been presented for the lag angle compensation in the LAWS lag angle compensation system. Frequency and time domain simulations were carried out to evaluate the performance of the proposed design. For the telescope rotational speed range of 6 - 12 rpm tested, we find that the design meets the performance requirements. The mirror dynamic range for 6 - 12 rpm speed range lies approximately between 20 and 40 mR.

3.2.6 Risk Reduction

Significant reduction of technical, operational and cost risks has been accomplished through the major technical trades and cost estimations performed during the Phase 2 contract. In addition, substantial IR&D efforts and related technology developments have been focussed on the LAWS program objectives.

The technical trades are interconnected. The thermal analysis provided insight into the thermal baffle and primary mirror coating requirements, the configuration trades sharpened the definition of the thermal environment relative to solar exposure and mirror heating. The selection of an aluminum optical coating for the primary mirror, based on thermal considerations, had an effect on the polarization analysis and system throughput. Cost and risk reduction were achieved by eliminating (with Project and Science Team concurrence) the complexity of items such as a variable scan angle. Finally, there were several trades in the optical design that alleviated error budgets and tolerances, driving toward a reduced risk, lower cost optical subsystem.

The targets of the trade studies, facilitated by the tools we have developed are shown below. We are confident that our study efforts will result in achieving each of these targets in the final LAWS hardware and mission operations.

- Optical heterodyne system with efficiency almost double the initial estimates (20% versus 10%)
- Optical subsystem weight 312 kg (versus 350 kg allocation), dynamically balanced
- Adaptation of space-proven BAPTA for scan bearing design (no on-orbit failures in over 75 satellites, 11 years average life)
- Meet pointing requirements with 30% margin
- Cost estimates performed 3 ways: top down, bottoms up, parametric. All agree to ±10%.

3.2.6.1 Operational Risk Reduction

Our Phase 2 reliability assessment for the Optical Subsystem indicated that the Angular Displacement Sensor (ADS) used in the image motion compensation control is the reliability-

limiting component. The specific device we have selected for this application is the Systron-Donner Model 8301 Fluid Rotor Inertial Angular Displacement Sensor, used successfully in the Landsat Thematic Mapper program. As a result of the analysis, we are now planning stand-by redundancy for this component.

The table below illustrates the reliability design philosophy that we have adopted aincorporating redundancy where appropriate, and adequate design margins elsewhere. Since many of the components of the Optical Subsystem are adaptations of previously space-qualified subsystems, many of the desirable redundancies are already available.

Table 3.2-8 Operation Risk Reduction

Component/Ass'y	Failure Mode	Approach for Reliability	System Impact
Scan Bearing	Bearing Noise	Design Margin	Minimal
ADS	Fixed output	A/B Redundancy	Minimal
Pointing Control Electronics	Various	A/B Redundancy	Minimal
Scan Torquer	Shorts, opens	Dual windings, Redundant	Minimal
Slip Rings	Wearout, noise	Redundant rings/brushes	Minimal
LAC, IMC Mirrors	Shorts, opens	Redundant Actuators	Minimal

The Hughes Aircraft experience with the bearing and power transfer assembly (BAPTA) that we have adapted for use as the LAWS scan bearing, has successfully performed in space on over 100 spin-stabilized communications satellites with no failures over an average life of eleven years. This heritage gives us confidence that the LAWS scan bearing will be a low-risk component of the optical subsystem. Its design and fabrication is certainly well within the state of the art. In addition, Hughes Danbury bearing testing (performed under IR&D funding) shows that flight-quality bearings of the large size needed by the design will meet the stringent high-frequency angular runout requirement.

The other items in the table above and the approach for reliability are representative of standard practice in high-precision space instrumentation. In every case, these techniques have been successfully applied to space hardware at Hughes Danbury and elsewhere.

As reported in the DR's, the five-year probability of success for the Optical Subsystem is 0.9811.

3.2.6.2 Conclusion

Risks in the LAWS program have been mitigated by a combination of Government and corporate investment. The lists below illustrate some of the tangible assets that have been developed through the support of corporate investment in the program. HDOS IR&D efforts are continuing, subject to the perceptions of the general status of the program. Other concurrent programs at HDOS have developed components that we plan to incorporate in the LAWS instrument. Examples of these are the fast steering mirrors and servo for the lag angle compensator and the tip-tilt beam alignment mirrors.

Long Term Corporate and Team Commitment

- Windsat Studies
- Corporate financial investment (IR&D, pre-phase C/D efforts)
- Schedule and cost planning for phase C/D in place

Hardware Assets at Hughes Danbury

- Flight quality scan bearing set, bearing test instrumentation
- Image motion compensation design and hardware available for experiments
- Design of lag-angle compensator, and hardware for demonstration. Available for future upgrading
- Hughes Aircraft heritage in communications satellite despun platforms

Related Hardware

- ABCS breadboard with HOE's and Hartmann wavefront sensor
- Fast steering mirrors and tip-tilt alignment mirrors

Hughes Danbury is positioned to support GE in executing the LAWS hardware program. We have the heritage, IR&D and corporate management and technology to perform well during the construction and flight mission phases of the program. The semi-annual budgetary cost estimates performed during the LAWS Phase 1 and 2 studies have informed the management structure about the LAWS program. The Hughes Danbury functional groups are up to speed concerning the programmatic requirements and have approved the estimates furnished to GE and to NASA. Detailed schedules and milestones have been worked out, assuring minimal cost and schedule risk for NASA.

3.3. Laser Subsystem

3.3.1 Laser Subsystem Requirements

The Laser Subsystem performance and interface requirements are summarized in this subsection.

3.3.1.1 Performance Requirements:

The rationale for selection and selected values are presented for the following parameters: pulse energy, pulse repetition rate, pulse length, wavelength, temporal coherence and chirp, spatial coherence, beam jitter, lifetime, power, thermal control, and mechanical disturbances.

Pulse Energy

The pulse energy requirement of 15 J in the far field is derived from the need for adequate lidar photodetector output signal-to-noise ratio (SNR). The SNR is also a function of other system parameters (primarily telescope size, and system losses), atmospheric parameters (primarily the aerosol backscatter coefficient), and the measurement range. The results of computer simulations of the lidar velocity measurement process indicate that a 15-J pulse energy/1.5-m optical diameter combination is optimum for the mission measurement scenario and assumed atmospheric parameters.

Pulse Repetition Rate

A single lidar pulse yields an estimate of the radial velocity within each range resolution element along its line of sight. To ascertain the total horizontal vector within a localized region on the earth's surface, the region must also be interrogated from other directions. This requirement, and, of course, the need for interrogating diverse areas, dictates that the laser be pulsed repetitively while the line of sight is being scanned. The scanning is accomplished by conically scanning the telescope line of sight, since this approach is the only one compatible with low acceleration loads on the platform. Consideration of the scan pattern formed for various scan rotation and pulse repetition rates have indicated the need for an orbit average pulse repetition rate of 5 Hz, with a maximum of 20 Hz. Another requirement is that the pulsing be asynchronous to allow adjustment of the sampling rate to adjust for natural oversampling at high latitudes and at scan azimuths where velocity vector measurements are not possible (i.e., near the polar and latitudinal planes).

Pulse Length

The pulse length is determined to first order by the range resolution requirement for the lidar. The vertical resolution requirement is 1 km, which for the 45-degree Nadir angle translates to approximately 1.4 km, radially. This requirement can be met by pulse durations of up to 10 μs. Because of speckle, however, it is desirable to obtain several independent estimates within a resolution element to effect smoothing of the Doppler estimate. Since a new speckle estimate is obtained in a time period equal to the pulse duration, a pulse length shorter than 10 μs is required. Speckle statistics (refer to "Radar Observation of the Atmosphere," Louis J. Battan, University of Chicago Press, 1973), indicates that averaging 3 to 5 independent speckle estimates is close to optimum. Laser efficiency considerations indicate that a pulse duration of 3 μs is preferred. The shorter pulse duration also keeps open the option of enhanced range resolution for atmospheric research investigations.

Wavelength

The laser wavelength selection was based on two factors. Minimization of extinction by atmospheric CO_2 requires that the active laser CO_2 molecule be a rare isotope. Since enhanced aerosol backscattering is expected (and has been reported) in a narrow wavelength band in the vicinity of 9.11 μm, the $^{12}C^{18}O_2$ isotope was selected. The R(20) line of Band II of this isotope oscillates at a wavenumber of 1097.1506 cm^{-1}, or a wavelength of 9.1145 μm. STI Optronics recently completed a program to measure the detailed lasing characteristics of this molecule during a program funded by the Air Force Geophysical Laboratory and the NASA/Marshall Space Flight Center.

Temporal Coherence and Chirp

Temporal coherence refers to frequency variations as a function of time during the laser pulse, or frequency chirp, and is caused by refractive index variations in the gas within the laser cavity during pulse formation. Excessive chirp increases the pulse bandwidth and degrades the Doppler resolution. Ideally, the chirp is kept small relative to the transform limit pulse bandwidth (given in Hertz by the inverse of the pulse duration). The FWHM spectral width of the (baseline 3 μs) pulse including transform limit and chirp effects shall not exceed 250 kHz. Flow-induced Doppler (wind turbulence and shear) would result in additional broadening.

Spatial Coherence (at Laser Exit)

Spatial coherence refers to phase distortions across the transmitter laser wavefront, which causes it to be propagated as a non-diffraction-limited beam and consequently spill radiation

outside the diffraction limited field of view of the lidar receiver, contributing to a signal loss. The rms optical path difference (OPD_{rms}) across the laser beam is related to two popular measures of phase distortion, viz., the beam quality (B.Q.) and Strehl ratio, by the following relations:

$$B.Q.=\exp\frac{1}{2}\left[\left(\frac{2\pi}{\lambda}\right)OPD_{rms}\right]^2$$

$$\text{Strehl Ratio} = \exp-\left[\left(\frac{2\pi}{\lambda}\right)OPD_{rms}\right]^2$$

The Strehl ratio is a useful measure, since it is the ratio of the signal that can be expected relative to that possible for an undistorted beam. The baseline specification for the transmitter laser is a B.Q.=1.1, which corresponds to a Strehl ratio of 0.826 and an rms OPD = 0.0695 waves. A Strehl ratio of 0.826 represents an SNR loss of 0.83.dB. In practice, the 0.0695 wave rms OPD is apportioned among all the potential contributors within the laser e.g. the cavity optics, optical truss, flow loop, etc. and these components are designed to meet these specifications.

Beam Jitter (at Laser Exit)

Beam jitter refers to the directional variation in the propagation direction of successive laser pulses. The baseline specification is 25-μr rms at the laser exit, which is approximately one third of that available to the total instrument. Note that this translates to less than 1 μr at the telescope output, since it is decreased by the telescope magnification. Excessive beam jitter, if uncompensated, would place the interaction region of the transmit beam on earth outside of the field of view of the lidar receiver.

Lifetime

The instrument shall have a lifetime of five years, which translates to approximately 10^9 shots.

Power

The overall efficiency of the laser shall exceed 5% so that the instrument can meet the 2.2-kW input power limitation. The Laser Subsystem load can be subdivided into a variable component (that draws the major part of the average power), which is due to the laser gain module PFN charging cycle, and a relatively constant component for the gain module fan and all the accessory electronic components.

Thermal Control

The Laser Subsystem thermal control requirements consist of a thermal blanket to isolate the laser from external radiation sources and the laser fluid loop to maintain the operating temperature of the laser gas at the desired 300-K value. The laser fluid loop is a system component and not part of the Laser Subsystem. The requirements are set solely by the Laser Subsystem, however. The laser fluid loop pumps fluid through the laser heat exchanger and pulsed power system heat exchangers in series, which extracts heat from the heated laser gas and the pulsed power components, respectively. Low-volume parallel loops dissipate small heat loads from the CW laser, acousto-optic modulator and resonator optics, respectively. A design driver for the laser fluid loop is the requirement to minimize the temperature gradient across the laser and pulsed power heat exchangers (to 2.5 °C) in order to minimize gas density fluctuations. This requirement translates to a high fluid flow rate system. On a per pulse basis, the gain module heat exchanger dissipates 162 J. The pulse power modulator heat exchanger load on a similar basis is 32 J/pulse.

Mechanical Disturbances

The laser gain module is a significant generator of acoustic disturbances. These disturbances transmit through the gain module structure to the instrument platform attachment points. Contributors to these disturbances are the electrical discharge, fan rotation, and the cycling of the laser gas around the flow loop. Vibration isolation stages are incorporated into the gain module/instrument platform attachments with launch clamps to short circuit the former during launch.

3.3.1.2 Interface Requirements

Interface requirements are separated into the categories of Mechanical, Thermal, Power, Optical and Command, Control and Telemetry.

Mechanical Interfaces

The Laser Subsystem mechanical interfaces are detailed below.

Gain Module Support

The gain module is supported by 4 vibration isolator mounts located as indicated in Figure 3.3-1. The acoustic disturbance power spectral density on the gain module side of the support due to gain module disturbances shall not exceed 0.003 g^2/Hz per axis over the band-pass 4.0 through

25.0 Hz. The isolator resonant frequency will is 2.5 Hz to isolate the primary gain module oscillation modes. Launch clamps will be installed.

Optical Component Support

The location of transmitter optical components on the optical truss is shown in Figure 3.3-1. The optical truss is hard-mounted to the LAWS instrument platform via four hard-points as shown.

Electronic Units Supports

Two Laser Subsystem electronic units (the control computer and the high-voltage laser power supply, respectively) are attached to the system coldplate.

Thermal Interfaces

The Laser Subsystem thermal interfaces are detailed below.

Gain Module Cooling Fluid Loop

The system will provide an active cooling loop, which will remove 1667-W from the gain module during nominal 15-J, 5-Hz operation. The cooling loop will provide a maximum fluid flow of 1667-lb/hr at a differential pressure of 1.0 psig. . Inlet and outlet temperature differential shall not exceed 2.5 °K at a nominal inlet temperature of 297 °K. The working fluid will be water. The laser fluid loop will be operational a minimum of 20 minutes before each laser start-up. The loop will also support the dissipation of minor heat loads from the cw laser, electro-optic modulator and the resonator optics. The interface with the system will be at the hose couplings attached to the gain module.

Laser Insulation Blanket

The system thermal subsystem consists of a thermal blanket and radiation shield that surrounds the laser subsystem (transmitter gain and optical modules) to minimize ambient thermal flux loading. The effective thermal conductivity of the blanket will be sufficiently low to provide a maximum flux of 0.05 BTU/ft^2/hr during the laser on time.

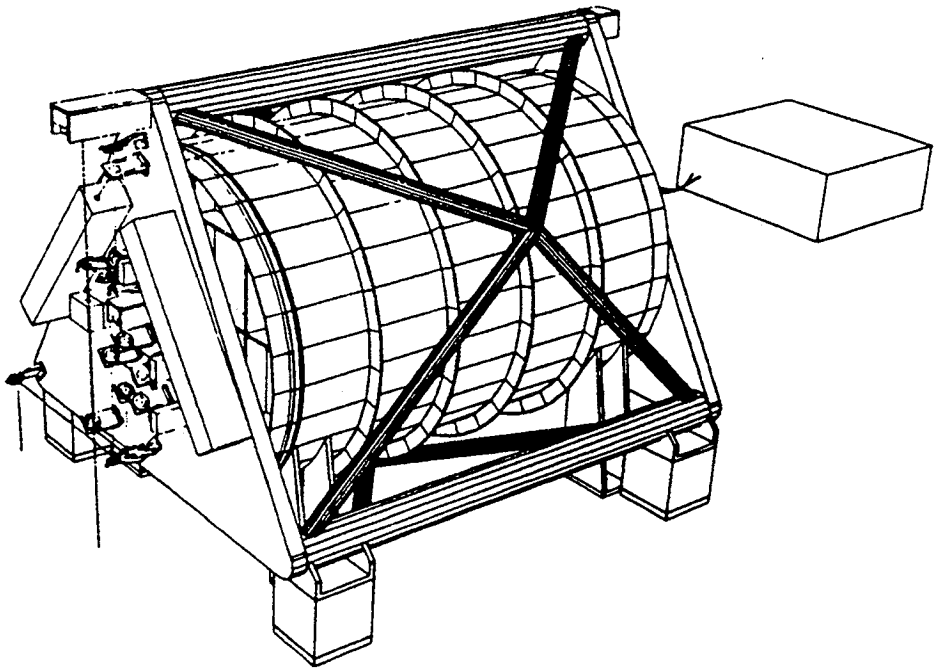

Figure 3.3-1. Laser Mechanical Configuration

Electronic Units

The Laser Subsystem control computer and the high-voltage laser power supplies are attached to a platform coldplate.

Power Interfaces

All the laser subsystems will interface with the 120 ± 4, -VDC supply aboard the platform. Voltage requirements within the laser are of two types: low voltage for housekeeping, and high voltage for capacitor charging within the pulsed power assembly of the transmitter.

Housekeeping Power (120 VDC)

Housekeeping power is used for 'benign', low voltage loads. These loads and their projected power requirements are:

1. Fan	20 W
2. Control System	30 W
3. Injection/Reference Oscillator Laser	40 W
4. Acousto-Optic Modulator	40 W

To attain the quoted power usage, the RF power to the injection oscillator and acousto-optic modulator will be duty cycled for periods of 10 msec at the pulse repetition rate (nominally 5 Hz). The interface with the system will be at the power coupling attached to the Laser Subsystem power distribution panel.

High Voltage System Power

High voltage power is delivered at nominally ±35 kVDC for charging of the pulsed power slow stages. Charging is directly into a capacitative load, and so it is understood that this voltage will vary substantially from nominal during the charge cycle. The switchable ±35-kVDC supplies will derive their input power from the 120-VDC bus. Accommodation is made within the laser subsystem for varying the charging cycle as a function of the pulse repetition rate and charging status of the solar array and batteries. The interface with the system will be at the power coupling attached to the high-voltage power supply.

Optical Interfaces

The Laser Subsystem provides pulsed laser output for transmission down to the atmosphere and also a stabilized CW reference beam to the receiver to function as the receiver reference (Local Oscillator) beam. The CW reference laser(s) also provides the injection laser beam for the gain module and its interfaces are internal to the laser and not included here.
The interfaces to the optical module is defined entirely in terms of the optical characteristics of the two laser beams generated by the Laser Subsystem at their respective interface planes.

Transmit Laser Pulse

Interface Plane

The interface to the Optical Subsystem is defined at the exit of the beam directing mirror located downstream of the transmitter laser exit, and located at the apex of the triangular optical bench, see Figure 3.3-1.

Beam Size and Shape

The size of the delivered pulsed beam is 5 cm in diameter. Beam apodization amplitude and phase profiles have been calculated for the baseline resonator design, see Figure 3.3-2. Profiles have also been generated for several representative values of the beam misalignment envelope.

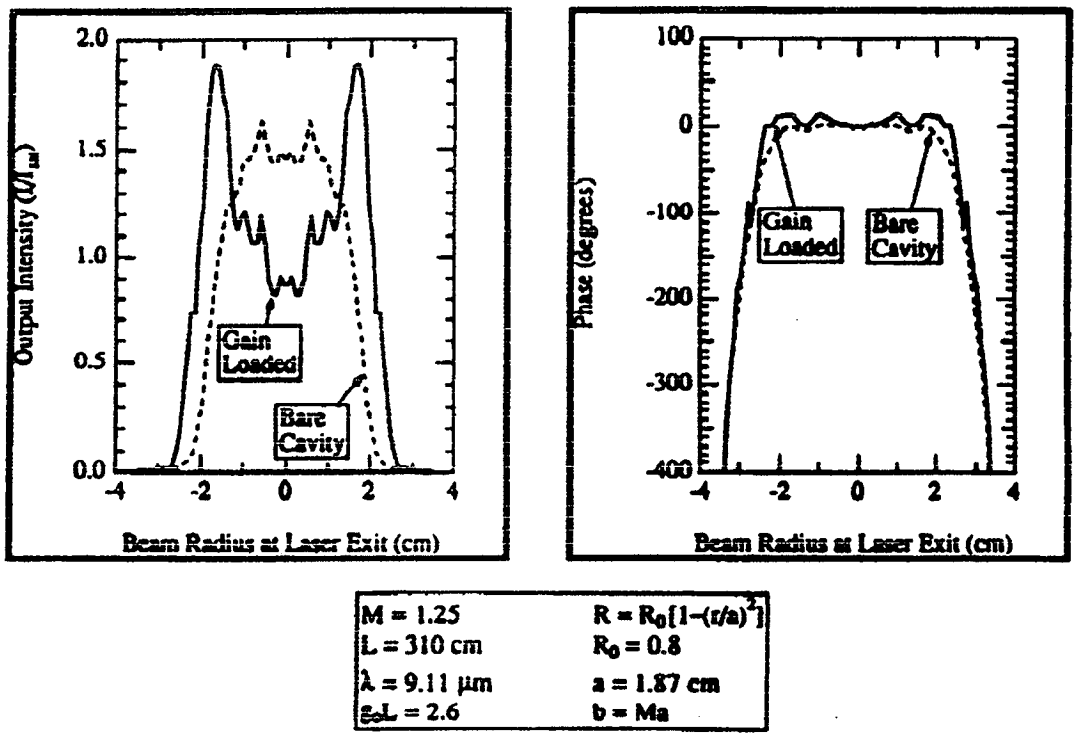

Figure 3.3-2 Intensity and Phase Profiles at Laser Exit of Gain Loaded vs Bare Cavity Mode

Beam Energy

The optical energy in the delivered beam is nominally 20 J of which 15 J is considered useful radar energy. However, the full 20 J needs to be considered in thermal control, optical damage analyses, etc.

Beam Power

The average optical power integrated over the interface is variable because of variations in repetition rate. The mean value is 100 W (20-J at 5-Hz). Peak optical power is variable in both the beam cross section and time and can exceed 1 MW/cm^2. Reference should be made to Figures 3.3-2 (spatial profile) and 3.3-3 (temporal profile) for basic input to calculate peak-power profiles.

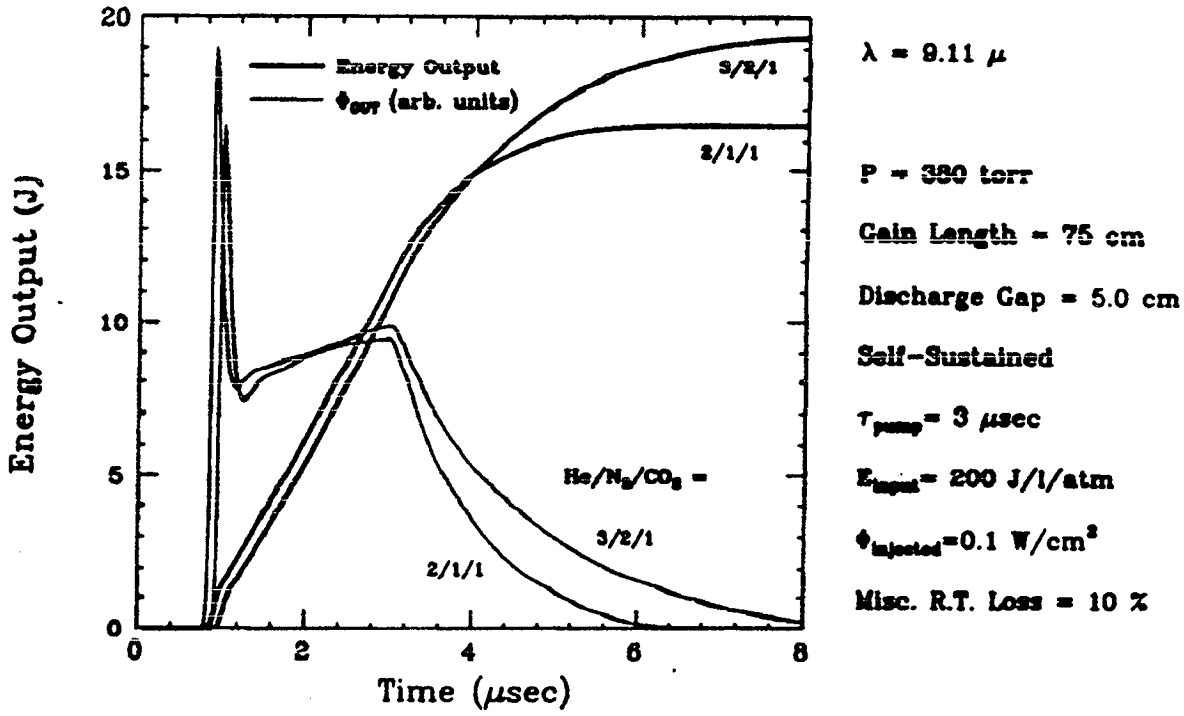

Figure 3.3-3 LAWS Pulse Temporal Profile

Beam Jitter

Beam Jitter shall not exceed 25 μr rms at the interface plane.

Collimation

The delivered transmitter beam is nominally collimated. The deviation from perfect collimation will be accommodated within the overall beam transmitter beam quality budget. It is understood that the basic divergence evident in Figure 3.3-2 will be corrected at the surface of the beam director mirror downstream of the laser output.

Root-Mean-Square Phase Deviation

The root-mean-square phase deviation from the nominal wavefront shall not exceed 30 degrees. Beam Quality shall not exceed 1.1x the diffraction limit and the Strehl Ratio shall not be less than 0.82.

Wavelength

The Pulsed Oscillator laser operates on the IIR(20) transition of the $^{12}C^{18}O_2$ isotopic form of carbon dioxide.

Beam Frequency

The oscillation frequency of the transmit laser pulse is controlled by injection of a sample of the output of the quasi-CW reference laser after it has been upshifted by 40 MHz using an acousto-optic modulator. This establishes the IF of the coherent lidar to be 40 MHz. The frequency of the pulsed oscillator output after coherent detection using the (unshifted) reference laser beam as a local oscillator will differ from the nominal IF frequency because of chirp, mode formation effects and vibration. A sample of the detector coherent output (RF signal) is provided to the receiver as specified in the Command, Control and Telemetry interface requirements.

Laser Tolerance to Retro-reflected Light

Stray reflections from components downstream of the pulsed oscillator resonator can lead to spurious mode build-up effects. Effective reflectance of components downstream of the injection laser shall not exceed 0.01% to eliminate this possibility. This effectively prohibits on-axis partial reflections from transmissive components. Note that feedback into the injection oscillator from the transmitter will be reduced substantially by an acousto-optic modulator/isolator.

Polarization

The beam is linearly polarized (E vector normal to the plane of the resonator).

Local Oscillator Beam

Interface Plane

The reference oscillator beam characteristics are defined at the exit plane of the final beam directing mirror on the laser optical truss, the eight o'clock position on the triangular optical bench. The subsequent transfer optics are part of the Optical Subsystem.

Size and Shape

The delivered reference oscillator beam is Gaussian in intensity profile and 3 mm in diameter.

Wavelength and Frequency

The Local Oscillator laser operates on the IIR(20) line of the $^{12}C^{18}O_2$ isotopic form of carbon dioxide. The Local Oscillator operates at line center as determined by a hill-climbing servo-loop.

Power

Nominal Local Oscillator power at the interface is 50 mW and is operated in a quasi-CW mode (enabled for a period of 10 ms) at the pulse repetition frequency to minimize power drain.

Beam Jitter

Beam Jitter shall not exceed 10-μr rms at the interface plane.

Polarization

The Local Oscillator beam is linearly polarized (E vector normal to the the plane of the resonator)

Command, Control and Telemetry Interfaces

The command and control interface between the Laser Subsystem and the LAWS System computer consists of:

1) A logical link across a MIL-1773 fiber optic data bus. Information is transferred across this interface to perform the following functions:

Laser Firing Synchronization

A fire-when-ready request is made to the Laser Subsystem computer by the System computer for synchronization of laser shots. This initiates a laser firing command by the Laser Subsystem computer to coincide with the next laser servo dither cycle zero crossing.

Charging Cycle Synchronization

A PFN charging cycle initiation command is issued by the System computer accompanied by a charging rate command consistent with the selected pulse repetition rate, solar array output capability and battery charge status.

Health and Status

Outputs of sensors are interpreted by the Laser Subsystem computer and a GO/NO-GO signal is transferred to the System computer to indicate whether laser subsystem performance is

within the operating envelope. Sensor outputs are also made available to the System computer for transmission to ground if desired.

Laser System Reconfiguration

Periodic requests to reconfigure the laser are made to the Laser Subsystem computer by the System computer. Examples of such requests include firing of pyrotechnic charges, e.g , launch restraints and electrode polarity reversal.

2) An RF link along a 50-ohm coax line.

Frequency Offset

The difference in frequency between the reference and transmit lasers is sensed by a photodetector and the resulting RF beat is provided to the System Doppler processor for normalization of the wind-velocity estimate.

3.3.2. Functional Description

The Laser Subsystem consists of all the components required for the generation and frequency control of two CO_2 laser beams, the transmitter and reference beams, respectively. The transmitter (pulsed oscillator) laser generates a continuous train of single-frequency pulses (15-J energy, 3-μs duration) at an average PRF of 5 Hz (20-Hz peak), which is delivered to the Optical Subsystem for transmission to Earth. The pulsed oscillator excitation mechanism is a self-sustained corona preionized discharge. The frequency of the transmitter laser is controlled by injecting it with a sample of a 5-W highly-stable CW laser beam. Another sample is delivered to the Receiver Subsystem to function as the local-oscillator beam. The laser subsystem receives input power from the sensor power distribution panel and delivers waste heat to the sensor thermal radiator. It receives control information from the sensor computer.

Block Diagram of the LAWS Laser Subsystem

A block diagram of the Laser Subsystem is shown in Figure 3.3-4. The subsystem consists of three major modules, the transmitter gain, optical and the control and diagnostics modules, respectively. The transmitter gain module is attached to the instrument platform using vibrational isolation mounts to protect the instrument from vibrational perturbations generated within the module. The optical module consists of all the optical components and their supporting structures, the optical benches, which are in turn supported by the truss and hard mounted to the instrument platform. The connections to the optical benches are shown throughout the diagram. The controls

and diagnostics module accomplishes sequencing of laser operation, the control of optical components, and also conducts system health checks. The following is a discussion of the numbered elements of the Laser Subsystem as displayed in Figure 3.3-4.

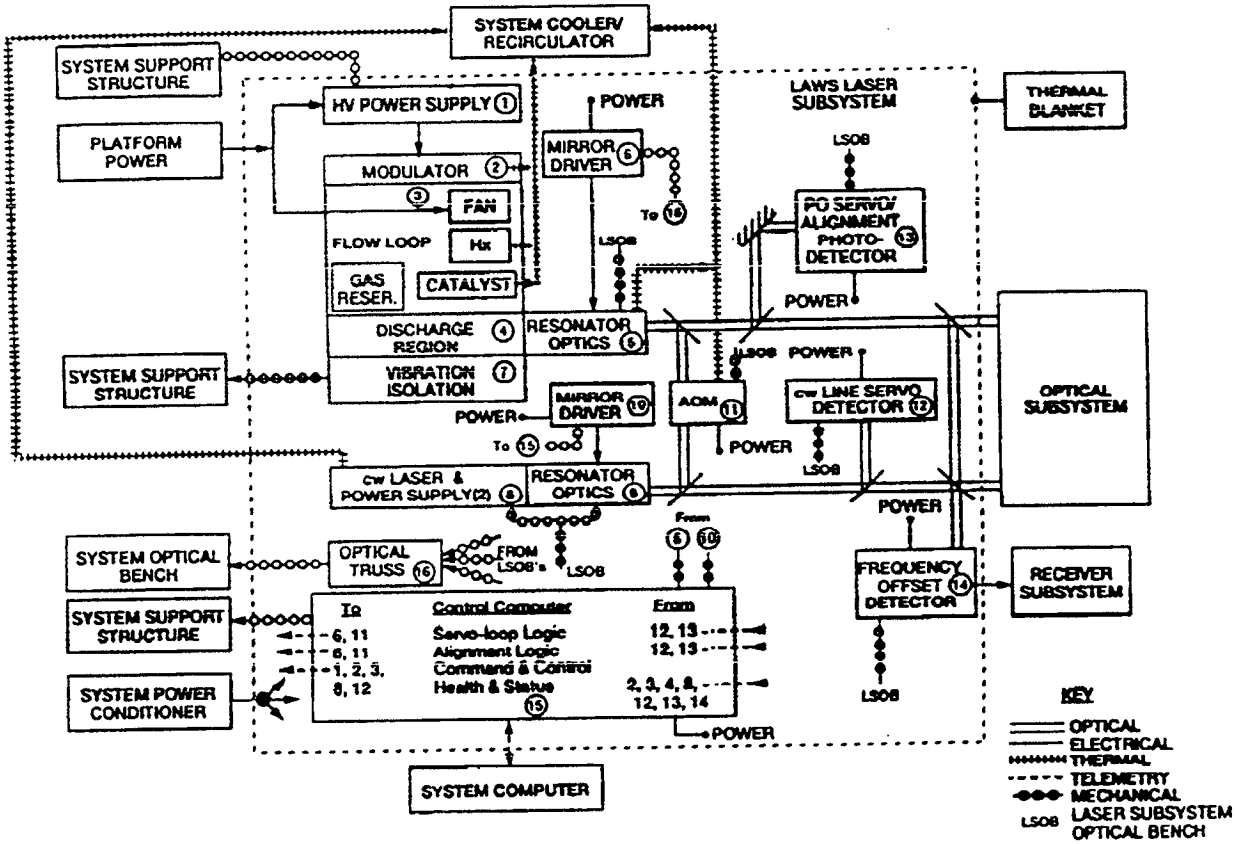

Figure 3.3-4 Laser Subsystem Block Diagram

Optical Schematic of the LAWS Laser

The optical schematic of the LAWS laser is shown in Figure 3.3-5. Radiation from a low-power CW RF-pumped laser is line center-locked and its output provided to the receiver as the local oscillator beam and also injected into the transmitter laser through the zeroth order of a Littrow grating. The CW beam that exits the transmitter cavity via this path is used to tune the transmitter laser cavity to the injection frequency via an active control circuit, while the pulsed output is processed to provide a correction for the offset between the transmitted and injection frequencies. The latter correction is provided to the system signal processor. The Bragg cell acousto-optic modulator in the transmitter injection path is included to provide isolation of the injection/local oscillator laser from downstream reflections. Accommodation is made for a

redundant CW laser. The cavity incorporates a graded reflectivity feedback/output coupler which was chosen because of its superior mode properties, in particular, its mode separation margin and excellent far-field pattern properties. A lens in the cavity is used as an alternative for a concave grating to minimize astigmatism.

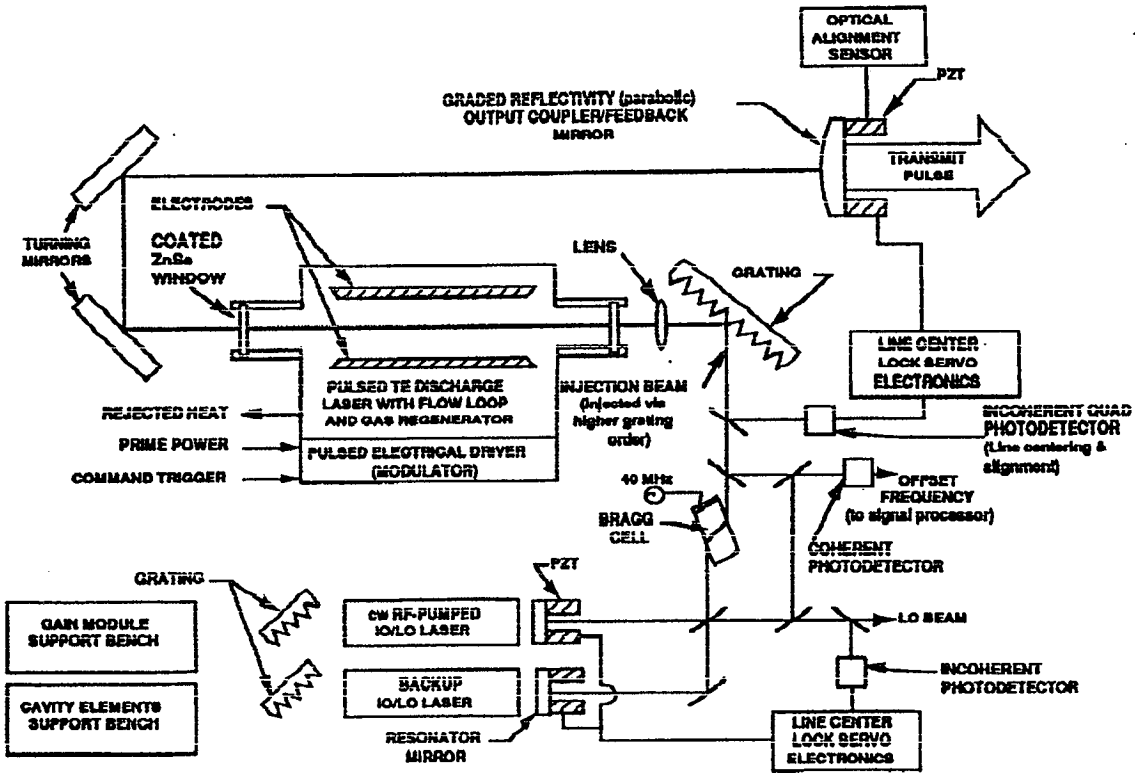

Figure 3.3-5 Optical Schematic of Laser Subsystem

HV (High Voltage) Power Supply (1)

The HV power supply is mounted to the system bench and remote from the gain and optical modules, and is powered by the 120-V DC on-board supply. It is a switchable bipolar supply that generates ± 30-kV supply lines for the two PFNs that constitute the modulator, which drives the laser discharge. The charging cycle occupies a significant fraction (variable) of the interpulse period. The charging rate is continuously variable and is determined by a charging rate command passed to the laser subsystem along with the power supply enable signal. The charging rate can be programmed to vary with the laser prf or optimised to accomodate available platform peak and average power capabilities as determined by the solar panel power and battery charge status.

Modulator (2)

The baseline modulator design consists of two 'type-E' pulse-forming networks (PFN's) connected in series through the laser head in a bi-polar arrangement. Ten-section, matched-

impedance PFN's will provide 60 kV to sustain the required flat-topped discharge pulse, while minimizing undesirable reflections, and optimizing the energy transfer efficiency. The bipolar scheme reduces the electrical stress from the high-voltage electrodes to ground by a factor of more than two, hence, significantly decreasing the probability for electrical flash-over, and it creates substantially improved electric field patterns between the electrodes, thereby producing a highly-uniform discharge. Modulator components are cooled by a fluid coolant circulated by the system laser fluid loop.

Flow Loop (3)

The flow loop performs the function of laser gas conditioning. The laser gas is circulated around the laser flow loop such that successive laser pulses are derived from newly-conditioned volumes of gas. The motive force for this circulation is provided by the fan that derives its power from the 120-V DC on-board supply. During its trip around the flow loop, a given volume of gas encounters the catalyst bed that reverses the CO formation due to the discharge, the heat exchanger (HX), which extracts the heat added by the discharge and also implements general pacification of the gas flow. The acoustic dampers incorporated in the flow loop attenuates acoustic and shock waves generated by the discharge. The net result of flow loop action is to maintain the density uniformity in the discharge region at the time of pulse firing to within 0.1%. The system laser fluid loop circulates fluid through the heat exchanger.

Discharge Region (4)

The discharge region is a 5-cm x 5-cm channel down the length of the laser (75 cm) from which laser energy is extracted during the period of the laser discharge. It consists of two electrodes across which a high voltage is developed. The anode is perforated (screened) such that the ultra-violet light, generated by a corona discharge behind the electrode, can penetrate the electrode and pre-ionize the gas in the discharge region prior to firing the main discharge. For corona bar redundancy, both electrodes are perforated, with the ability to reverse polarities of the pulse power pulses fed to the electrodes.

Resonator Optics (Pulsed Power Oscillator) (5)

The resonator optics provide the feedback required for laser action, and control of the output mode. The main elements are the two cavity extremity optic elements, the graded reflectivity mirror used for feedback purposes, and the diffraction grating that serves as the back mirror (or primary mirror). The diffraction grating also serves to couple the injection beam from the CW laser into the laser cavity. Also included in the resonator optics are the gain module windows (attached

to the gain module), and the intracavity lens used for focus control (compensation for window heating and lack of grating curvature). All the resonator optics, other than the gain module windows, are attached to the Laser Subsystem optical bench. The resonator optics are cooled using fluid obtained from the system laser fluid loop.

Mirror Driver (Pulsed Power Oscillator) (6)

The two cavity extremity optic element mounts incorporate piezotransducer actuators, of the low-voltage type, that are controlled by a mirror driver, which is a programmable voltage source. The control signals for the mirror driver are derived from the Control Computer and are derived from servo-loop logic and alignment algorithms. The mirror driver is physically located within the Control Computer box [see (15)] and obtains its input power from the 120-V on-board supply.

Vibration Isolation and Launch Clamps (7)

Vibration isolation mounts attach the gain module to the system support structure. During on-orbit operations, the vibration isolators are designed to minimize coupling of vibrations caused by the laser firing into the system structure. Launch clamps are installed for launch to limit launch loads and gain module displacements.

CW Laser + Power Supply (8)

Output from the CW laser is subdivided into two beams, one of which is delivered to the Optical Subsystem to act as the local oscillator beam and the other is used internally within the Laser Subsystem for injection into the power oscillator cavity to control its oscillation frequency and mode formation. The laser is pumped by radio frequency energy, whose source is powered by the 120-V DC on-board power. To conserve power, the RF energy is applied to the laser in a quasi-CW mode, for periods sufficiently long to envelope the time for servo-loop locking and signal reception, typically a few milliseconds. The CW laser and its power supply are an integrated unit that is supported by the Laser Subsystem optical bench. The CW laser gain cell and power supply are cooled by fluid from the system laser fluid loop. Dual CW lasers and power supplies are included for redundancy.

Resonator Optics (CW Laser) (9)

The resonator optics for the CW laser consist of the two laser extremity elements, a diffraction grating and an output coupler, respectively. They are supported by the Laser Subsystem optical bench.

Mirror Driver (CW Laser) (10)

The output coupler optic element mount incorporates piezotransducer actuators, of the low-voltage type, that are controlled by a mirror driver that is a programmable voltage source. The control signals for the mirror driver are derived from the Control Computer and are derived from servo-loop logic and alignment algorithms. The mirror driver is physically located within the Control Computer box [see (15)] and obtains its input power from the 120-V on-board supply.

Acousto-Optic Modulator (11)

Prior to being injected into the power oscillator transmitter laser, the beam from the CW laser is upshifted in frequency (by 40 MHz) using an acousto-optic modulator. The radiation, retroreflected by downstream components, is further upshifted by the same amount, and out of the gain bandwidth of the CW laser. This effectively isolates the CW laser from the power oscillator transmitter laser during the servo locking and injection process. The RF input to the acousto-optic modulator is switched off after the pulse is generated and remains off until the servo-locking process for the next pulse is initiated. This effectively eliminates a path for the pulsed output to enter the injection circuit, and also reduces prime power drain. The acousto-optic crystal is cooled by fluid tapped from the laser fluid loop, and the modulator is attached to the Laser Subsystem Optical Bench. The RF power supply is integrated into the control electronics module.

CW Line Servo-Detector (12)

This quadrant pyroelectric photodetector samples the output of the cw laser, and its output provides the feedback voltage for the line centering and alignment servo's. The photosensitive element is not cooled. It derives its power from the Platform power and is physically attached to the Laser Subsystem optical bench.

Power Oscillator Servo/Alignment Photodetector (13)

This quadrant pyroelectric photodetector samples the CW output of the power oscillator laser and its output provides the feedback voltage for the line centering and alignment servos. The photosensitive element is not cooled. It derives its power from the Platform power and is physically attached to the Laser Subsystem optical bench.

Frequency Offset Detector (14)

This pyroelectric photodetector samples the photomixed CW output of the CW laser and the pulsed output of the transmitter such that the frequency difference is measured for each pulse and provided to the Receiver Subsystem in the form of an RF signal having this frequency. The

photosensitive element is not cooled. It derives its power from the Platform power and is physically attached to the Laser Subsystem optical bench.

Control Computer (15)

The control computer accomplishes sequencing of laser operation, the control of optical components and also conducts system health checks. All communications with the system computer is routed through it.

Servo loop feedback signals are obtained from the CW line-servo detector (12) and the Power Oscillator Servo/Alignment detector (13), and cavity length control signals delivered to the mirror drivers (6) and (10).

On command from the System computer, control signals are delivered to the high-voltage power supply (1) to set the charging rate and initiate the charging cycle to the modulator, (2) to initiate the discharge cycle, to the flow loop, (3) for fan-speed control and electrode polarity reversal, to the cw laser (8) to activate the RF power supply at the appropriate times, and the acousto-optic modulator (11) to activate the RF power supply at the appropriate times.
Health and status signals are monitored and transferred to the System Computer. They include the following:

- Temperature, coolant flow and high-voltage breakdown indicators within the modulator (2).
- Heat exchanger and catalyst temperature indicators within the flow loop (3)
- Flow loop flow sensor (3)
- Discharge region gas arcing indicators (photodiodes) at both ends of the gain module (4).
- CW laser power indicator (8)

Optical Truss (16)

The Optical Truss provides an athermal support for the Laser Subsystem optical benches. It is hard mounted to the system Optical bench.

3.3.3. Performance Characteristics

Pertinent LAWS laser subsystem parameters are summarized in Table 3.3-1.

Table 3.3-1 Summary of LAWS Laser Subsystem Parameters.

PARAMETER	VALUE
Performance:	
Pulse Energy	15 J (Useful), 20-J Total
Pulse Repetition Rate	10-Hz Average (asynch), 20-Hz Max.
Pulse Duration	3 μs within FWHM
Wavelength	9.11 μm
Temporal Coherence (Chirp,Transform Limit)	200 kHz within FWHM
Spatial Coherence at Laser Exit	Beam Quality < 1.1, Strehl Ratio > 0.85
Beam Jitter at Laser Exit	< 25 μr
Frequency Jitter	< 1 MHz
Far-field Conversion	>80%
Accommodations:	
Weight	221 kg
Efficiency (wall plug) at 10-Hz PRF	>6%
Lifetime	$>10^9$ shots
Gain Module:	
Discharge (Gain Region) Length	75 cm
Discharge Cross Section	5 x 5 cm
Cavity Pressure	0.5 atm
Discharge Loading	200 J/(liter-atm)
Pump Pulse Duration	3 μs
Gas Mix ($He/N_2/CO_2$)	3/2/1
Resonator:	
Beam Diameter	5 cm
Resonator Length	3.1 m
Resonator Magnification	1.25

The baseline LAWS pulse temporal profile calculated using available STI simulation codes, and the above parameters as input are shown in Figure 3.3-6. Also shown is the integrated energy profile with time. The 15-J useful pulse energy contribution is defined to be that emitted beginning soon after the trailing edge of the gain-switched spike up to the time corresponding to the decay to half amplitude of the following pulse. The total energy within the pulse is 20 J, of which the 1.5-J

contribution due to the gain-switched spike is considered to be excessively transform-limit broadened (and thus not useful for Doppler measurement), and the approximate 3.5 J contained in the trailing edge is discounted because of excessive chirp. This interpretation is subject to an update pending consideration of Performance Breadboard chirp and pulse bandwidth experimental data. Chirp and pulse bandwidth predictions for the baseline laser parameters are displayed in Figure 3.3-7.

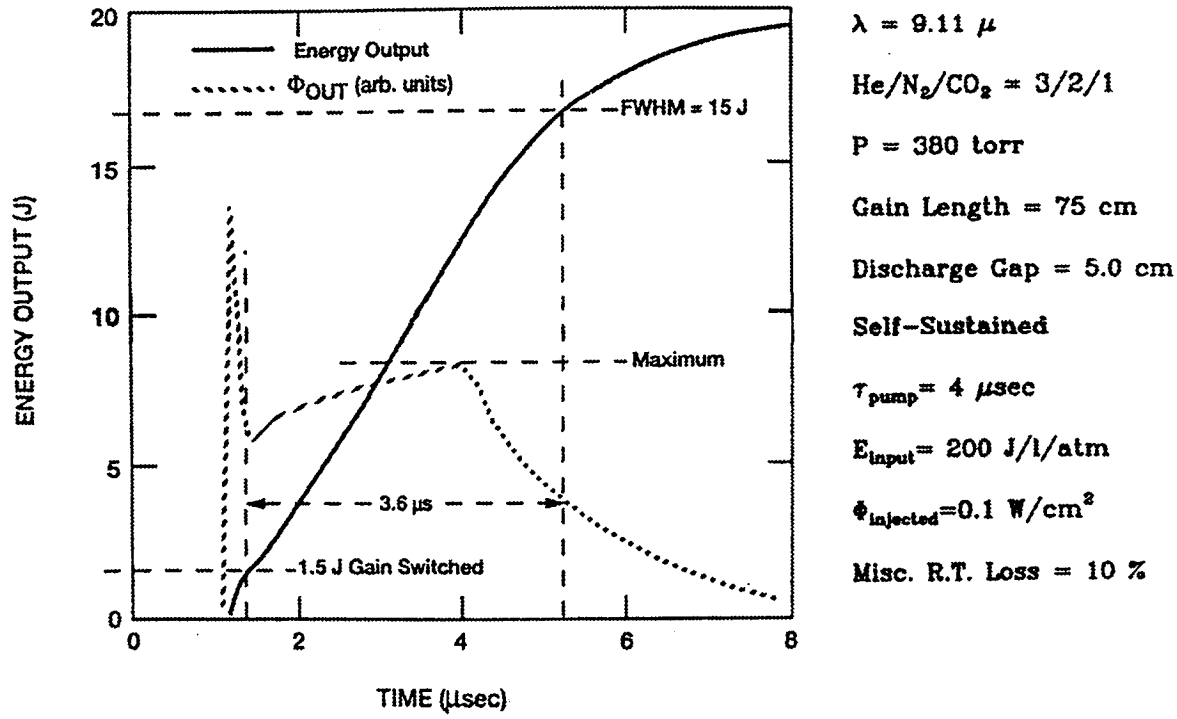

Figure 3.3-6. Baseline LAWS Pulse Temporal Profile

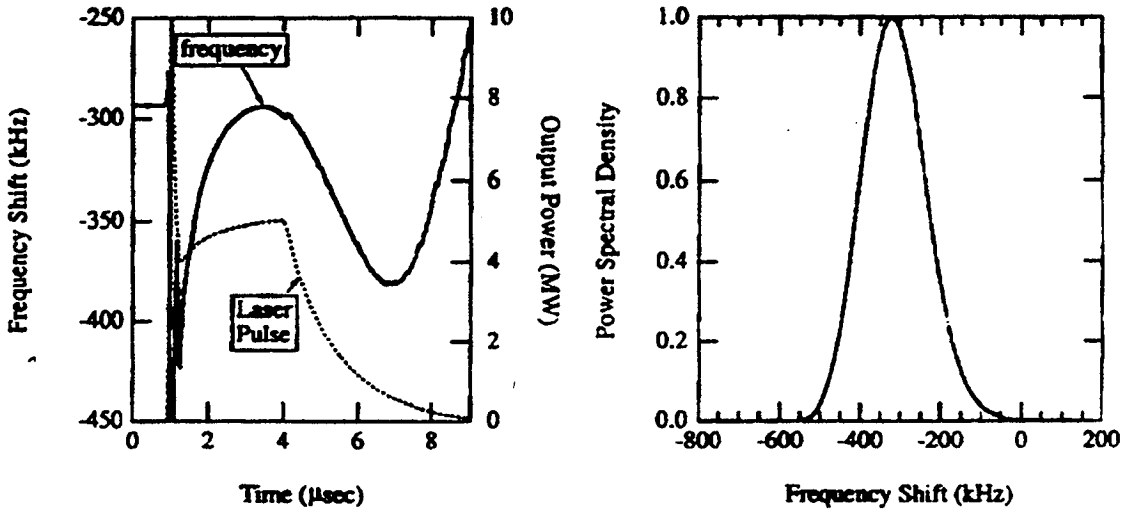

Figure 3.3-7. Preliminary Estimates of Gasdynamic Chirp in LAWS Laser

Shown in Figure 3.3-8 are the modeled laser output radial intensity and phase profiles. In Figure 3.3-9 are shown the modeled radial intensity and encircled energy distributions after propagation into the far field, showing that in excess of 80% of the transmitted energy is propagated within the central diffraction lobe.

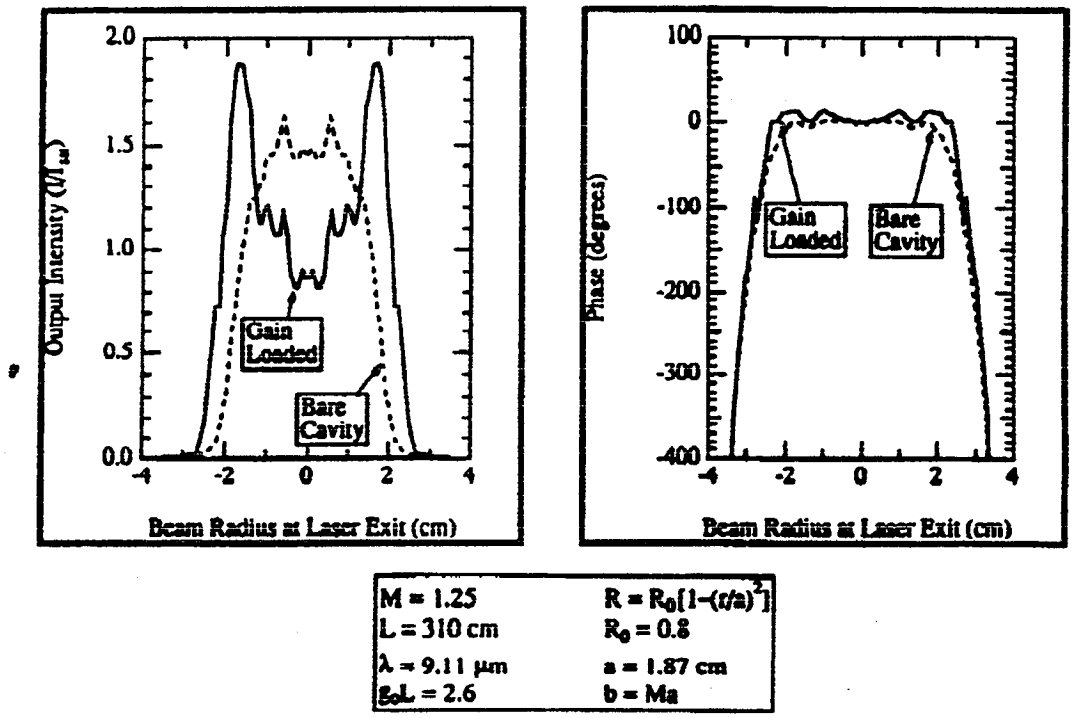

Figure 3.3-8. Intensity and Phase Profiles at LAWS Laser Exit

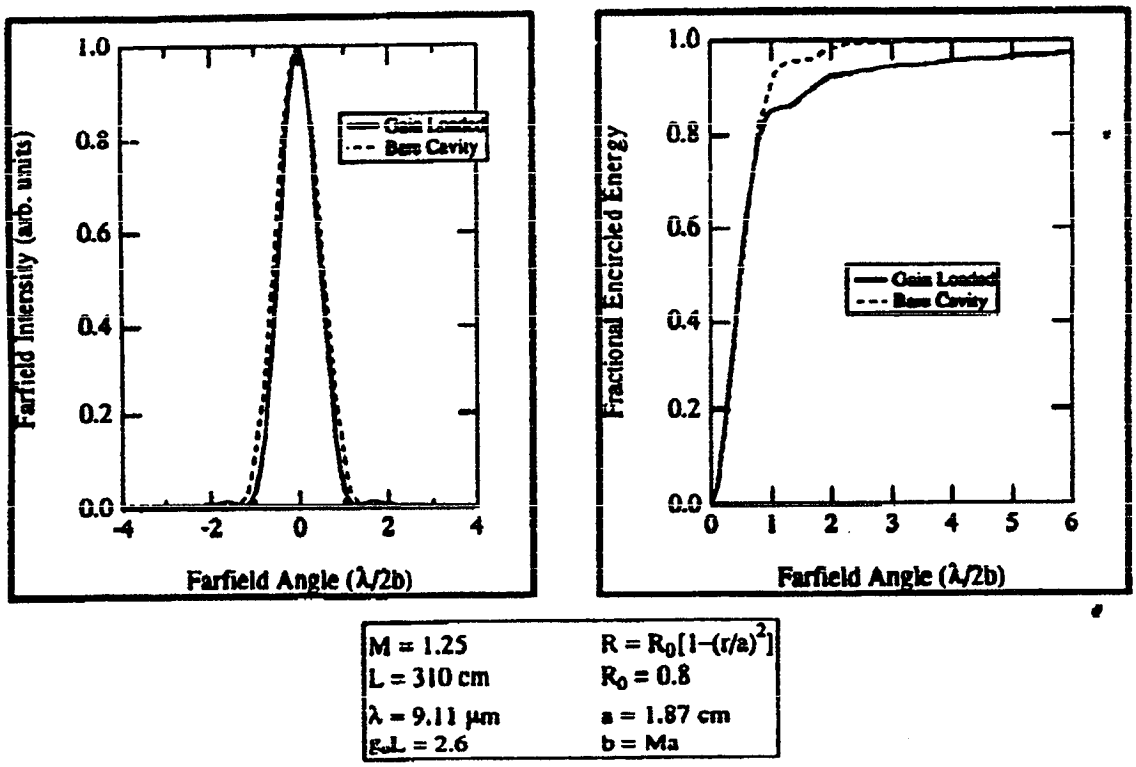

Figure 3.3-9. Far-Field Intensity and Encircled Energy Porfiles at LAWS Laser Exit

3.3.4. Analyses and Trades

3.3.4.1 Stress Analysis

Stress analysis of the major LAWS Laser Subsystem components has been performed to: guide the design and weight trade-off studies, to assure component integrity under typical launch and operational loads, and to evaluate component ability to maintain optical alignment during operation. The structure that was analyzed is shown in Figure 3.3-10. The figure shows the triangular cross-section of the truss structure draped over the cylindrical gain module. The gain module is attached to the system bench via vibration isolators with 2.5-Hz resonant frequency to decouple gain module vibrations from the balance of the system. The isolators are clamped during launch. The optical truss is hard-mounted to the system bench.

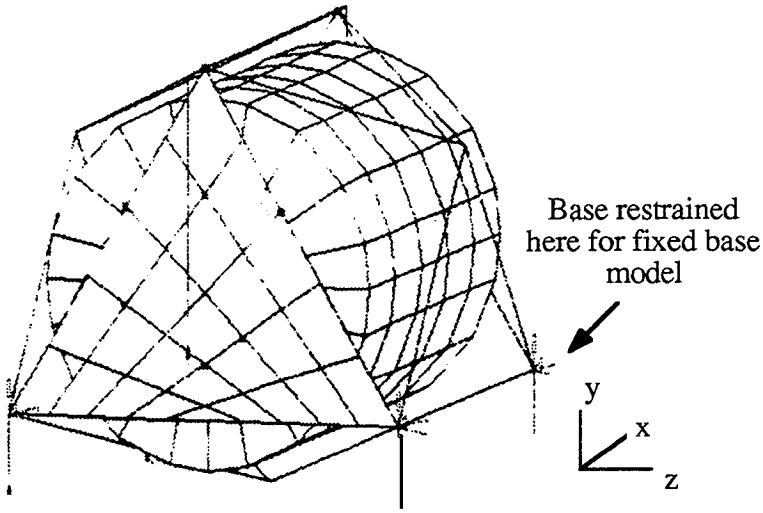

Figure 3.3-10 LAWS Laser Subsystem Structural Model

The gain module is simulated by a point mass with 3 component vibration inputs assigned to the gain module side of the decoupling isolator (during laser operation). This is considered adequate for this phase of the program, since minor deflections and displacements of the gain module are not critical for Laser Subsystem operation. Detailed stress analysis within the gain module has thus been limited to local load calculations on various components, e.g., the cylindrical shell, bulkheads, vanes, pulse power tubes, flow liners, and heat exchanger to determine adequate material thicknesses.

Due to the stringent deflection and displacement limits on the resonator optical components, a more complex model has been adopted for the optical truss. The tubes are constructed of graphite epoxy. The end plates, which support the optical components, have graphite/epoxy face and edge plates with an aluminum honeycomb core. The materials are chosen for their desirable properties of stiffness- and strength-to-weight ratios, damping, fatigue, and thermal characteristics as well as for their service in similar applications. Materials properties are based on: *Advanced Thermoset Properties*, Leslie, J.C., Van Nostrand Press, New York, 1986. Materials properties for both tubing and sandwich face plates are listed in Table 3.3-2. For preliminary purposes, all elements are given the same properties, and the laminates are assumed to be isotropic. The graphite/epoxy composite is based on ultra-high modulus graphite fiber.

Table 3.3-2 Materials Properties Used in LAWS Analysis

Elastic Modulus	17×10^6 psi
Shear Modulus	7×10^5 psi
Density	0.066 lbs/in^3
Tensile and Compressive Strength	35 ksi (ultimate)

The weight of the truss parts total 32 lbs, which when combined with the weight of components mounted on the end plates of 24 lbs, gives a total weight of 56 lbs. Shock isolator weights are an additional 4 lbs.

The main longitudinal tubes are 3.25-in O.D. with a wall thickness of 0.05 in. The optics tube, coaxial with the longitudinal tube is 2.65-in O.D., and has a wall thickness of 0.05 in, leaving a clear inner bore of 2.55 in (or 6.48 cm), less dimensional tolerances and dynamic and thermal distortion. Truss members are tubes of 1.25-in O.D., with walls of thickness 0.05 in. The sandwich end plates are reinforced by stiffeners along the edges that distribute load at the corners where the truss members join the plate. These edge stiffeners are given weight and structural properties equal to x1.25 of the truss tubular elements.

The structural elements were adjusted to achieve a conservative design in regard to stresses and especially deflections during operation. At the upper bound loads, rotation of the optical components was found to be excessive, and the structure was modified to uncouple the structural member carrying the optical elements from the load bearing structural elements which maintain the overall shape of the assembly. This reduced rotation of the optical elements from 5.5×10^{-3} deg. to 3×10^{-5} deg., relative to the end plates.

The finite element model includes the tubular grid structure, the stiffened plates and the upper optics concentric tubes. Lumped masses on both plates and on the extended optics tube represent the optic components. Preliminary analyses conducted consisted of static and dynamic response calculations using the model. The dynamic results are discussed in Section 3.3.4.2. The static analysis computed stress and deflection under a 1-G loading, and can be considered linear over the loading range of interest as presented in the GIIS.

Simulated end plate stresses are shown in Figure 3.3-11 for the 1-G static acceleration load. The stresses peak at 80 psi. Similar stress data for other axes, and for random analyses show similar stresses. Stresses in tubular members are below 200 psi for both random and static loads.

Von Mises Stress Maximum = 80 psi

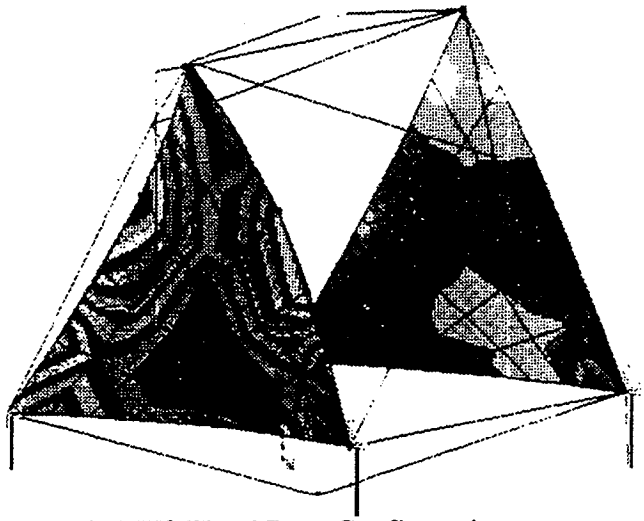

LAWS Fixed Base Configuration

Figure 3.3-11 End Plate Stresses for 1-G Static Load

The LAWS truss mass properties were calculated and the results are shown in Table 3.3-3.

Table 3.3-3 LAWS Truss Mass Properties Mass Moment Information

Weight	56.00 Ibs					
Mass	0.15 Ibs/(in/sec2)					
Mass Moment of Inertia W.R.T. C.G.	IX	29.42	IY	77.27	IZ	80.80
Mass Product of Inertia W.R.T. C.G.	PXY	7.54	PXZ	-0.46	PYZ	-0.41
Radii of Gyration W.R.T. C.G.	RX	14.24	RY	23.08	RZ	23.60
Center of Gravity	CGx	17.36	CGy	15.51	CGz	0.18
Principal Mass Moment of Inertia	P1	80.85	P2	78.39	P3	28.26
Principal Radii of Gyration	R1	23.61	R2	23.25	R3	13.96
Principal Axes (Direction Cosines in	N11	0.01	N12	0.01	N13	-0.09
Rows W.R.T. C.G.)	N21	0.15	N22	-9.79	N23	0.13
	N31	-9.88	N32	-0.15	N33	0.01

Reference is made to the coordinate system of the FEM model, with x, y, and z as shown on the model diagrams. Origin of the x-y-z system is on the centerline of the model and on the lower edge

of the nearer triangular end plate, shown in Figure 3.3-10. The axes shown on the figure indicated direction only and not the location of the origin.

3.3.4.2 Dynamic Analysis

As stated previously, the gain module is simulated by a point mass with 3 component vibration inputs assigned to the gain module side of the decoupling isolator (tuned to a frequency of 2.5 Hz) during laser operation. Initial vibrational estimates utilized were a uniform psd of 0.03 g^2/Hz in the x and y directions over a 4- to 4.5-Hz pass band and bounded by -12 dB/octave skirts, and an order of magnitude less (0.003 g^2/Hz) in the z direction. This scenario was assumed for initial system wide interaction evaluations. These values will be updated by vibration data taken on the Breadboard device as this data becomes available. They are conservative when compared with available data on the CO_2 Laser Testbed (CO_2LT) currently being used for life testing.
Dynamic analysis was performed for optical truss natural frequencies, and for response to random vibration at a level of 0.15 g^2/Hz from 0 to 400 Hz for an overall input of 8-G rms consistent with GIIS Delta launch loads. The natural frequencies calculated for the LAWS optical truss are listed in Table 3.3-4.

Table 3.3-4 Natural Frequencies for LAWS Truss

Frequency Number	Frequency (cycles/sec)
1	104.59
2	163.38
3	177.71
4	188.83
5	252.42
6	265 59
7	309.49
8	333.76
9	348.26
10	385.11

3.3.4.3 Chirp Analysis

Numerical simulation methods to accommodate the calculation of the frequency characteristics of the laser pulse have been developed at STI over a period of years using company funding. The current code provides a relatively complete description of CO_2 laser unstable resonator output. More specifically, it generates simulations for:

- Time-dependent evolution of the optical power and energy within the pulse
- Radial phase and amplitude profiles

- Sensitivity to intracavity phase distortions and optical component misalignments (beam quality)
- Discrimination against higher-order transverse modes
- Time-dependent output frequency (chirp)

This particular code couples the full-time-dependent laser kinetics, mode development (optics), and the gas fluid dynamics used for high fidelity analyses of advanced point designs. The code is based on Siegman's exact cavity equations of motion, which expands the cavity field in terms of the bare-cavity multi-transverse modes. Multi-sheet optical path differences can be included to simulate misaligned optics, aberrations, etc. It supports a time-dependent saturable gain model and is coupled to a fluid dynamics solver to predict mode-medium instabilities e.g. chirp.
An example of code output is shown in Figures 3.3-12. This shows the pulse temporal optical power and chirp profiles and the pulse output power spectrum. The calculated gas heating profile is shown in the left-most plot of Figure 3.3-13. The thermal expansion of the gas occurs where the gradients (actually the Laplacian) of the heating term is the largest. Since the heat distribution is nearly flat at the origin, $\Delta\rho/\rho$ is nearly zero at the origin and becomes significant only at the edge of the discharge. However at the edge of the discharge, the intensity of the extraction beam is small. Therefore the change in density at the outer edge of the discharge results in only a small change in the laser frequency. The right-most plots display the radial $\Delta\rho/\rho$ plots at two times into the pulse, and the degradation at the later times should be noted.

Our chirp modeling for TE CO_2 lasers with unstable resonators showed that the "classical" chirp models are poor approximations for large aperture unstable resonators. The heating distribution depends on the transverse-mode structure of the resonator that in our designs are strongly non-Gaussian. This is opposed to the "classical" models that assume Gaussian heating distributions.

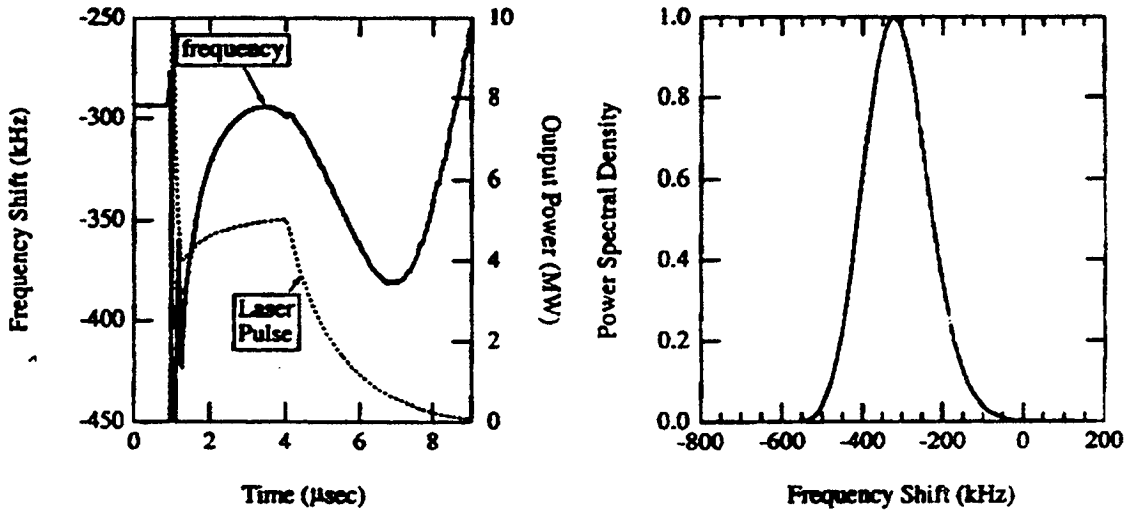

Figure 3.3-12 Laser Pulse Temporal Profile and Pulse Power Spectrum

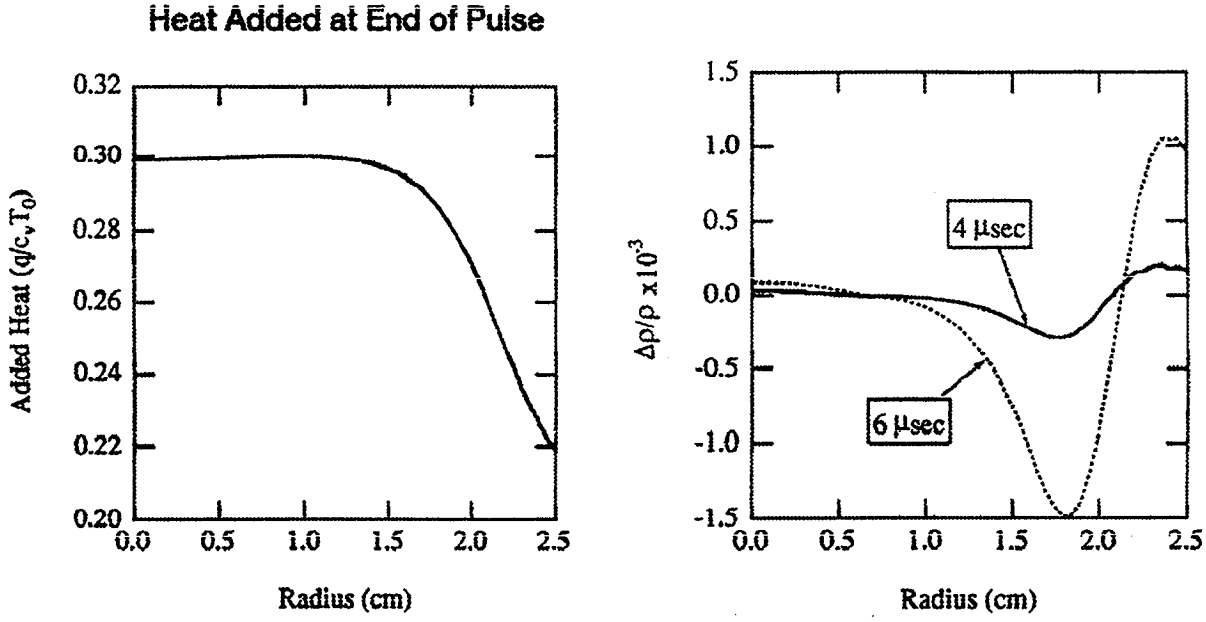

Figure 3.3-13 Low Predicted Chirp is Due to Unique Heating Profile

3.3.4.4 Resonator Analyses

Resonator analyses are conducted to establish the intensity and phase profiles of the output laser beam and its far-field propagation properties. Inputs to these analyses are the optical powers of the resonator optical elements and the gain region and resonator geometries. The initial step in analysis of a resonator is to invert the Fresnel-Kirchoff integral equation for the bare cavity to yield all the transverse oscillation modes (and in particular, their mode oscillation margins), and to

establish the modal basis set. Resonator designs for which the fundamental mode oscillation margin is substantial are analyzed further. The fundamental mode profiles calculated in this way are always in good agreement with the fundamental mode profiles calculated using the more conventional Fourier propagation approach. The Fourier approach is then used for gain-loaded resonator calculations. Examples of gain loaded and bare cavity modes (intensity and phase profiles) calculated for a typical LAWS resonator are shown in Figure 3.3-14 and in Figure 3.3-15 are shown the profiles after propagation to the far-field. The goal is to optimize the profile at the laser exit to maximize laser output while simultaneously maximizing the conversion of energy into the central lobe of the far-field.

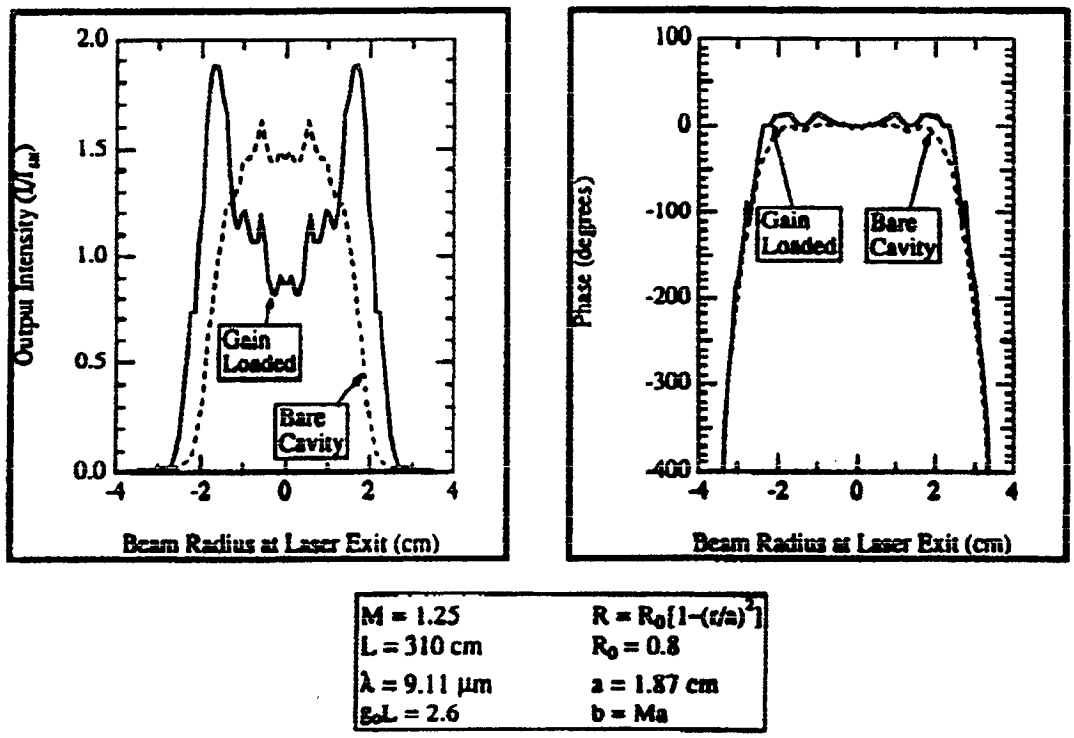

Figure 3.3-14 Intensity and Phase Profiles at Laser Exit of Gain Loaded vs Bare Cavity Mode

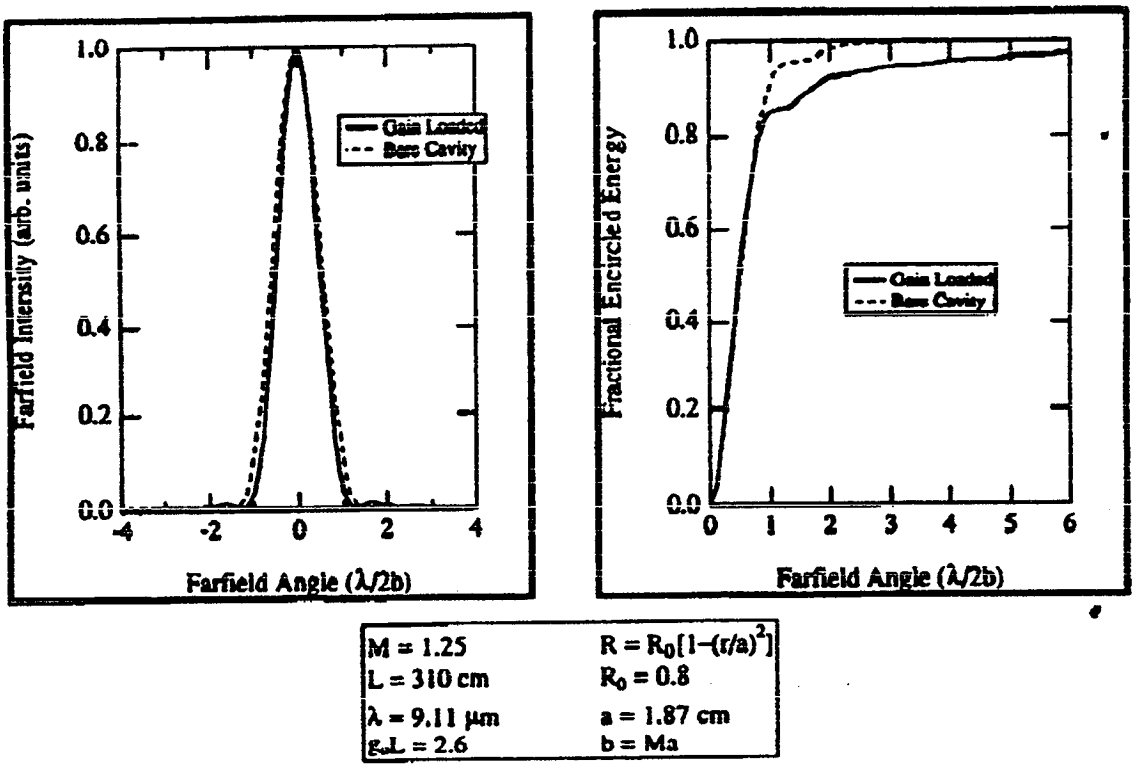

Figure 3.3-15 Far-Field Intensity and Encircled Energy Profiles at Laser Exit of Gain Loaded vs Bare Cavity Mode

The effects of mirror tilts are also examined to establish a specification for mirror vibration limits and for beam jitter control. In Figures 3.3-16 and 3.3-17 are shown 3-dimensional profiles of the modes for a perfectly-aligned resonator and one for which the output mirror has been tilted by 5 μr. Mode discrimination as a function of mirror tilt angle is plotted in Figure 3.3-18 and is used as an aid in establishing maximum allowable resonator mirror deflections. The optical effects of thermal heating are also analyzed to evaluate the effect on resonator performance of the heating of the gain module windows due to bulk absorption and coating losses. The optical power (focal properties) of the windows are a function of the temperature, since the refractive index of the ZnSe material is temperature dependent. Figure 3.3-19 shows transverse profiles, from ˇ to right, of the heat deposition rate, window temperature and the consequent optical path difference distortion introduced for typical LAWS parameters. This enables an assessment to be made of the optical compensation that the laser has to accommodate during start-up.

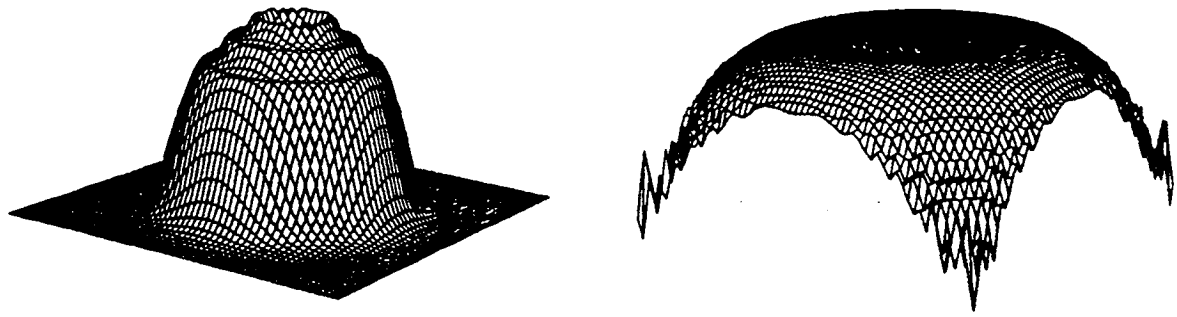

Figure 3.3-16 Intensity and Phase Profiles at Laser Exit of Perfectly-Aligned Resonator

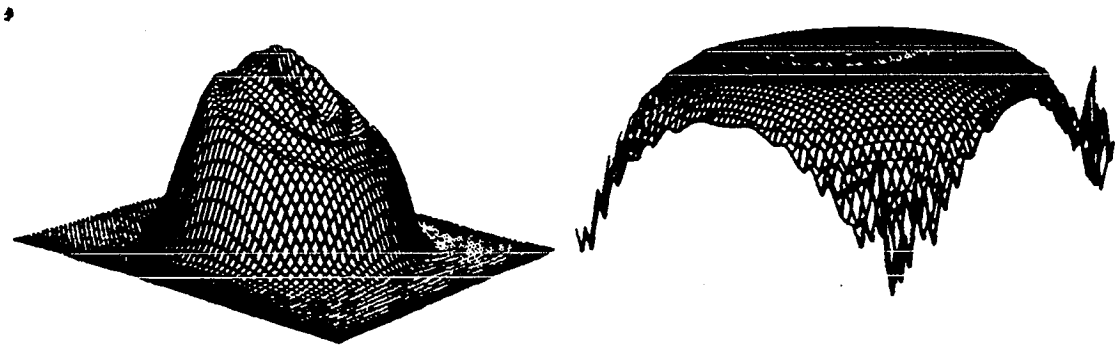

Figure 3.3-17 Intensity and Phase Profiles at Laser Exit of Resonator with 5-μr Output Mirror Tilt

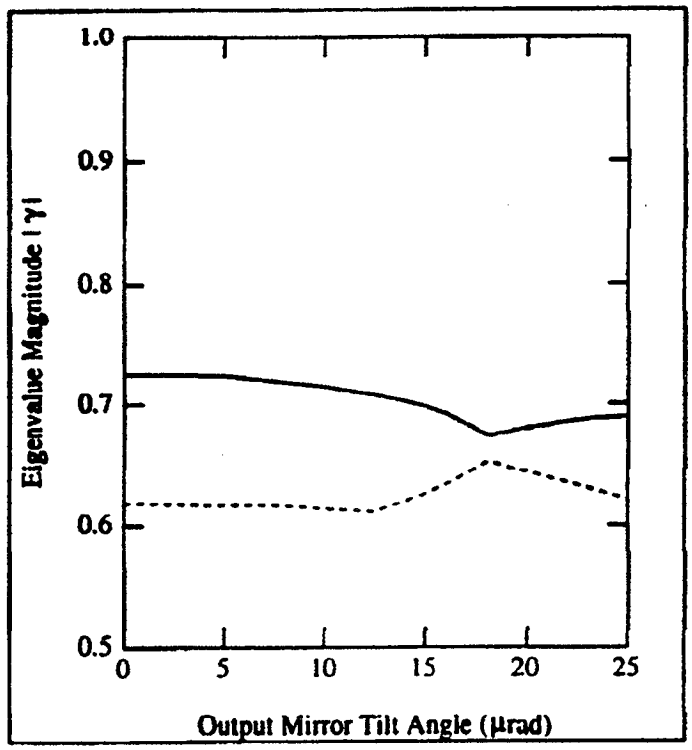

Figure 3.3-18 Mode Discrimination as a Function of Mirror Tilt

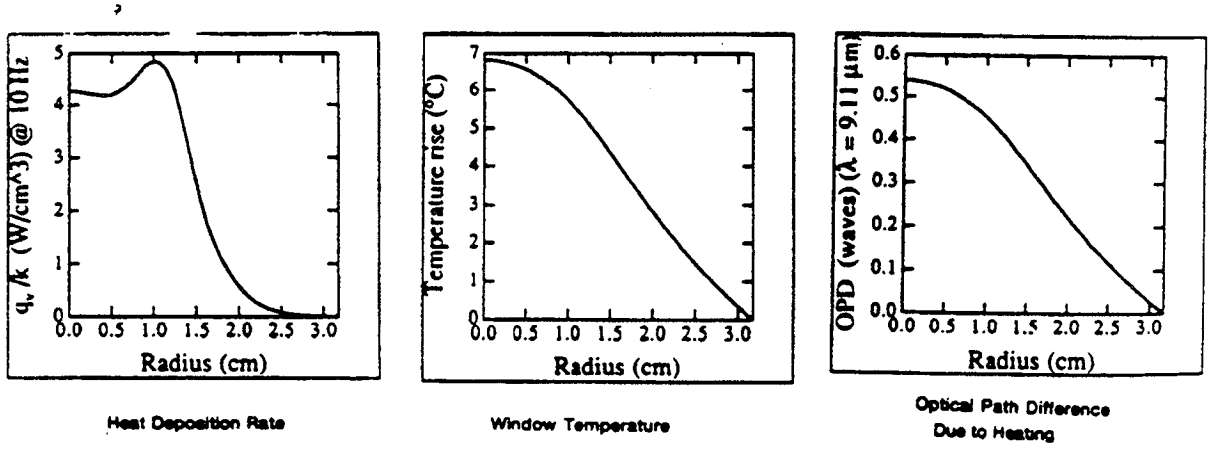

Figure 3.3-19 Thermal Lensing Calculation for the LAWS Laser Gain Module Windows

3.3.4.5 Pulse-Power Trades and Analysis

For pulse-power parameter trades, the Pulse Forming Network (PFN) is modeled as an equivalent PFN circuit. Figure 3.3-20 is an example of such a circuit for a 10-section PFN, where C_1 - C_{10} and L_1 - L_{10} are the section inductances and capacitances, where L_1 also includes the switch and cable inductance, R is the total circuit resistance including the conductors, connections, capacitors and switches and C_0 is the corona bar capacitance. The discharge is modeled as detailed in the description of our Laser Kinetics code (Next section 3.3.4.6) to which the PFN code is coupled. Input parameters include the component values, charge voltage, active gas volume, gas mixture, and pressure. Outputs include the current and voltage waveforms, discharge resistance, di/dt's, energy depositions, laser output and pump energy. SPICE models have also been used to analyze fault modes and as an aid in initially specifying component values.

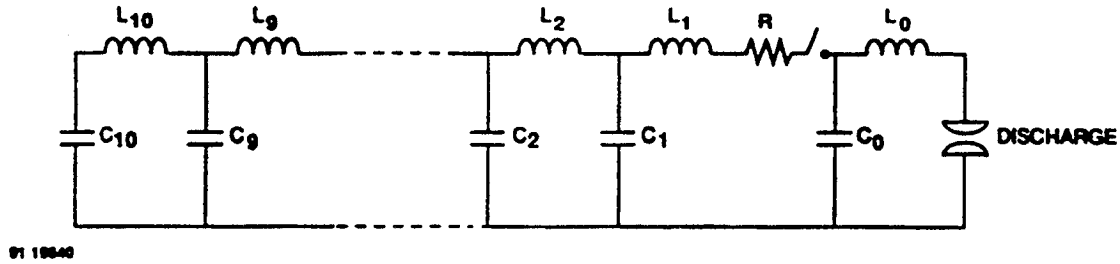

Figure 3.3-20 Modulator 10 Element Circuit Model

An example simulated PFN output is shown in Figure 3.3-21 and displays excellent pulse shape, impedance matching, and, hence, energy transfer efficiencies. Both the discharge and PFN impedances are approximately 10 ohms. The post-pulse voltage amplitude is low enough so that late time arcing is not likely to be a problem. The negative portion of the post pulse will be eliminated using an end-of-line clipper, which is not included in the model, and the positive excursions can be minimized by further optimization of the parameters of the first few PFN sections.

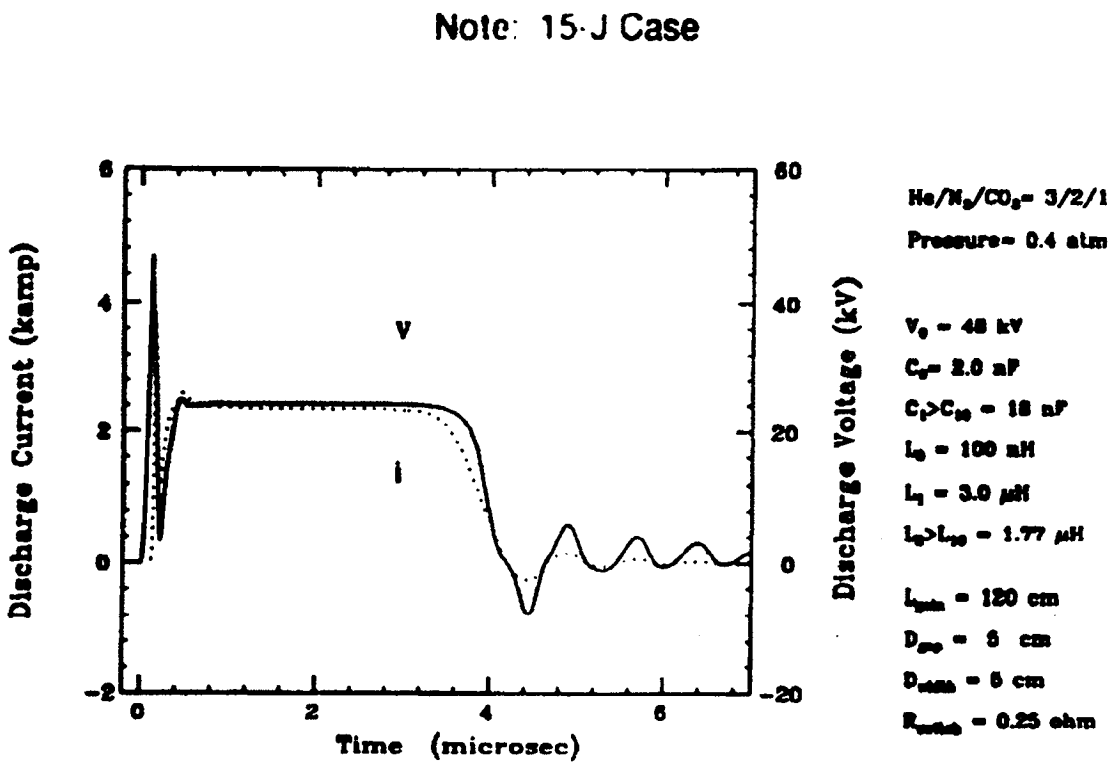

Figure 3.3-21 LAWS Pulse Power Current and Voltage Profiles

Figure 3.3-22 shows measured discharge current traces of the Performance Breadboard Pulse power system into a dummy load during shakedown testing. The upper pair are single shots of the bi-polar outputs and the lower pair a superposition of 25,000 shots at a 30-kV output voltage, the Performance Breadboard design value.

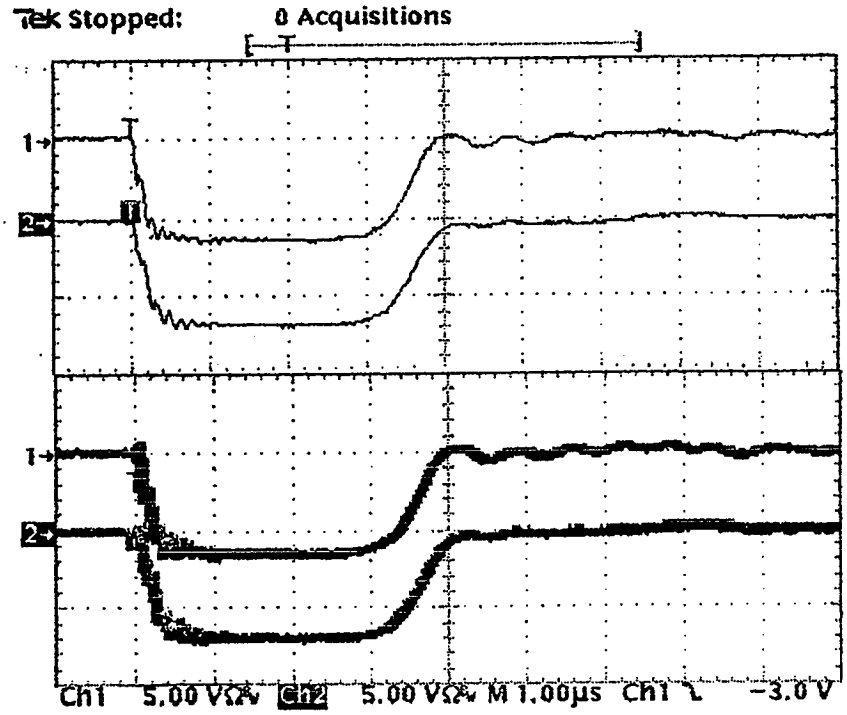

Figure 3.3-22 Performance Breadboard Pulse Power System Current Traces at 30-kV Output Voltage

3.3.4.6 Laser Kinetics/Pulse Energy Assessments

Pulse temporal profile and pulse energy assessments have been generated using STI's kinetics codes. Trade studies were conducted to investigate the effects of gas mixture, pump pulse energy and duration, cavity pressure, discharge loading, gain length and cross-section, injected power and isotope selection on the pulsed laser output.

STI's kinetics code is a two-part computer model. The first part solves the Boltzmann equation for the electron distribution function versus E/N and utilizes the electrical cross sections for He, N_2, and CO_2 as input. The electron excitation cross sections are then integrated over the electron energy distribution functions to give the distribution of pump energy among the excitation channels as a function of E/N. The excitation rates as a function of E/N are then placed in a look-up table to be used as input to the kinetics model. The kinetics model is a five-temperature model that uses input voltage and current pulses plus the excitation rates from the Boltzmann solver to calculate the five temperatures as a function of time. The five temperatures are the translational temperature, N_2 vibrational vibrational temperature, the CO_2 symmetric and asymmetric stretch-mode vibrational temperatures, and the CO_2 bending-mode temperature. The model assumes full

equilibration within each mode, and, also, that the translational and rotational temperatures are in equilibrium. The kinetics model includes the rates for intermode vibrational transfer and for vibration-translation relaxation-relaxation, so that the mode temperatures can be calculated as a function of time. The rate constants, used along with their corresponding temperature dependence, were obtained from the literature when available. For the rare isotopes of interest these were experimentally measured by STI during various experimental programs. The small-signal gain is then calculated as a function of time by evaluating the appropriate Boltzmann factors for the vibrational and rotational populations for the upper and lower levels and subtracting them to determine the population difference.

For use with the $^{12}C^{18}O_2$ isotope, the model was also updated to incorporate the smaller energy spacings for this isotope. The optical extraction portion of the CO_2 laser kinetics code is a one-dimensional model that assumes uniform extraction over the full cross-section of the beam and can model either an oscillator or an amplifier configuration. (Note that in the most general simulations we conduct, e.g., as used for the chirp calculations - Sec 3.3.4.3, the one-dimensional restriction is removed and the simulations become two-dimensional). The oscillator model treats the build-up from an initial intensity, which can be either background fluorescence or an injected signal. The model accommodates mirror separations that are longer than the active length, and losses that are lumped in with the mirror reflectivities. The optical model is fully coupled with the kinetics model so that the effect of the energy extraction is fed back into the kinetics model and is used to update the gain and mode temperatures.

Example of predictions generated by the code are shown in Figures 3.3-23 and 3.3-24. In the former, the temporal distribution of the pulse optical power profile and the integrated energy within the pulse are displayed for typical LAWS laser parameters to illustrate the dependence of output on gas mixtures. The latter figure shows similar plots for various pump-pulse durations. These codes have been used intensively during the selection process for the LAWS Baseline laser parameters.

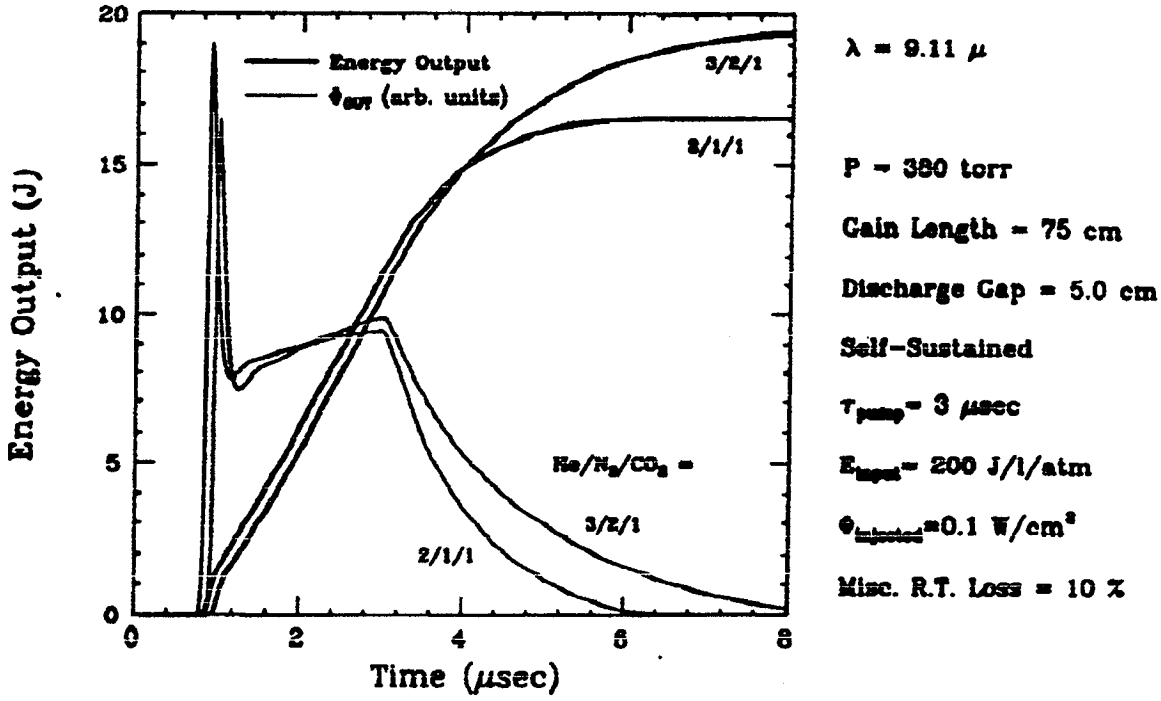

Figure 3.3-23 Kinetics Code O/P Showing Pulse Temporal Behavior for Various Gas Mixes

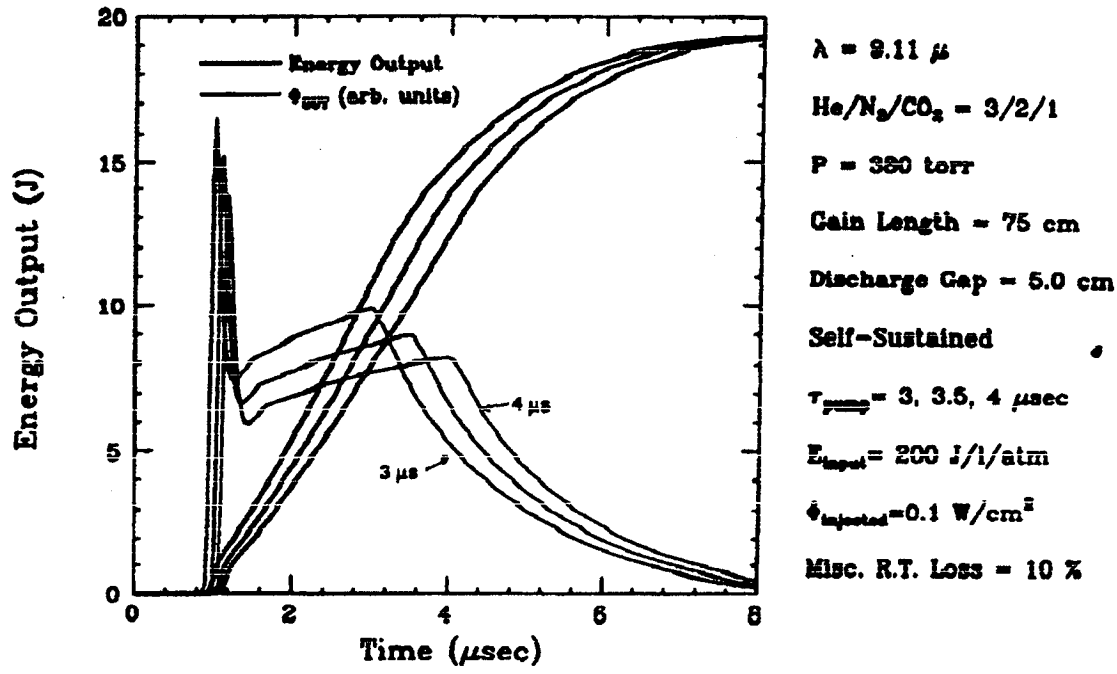

Figure 3.3-24 Code O/P Showing Pulse Temporal Behavior for Various Pump Pulse Durations

3.3.4.7 Flow Loop Trades and Analyses

An unwanted product of the discharge pumping process is local heating and pressurization of the gas in the laser cavity. The resulting pressure and temperature disturbances would, if allowed to persist, product large gas density variations and associated refractive index variations. These effects degrade the beam quality severely, and can even lead to discharge arcs. The flow loop is, therefore, designed to rapidly remove the discharge-induced gas density nonuniformities between successive laser pulses.

The propagation and attenuation of the acoustic waves in the flow loop are calculated using a computational model based on the flux-corrected transport (FCT) unsteady gasdynamic flow algorithm developed at the Naval Research Laboratories. This algorithm is able to accurately model both the high-amplitude phenomena at the beginning of the pressure relaxation and the small-amplitude residual disturbances following attenuation of the pressure pulses by the mufflers. The calculations indicate that the residual pressure-induced density fluctuations in the optical cavity are lower than the budgeted figure with the current muffler design. Figure 3.3-25 shows the pressure-induced relative density fluctuations (log to base 10) in the optical cavity as a function of time. Two consecutive pulses are shown. The initially high-density variations are attenuated by at least two orders of magnitude between pulses by the action of the acoustic attenuators.

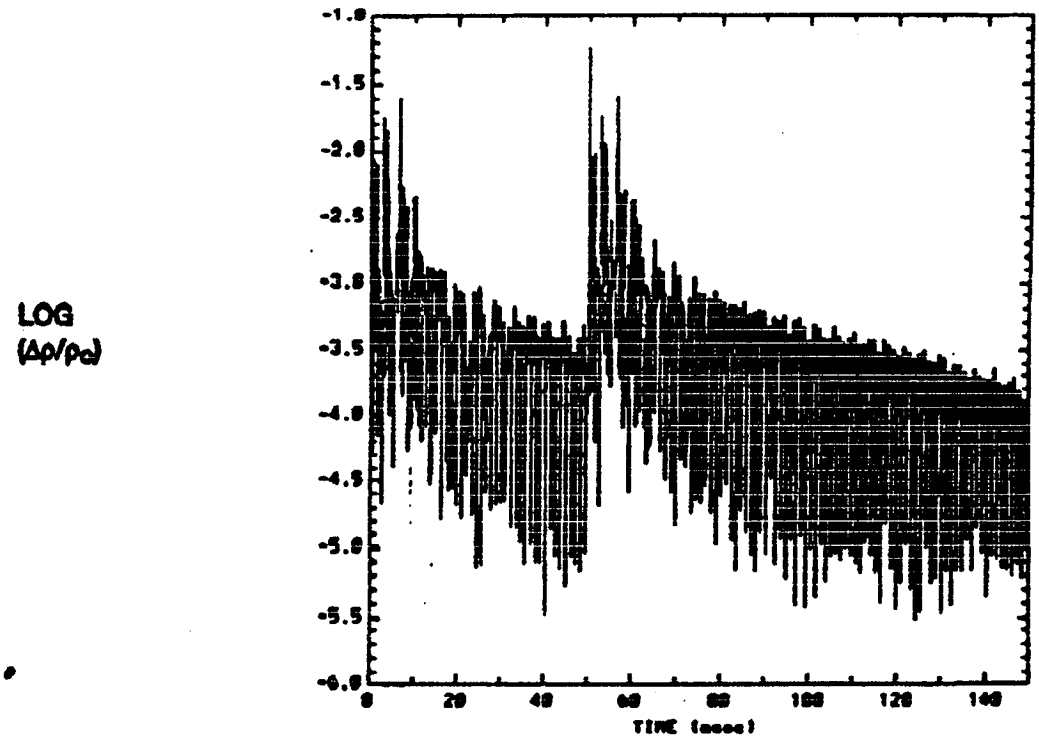

Figure 3.3-25 Damping of Pressure-Induced Density Variations Between Pulses

The heat exchanger is designed to remove the mean thermal energy of the gas and gas temperature oscillations about the mean temperature. Standard steady heat exchanger theory is used to calculate the mean temperature decay and unsteady theory to analyze the decay of the temperature oscillations.

Boundary layer theory, in particular the momentum-integral method, was used to calculate the rate of growth of boundary layers in the cavity region.

A catalyst bed was designed using the LASCAT code developed by Herz, et.al., under contract to NASA. The code models the performance of catalyst coated onto a rectangular monolith structure. The code includes the effect of heat and mass transfer in the gas, diffusion through the pores of the monolith structure and chemical reaction at the catalyst. The primary effect of the catalyst structure on the flow loop design is that its pressure drop represents approximately half of the pressure losses, which the cross-flow fan must be designed to overcome (the other half being due mostly to the heat exchanger).

3.3.4.8 Discharge Region Trades and Analyses

The electrostatic field surrounding the electrodes is calculated by solving the Poisson equation for the complex electrode geometry. This is accomplished using STI's TOPAZ code, which generates the equipotential lines surrounding the electrodes, as shown in Figure 3.3-26 for a typical electrode configuration. In this example, the average electric field potential around the discharge area is ≤6 kV/cm or sufficiently low to prevent the occurrence of spurious discharges and/or tracking. The area of greatest concern is the "triple point" or the region where the electrode, insulator and the gas meet. The simulation shows that there is no significant stress build up at this region as would be evident by congestion of equipotential lines. There is evidence of compression of the potential lines between the underside of the electrode and the ground assembly, but this is acceptable since the insulator has a much higher dielectric strength than the gas. The stress in the insulator is about 70 V/mil and the insulator is rated to 400 V/mil. Figure 3.3-27 is a plot of the maximum potentials along the electrode and the insulator from the centerline out to 15 cm. A small amount of enhancement, about 5%, is evident where the electrode curves away from the discharge but is within the acceptable range. The region around the "triple point" actually displays a depression of the electric field to between 50 and 80% of the nominal value.

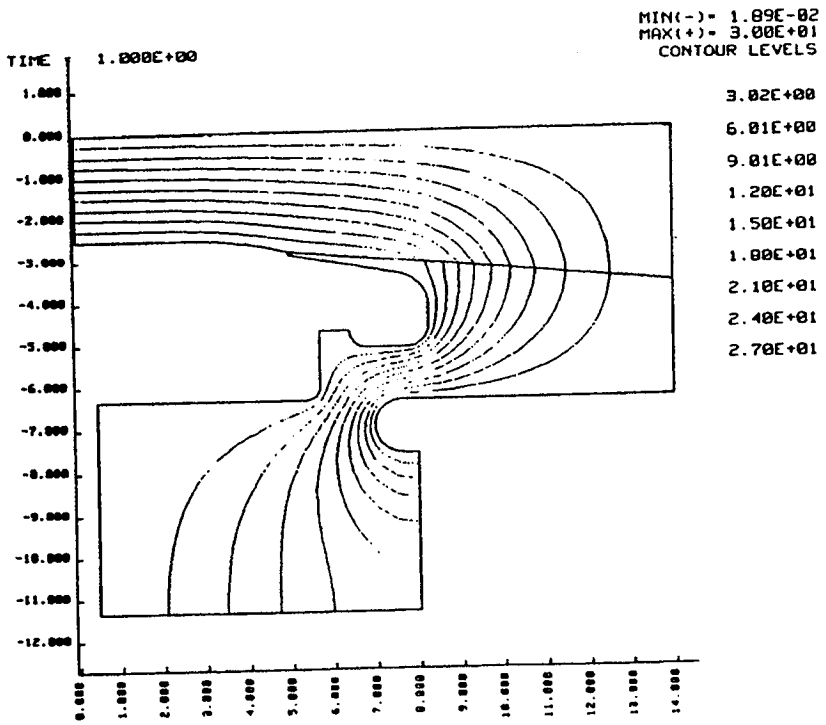

Figure 3.3-26 Discharge Region Potential Contours

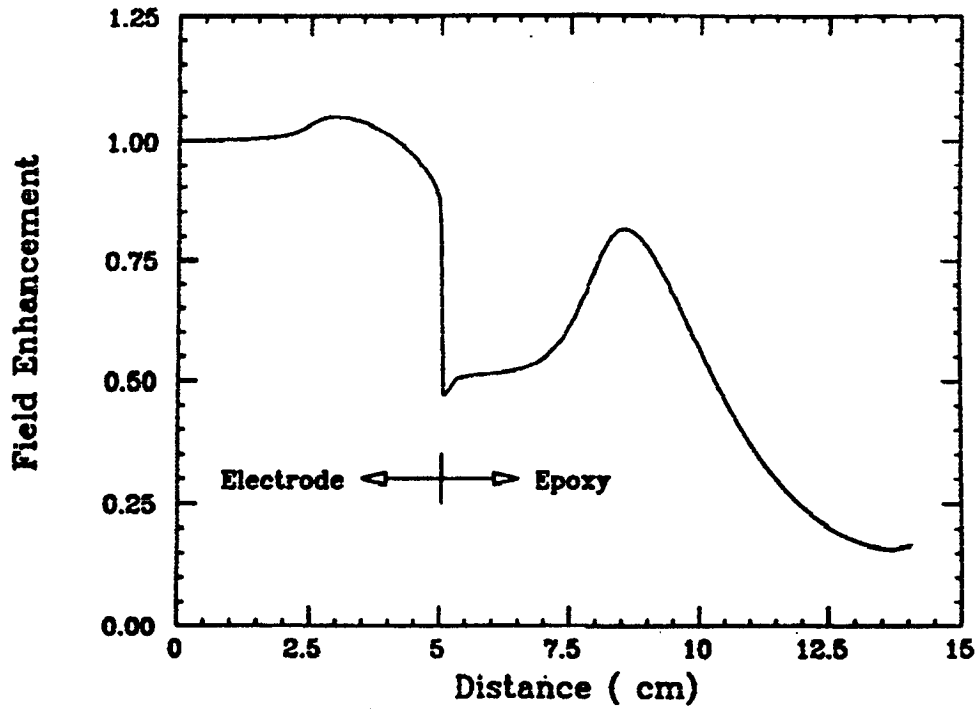

Figure 3.3-27 Electric Field Enhancement at Gas Surface Interface

3.3.5. *Preliminary Design*

The Laser Subsystem preliminary design is depicted in the isometric drawing of Figure 3.3-28 and in the side and end elevations of Figures 3.3-29 and 3.3-30. The Gain Module (cylindrical vessel) is attached to the system platform via supports that incorporate vibration isolators. The (triangular cross-section) optical truss, to which the Laser Subsystem optical benches are attached, is draped over the Gain Module.and is hard-mounted to the System platform. The control and diagnostics and high-voltage power supplies (for the Gain Module pulse forming network) are located on the platform cold plates. Umbilicals connect the gain module heat-exchanger, optics, CW laser and acousto-optic cooling loops to the laser fluid loop and also the components requiring electrical power to the system bus. A Gain Module cross-sectional drawing is shown in Figure 3.3-31.

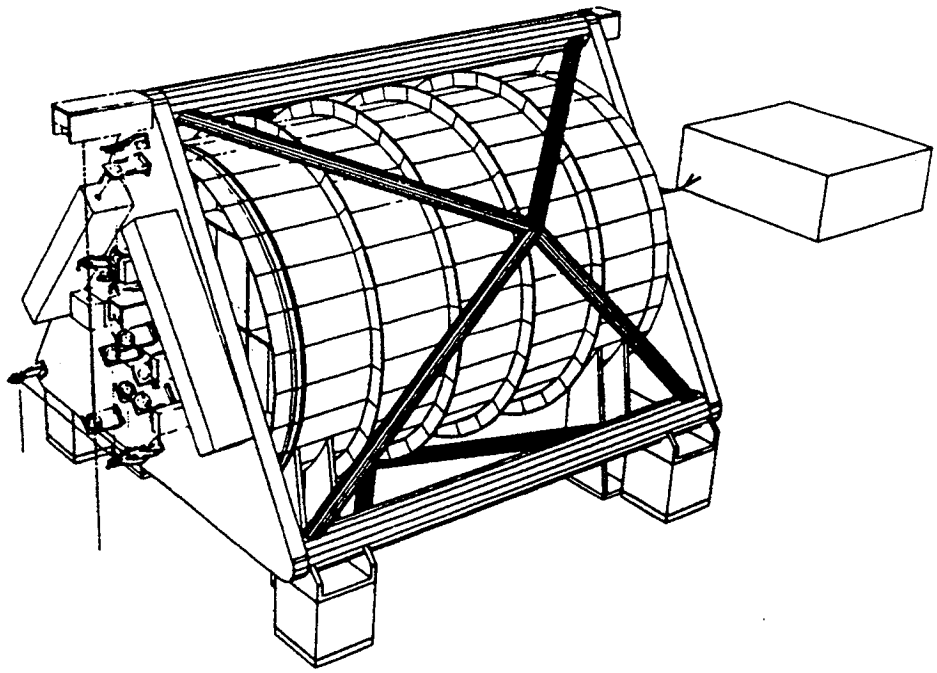

Figure 3.3-28 Laser Subsystem Isometric Drawing

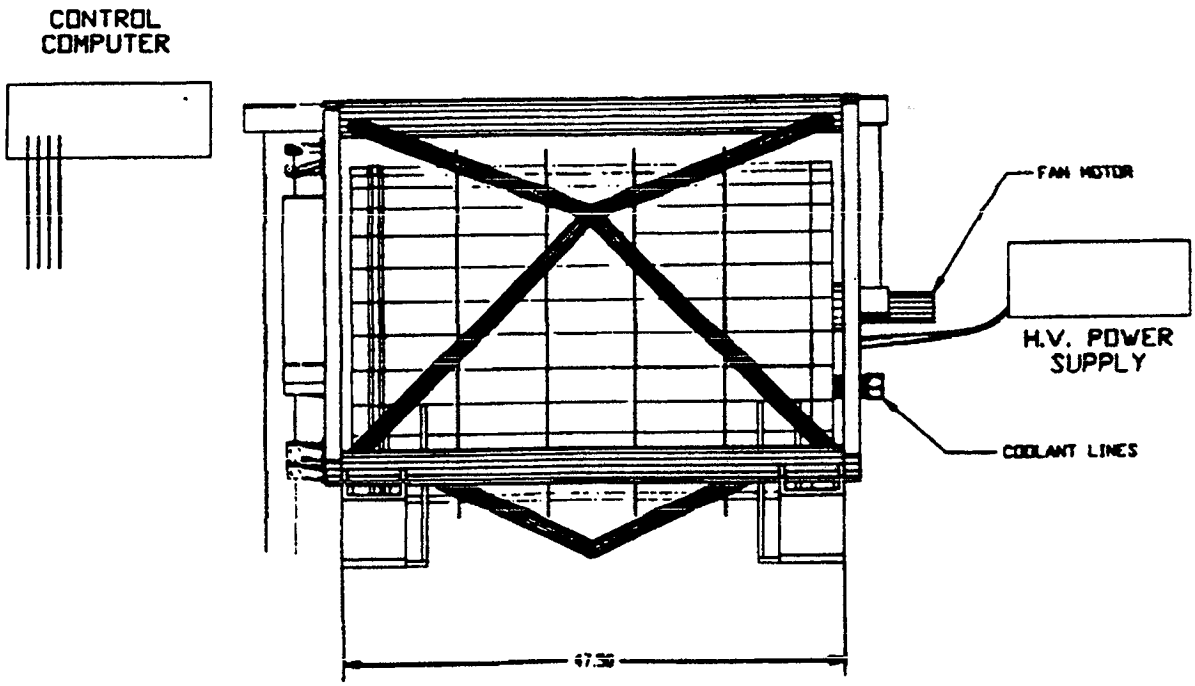

Figure 3.3-29 Laser Subsystem Envelope (Length)

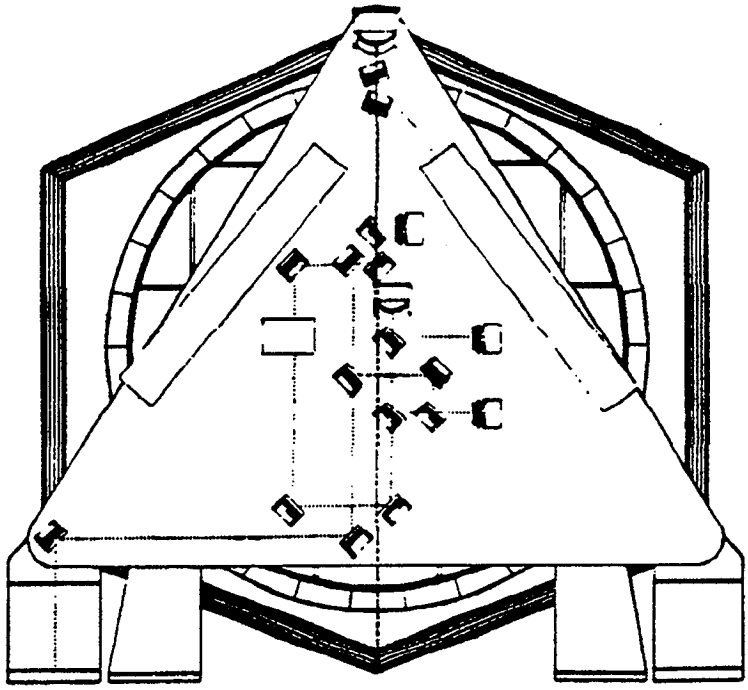

Figure 3.3-30 Laser Subsystem Envelope (Width and Height)

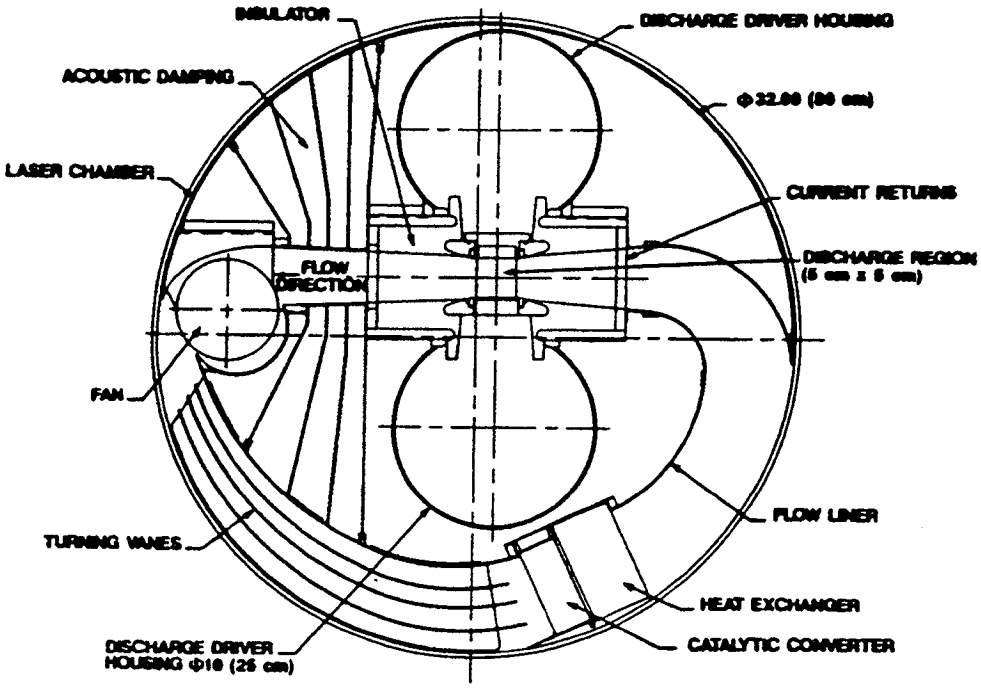

Figure3.3-31 Laser Gain Module Cross Section

Significant features of the Gain Module include the following:

- Bipolar electrodes for a more uniform electric field while in addition the lower voltage requirement reduces insulating and tracking problems.
- Corona preionization for flow compatibility.
- Long-life barium titanate corona bars behind each electrode with the ability to select the active corona bar to provide redundancy.
- Electrode embedded in insulator for less than 1x field enhancement at the triple-point.
- Use of a low risk fan/bearing design with allowance for a redundant fan motor.
- Reserved space in the flow loop for an integral catalytic converter.
- Passive window purge to prevent material build-up on ZnSe gain-module windows.
- Simple and proven heat exchanger design constructed from relatively-light thermally-conductive materials.
- PFN's are installed within the laser head behind each electrode and are isolated from the laser gas, which arrangement also provides effective EMI shielding.

Weight estimates for the Gain Module preliminary design are given in Table 3.3-5. Estimates were generated for both aluminum and graphite epoxy construction. For the majority of components the weight estimates are common. The greatest weight-savings resulting from the use of graphite epoxy applies to the shell construction, discharge driver housing and the internal structure. A laser subsystem-wide weight summary is given in Table 3.3-6.

Table 3.3-5 Gain Module "Bottom-up" Weight Estimates by Component

SUBASSEMBLY	ALUMINUM ASSEMBLY (kg)	CARBON COMPOSITE ASSEMBLY (kg)
Electrode/Insulator	29.5	29.5
Chamber/Internal Structure	45.2	27.0
Fan/Bearings/Motor/etc.	7.2	6.5
Catalytic Monolith/Assso.	10.1	10.1
Heat Exchanger	8.4	8.4
Corona Bars	5.3	5.3
Windows/Holders	0.9	0.9
Shocks Mounts/Asso.	3.6	3.6
RFI and Acoustic Materials	1.0	3.1
	111.2	94.4

Pulsed Power System Design

The baseline modulator (pulsed-power) design consists of two 'type-E' pulse forming networks (PFN's) connected in series through the laser head in a bipolar arrangement. Ten-section, matched-impedance PFN's will provide 60 kV to initiate, and 30 kV to sustain the required flat-topped discharge, while simultaneously minimizing undesirable reflections, and optimizing the energy transfer efficiency. The bipolar scheme reduces the electrical stress from the high voltage electrodes to ground by a factor of more than two, hence, significantly decreasing the probability for electric flashover; and it creates substantially improved electric field patterns between the electrodes, thereby producing a highly uniform gas discharge.

Polypropylene dielectric will yield the lightest weight and most efficient capacitors available today, with demonstrated lifetimes of greater than 1×10^9 shots. The output switch(es) will consist of a series stack of twelve, 3300 V, gate turn off (GTO) thyristor junctions, which will be packaged inside a single housing in order to economize both size and weight. Gate turn off is a misnomer for these devices since they will be optimized for high di/dt and low loss turn on

performance, and will, therefore, not have turn off capabilities. Switching efficiency and di/dt capabilities will be enhanced via the incorporation of a series saturable reactor, which permits the trigger and RC snubber generated plasmas to spread, thus creating a larger active area, prior to the conduction of the primary current pulse. The PFN inductors will consist of a single-layer, fifty-turn, helical solenoid, with capacitor taps every five turns.

Table 3.3-6 Laser Subsystem-wide "Bottom-up" Weight Estimates by Component

ITEM	WEIGHT (kg) (Gr/Ep Shell)	WEIGHT (kg) (Al Shell)
Transmitter Gain Module		
Pulsed Power	82.0	82.0
Shell/Flow Loop/Discharge Region	94.40	111.20
Thermal and Control Power Interfaces	10.0	10.0
Total Weight Transmitter Gain Module	186.40	203.20
Optical Module		
Truss	15.00	15.00
Injection.Local Oscillator Lasers	5.00	5.00
Miscellaneous Optics	5.00	5.00
Total Weight Optical Module	25.00	25.00
Control and Diagnostics Module		
Servo-Loop Electronics	5.00	5.00
Auxiliary Electronics	5.00	5.00
Total Weight Controls and Diagnostics Module	10.00	10.00
TOTAL WEIGHT LASER SUBSYSTEM	221.40	238.20
TOTAL WEIGHT LASER SUBSYSTEM + 10% CONTINGENCY	243.50	262.02

Modulator fault protection will be incorporated to prevent the occurrence of permanent damage due to laser head arcs, switch prefires, etc. End of line clipper circuits, consisting of diodes and PFN impedance matching resistors, will absorb any reflected energy (e.g., due to a laser head arc) thereby preventing damaging capacitor voltage reversals and minimizing reverse currents through the thyristor stack. The manufacturer will incorporate multiple avalanche diode junctions inside a common housing to economize on size and weight. Anti-parallel companion diodes will conduct potentially damaging reverse currents away from the thyristors, and will

simultaneously clamp thyristor reverse voltages well below damage thresholds. RC snubber networks will grade both DC and transient voltages uniformly across the thyristor junctions, and breakover diode (BOD) circuits will safely trigger the thyristor stack if the voltage across the stack exceeds established limits.

A redundant capacitor charging power supply will be provided, and risks are likely to reduced further if, as is expected, the single switch mode of operation is successful. In this operating mode, the laser gas acts as the switch for the negative modulator. Triggering occurs when the positive modulator is fired, resulting in the initiation of the corona bar preionization and voltage doubling across the laser head, thus breaking down the laser gas. If successful, our system design includes a completely redundant switch and trigger system. Also note that the 3300 volt thyristor junctions will be operated at 2500 volts, hence 25% of the switch junctions would have to fail before BOD initiated triggering would force the system to be operated at reduced voltages. And finally, the highly probable concept of capacitor fusing would allow the failure of 10-20% of the capacitors before the impact on the pulse shape or output energy would become significant.

The power supply charging rate will be variable, and can be set to accommodate the available platform power, thereby achieving optimum performance for platform average and peak power capabilities.

An end-view of the Pulse-power system is shown in Figure 3.3-32, and a side view in Figure 3.3-33. The package is not shown complete; missing are the companion diodes, snubbers, trigger system, protection circuitry, and the mechanical support structure. While these items are not shown, their sizes and locations are commensurate with the additional available space.

The weights and volumes shown in Table 3.3-7 are derived from the baseline modulator design. The estimates include a completely redundant charging power supply system, and a potentially redundant output switch and trigger system. Redundancy of the output switch depends on the success of the single switch mode of operation, which is currently estimated to have an 80% chance of success. In this operating mode, the laser gas acts as the switch for the negative modulator. Triggering occurs when the positive modulator is fired, resulting in the initiation of the corona bar preionization and voltage doubling across the laser head, thus breaking down the laser gas.

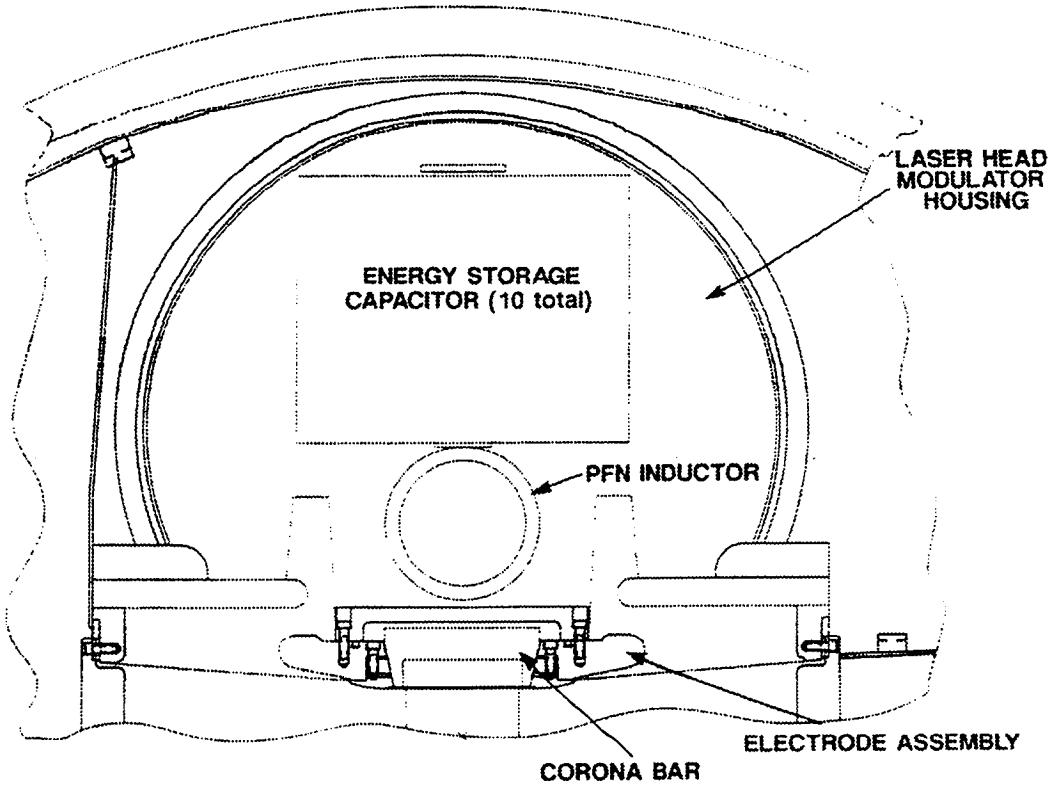

Figure 3.3-32 Pulse Power System Cross Sectional View

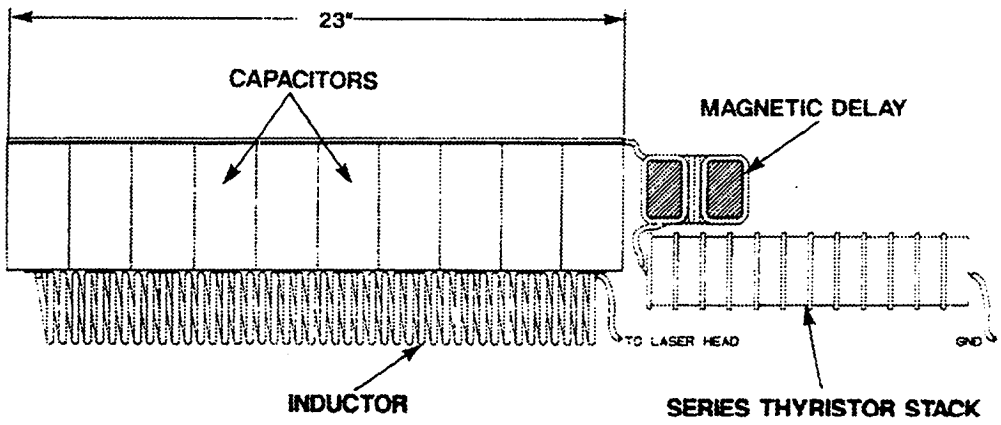

Figure 3.3-33 Pulse Power System Side View

Table 3.3-7 Pulsed Power System "Bottom-up" Weight Estimates by Component

ITEM	WEIGHT (kg)	VOLUME (m^3)
PFN:		
• Capacitor	22.2	0.0181
• Inductors	0.3	0.0024
• Mechanical Support	4.6	0.0046
Switches(1)		
• GTOs	7.2	0.0025
• Saturable Reactors	2.9	0.0004
• Companion Diodes	3.2	0.0004
• Snubbers	1.6	0.0005
• Mechanical Support	1.8	0.0006
Trigger System(1)		
• Pulse Networks	1.9	0.0005
• Transformers	2.3	0.0005
• Charging/Triggering	2.4	0.0005
Fault Protection	3.7	0.0005
Power Supply (2)	26.6	0.0378
Diagnostic Sensors	0.5	0.0002
Corona Bar Ballast Capacitors	0.8	0.0002
TOTALS	82.0	0.697

(1) Includes redundant switch/trigger system, contingent on feasibility of single-switch operation

(2) Includes redundant power supply

A pulsed power system efficiency budget is summarized in Table 3.3-8. The charging cycle has two primary loss mechanisms; the inherent inefficiencies of the charging power supply, and the leakage currents associated with the solid state switches. Discharge cycle losses mechanisms include: 1) thyristor turn on and resistance, 2) PFN capacitor dielectric and resistance, 3) PFN inductor resistance, 4) saturable reactor magnetics, 5) snubber, trigger, and BOD fault trigger systems, and 6) gas ionization.

Table 3.3-8 Pulse Power System Power Efficiency Breakdown by Component

ITEM	LOSS MECHANISM	ENERGY LOSS(%)
Charging Cycle		
• Power Supply		10.0
• GTOs	Leakage current	2..8
• Companion Diodes	Leakage current	0.3
• Protection Diodes	Leakage current	1.7
• Trigger Circuit	Charging and leakage	0.4
Discharge Cycle		
• Capacitors	Resistive and dielectric losses	2.5
• Inductors	Resistive losses	1.2
• GTOs	Turn-on and resistive losses	6.8
• Saturable Reactor	Magnetic switch losses	0.4
• Snubber Capacitors	All energy is lost	1.4
• Corona Bar	Ionize gas and establish discharge	1.7
Capacitors		
Total System Energy Losses		29.2 → η = 70.8%

Consistent With 6% Overall Efficiency

Injection/Local Oscillator Laser(s)

Our baseline design includes a redundant IO/LO laser, and, presumably, the on-orbit mode of operation would be to switch between these two lasers periodically. We also plan to operate the laser in a quasi-CW mode to conserve power, i.e., only during the period starting a millisecond before the transmit pulse generation (to facilitate locking and injection) through return reception, by modulating the RF excitation. These lasers could be either of the waveguide or wide-bore TEM_{00} type. Long-life experience with the latter type is limited; however, currently, they are the most popular "mass market" CO_2 lasers, e.g., the Synrad lasers. General Motors/Hughes have waveguide lasers under long-life test, currently at the >30,000-hour level, and manufactured using the same procedures and to the same cleanliness standards as space-qualified TWT's. These tests are being conducted under both CW and pulsed RF power supply modulation.They are apparently available commercially.

We have a preference for the wide-bore type because of the better grating line selectivity afforded by the larger beam cross section. We have had difficulties using the waveguide approach in maintaining line selectivity even over the 10 μm, or so length scanning required for line-control. These difficulties, however, may not be insurmountable.

Acousto-Optic Modulator

Our baseline design includes an acousto-optic modulator to increase the isolation between the power oscillator and the injection laser. We plan to operate the modulator in a quasi-CW mode to conserve power, i.e., only during the period starting a millisecond before the transmit pulse generation (to facilitate locking and injection) through laser pulse transmission, by modulating the RF excitation. The baseline modulator design consists of a Germanium crystal excited by a crystal transducer at some convenient RF, e.g., 40 MHz and are available commercially.

Photodetectors

Baseline photodetector selection consists of commercially-available pyroelectric quads for laser control and room temperature HgCdTe for the coherent frequency offset determination.

3.3.6 Risk Reduction

Redundancy features incorporated in the design baseline include:

Dual Injection/Local Oscillator Lasers

Dual injection/local oscillator lasers have been incorporated in our optical design for reasons of redundancy. Only one is powered up at a given time and active status would be exchanged between the lasers periodically. Coolant flow through the lasers is not interrupted so as to maintain laser temperature within operational limits.

Redundant Corona Bar

A symmetric discharge electrode arrangement incorporating a corona bar behind each of the perforated electrodes provides redundancy against corona bar failure. The corona bar behind the positive electrode (anode) is made active and the failure mode consists of activating the corona bar behind the opposite electrode while simultaneously reversing the polarities of the voltages applied to the electrodes using programmable switches.

Redundant High-Voltage Power Supply

Redundant Control Electronics

Gas Supply with Controls

The concept entails carrying on-board a pressurized sphere containing the laser gas mixture at a pressure sufficient to provide several fills. The gas would periodically be metered into the laser after evacuation of the laser gain volume into space. Sphere design data and acceptable pressurizing values were obtained from the Spacelab Accommodations Handbook. Pyrotechnic valves are incorporated to isolate the high-pressure sphere during launch for reasons of safety.
Total weight impact for a 10, 50, and 100 fill capability was estimated at 4, 12 and 26 kg, respectively, including all plumbing valves gauges and controls.

3.4 Receiver Subsystem

3.4.1 Receiver Requirements

The top-level LAWS receiver requirements are given in Table 3.4-1.

Table 3.4-1 Receiver Subsystem Requirements

RECEIVER SUBSYSTEM	
Detection Method	Heterodyne
Detector	5-Element HgCdTe
Bandwidth	1.2 GHz
Quantum Efficiency	40% at Maximum Bandwidth
Dynamic Range	60 dB
Calibration	On-Board Intensity and Velocity Calibration

3.4.2 Receiver Functional Description

The primary function of the Receiver Subsystem is to measure the Doppler shift of the laser energy reflected from the atmosphere. This Doppler shift is measured as an RF beat frequency between the reflected signal and the local oscillator (LO) radiation and is detected on the baseband 9.11 μm wavelength. The Doppler shift due to the spacecraft motion and the Earth rotation must be removed by the intermediate frequency (IF) electronics. The receiver then digitizes and stores the raw data for use in the system signal processor and for downlink.

The three major constituents of the Receiver Subsystem are shown in the block diagram of Figure 3.4-1. The detector is a five-element array which both detects the return signal and determines the alignment of the image for compensation of long term image drift. The dewar housing includes the detectors, the dual Split-Stirling Cryocooling System, and the IF electronics. The Mercury Cadmium Telluride (MCT) detectors are housed within a cryogenic dewar and

maintained at a 77K operating temperature. These detectors are photovoltaic diodes, and produce an RF signal corresponding to the mixing of the LO and the reflected signal. The pre-amps located on the outside of the dewar housing amplify this signal for input to the IF electronics. The IF electronics remove the spacecraft velocity and Earth rotation from the signal, and further process the signal into I and Q components. The IF electronics then digitizes and buffers the signal for use by the Doppler Processor in the Digital Subsystem.

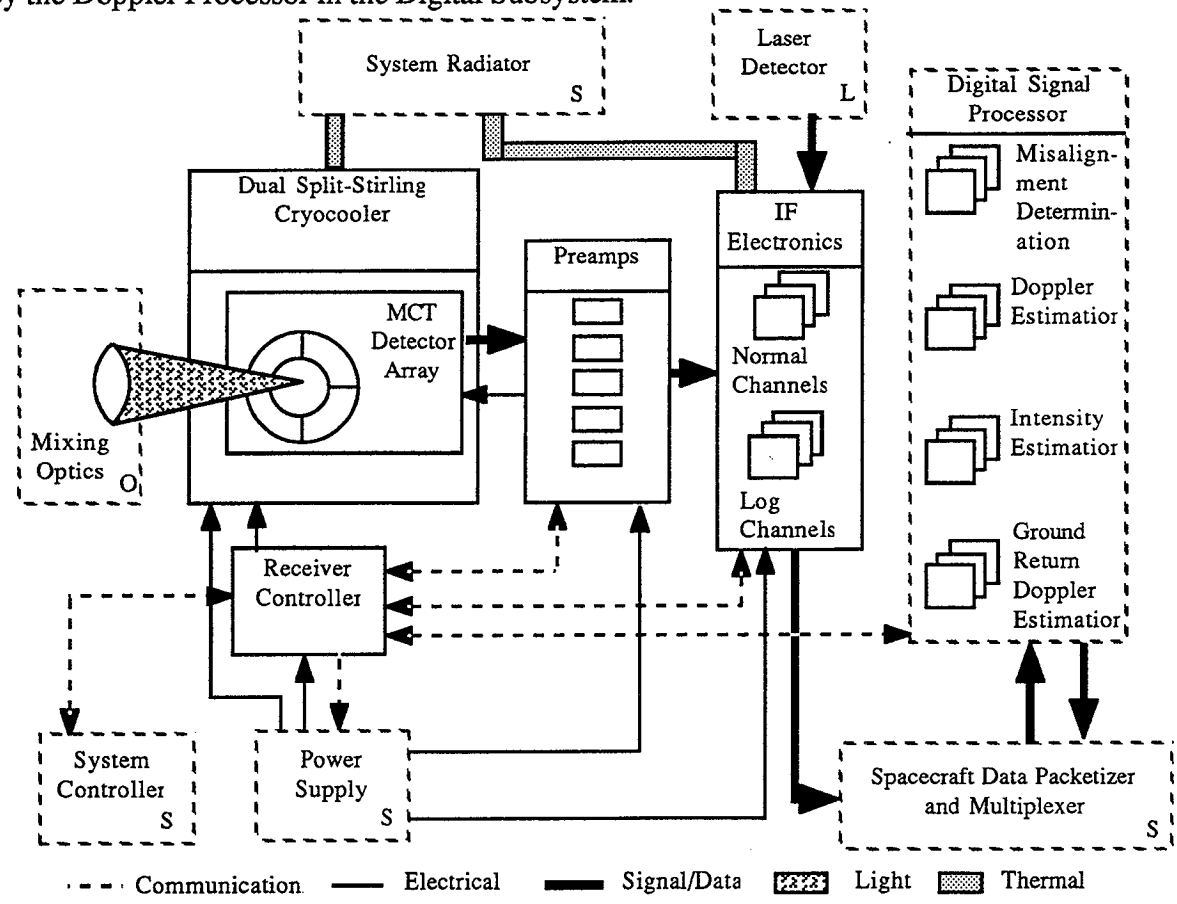

Figure 3.4-1 Receiver Subsystem Block Diagram

3.4.3 *Receiver Performance Characteristics*

Spectral Response.

The spectral response of a typical MCT diode is shown in Figure 3.4-2. The data shown here are for a typical diode which was designed for a peak response at 10.591 μm. The peak is typically rather flat. As seen in the Figure, the response is quite uniform from 10 to 11 μm. The frequency response is controlled in the wafer manufacturing stage by varying the parameter, x, in the formula for MCT, $Hg_{1-x}Cd_xTe$.

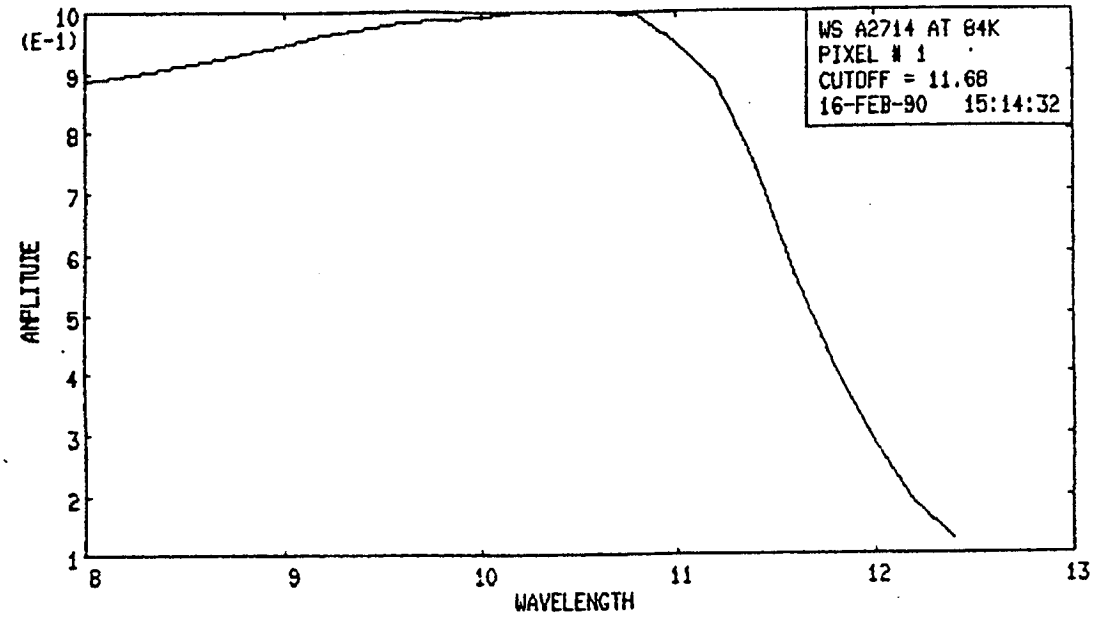

Figure 3.4-2 MCT Spectral Response

I-V Characteristics.

Figure 3.4-3 shows the I-V characteristics for a typical MCT diode as a function of LO power. The photocurrent can be estimated from the plot. Curve 10 shows that the response for an LO power of 0.60 mW is about 4 mA current at 0.5 V reverse bias. The 1 mA breakdown voltage is defined as the reverse bias voltage which draws 1 mA with no L0 power. From the Figure it can be seen that for this diode the value is approximately -2.8 Volts.

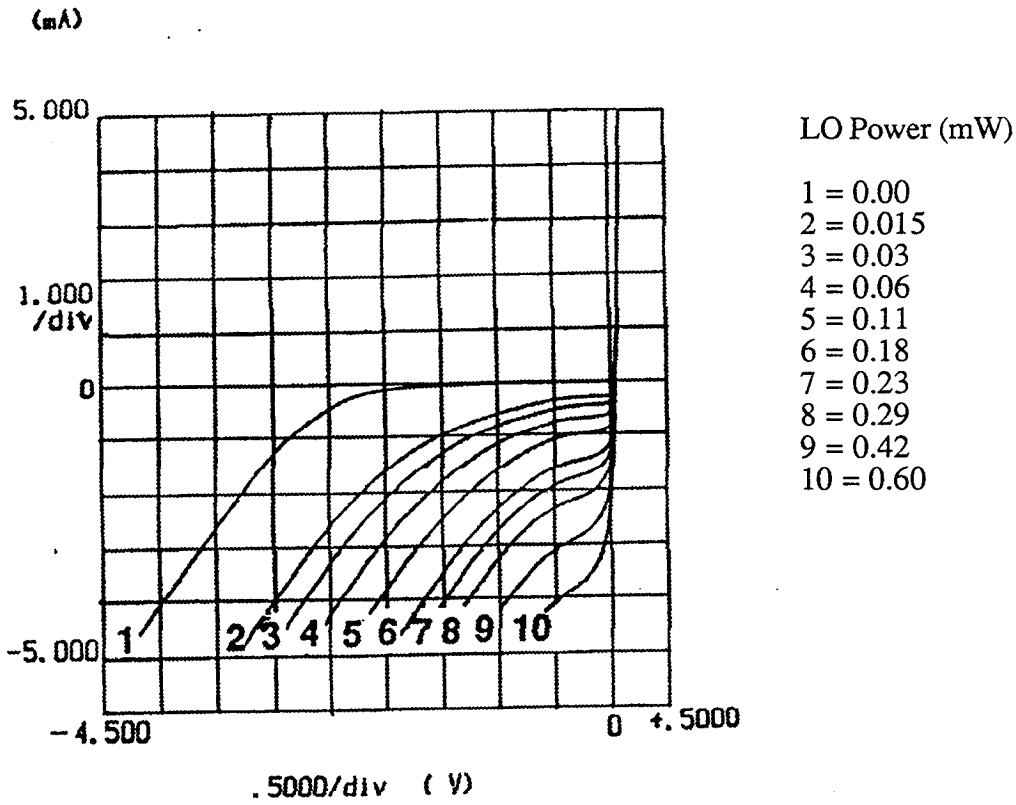

Figure 3.4-3 MCT I-V Characteristics vs. LO Power

Effective Heterodyne Quantum Efficiency.

The effective heterodyne quantum efficiency, EHQE, is defined by the relation

$$\eta_{EH} = \frac{\eta_{AC}^2}{\eta_{DC}}$$

where η_{DC} is the DC quantum efficiency and η_{AC} is the AC quantum efficiency. The AC quantum efficiency and therefore the effective heterodyne quantum efficiency is strongly frequency dependent. Figure 3.4-4 shows the frequency response for a typical high bandwidth MCT detector. As can be seen from the Figure the quantum efficiency drops by about 3 db from DC to 1 GHz. However values of greater than 40% at 1 GHz are attainable.

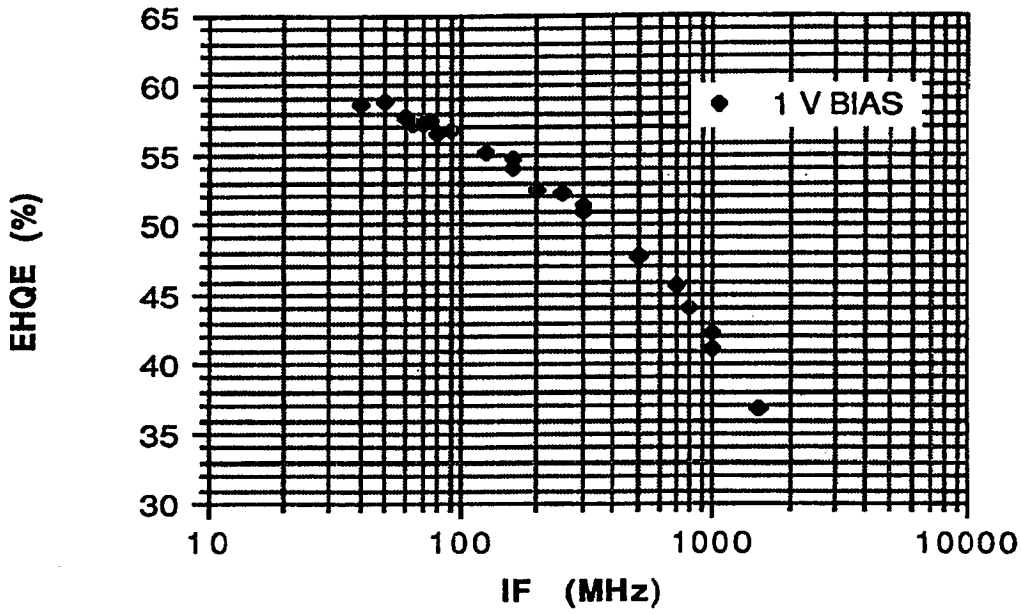

Figure 3.4-4 MCT Quantum Efficiency vs. RF Frequency

The detector quantum efficiency, η_{EH}, is dependent on the applied bias voltage. Figure 3.4-5 shows a family of curves of quantum efficiency versus reverse bias voltage for several values of RF frequency. As can be seen from the Figure, the peak response shifts to higher reverse bias voltage at the higher RF frequencies.

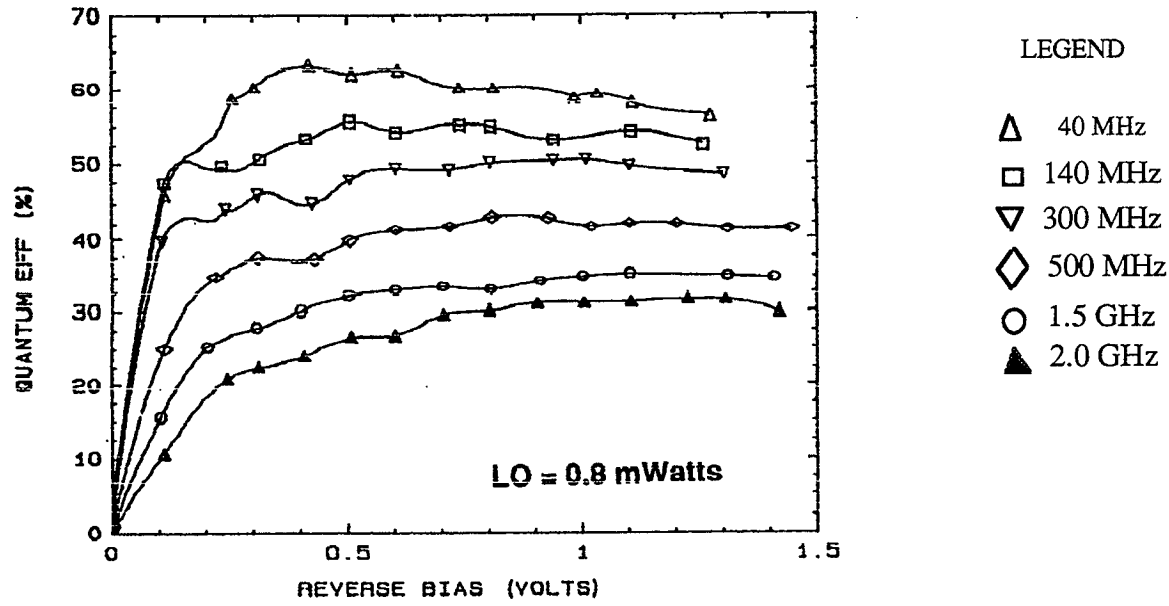

Figure 3.4-5 MCT Quantum Efficiency vs. Bias Voltage

The detector EHQE is apparently dependent on the applied LO power as is seen from Figure 3.4-6. However, the EHQE is not dependent on LO power when operating in the shot noise limit. The figure shows the shot noise limit is reached at an LO power of about 0.5 mw. For LO power less than about 0.5 mW, the detector is not operating in the shot noise limit. That is the total noise power, $\langle i_{TOT}^2 \rangle$ has a significant contribution from sources other than the LO. Therefore, system noise power, $\langle i_{SYS}^2 \rangle$, must be added to the shot noise power, $\langle i_{LO}^2 \rangle$, such that

$$\langle i_{TOT}^2 \rangle = \langle i_{LO}^2 \rangle + \langle i_{SYS}^2 \rangle$$

In general the relation

$$\eta_{EH} = \frac{\eta_{AC}^2 \langle i_{LO}^2 \rangle}{\eta_{DC} \langle i_{TOT}^2 \rangle}$$

should be used to calculate the quantum efficiency when the noise measurement contains contributors other than shot noise.

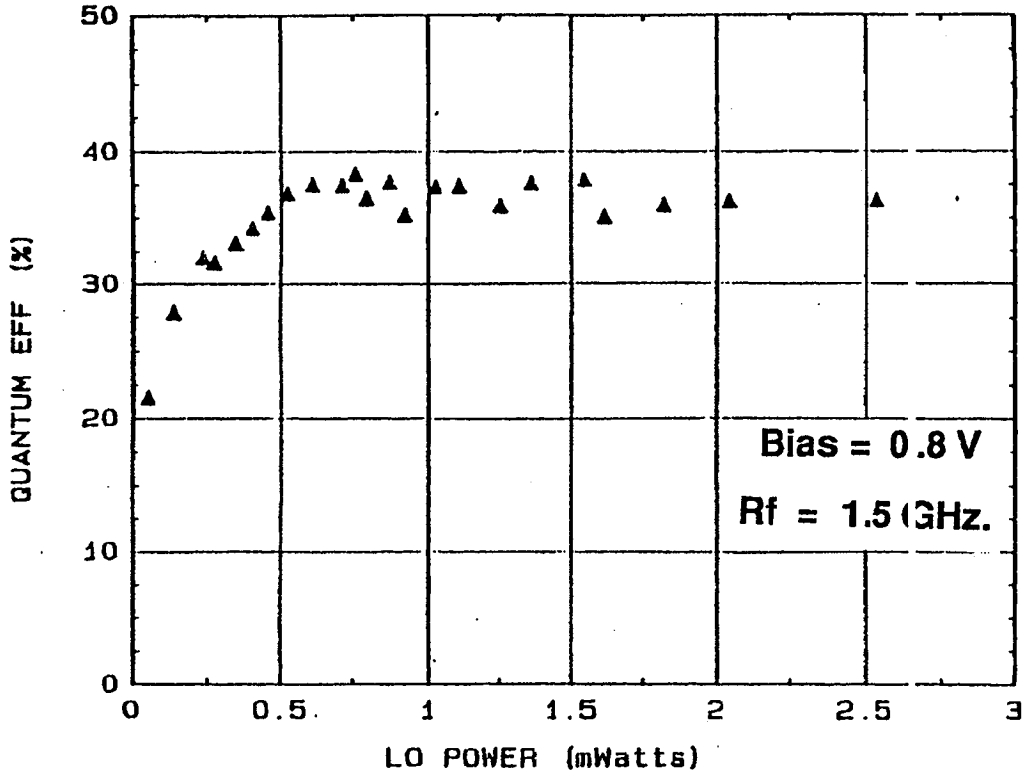

Figure 3.4-6 MCT Quantum Efficiency vs. LO Power

3.4.4 Receiver Analyses and Trades

3.4.4.1 Beam Truncation Effects

The beam truncation loss is defined as the loss due to truncation of the Gaussian beam by the transmitting aperture, including the diffraction effects and the obscuration. This factor represents the ratio of the energy collected by the receiver with truncation relative to the received energy without any transmitter truncation. Previous lidar calculations have used a beam truncation factor of 0.46 based on the literature. This loss factor has been investigated using OASIS for both the hypothetical Gaussian beam and the predicted beam shapes for the graded reflectivity and scraper mirror laser output couplers.

The optimum amount of truncation was determined for the limited 1.5 m diameter aperture. The larger the ratio of beam waist to aperture, the more obscuration and subsequent diffraction of the output laser beam. However, a small ratio results in a large beam divergence. Analysis by Hughes Danbury showed that the optimum ratio is 0.8 times the Gaussian beam 1/e size. This same calculation was performed at GE using the industry standard code OASIS. The result is shown in Figure 3.4-7. An assumption required by OASIS is that the beam is reflected by a perfect mirror rather than the true multiple reflections from a large number of independent scatterers. This simplification introduces a small error in the calculation since the return beam is essentially a plane wave over the receive aperture (a very broad Gaussian) rather than the true convolution of many independent point sources. This is the same assumption made in previous calculations and produces only a small error.

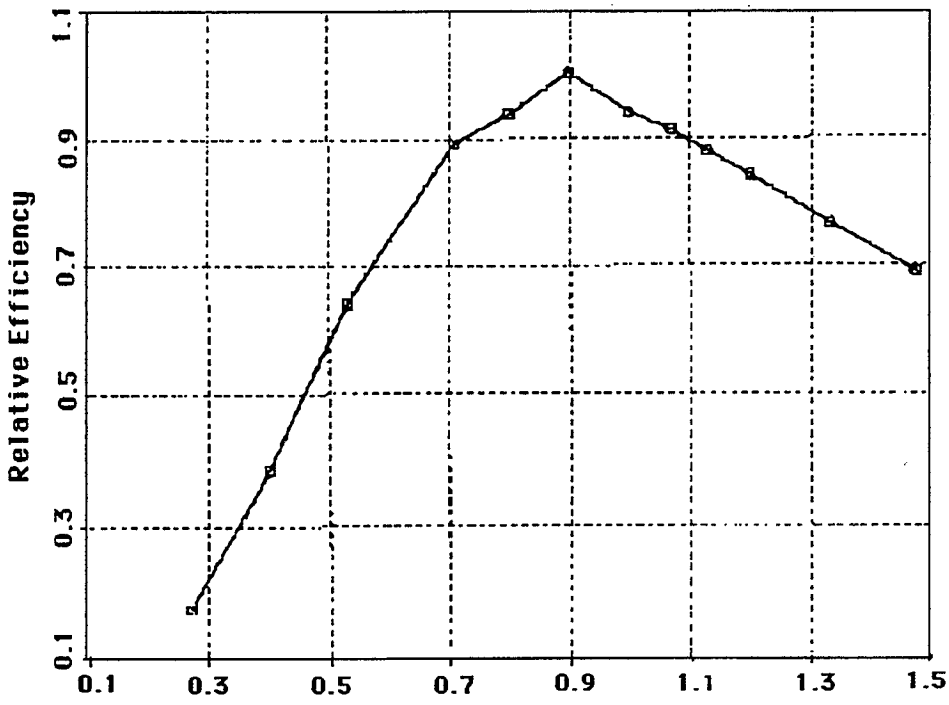

Figure 3.4-7 Relative Efficiency Using Oasis Gaussian Beam Profile

Figure 3.4-7 shows that the optimum truncation ratio for the Gaussian beam calculated using OASIS is about 0.9 times the 1/e beam size. This is slightly larger than the result obtained by Hughes Danbury and can probably be attributed to the above assumption as well as the accuracy of the OASIS code. The same calculation has been performed using the STI-supplied graded reflectivity coupler beam profile and is shown in Figure 3.4-8. The optimum is 1.6 times the beam radius, which agrees with results obtained at Hughes Danbury. In this case, the beam radius is

defined as the point where the beam intensity falls to zero since it is not a Gaussian beam. Figure 3.4-9 shows the optimum truncation ratio for the scraper mirror output calculated using OASIS to be about 0.95.

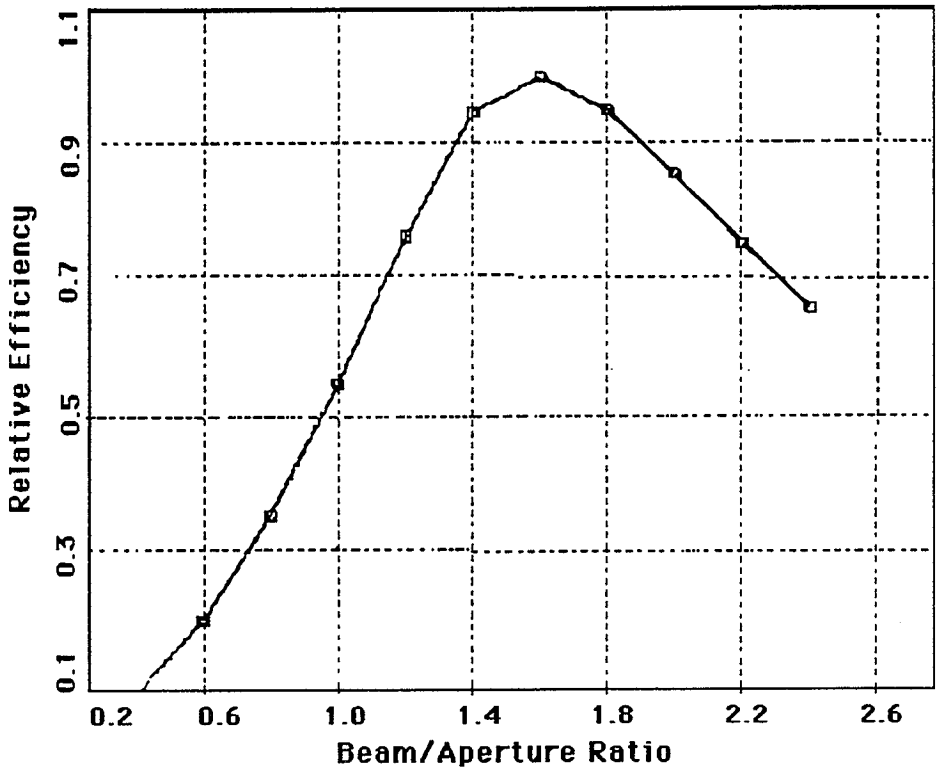

Figure 3.4-8 Relative Efficiency Using STI Beam Profile

The actual truncation loss factor for the optimum beam truncation was determined. This factor, together with the heterodyne efficiency calculated using the GE code HETEVAL, determine the effective SNR, or EFFSNR. The Hughes Danbury results show the maximum EFFSNR to be about 0.42 for both the Gaussian and graded reflectivity output profiles. Using the optimum truncation suggested by Hughes Danbury for the Gaussian beam, 0.8 times the 1/e radius, a Gaussian truncation factor of 0.61 was calculated using OASIS, resulting in a combined EFFSNR of 0.43. This result is in excellent agreement with the Hughes Danbury result.

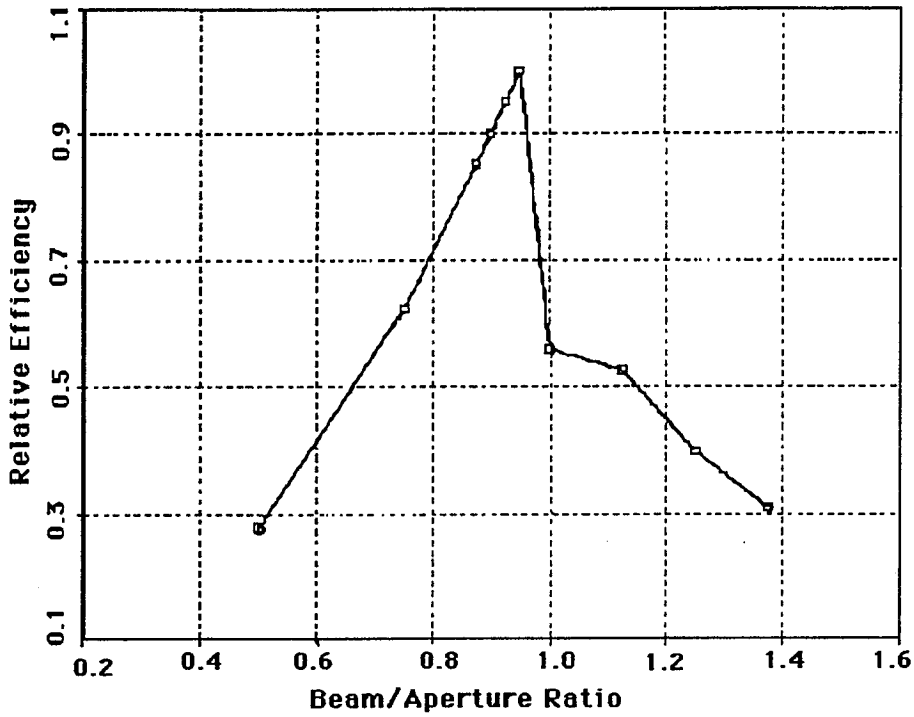

Figure 3.4-9 Relative Efficiency Using Oasis Scraper Mirror Beam Profile

The truncation loss term for the graded reflectivity mirror using OASIS is 0.72 for the optimum truncation ratio. The total EFFSNR in this case is then 0.51, somewhat better than for the Gaussian beam. The Hughes Danbury analysis shows little difference in the optimum EFFSNR between the Gaussian and graded reflectivity outputs. Finally, the optimum beam-to-aperture truncation ratio for the scraper mirror output is about 0.95. The result is a truncation loss of 0.45 which is significantly less than that for either the Gaussian beam or the graded reflectivity output beam. The combined EFFSNR is 0.32 for the scraper mirror, about 1/3 less than the graded reflectivity EFFSNR. Table 3.4-1 compares the OASIS results for the three beam profiles. The overall system efficiency is the EFFSNR times the total optical throughput and the detector quantum efficiency. The EFFSNR has been further reduced by about 1 dB due to the telescope pointing error.

Table 3.4-1 OASIS Efficiency Calculations

Beam Type	Optimum Ratio (Beam/Aper)	Truncation Loss	EFFSNR*
Gaussian	0.8*	.61	.43
Graded Ref.	1.6	.72	.51
Scraper	0.95	.45	.32

* After Noll (Hughes Danbury)

Conclusions and observations from this analysis are:

1) The heterodyne efficiency (or EFFSNR) of a coherent lidar using a laser beam produced by a scraper mirror resonator is about 1/3 less than one which uses a graded reflectivity resonator.

2) There are some caveats to the use of OASIS for calculations of this type which should be borne in mind. The OASIS program performs automatic scaling of the beam array during propagation which can cause large round-off errors for large distances (1200 km was used) and beams that do not have smooth profiles (like the scraper mirror beam). There are several ways to overcome some of these errors, but they may be inaccurate. OASIS works very well for propagation over short distances and for Gaussian beams but other cases should be carefully checked for accuracy and consistency. (Note that this caveat in no way changes our conclusions regarding the superiority of a graded reflectivity resonator over a scraper mirror resonator for coherent lidar applications).

3) In general, there is good agreement between the results obtained at GE using OASIS and those from Hughes Danbury using an analytical code. The Hughes results for the scraper mirror show an EFFSNR of around 0.20, somewhat less than the GE results. The difference is probably in the optimum beam-to-aperture truncation ratio; the Hughes value for the Gaussian beam was 0.8 and the GE value was 0.9. The difference in these values (in the scraper mirror case) would account for the discrepancy.

3.4.4.2 CO_2 Modulator Trades.

The signal returned from the atmosphere contains a large Doppler shift of up to about ±1.2 GHz due to the motion of the spacecraft. The Doppler shift due to the wind is much smaller occupying a bandwidth of about ±20 MHz. Although the spacecraft Doppler shift varies sinusoidally as the telescope scans about nadir, the detector nevertheless must operate for considerable lengths of time at frequencies much higher than the signal bandwidth. At such elevated frequencies the quantum efficincy of the detector is less than optimum.

A potential way to improve the overall system efficiency is therefore to optically beat the received signal down to baseband, prior to detection, where the HgCdTe detector quantum efficiency is optimal. The following sections describe methods of achieving this using optical

modulators, to frequency sweep the LO, and the system trade-off studies performed to determine if such an approach was worth baselining.

The basic optical modulator considered consists of a CdTe-buffered GaAs thin-slab waveguide with a relatively flat frequency response between 8 and 18 GHz. Measurements have shown a 27.7 mW output in a single sideband using as input a 10-W laser and 20 W of microwave power in CW operation. The single-sideband selection and carrier reduction would then be performed using a pair of Fabry-Perot filters. The first filter could be a fixed reflection/transmission filter which would block the carrier. The second filter would be scanned to select the desired sideband. The output beam is slightly elliptical and would probably require a cylindrical lens for a heterodyne system. The frequency accuracy and stability of the modulator is limited by the LO linewidth and stability. Figure 3.4-10 is a block diagram of the entire modulator assembly. We considered 2 ways of using such modulators.

One option is to use an LO laser line which is separated from the transmitter laser by the 8 to 18 GHz modulation frequency. This would require either a second laser for injection seeding or possibly a second, fixed modulator for the injection beam. Another option is to use a 9.11 μm isotopic injection oscillator/local oscillator and use two modulators back-to-back in the LO path.

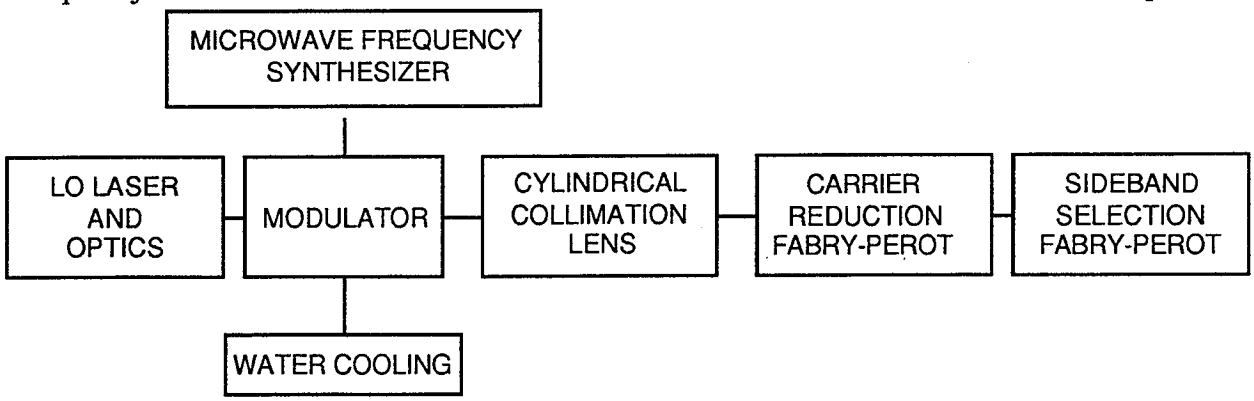

Figure 3.4-10 Modulator Layout

The potential use of a swept optical LO in a LAWS-type instrument involves many trades including power, performance and risk. The first question to be answered is whether or not there is a suitable CO_2 laser line separated by 8 to 18 GHz from the 9.11452 isotopic CO_2 line. The following Table lists the only available CO_2 laser lines which meet (or nearly meet) these requirements.

The three normal isotopic lines shown in Table 3.4-2 are slightly outside the published linear range of the modulator, 8 to 18 GHz, but may be useful. The 0^{18} R(29) line falls in the relatively linear range of the modulator, but must also be checked in terms of power. Even though

the laser gain curve peaks around the R(20) line (shown in boldface in Table 3.4-2), the R(29) line may be sufficient, since probably only about 45 Watts from the IO/LO laser are required. Another transmit laser option is the P(20), 11.1494 μm, line using a C^{13} isotope as shown in boldface in Table 3.4-3. This option has 2 lines within the "flat" band of the modulator, both of which are isotopic, shown in Table 3.4-3.

Table 3.4-2 Available Laser Lines Near 9.11μm

Isotope	Shift	Line	Transition
Normal	+ 30.7 GHz	9.10623	00°1 0 → 2°0 Band R(58)
0^{18}	+ 22.3 GHz	9.10855	00°2 → 02°1 Band R(31)
Normal	+ 6.56 GHz	9.11291	00°1 → 02°0 Band R(56)
0^{18}	0	**9.11452**	**00°1 → 02°0 Band R(20)**
0^{18}	- 10 GHz	9.11737	00°2 → 02°1 Band R(29)
Normal	- 19.75 GHz	9.11979	00°1 → 02°0 Band R(54)
0^{18}	- 34.8 GHz	9.12438	00°1 → 02°0 Band R(18)

Table 3.4-3 Available Laser Lines Near 11.15μm

Isotope	Shift	Line	Transition
C^{14}	- 34.9 GHz	11.13520	00°1 → 10°0 Band R(46)
Normal	- 3.3 GHz	11.14829	$0^{1}1 \rightarrow 11^{1}0$ Band P(34)
C^{13}	**0**	**11.14940**	**00°1 → 10°0 Band P(20)**
C^{14}	+ 1.0 GHz	11.14968	00°1 → 10°0 Band R(44)
C^{13}	+ 1.6 GHz	11.15033	00°2 → 10°1 Band P(17)
$C^{14}0^{18}$	+ 10.6 GHz	11.15407	00°1 → 10°0 Band R(10)
$C^{30}0^{18}$	+ 13.7 GHz	11.15537	00°1 → 10°0 Band P(40)
Normal	+ 21.7 GHz	11.15867	00°1 → 10°0 Band P(66)
C^{14}	+ 35.5 GHz	11.16443	00°1 → 10°0 Band R(42)

Assuming there is a suitable pair of wavelengths for efficient modulator operation, several other system issues must be addressed, including: power, performance, risk, cost, weight, and reliability requirements. The system block diagram for the three options, 1) high-bandwidth detection, 2) high-bandwidth modulation using two separated laser lines, and 3) modulation of the LO laser twice, are shown in Figures 3.4-11, 12 and 13, respectively. The obvious differences in the block diagrams are: 1) the modulator approaches require two modulators (and therefore two RF frequency synthesizers), 2) the modulator schemes require several Fabry-Perot filters, 3) the RF frequency synthesizer must drive N channels in the baseline design (the baseline detector is a 5-element circular array), and 4) the need for additional optics in the modulator approach. The receiver requirement which clearly favors the modulator approach is that the detector operates at a significantly lower frequency, 40 MHz rather than 1.2 GHz, resulting in a factor of almost two improvement in quantum efficiency.

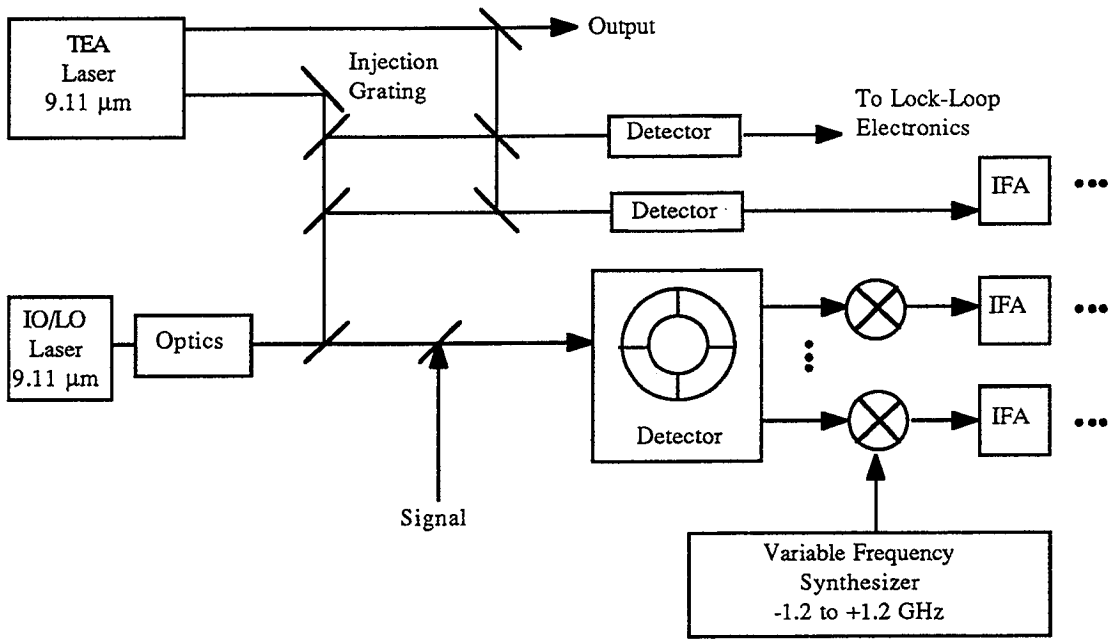

Figure 3.4-11 Baseline LAWS Block Diagram

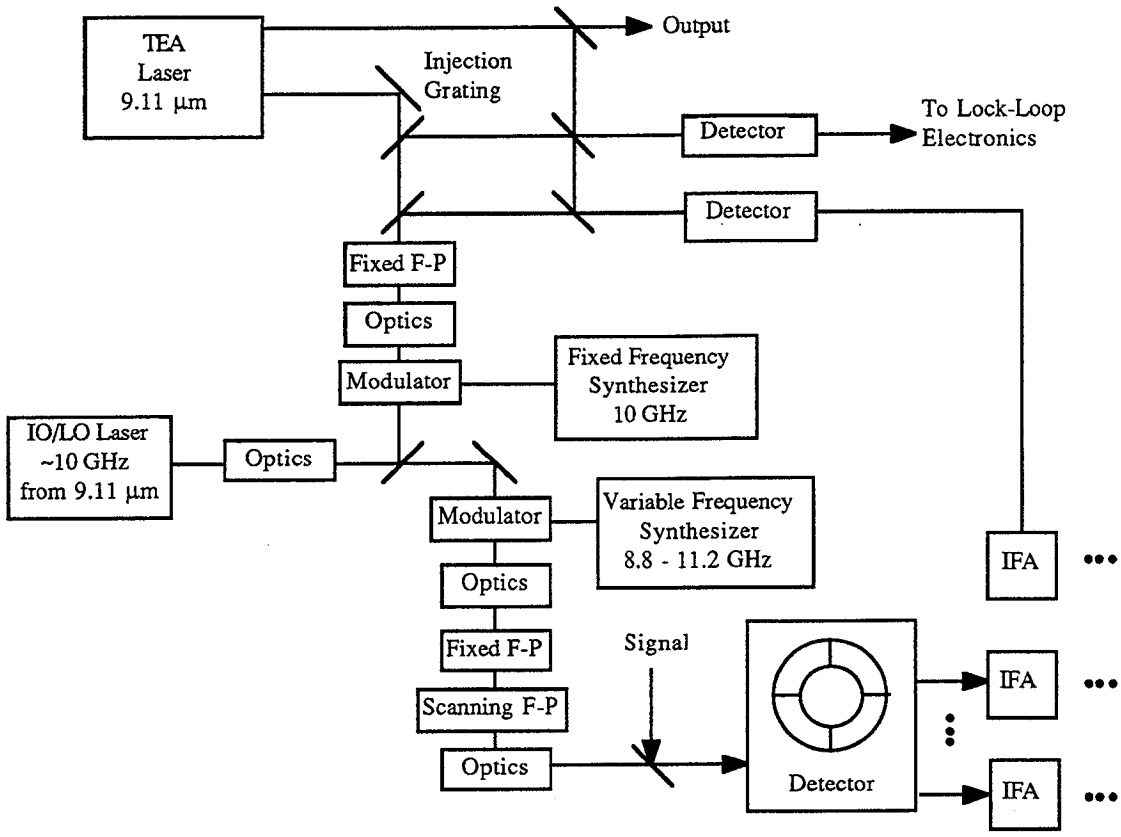

Figure 3.4-12 Tunable Modulator Option 1

The other major system consideration is the required power. The baseline LAWS receiver required 140 Watts, with 80 Watts utilized by the cooler. The baseline Laser Subsystem required 100 Watts for the IO/LO laser and the servo-loop electronics. The IO/LO laser uses 50 Watts input and has a 5-Watt output, or a 10% efficiency. For this comparison, it is assumed that an LO power requirement of 5 mWatts per detector for all of the options is valid and that only 50% of the laser energy reaches the detector. It is also assumed that all options use a 5-element detector. Therefore, 50 mWatts of LO laser power is required. Table 3.4-4 compares the power requirements for the baseline and 2 modulator options.

Table 3.4-4 Power Requirements

	Baseline	Option 1	Option 2
IO/LO Laser	50	450	550
Detector Bias	9	2	2
RF Freq. Syn.	25	40	40
Cooling	80	40	40
Fabry-Perot	0	8	8
Total	164	540	640

Option 1 consists of an IO/LO laser with a line slightly removed from the 9.11 μm laser line. This option appears to be a viable alternative to the use of high-bandwidth detectors. Although this requires two modulators, one may be a relatively simple resonant cavity device to provide a constant 10 GHz offset with an efficiency around 10%. Assuming a 99% reflective injection grating (the present design) and a required injection power of 40 mW, about 40 Watts is required for the IO beam. Again, assuming 50 mW is needed for the LO and the modulator efficiency is 1%, 5 Watts are needed for the LO beam. The total IO/LO laser power requirement is 45 Watts compared to the present 5 Watt requirement.

Option 2 requires more power than Option 1 due to the low efficiency associated with placing two modulators back-to-back. These calculations assume a 10% efficiency for a fixed offset modulator (a resonant cavity type, for example) and a 1% efficiency for the variable modulator. These efficiencies can probably be improved and a different injection design may lower the required IO laser power which is driving the IO/LO laser power in Option 1 (40 Watts for the IO laser and 5 Watts for the LO).

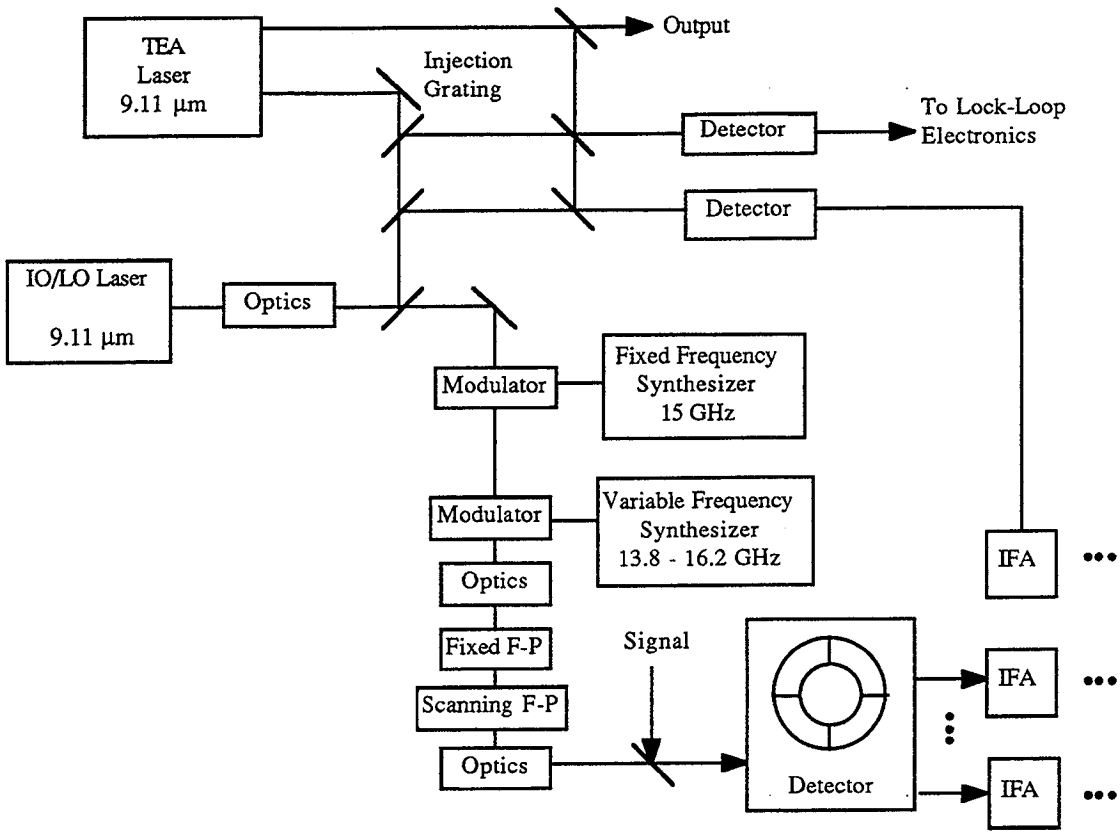

Figure 3.4-13 Tunable Modulator Option 2

There are several other options for reducing the detector bandwidth which may be investigated. These include: 1) using a simpler EO modulator to remove some or all of the 1.2 GHz, 2) use a fixed (plus and minus) frequency offset to reduce the detector bandwidth to 600 MHz. A fixed resonant cavity modulator has an efficiency up to 10 times greater than that for a variable frequency, traveling wave device.

Table 3.4-5 compares the advantages and disadvantages of each approach, quantitatively where possible. The conclusions of this analysis are:

1) An option of using an IO/LO laser slightly removed from the 9.11 μm TEA laser and shifting both the IO and LO beams appears feasible. The power requirements are significantly higher than the baseline, but could probably be reduced, especially with an alternate injection design. This option requires a 45 Watt IO/LO laser, 40 Watts for injecting the TEA laser and 5 Watts for the local oscillator.

2) Another option of using back-to-back modulators also appears possible but requires over three times the power of the current design. However, it uses the same IO/LO laser (although higher power) as the present design.

Given the complexity of the optical modulator approaches, the developmental nature of the modulators, the increased power required and the >40% performance demonstrated from GE HgCdTe detectors at 1 GHz, our baseline of high bandwidth detection remains the chosen approach.

Table 3.4-5 Summary of Options

Issue	Baseline	Shifted IO/LO	Back-to-back Modulators	Bulk Crystal Modulator
Modulator Drive Receiver Power Cooler Power IO/LO Power	0 60 80 50	40 40 40 450	40 40 40 550	40 40 40 1000
Total Power (w)	190	570	670	1120
Detector QE	30-40%	60-70%	60-70%	60-70%
Issues and Challenges	Detector, Cooler	IO/LO Laser, Modulators	Modulators	Efficiency (Power)
General Comments	Higher Cooling Reqm't	May allow use of array and deletion of alignment system		

3.4.4.3 On Board Calibration Studies.

As well as being required to measure wind velocity, LAWS is required to provide estimates of the atmospheric backscattering coefficient. The measurement of the magnitude of the backscatter requires a knowledge of the signal-to-noise ratio and hence a knowledge of the detector effective heterodyne quantum efficiency and the optical mixing efficiency. This study investigated the possibility of providing an on board capability to calibrate these quantities.

Effective Heterodyne Quantum Efficiency, EHQE

The EHQE measures the ability of the detector to respond to the intermediate frequencies created in the mixing process. The EHQE is strongly RF frequency-dependent. Therefore, a good knowledge of EHQE vs. RF frequency from 40 MHz to 2 GHz is required to measure the intensity

of the backscatter. To achieve on-orbit calibration, a known source capable of generating signals over the 2 GHz range of intermediate frequencies is required. This can be achieved using a blackbody source and an optical spike filter with 0.1 to 0.4 micron width centered at the LO frequency. A pre-determined set of fixed narrow band RF filters will then be consecutively selected, the signal from each filter is then attenuated or amplified to achieve a power level compatible with the IF electronics. The IF electronics and associated processing will measure signal-to-noise and evaluate the EHQE using the relation

$$\eta_{EH} = \frac{\left[e^{h\nu_{LO}/k\, t_{BB}} - 1\right]}{\sqrt{2}\; t_t} \sqrt{\frac{B_o}{B_{IF}}} \left(\frac{S}{N}\right)_{\nu\ measured}$$

where:

S/N is the measured voltage signal-to-noise ratio
B_O is the noise bandwidth of the lock-in amplifier
B_{IF} is the intermediate frequency (IF) bandwidth of the RF amplifiers
ν_{LO} is the frequency of the LO laser
t_t is the transmission of the optics, including a chopper factor
t_{BB} is the blackbody temperature
k is Boltzmann's constant, and
h is Planck's constant

The equation parameters and scale factors are defined in detail in "Long-Wave Photodiode Development," D.L. Spears, Project Report NAS-1, prepared for NASA Goddard Space Flight Center, 16 August 1983. This calibration procedure will interrupt normal operations for about ten minutes, and should be done once or twice a week at the beginning of operations. The calibration procedure will be conducted at less frequent intervals if the EHQE vs. RF frequency remains stable. The procedure for the EHQE vs. RF frequency calibration will be documented in the appropriate procedure during Phase C/D. The required steps are outlined below.

1. Verify that the temperature and bias current are nominal. Adjust the LO position to maximize the bias current to ensure that the optimal photon flux is incident upon the detector.

2. Turn on the blackbody and wait until the blackbody temperature reaches 1173K.

3. Keep the LO on the detector, but assure that no other signal is present.

4. Initiate the calibration program, which automatically reads the signal from each of the chosen fixed filters, measures the signal-to-noise, and calculates the EHQE for the chosen frequencies.

5. Turn off the blackbody.

6. Compare the EHQE vs. RF frequency obtained to the pre-launch values, update the backscatter calibration factors as required, and resume operations.

Alignment Calibration

The calibration of the alignment and mixing efficiency can be accomplished using the method of Frehlich and Kavaya (as described in "Coherent Laser Radar Performance for General Atmospheric Refractive Turbulence," 3/4/91). This method assumes that the EHQE is known and uses the relation

$$\eta_{EH}\,\eta_{MIX} = \frac{t_L A}{A_{TR}} = \frac{\langle i_s^2 \rangle}{2\langle I_{DC} \rangle \langle I_s \rangle}$$

where η_{MIX} is the factor which characterizes the mixing efficiency, I_{DC} is the DC current due to the LO, I_S is the direct detection signal current due to the backscatter field, and i_S is the intermediate frequency (IF) signal current at the frequency $\Delta\omega = \omega_{LO} - \omega << \omega$. (the additional parameters are described in the referenced publication). These three aforementioned measured quantities are then compared to the known EHQE. Any discrepancy can be attributed to misalignment which can, in principle, be corrected or accounted for in a calibration factor. The measurement of the three current components can be accomplished in the following manner. First, the DC current due to the LO is measured as the bias current with no signal pulse, and is on the order of 5 mA. However, the direct detection signal current due to the backscatter field will be small by comparison (see Figure 3.4-14). Therefore, the DC bias current must be measured with an uncertainty less than the magnitude of the signal current due to the backscatter field. If the backscatter field is due to ground reflection, then the current pulse is of the order of 10^7 electrons over a 3 μs time span, or about a 1

μA spike for 3 μs. The bias current must then be measured to better than five or six significant figures, 10^{-8} or 10^{-9} A. The pulse due to the backscatter field will be measured using the matched filter tuned to 333 kHz and the low pass filter shown in Figure 3.4-15 to read the voltage across a standard resistor in the bias circuit. A digital read-out of the matched filter will then be used as input to the Digital Signal Processor (DSP). The mixing current can be simultaneously measured using a second matched filter at 333 kHz in conjunction with a rectifier and a high pass filter. The digital output from this matched filter is also used as input to the DSP for calibration processing.

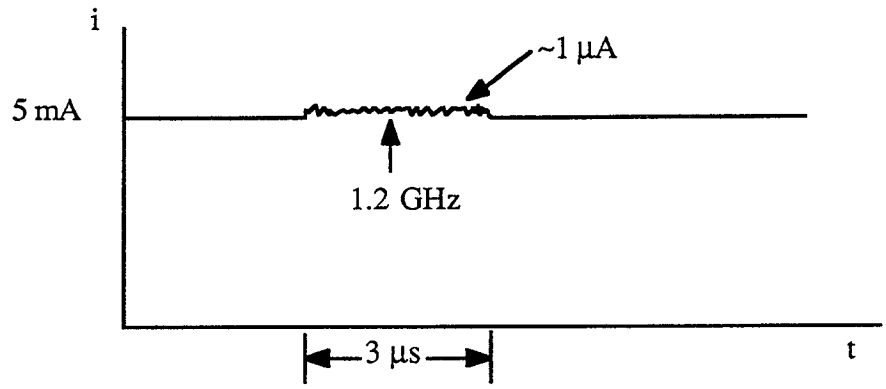

Figure 3.4-14 MCT Detector Bias Current During a Ground Return

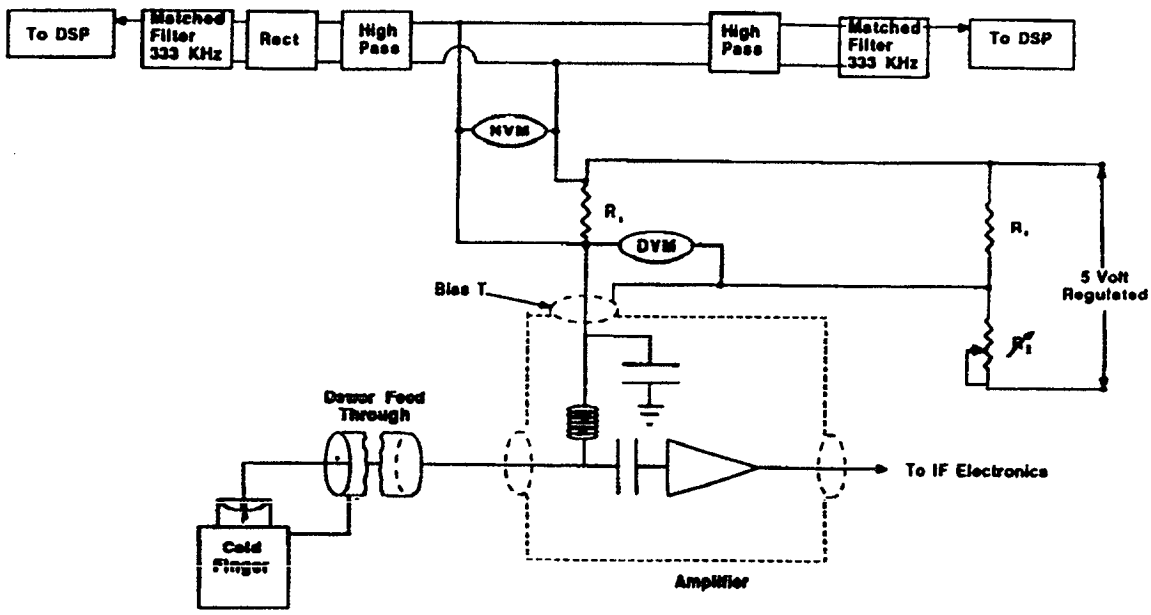

Figure 3.4-15 Enhanced Bias Circuit

Conclusions

The on board calibration of the EHQE was not baselined since all of the experimental evidence to date indicates that the EHQE remains constant as long as the I-V curve remains stable. Therefore the monitoring of the I-V characteristics and the DC quantum efficiency is sufficient to establish with a good degree of confidence that the pre-launch values of EHQE as a function of RF frequency are still valid. However, there is no way of determining the change in EHQE versus RF frequency in the event that changes occur in the I-V curves, or in the DC quantum efficiency. Since the measure of the backscatter magnitude is not the primary mission, the possible increased accuracy derived from the recalibration of EHQE versus RF frequency is not sufficient to warrant the the additional cost and added system complexity.

The evaluation of optical mixing efficiency using the method of Frehlich and Kavaya is at this time also not selected. There is no data which indicates the possible increase in backscatter magnitude accuracy which this method will yield. However, the mixing efficiency may be more susceptible to on orbit change than is the EHQE. This is primarily due to the possible change in alignment resulting from thermal effects or vibrations. Alignment calibration therefore merits consideration for on orbit evaluation and we recommend the evaluation of the method using a ground test to determine the accuracy with which alignment can be determined versus the cost and added system complexity.

3.4.5 Receiver Preliminary Design

The Receiver Subsystem consists of three major constituents: the dewar assembly including the Mercury Cadmium Telluride (MCT) detectors, the cooling mechanisms, and the electronics. The MCT detectors respond to the beat frequency of the LO mixing with the reflected signal. The detectors operate in the photovoltaic mode and require an operating temperature of 77K. This operating temperature is achieved by mounting the MCT photodiodes onto the cold finger of a cryogenic dewar.

3.4.5.1 Dewar System

The dewar is cooled by a pair of Split-Stirling cryocoolers. The top view of the dewar is shown in Figure 3.4-16. The system consists of four cyrocoolers- only two opposing coolers are operational, and the other two are included for redundancy. The cylindrical design of the dewar ensures that vibrations due to the cooler displacers are not translated to the detector mounts. This dewar design has a natural frequency of greater than 2000 Hz which will be insensitive to the 40

Hz driving force of the displacer. The dewar assembly side view is shown in Figure 3.4-17. The mounting ring rigidly holds the mounting board, shown in Figure 3.4-18, via thermally isolating pins. The mounting board is an electrical insulator with a dielectric constant of 10 to match that of the carrier board. The carrier board is shown in Figure 3.4-19. The matching of dielectric constants is necessary to ensure the impedance matching along the RF coplanar waveguides which carry the signal from the MCT detector to the preamplifiers located on the outer dewar wall. If the mechanical load on the carrier board is less than five ounces and the board is manufactured of 0.2-inch thick Al_2O_3, then the natural frequency of the board is greater than 600 Hz. This frequency should also be insensitive to the 40 Hz driving force of the cooler displacers.

3.4.5.2 Cooling System

The cooling system chosen as the baseline for system design purposes is the British Aerospace 80K Stirling Cycle Cooler shown in Figure 3.4-20. This system consists of a displacer and a compressor connected by a coolant transfer tube. The system operates in a closed cycle, and does not require any expendable cryogenic cooling agent. The cooler capability is summarized in Figure 3.4-21. It can be seen in the figure that a single cooler operating between 80K at the cold finger and 300K ambient can remove a heat load of 0.8 Watts. A pair of coolers, therefore, is more than adequate for handling the anticipated heat load of 0.88 W. This predicted heat load includes the parasitic heat loss due to radiation and conduction from the support board and the connecting wires. The addition of a pair of redundant coolers which are not operating but are in contact with the cold finger adds an additional heat load of 0.3 W. The 1.18 W total heat load is well within the capability of a pair of BAe Split-Stirling coolers. The concern that vibrations induced by the cooler displacer will cause operational alignment problems is under study at JPL. The cooler vibrational data results from the study are shown in Figure 3.4-22 (Reference: "Characterization of Miniature Stirling Cycle Cyrocoolers for Space Application," R.G. Ross, Jr., D.L. Johnson, and R.S. Sugimura, Jet Propulsion Lab., California Institute of Technology, Pasadena, CA., Proceedings of the Sixth International Cryocooler Conference, Plymouth, MA., Oct. 25, 1990). The low-level residual forces shown in the figure are achieved using back-to-back displacers and low-level drive electronics with 40, 120 and 160 Hz nulling. Using the residual forces as the driving force spectrum, the longitudinal response of a dewar with a weight of 10 lbs., an inertia of 400 lb-in^2, and a Q of 20 is indicated in Figure 3.4-22, as a function of the dewar's fundamental frequency. This analysis indicates that the dewar system should have all fundamental frequencies greater than 200 or 300 Hz, in order to meet the 1.2 μm specification on detector alignment. This requirement has driven the dewar design presented above.

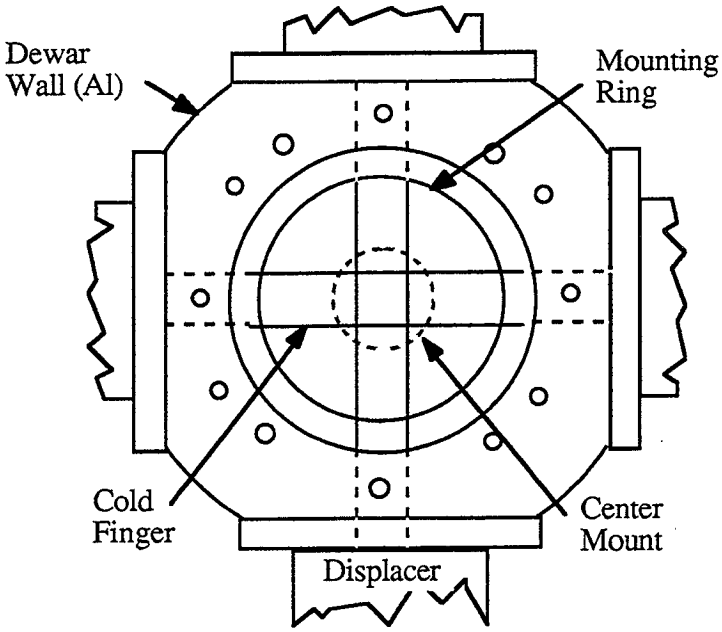

Figure 3.4-16 Dewar Top-View

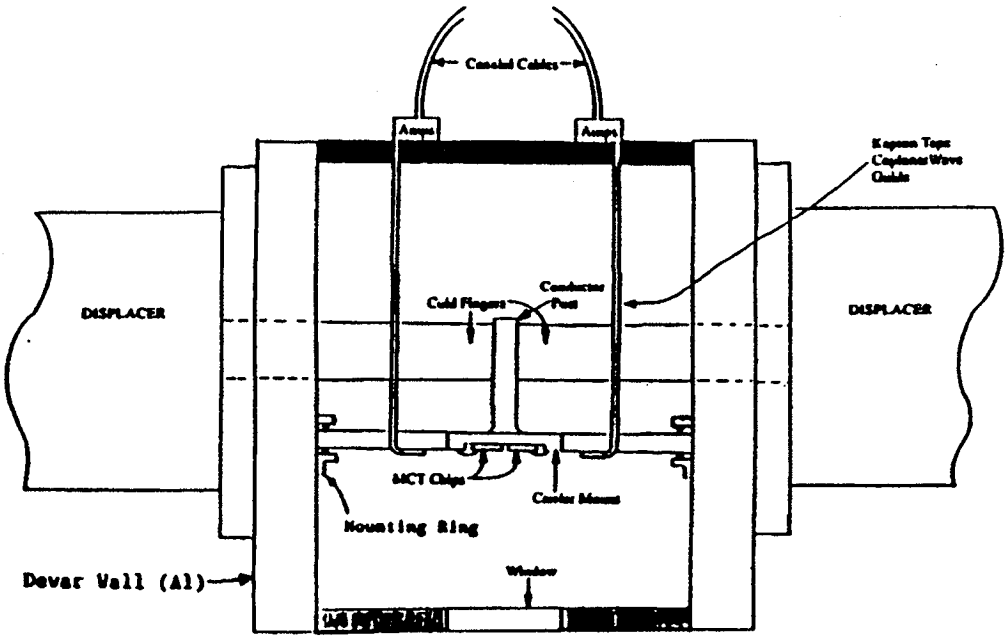

Figure 3.4-17 Dewar Assembly Side View

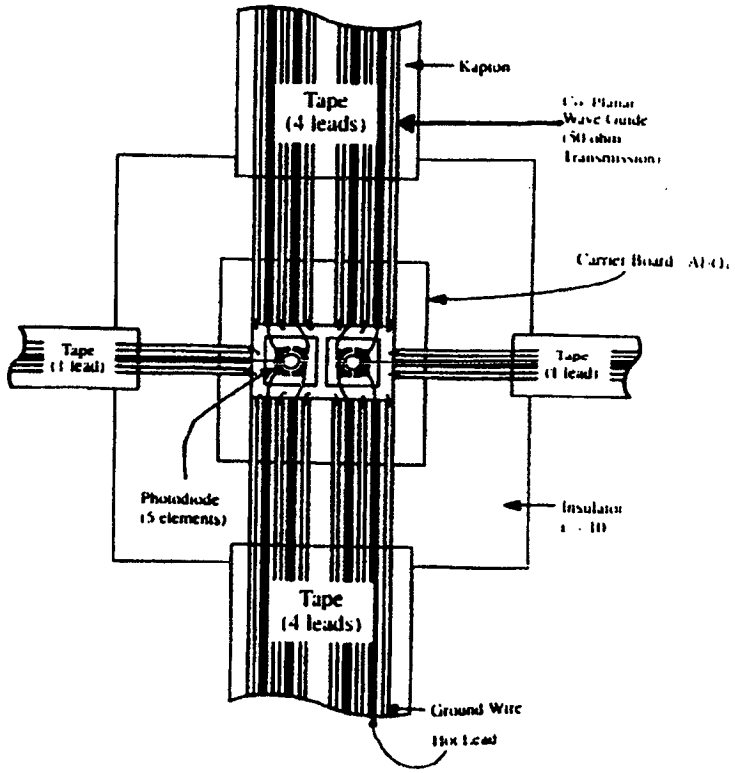

Figure 3.4-18 Detector Mounting Board

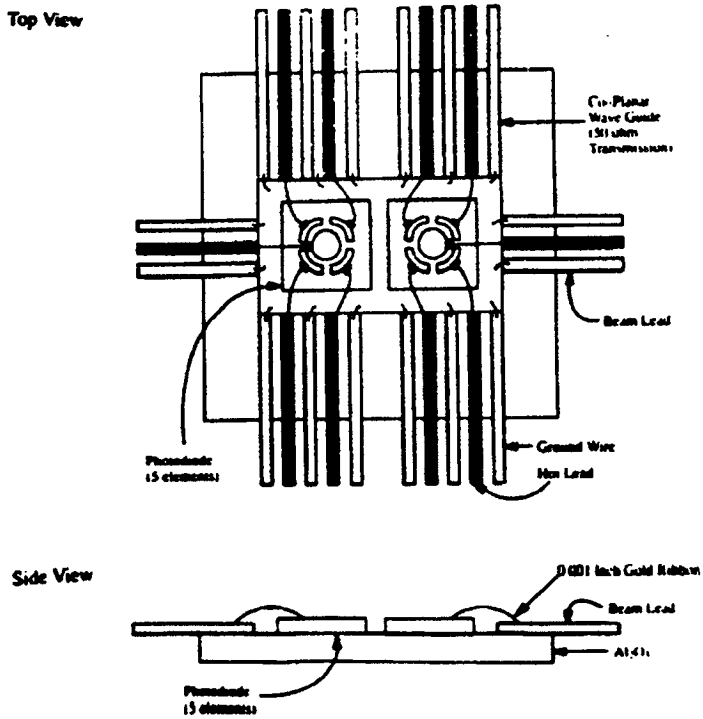

Figure 3.4-19 Detector Carrier Board

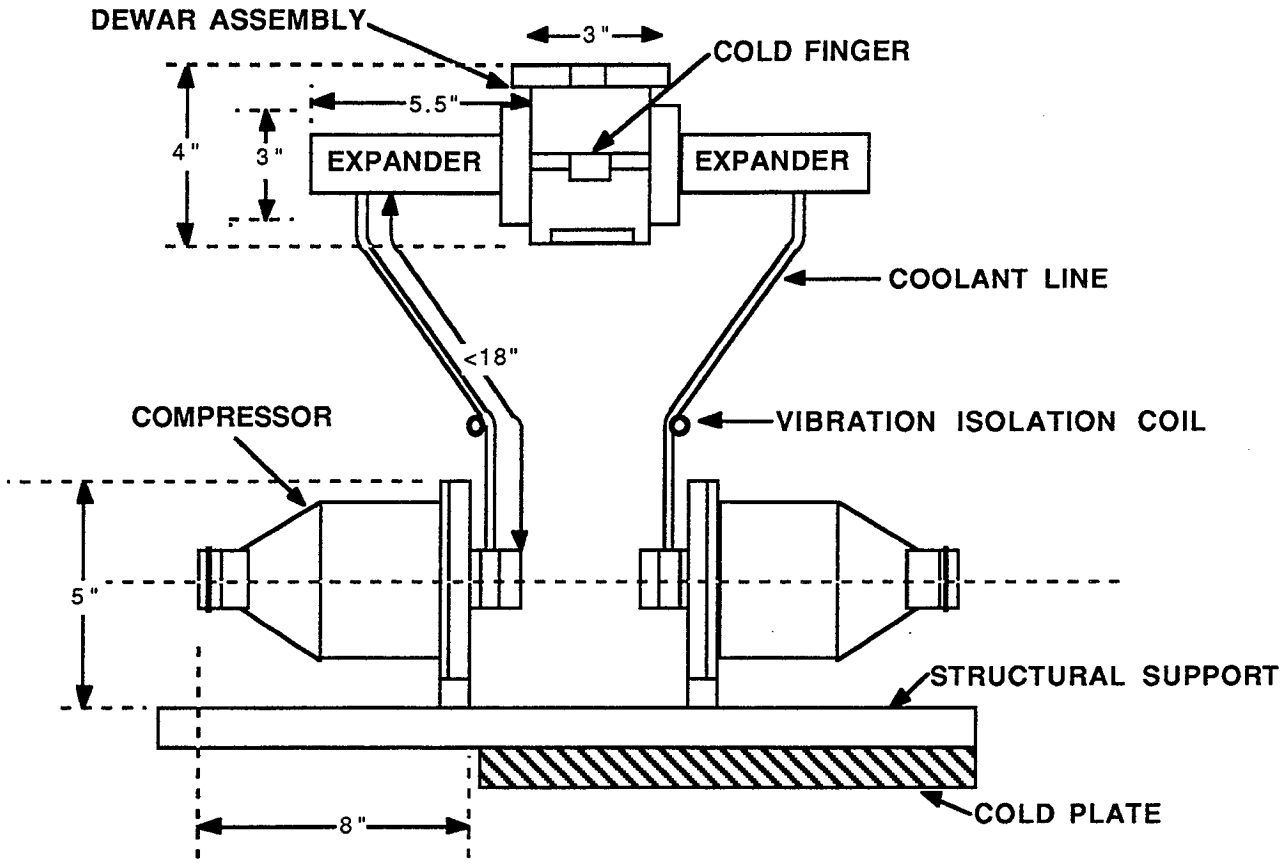

Figure .3.4-20 Detector Cooler Subsystem

- **Detector Heat Load**
  - **LO power = 1-2 mwatts/element (10-30 watts/sqcm)= 5-10 mw total**
  - **Reverse bias = 1 v, 6 mamps/element = 30 mw total**
  - **Total thermal dissipation load < .1 w**
- **Parasitic Heat Loads**
  - **Includes redundant array, wires, mounting structure**
  - **Radiant heating of chip carrier < .08 w**
  - **Radiant heating of support board < .60 w**
  - **Conductive heating via support board < .20 w**
  - **Parasitic Heat Load Due To Redundant Coolers < .30 w**
- **Total parasitic load < 1.18w**

Figure 3.4-21 Cooler Heat Load and Capability

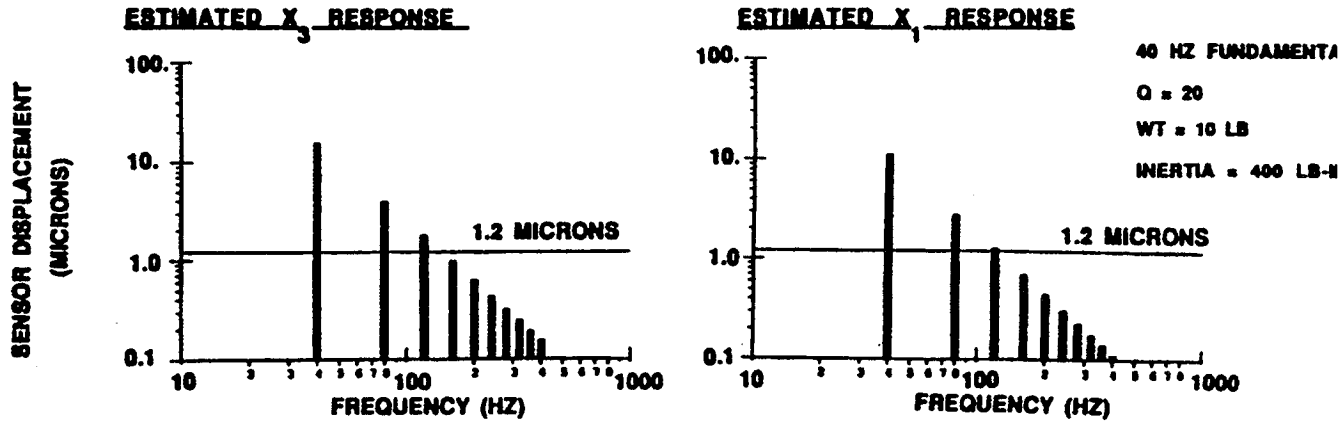

Figure 3.4-22 Cooler Vibrational Analysis

3.4.5.3 Electronics

The electronics consist of the bank of preamplifiers, each connected directly to a detector element, and associated IF electronics. The baseline preamplifier design is a silicon bipolar device. The 5 amplifiers are mounted on the outer dewar wall where the temperature is ambient, approximately 300K.

During Phase I of LAWS our baseline choice for the receiver preamplifier was a GaAs FET operating at about 120 K. The GaAs preamplifier has a noise figure of about 0.5 dB whereas the silicon bipolar noise figure is about 3 dB. The power required for the Split-Sterling cooler needed to cool the 5 amplifiers (the detector has 5 elements, each preamp dissipates about 0.3 W) was about 200 W.

During Phase II we decided that the receiver power requirement was too high. The switch to silicon bipolars which are uncooled (indeed they cannot be cooled below 200 K due to carrier freeze-out), has reduced the power required for the cooler to 80 Watts.

Unlike GaAs, the silicon bipolar can operate over the entire frequency range of DC to 1.2 GHz. Measurements in our laboratory indicate that state-of-the-art HgCdTe detectors can operate with 10-20 W/cm^2 of local oscillator power which is sufficient to achieve a shot noise level about 3 dB above the noise floor of the electronics, including the preamplifiers. Receiver performance has not suffered due to the change of amplifier.

The amplified signal enters from the preamplifier shown at the left of Figure 3.4-23. The dynamic range of the IF electronics is indicated at the input. The first function of the IF electronics is to remove the Doppler shift due to the spacecraft motion and that due to the Earth's rotation. A

synthesized RF source and a 100 MHz yittrium-indium-garnet (YIG)-tuned bandpass filter serve this purpose. The LO mixes the signal down to a central frequency of 100 MHz chosen to provide a sufficient guard band around the 40 MHz-wide signal centered at 100 MHz. The mixer is followed by a second amplifier and a bandpass filter centered at 100 MHz and two more stages of amplification separated by a limiter. The signal is then split into I and Q channels. These signals are passed through a low pass filter before being digitized by the A/D Converter and passed to the Digital Signal Processor. The A/D sampling rate has been set at 75 MHz to cover the entire frequency range of the signal. The present design is for a 10 bit A/D Converter. Figure 3.4-23 also shows the log channel which is split off via a coupler for strong signals from the Earth's surface or from clouds. The useful dynamic range at the input is from -111 dBm to -57 dBm for the I and Q channels, and from -76 dBm to -6 dBm for the log channel as indicated in the figure. The dynamic range at the output of each element is indicated in Table 3.4-6.

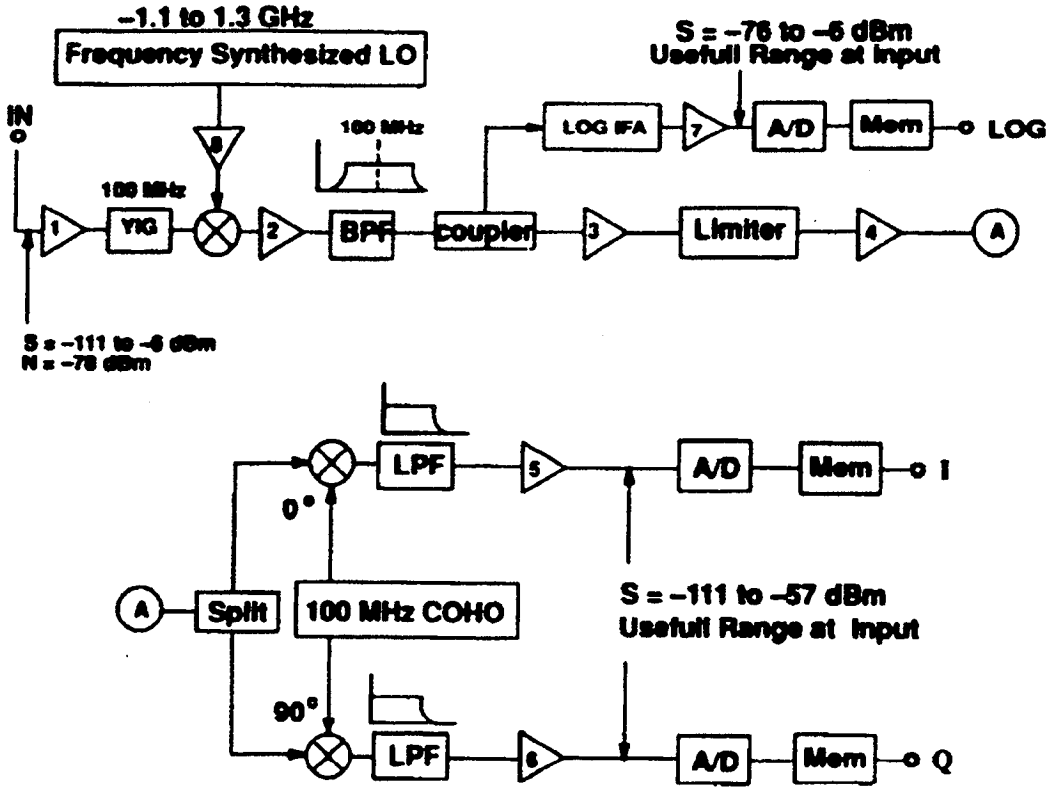

Figure 3.4-23 Receiver Electronics Block Diagram

Table 3.4-6 Dynamic Range at Channel Output

	Amp 1	YIG	Mixer	Amp 2	BP Filter	Amp 3	Amp 4	I/O Mixer
Low Signal (dBm)	-92	-98	-105	-95	-99	-71	-42	-51
High Signal (dBm)	+13	+7	0	+10	+6	+20	+20	+3
Noise BW (dBm)	-59	-78	-85	-75	-79	-51	-22	-31

3.5 Mechanical Subsystem

3.5.1 Requirements and Functional Desription

The Mechanical Subsystem supports the instrument subsystems and provides the necessary thermal and optical fields-of-view. The subsystem is designed to minimize the mechanical disturbances from the Platform/launch vehicle induced upon the LAWS subsystems. The subsystem consists of a planar optical bench kinematically mounted to the EOS Platform.

Preliminary weight estimates of the LAWS subsystems which must be supported by the Mechanical Subsystem are shown in Figure 3.5-1. The weight of the Mechanical Subsystem itself is included in the Figure. The configuration of the LAWS instrument is shown in Figure 3.5-2. The LAWS primary structure provides adequate stiffness to meet the minimum resonant frequency and avoidance zone requirements specified in the Atlas IIAS User's Guide. Stiffness criteria are based on a factor of 1.5x the levels specified for a payload in the Atlas IIAS User's Guide. This factor was used, since the LAWS will be mounted on the Platform, and is not the sole structure in the launch vehicle.

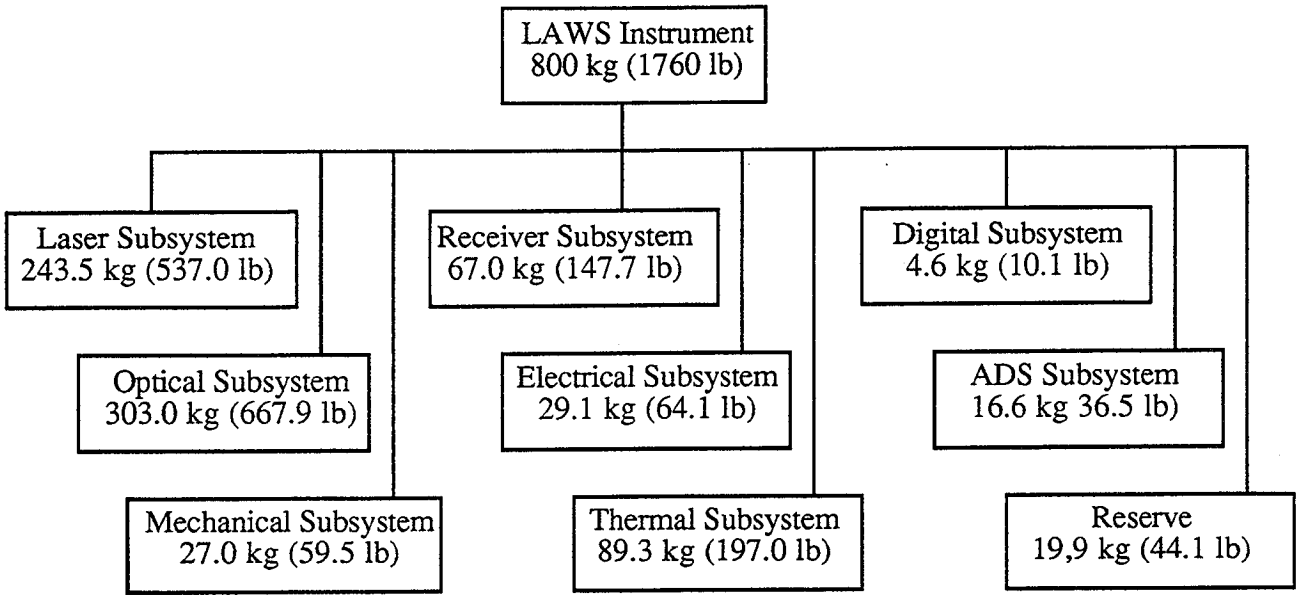

Figure 3.5-1 LAWS Subsystem Weight Estimates

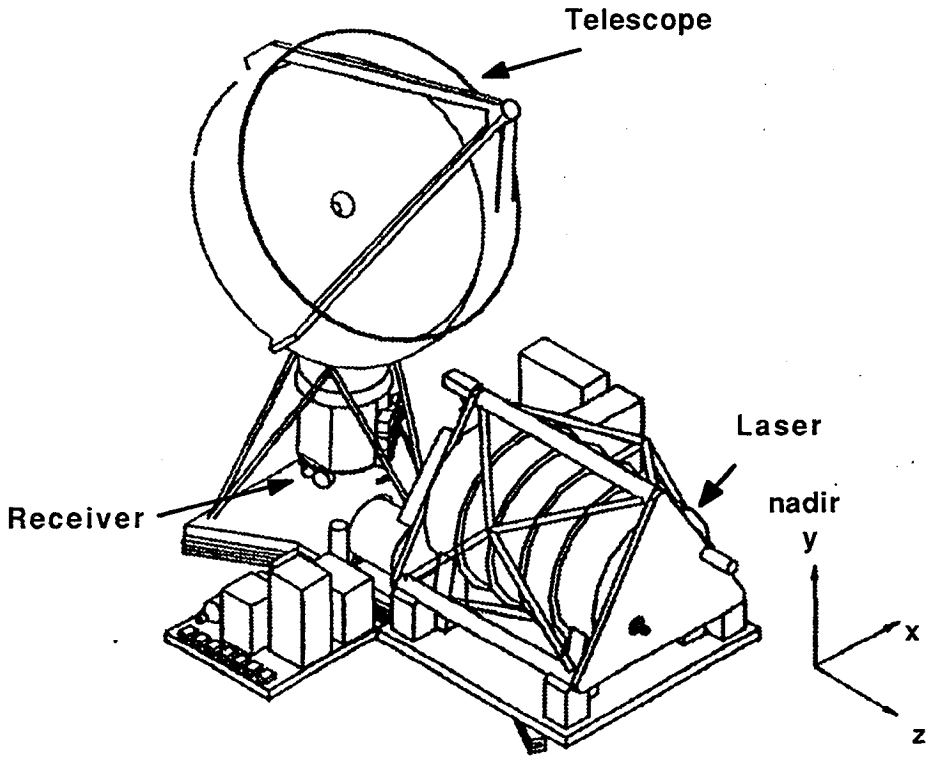

Figure 3.5-2 Preliminary LAWS Configuration

3.5.2 Trades and Analyses

3.5.2.1 Configuration Trade-Off Studies

The hexagonal structure of the spacecraft mounting surface was specified by NASA/MSFC. In our instrument design studies the LAWS instrument was mounted to this platform in two candidate configurations- a side- and an end-mount configuration. The advantages and disadvantages of each configuration were evaluated, and the end-mount configuration selected. The assessment of the two configurations is summarized below.

The structure for the side-mount configuration consists of graphite/epoxy tubes and titanium end fittings. The structure is based on the UARS spacecraft heritage. The end-mount requires a planar optical bench.

Side-Mount Configuration

The side-mount configuration is shown in Figure 3.5-3. The nadir direction is below the instrument, the sun is to the right, and the orbital plane is perpendicular to the plane of the paper. This configuration allows the instrument to be located on the shaded side of the Platform throughout the orbit, resulting in a benign thermal environment. The thermal environment eliminates the requirement for a sun shade or baffle on the telescope optics. This configuration provides locations for mounting radiators, and three radiator panels are included on the far side of the structure. The radiators allow for thermal dissipation from the LAWS electronics boxes with a minimum amount of heat pipes. The laser heat is dissipated using the laser fluid loop with heat exchangers that are interfaced to the Platform coldplates. Although this configuration would permit all of the required radiators to be located on the instrument structure, the 800 kg weight budget allocated to the LAWS instrument would be exceeded.

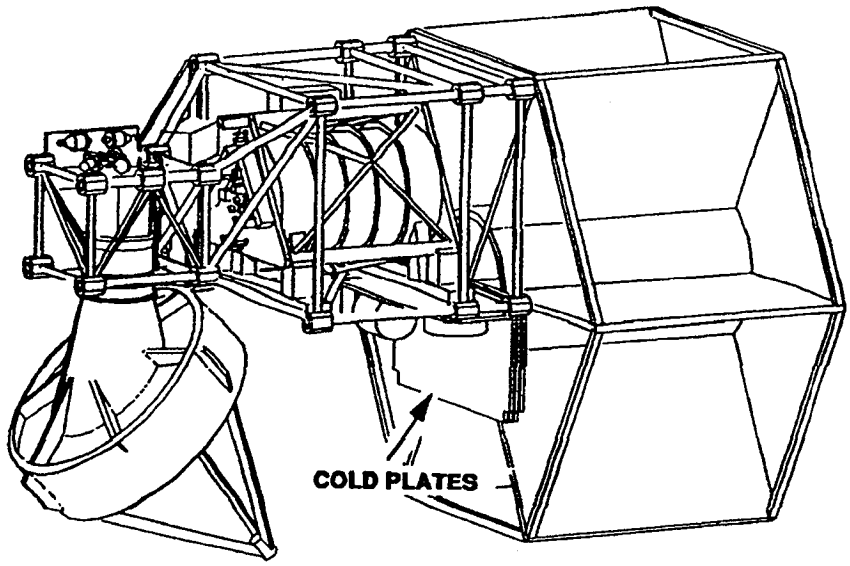

Figure 3.5-3 LAWS Side-Mount Configuration

Some of the disadvantages of the side-mount configuration include: the attitude control system must compensate for gravity-gradient torques with this configuration, and the instrument itself is unbalanced. This imbalance could be minimized by the addition of a separate nadir-facing instrument located below the laser (subject to power availability). However, the field of view of this instrument could be obstructed by the telescope during the telescope rotation.

End-Mount Configuration

The end-mount configuration was selected as the result of the configuration trade-off studies. This configuration is shown in Figure 3.5-4. In this configuration, the LAWS instrument is mounted so that the Platform flies in a gravity-gradient orientation. This orbit is more stable than the side-mount configuration, and less instrument structure is required, resulting in weight savings with the end-mount configuration. The end-mount configuration also is a more balanced configuration of the instrument, and is more easily accommodated in the Atlas IIAS launch vehicle fairing. A disadvantage of the configuration is that the instrument is located in the sun, and is therefore subject to a more severe thermal environment than with the side-mount configuration. Analysis by Hughes Danbury has shown, however, that a baffle or sun shade is not required to

protect the telescope optics. Accommodation of additional nadir-facing instrument may not be possible, since the configuration is more compact than the side-mount configuration.

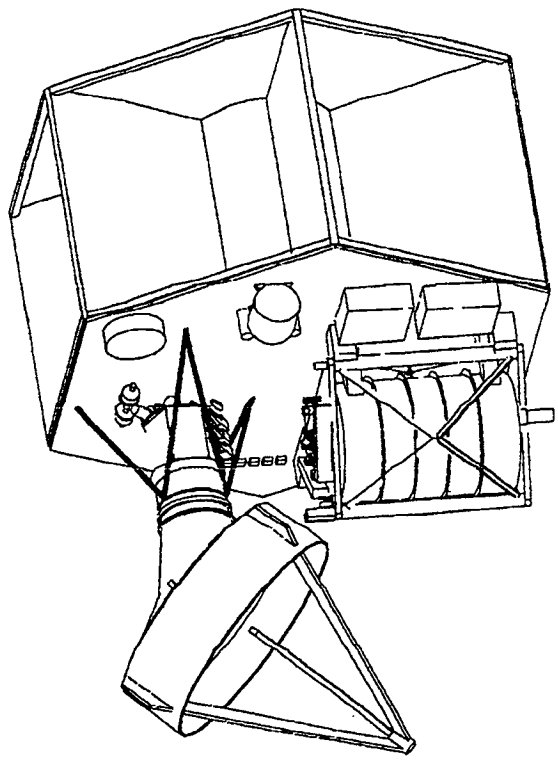

Figure 3.5-4 LAWS End-Mount Configuration

3.5.2.2 Mass Properties Analysis

The LAWS mass properties and center-of-gravity requirements must be compatible with the Atlas IIAS requirements. The mass properties report shall be established and maintained in accordance with Section 5.3.2 of DR-7, System Engineering and Integration Requirements. The result of a preliminary center-of-gravity calculation is presented in Figure 3.5-5. Three CG locations are shown: telescope, laser and LAWS total. The large dot shows the CG location for the total LAWS instrument at x=-0.3, y=31., and z=-6.7 inches (y is measured from the spacecraft station 135.75 in.). The total laser and telescope mass properties were obtained from the NASTRAN analytical models and are represented by the two smaller dots.The LAWS instrument CG includes the telescope, laser and all components but not the (GFE) cold plates. There has been

no attempt to locate all of the auxiliary electronics on the cold plates to position the instrument CG exactly along the launch vehicle thrust axis. This could be done when a more detailed spacecraft platform model became available.

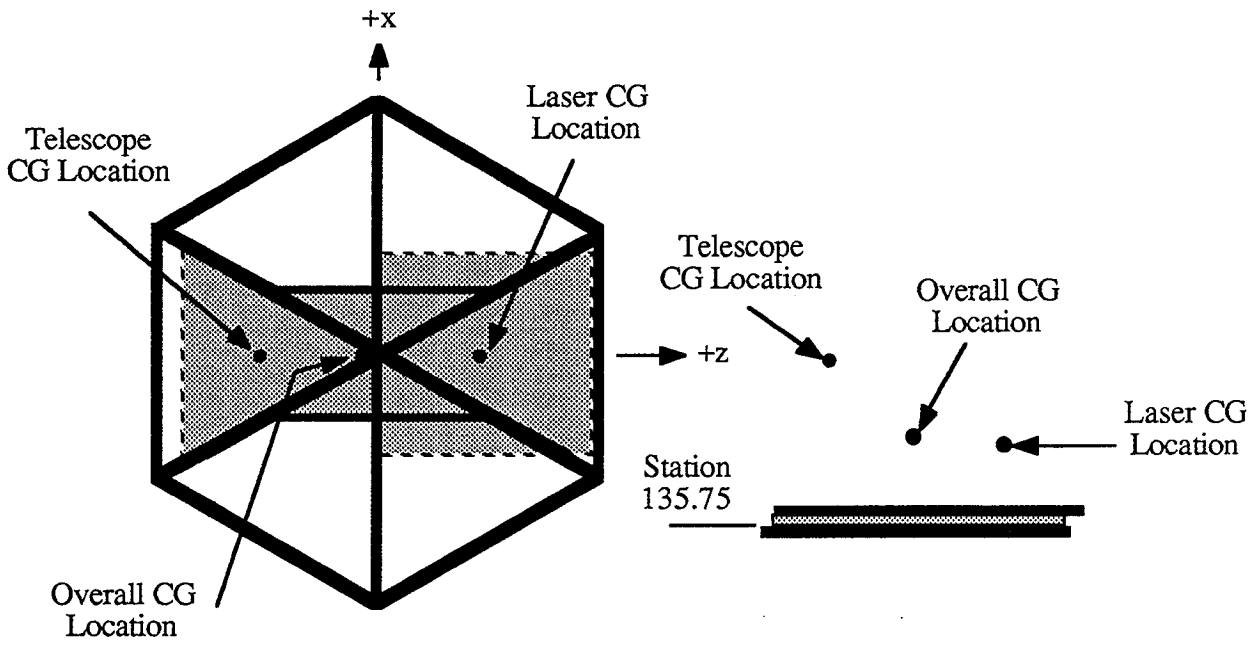

Figure 3.5-5 LAWS Instrument CG Locations

3.5.2.3 Jitter Analysis

A jitter analysis of the LAWS optical bench was performed using the LAWS finite element model (FEM) shown in Figure 3.5-6. Excitations were defined for the telescope rotation and laser operation, and applied to the FEM individually. Rotational responses on the telescope and the laser were well within the 250-μrad dynamic range of the shot-vector sensor. The excitations include the telescope imbalance and the laser excitation.

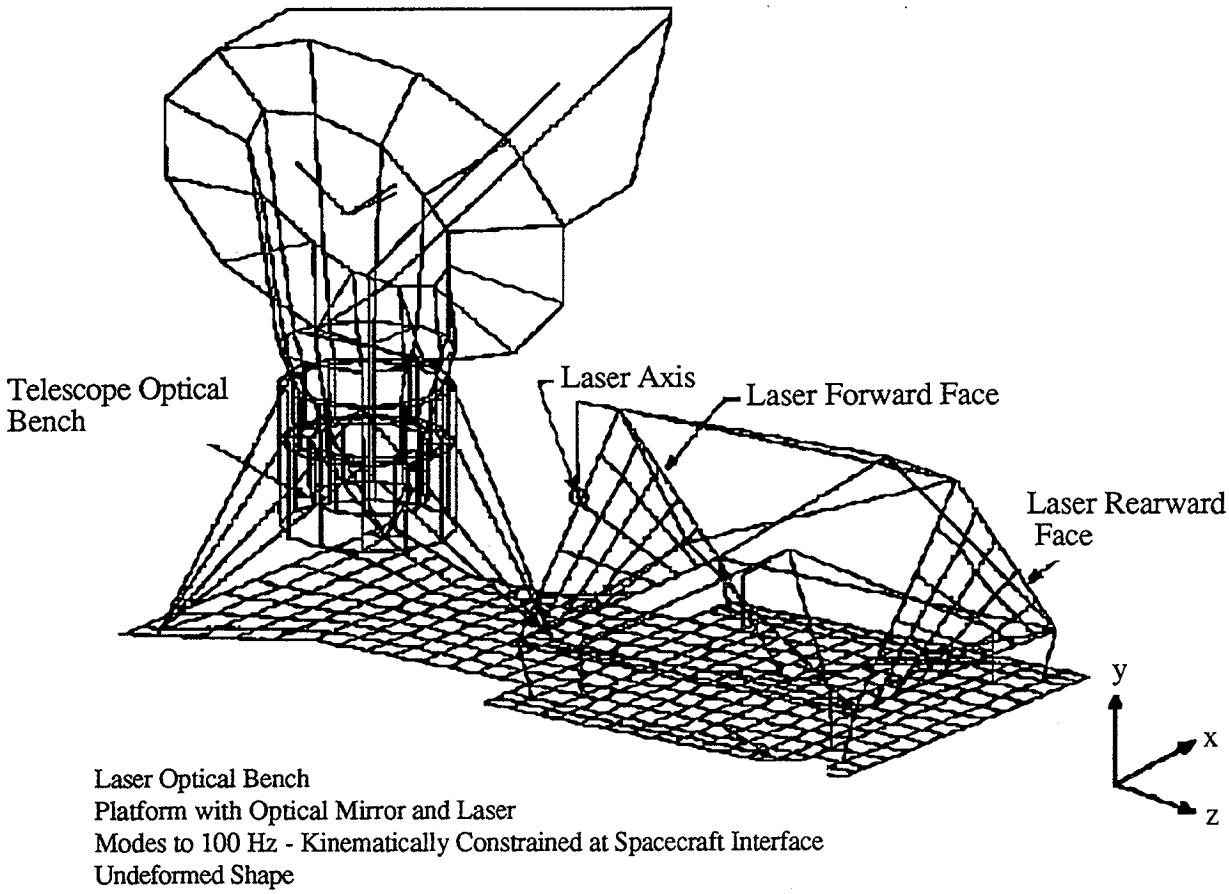

Figure 3.5-6 LAWS Finite Element Model

The telescope excitation is defined as a rotational imbalance which reacts against the non-rotating bearing housing structure. The magnitude of the imbalance is estimated by the ratio of an imbalance of 0.5 ft-lbs for an existing 6000-lb telescope to the weight of the LAWS telescope, 550 lbs.

$$\text{LAWS Imbalance} = (0.5 \text{ ft-lbs}) \times (550 \text{ lbs}/6000 \text{ lbs})$$
$$= 0.55 \text{ in-lbs.}$$

The excitation frequency matches the spin rate of the telescope, 12 RPM. The imbalance torque is applied to the non-rotating telescope housing, about the telescope rotational axis.

Random vibration levels were defined. The peak power spectral density, PSD, occurs within a 0.5 Hz frequency band of the laser's 4 Hz operational frequency (the laser operates at various repetition rates up to about 8 Hz throughout the orbit, 4 Hz was chosen as representative for the purposes of analysis). The random vibration levels are shown in Figure 3.5-7. A peak of 0.03 G^2/Hz (where G is the gravitational acceleration) is specified in the X and Y axes of the coordinate system shown in Figure 3.5-6, and a peak of 0.003 G^2/Hz for the Z axis. A roll-off of 12 dB/octave is assumed.

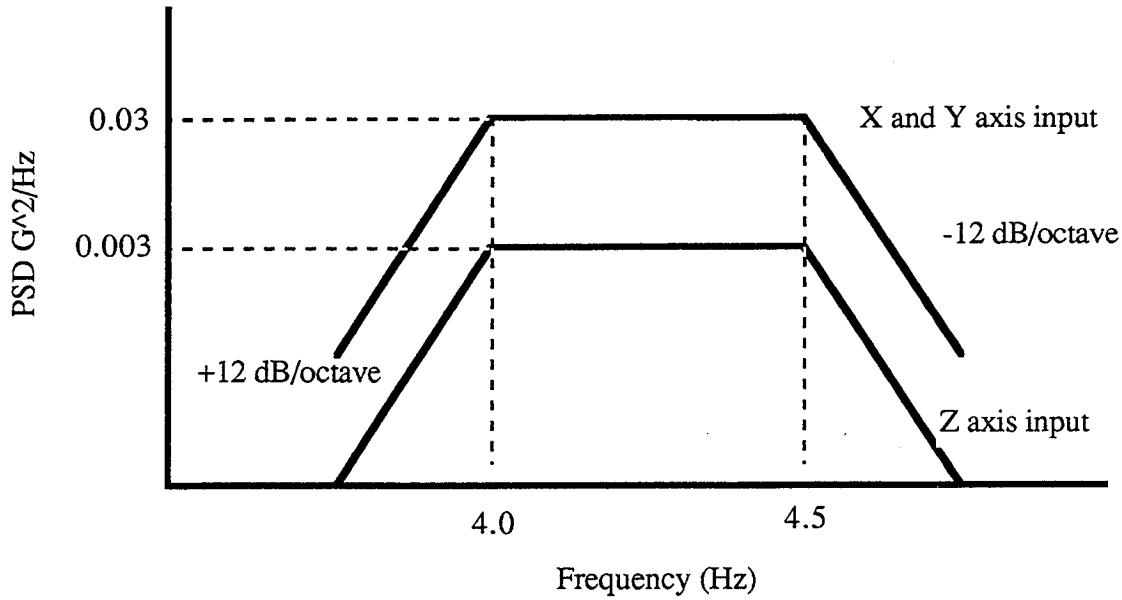

Figure 3.5-7 Laser Random Vibration Levels

The FEM was modified to include a change in the laser isolation stiffness that was originally defined in the STI model. The original model had isolation frequencies ranging from 2.7 to 4.2 Hz. After the change was incorporated, the isolation system was softened to shift the frequencies near 2.5 Hz away from the laser's operational frequency. The FEM was attached to ground, since the Platform bus is presently undefined. The true orbital model, therefore, awaits definition of this interface. The system modes are summarized in Table 3.5-1. A dynamic amplification factor, Q, of 250 is assumed for all modes except those of the damped laser isolation system where a Q factor of 4 is used.

Table 3.5-1 Summary of Orbital Modes

Mode	Frequency	Description
1	0.003	Telescope Rotation
2	2.38	Gain Module on Isolators
3	2.53	Gain Module on Isolators
4	2.69	Gain Module on Isolators
5	14.4	Telescope Lateral - x
6	17.5	Telescope Lateral - z
7	22.6	Gain Module on Isolators
8	23.1	Gain Module on Isolators
9	32.0	Telescope Lateral - z
10	35.0	Telescope & Laser Opposing with Torsion
11	36.8	Gain Module on Isolators
12	39.9	Telescope & Laser Opposing Lateral x with Torsion

Rotational responses were obtained about the X and Y axes. A rotational response about the Z axis will not affect the pointing accuracy of the laser.

Jitter responses due to the telescope imbalance are extremely small due to the relatively small magnitude of excitation. Responses of less than 0.1 micro-radians on both the telescope and the laser, indicate that a telescope imbalance in the range of 0.5 in-lbs. will not induce any pointing inaccuracies.

Peak responses due to the laser excitation are shown in Table 3.5-2. Peak values were obtained by multiplying rms results by three. Responses were calculated for each axis individually. A worst-case assumption of fully-correlated inputs in all three axis was utilized to determine the total imbalance. Therefore, the response due to the combined loading of X, Y and Z axes was obtained by summing the response in each axis. These worst-case peak responses are significantly highter than those from the telescope imbalance but are still well under the allocated 250-μrad budget (determined from the dynamic range of the shot vector sensor).

Table 3.5-2 Peak Responses Due to Laser Excitation

			Response in Micro-Radians			
			Single Input			Combined
Location	Node	Response	X	Y	Z	X, Y, Z
Laser Mirror	10091	θx	34.2	67.5	38.7	140.4
		θy	21.9	67.5	7.5	96.9
Laser Housing Forward Face	10028	θx	19.5	8.1	47.1	74.7
		θy	41.1	1.8	7.8	50.7
Laser Housing Rearward Face	10064	θx	18.3	17.7	44.1	80.1
		θy	51.6	37.2	9.0	97.8
Telescope Optical Bench	6120	θx	33.6	16.5	57.3	107.4
		θy	6.0	0.6	3.6	10.2

3.5.2.4 Dynamics and Stress Analyses

The Jitter Analysis presented in Section 3.5.2.3 is a piece of the dynamics analysis which will be performed in much greater detail in Phase C/D. Minimum resonant frequency requirements will be used to control the dynamic response of the LAWS and components to preclude dynamic interactions with the Atlas IIAS or the LAWS Attitude Determination Subsystem. These minimum resonant frequencies will be specified for the LAWS, component/subsystem mounting, and the deployed solar array. The LAWS primary structure shall be designed for inertia loads independent of any potential stiffening effect provided by subsystem modules or component installations. Modules and components will be treated as mass items only and structural components will be included in analyses of thermally-induced loads. For analyses of subassemblies, such as the equipment panels, a conservative estimate of the component stiffening effects will be included.

Dynamics loads will be determined for all quasi-static, vibroacoustic and transient loads expected in each design environment. The calculation of all dynamic loads shall include the effects of vehicle structural flexibilities and damping, and coupling of structural dynamics with the control

system and the external environment. Iterations of the dynamic load calculations shall be performed as necessary to reflect design changes and/or mathematical model refinements. The final set of dynamic loads will be determined with the use of experimental values of dynamic characteristics as obtained from appropriate tests and modal surveys.

A preliminary stress analysis was performed on the LAWS optical bench. The planar bench consists of aluminum honeycomb with graphite/epoxy facesheets stiffened with aluminum "C" channels. The LAWS telescope and laser are mounted to this structure. The bench is mounted quasi-kinematically in its plane by using one 3-axis, two 2-axis and five 1-axis mounts (8 total support points). The LAWS structure is shown in Figure 3.5-2. Figure 3.5-8 and Table 3.5-3 show the details of the platform construction and materials.

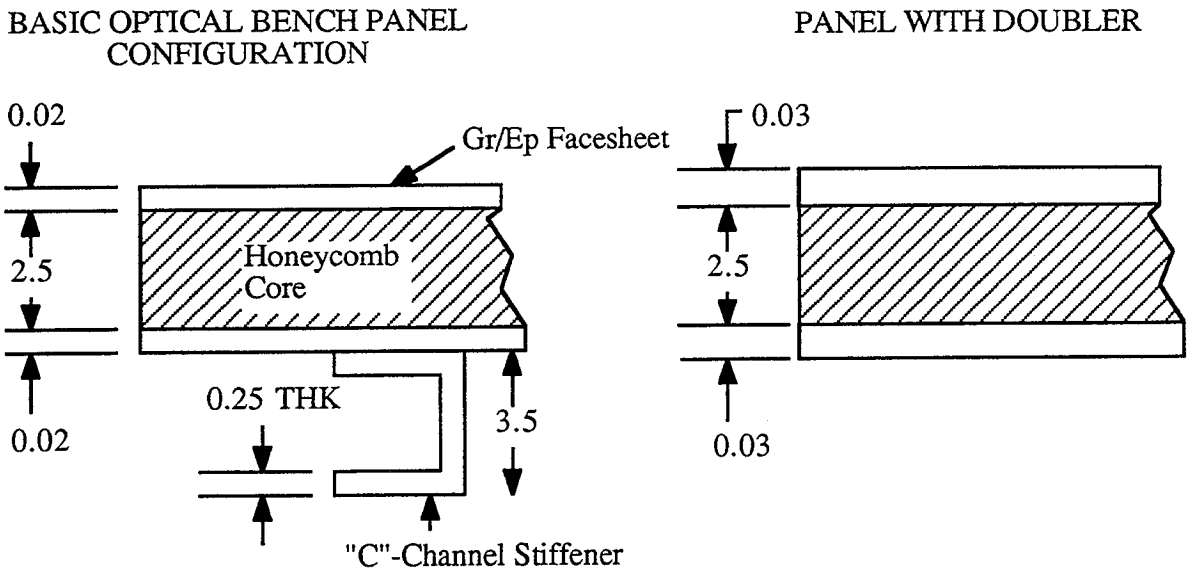

Figure 3.5-8 LAWS Optical Bench Panel Configuration

Table 3.5-3 LAWS Optical Bench Material Properties

Component/Material	E (Msi)	G (Msi)	μ	Density (lb/in^3)	Ftu (Ksi)	Fcu (Ksi)	Fsu (Ksi)
Facesheets: T50/Epoxy Quasi-Isotropic Laminate	10.0	3.85	0.3	0.10	60.0	35.0	26.0
C-Channel Stiffeners Aluminum 6061-T6	10.0	3.85	0.3	0.058	42.0	42.0	35.0

Honeycomb Material	Density (lb/ft^3)	Cell (in)	Gage (in)	G (Ksi)	Fsu (Psi)	Ec (ksi)
Baseline Core 5052 Aluminum	2.3	0.25	0.0010	15.0	62.0	58.0
Dense Core 5052 Aluminum	3.4	0.25	0.0015	22.0	130.0	115.0
Dense Core 5052 Aluminum	5.7	0.1875	0.0020	36.0	280.0	270.0

The structure was analyzed using the quasi-static loads appropriate to the launch environment of the ATLAS IIAS launch vehicle. These values are given in Table 3.5-4. Design factors of safety used in the stress analysis are 1.25 for yield and 1.40 for ultimate.

Table 3.5-4 Quasi-Static Design Load Factors

Launch Event	S/C Axial (G) (LAWS FEM Y Axis)	S/C Lateral (G) (LAWS FEM X & Z axes)
BECO	-11.4	±1.0
MECO	+4.0	±1.0
BECO/BPJ	-7.0	±4.0

To achieve positive margins of safety several local modifications to the basic bench design are required as follows: Dense core is required in the sandwich panel around the 3-axis and 2-axis mounts as well as at the locations where the telescope tripod and the fluid pump are mounted. Edge inserts embedded in the sandwich panel are also required at the 1-axis and 2-axis mount

locations to handle the high local transverse shear loads imparted to the panel. Also, facesheet doublers are required at the 3-axis location. Figure 3.5-9 shows these locations.

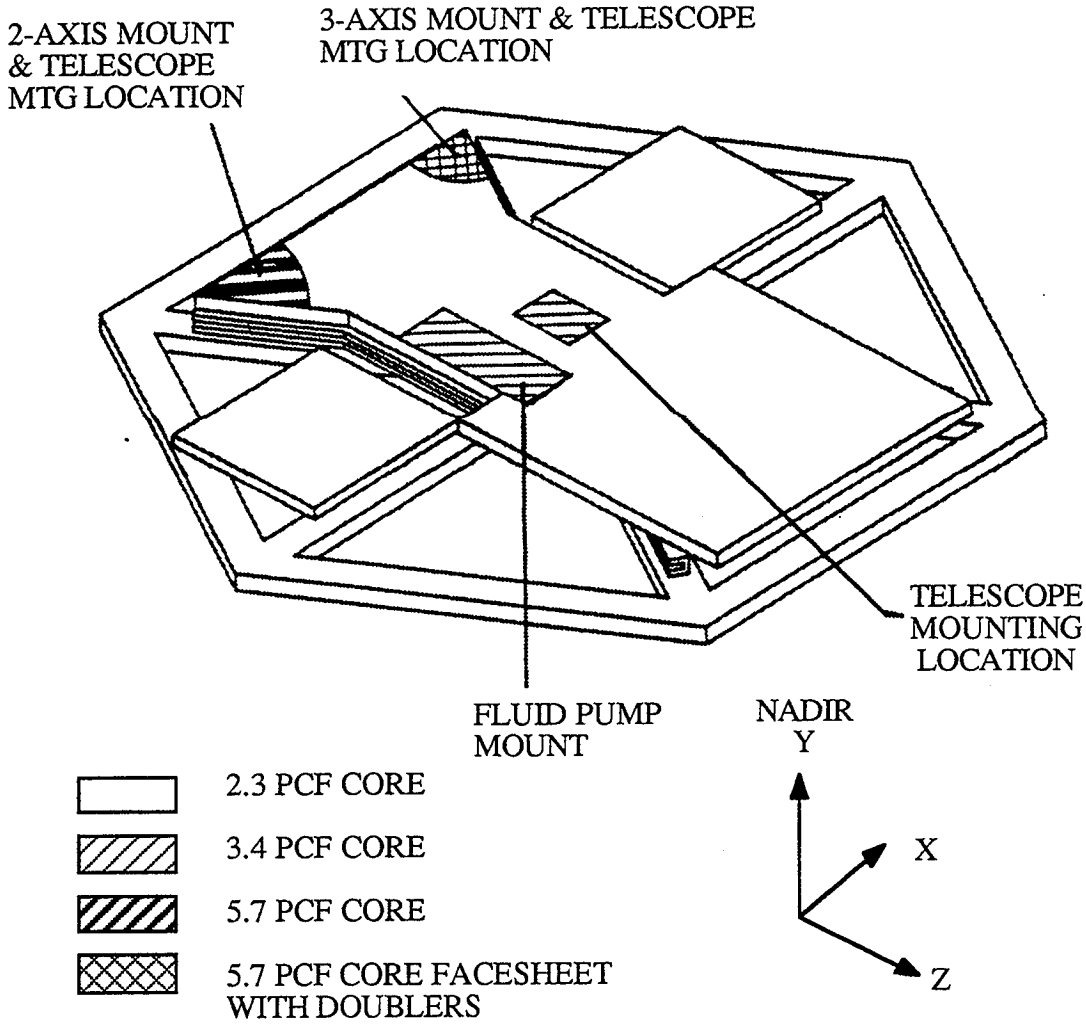

Figure 3.5-9 Location of Required Dense Core and Doublers on LAWS Bench

Positive margins of safety were calculated for all parts of the structure for all failure modes. Table 3.5-5 summarizes the minimum margins of safety for all the failure modes considered. Worst case enveloped loads are recovered for the kinematic mounts and listed in Table 3.5-6.

Table 3.5-5 Minimum Margins of Safety - LAWS Optical Bench

Location	Failure Mode	Margin of Safety
Honeycomb Sandwich Panel	Dimpling Failure (Ultimate)	0.008
	Transverse Shear of Core (Ultimate)	0.043
	Facesheet Failure (Ultimate)	0.041
	Wrinkling Failure (Ultimate)	0.05
	Shear Crimping Failure (Ultimate)	0.185
"C" Channel Stiffeners	Combined Tension and Bending	
	(Yield)	3.05
	(Ultimate)	3.34

Table 3.5-6 Maximum Enveloped Kinematic Mount Limit Loads for LAWS Bench

Kinematic Mount	Axial Load (lbs)	Lateral Load (lbs)
3-axis mount	1373 Tension	3213
	2109 Comp.	
2-axis mount	1242 Tension	1650
(-x, -z)	2029 Comp.	
2-axis mount	301 Tension	1411
(+x, +z)	271 Comp.	
1-axis mounts	3437 Tension	---
	2796 Comp.	

3.5.3 Preliminary Design

The detailed LAWS instrument mechanical drawings are provided in Appendix A.

3.6 Thermal Subsystem

3.6.1 Functional Description

The Thermal Subsystem consists of: a laser fluid loop for temperature-controlled removal of the Laser Assembly dissipated heat, and a passive thermal design for thermally coupling all of the other components to the spacecraft cold plates. The functions of these components are described below.

The laser fluid loop has been sized for a Laser 5 Hz average repetition rate. The primary loop components are shown schematically in Figure 3.6-1. A liquid/gas heat exchanger within the laser transfers the laser heat from its circulating gas to the circulating water loop. The heat generated from the other Laser components are transferred to the water via integral exchanger surfaces. A redundant pump ensures against a single-point failure. Electrical heaters maintain the water temperature above freezing during long non-operational periods.

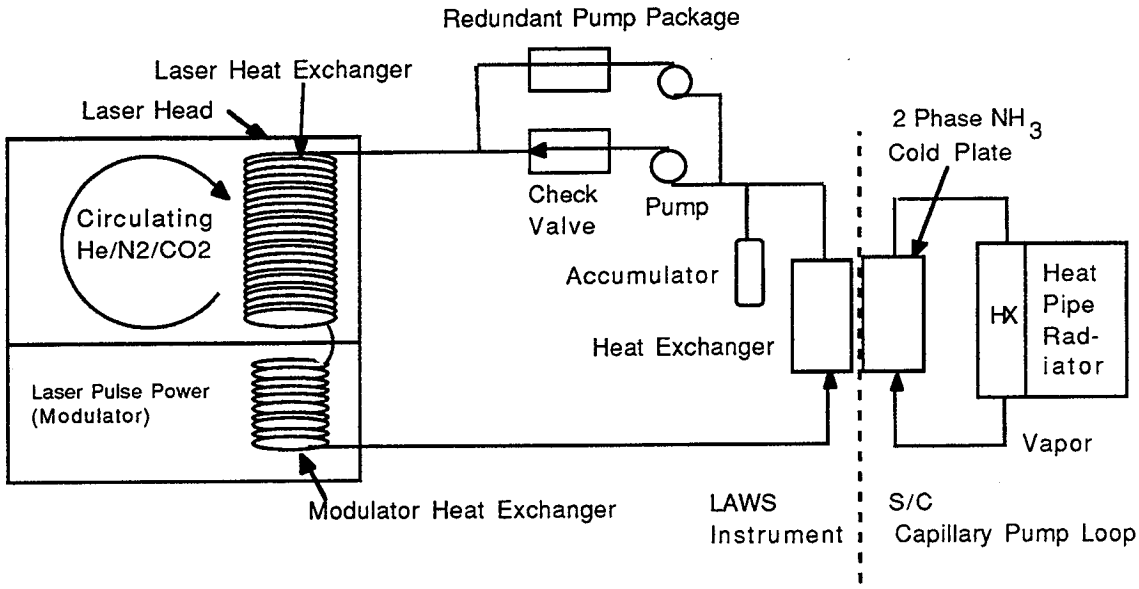

Figure 3.6-1 Laser Fluid Loop Components

All other thermally-dissipating and temperature-sensitive components are located and mounted so as to provide conductive or heat pipe coupling to the spacecraft coldplates. Figure 3.6-2 indicates the design locations of the component assemblies and the spacecraft coldplates. Fixed conductance heat pipes are used to transport heat from critical components to adjacent coldplates. Multi-layer insulation and thermo-optical coatings attenuate orbital thermal environment effects. The LAWS thermal design employs high-thermal resistance at each mechanical mounting interface to the spacecraft structure by use of low-thermal conductivity materials and the control of mounting contact area. This design minimizes the temperature gradients within the LAWS system.

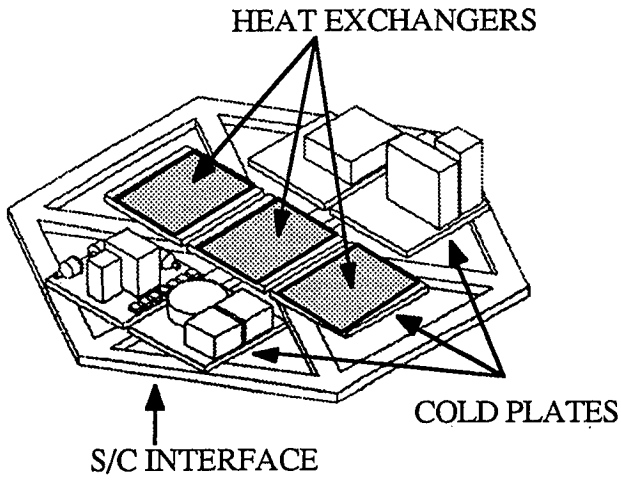

Figure 3.6-2 Spacecraft Cold Plate Locations

The thermal requirements for the laser coolant loop and the components requiring passive thermal control are summarized in the following sections.

Laser Coolant Loop

The laser coolant loop has been sized for the removal of the heat from the cw laser, the IO/LO laser, and the laser gas based on operation at a nominal 5-Hz orbit average rate. The 5-Hz operational rate was chosen after the analyses and trades described in section 3.6-2 and after considering the amount of time the laser needs to operate at a rate higher than nominal, for example in the Tropics.

The coolant loop capability to accommodate other laser operational repetition rates is shown in Figure 3.6.3, as laser gas temperature at the exchanger exit. Water was selected as the loop coolant due to its high thermal capacity and its favorable fluid properties. The design pump flow rate is 1227 lb/hr. This flow rate is based on a maximum 2.5 K fluid temperature rise which analysis has shown is required to maintain a laser gas density uniformity of 0.1% for high laser beam quality. This design, for example, allows 5 minutes operation at 10 Hz. The design coolant temperature at the laser gas/liquid heat exchanger inlet is 297 K. The design incorporates a redundant pump to ensure against a single point failure. Electrical heaters are used to maintain the coolant temperature above freezing during long non-operational periods.

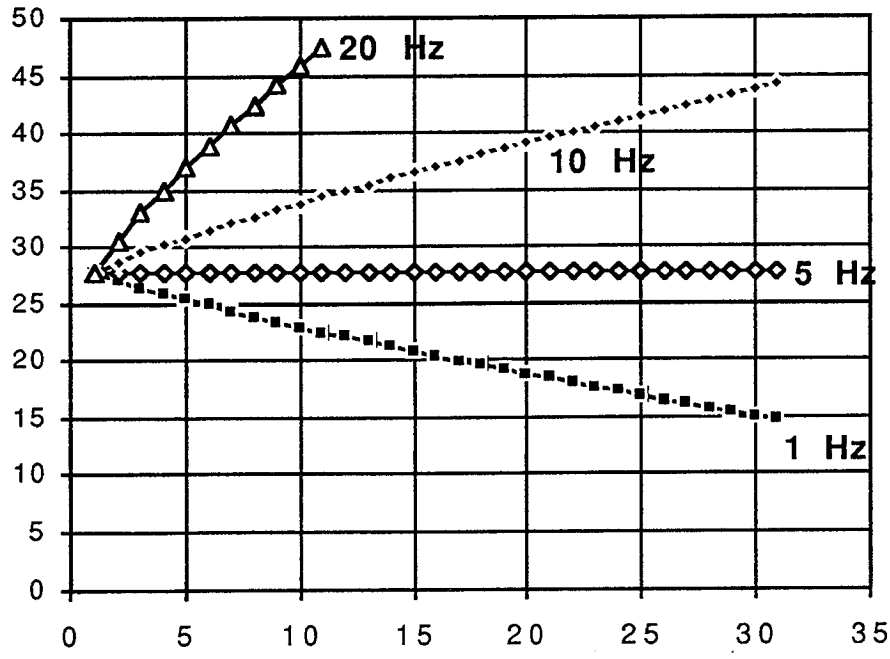

Figure 3.6-3 Laser Cooling Loop Capabilities

Passive Thermal Control

The remaining subsystem electronic, optical and mechanical components which dissipate heat or require temperature control are mounted to heat exchanger panels. These panels are in turn mounted to mating spacecraft coldplates for removal of the heat. Two fixed-conductance heat pipes are used to transport the thermal dissipation from the laser receiver cyrocooler compressors and expanders to the adjacent mounting panel/coldplate.

3.6.2 Trades and Analyses

An analytical thermal model was constructed to simulate the Laser Coolant Loop and its relation to the Laser Assembly. Preliminary trade-off studies were completed for candidate coolant fluids, pump flow rates, pump power, laser operational levels, heat exchanger temperature and pressure drops and component temperatures. The primary components and some of the characteristics that were assumed for use in the analytical model are shown in Figure 3.6-4. Water was selected as the coolant, based on these trade-off studies.

A parametric trade-off was made of laser repetition rate and coolant loop requirements. The results of this trade-off study are summarized in Figure 3.6-5. The predicted performance for the

selected 5-Hz Laser-repetition-rate design is also shown in Figure 3.6-5. The estimated Thermal Subsystem weights are given in Table 3.6-1.

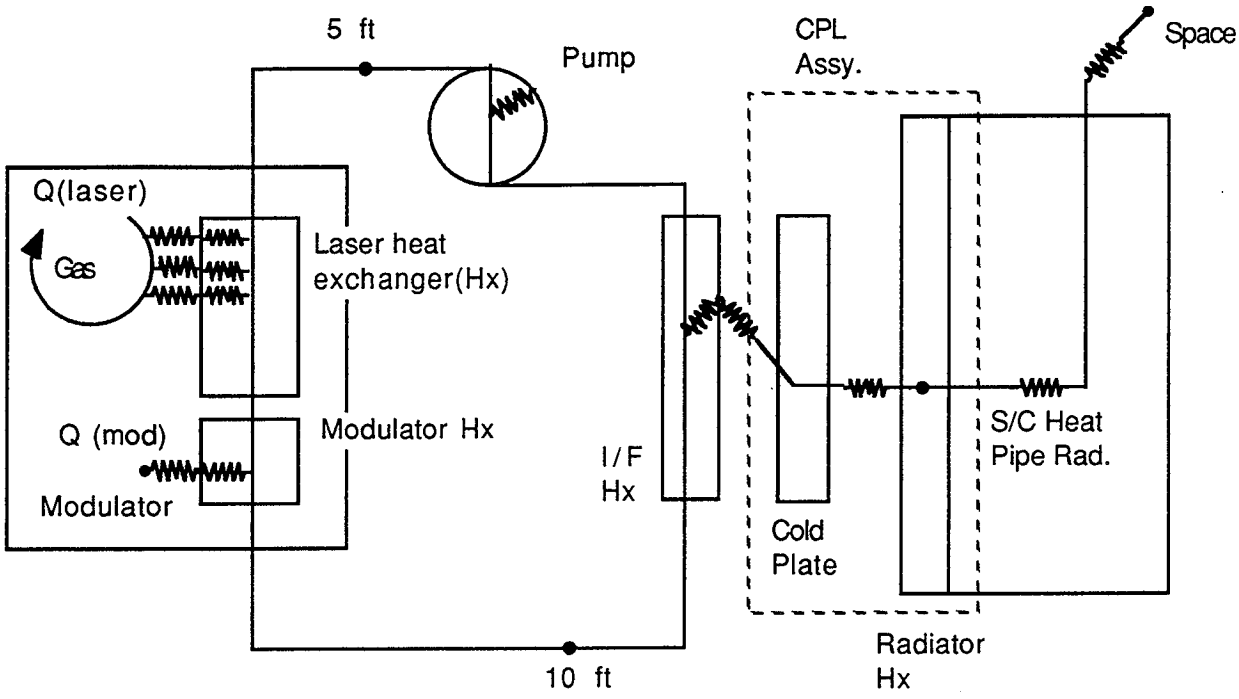

Figure 3.6-4 Laser Fluid Loop Analysis Model Description

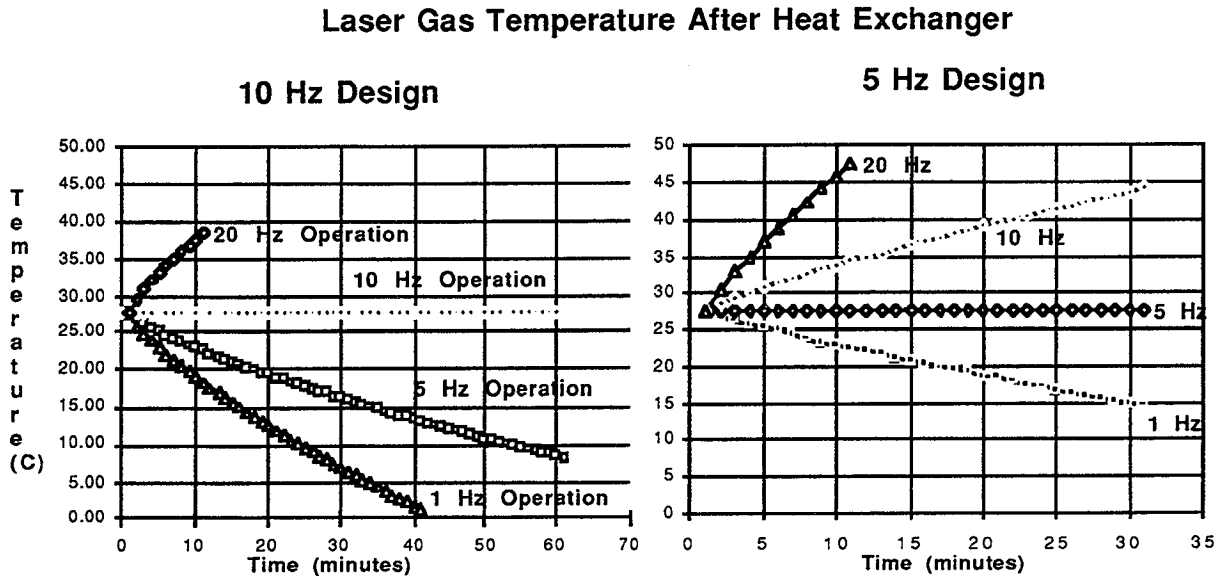

Figure 3.6-5 Results of Laser Cooling Loop Parametric Trades

Table 3.6-1 Thermal Subsystem Weights

	Mass	
	(lbs)	(kg)
Redundant Pump Package	35	15.9
Fluid Q/D Valves (10 Total)	22	10.0
Fluid Lines	16	7.3
S/C I/F Heat Exchanger	30	13.6
Panel Radiators*	62	28.1
Heat Pipes for Receiver	10	4.5
MLI Blankets (inc. Laser)	45	20.4
Heater Controller Assembly	12	5.4
TOTAL	232	105.2

*Side-Mount Configuration

Detailed thermal analyses of the laser fluid loop and the passive thermal design for the remaining Thermal Subsystem components will be conducted upon further definition of the spacecraft thermal interface in Phase C/D. The thermal design of the laser fluid loop and the passive thermal control of the component panel/coldplate were selected to minimize thermal coupling with the spacecraft, except through their heat exchanger and coldplate interfaces. The proposed design uses high thermal resistance materials and minimum contact areas at each of the mechanical spacecraft support points of the Thermal Subsystem. Heat flow across these interfaces will effect parasitic heat loads upon either the coolant loop or the component mounting thermal panels.

The design will employ high-performance multi-layer insulation (MLI) thermal blankets and thermo-optical coatings to attenuate the effects of the orbital thermal environment upon exposed subsystem surfaces. The orbital temperature response of the spacecraft mounting interfaces and further definition of the spacecraft orbital thermal environment are required to refine the current LAWS thermal model and to conduct more detailed LAWS System and Thermal Subsystem Analyses.

3.6.3 *Preliminary Design*

The LAWS thermal design concept utilizes mechanical and thermal mounting to five spacecraft coldplates. An exploded isometric view of this instrument/Platform interfaces is shown in Figure 3.6-6. The preliminary component layout and relative panel locations are based on a maximum local thermal flux of 1 W/in^2. The thermal design utilizes a fluid loop to dissipate the heat generated from the laser gas through a gas/liquid heat exchanger. The loop then transports this energy to a liquid heat exchanger mounted to a Platform coldplate interface. Water has been selected as the loop coolant. Electrical heaters will be employed to prevent the water from freezing during prolonged periods when the laser is not operational. The pump configuration selected is that of the current Shuttle water pump package. Thermal subsystem design includes control of bypass valves and expansion volume, and incorporates a redundant pump. The design coolant circulation rate is 1227 lb/hr, and the input power requirement is 200 W.

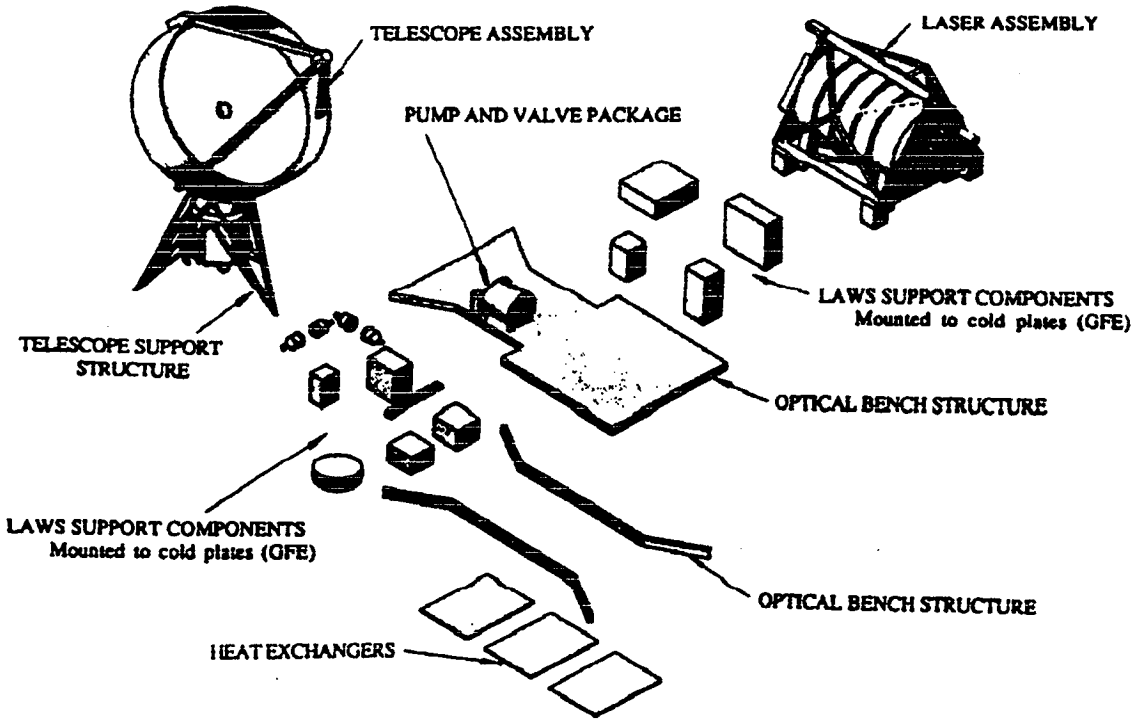

Figure 3.6-6 LAWS Exploded View

Fixed-conductance heat pipes will be required to transport heat from the cryocooler compressors and displacers to the adjacent mount panel/coldplate. Multi-layer insulation blankets and thermo-optical coatings will be required for thermal control of LAWS external surfaces.

The LAWS thermal design accounts for a high thermal resistance at each mechanical mounting interface between the LAWS and the Platform (except at the coldplates). The LAWS panel and structure design utilizes low TCE, high thermal conductivity materials to minimize temperature gradients and thermal distortion effects.

The component mounting panel layout is based only on satisfying a 1 W/in^2 maximum local thermal flux at the interface with the Platform coldplate. Refined panel/component layouts will be generated once the Platform thermal interface and LAWS orbital thermal environment are further defined.

3.7 Electrical Subsystem

3.7.1 Requirements and Functional Description

The Electrical Subsystem provides the required power to the LAWS subsystems. The power requirements for LAWS consist of a fixed or overhead power plus an amount which varies depending on the laser repetition rate. Power requirements are shown in Table 3.7-1 for two example modes of operation of the instrument. The actual mode of operation (i.e. the repetition rate of the laser) will vary up to a peak of 20 Hz as LAWS progresses around its orbit. For the 2 examples shown, the Survey Mode operating at a nominal rate of 5 Hz provides approximately 6 shots per 100 km x 100 km grid square at the ground while the High Rep Rate Mode operates at 10 Hz for placing a higher density of shots in regions of interest. Note that the length of time for which the High Rep Rate Mode can be used is limited by the thermal subsystem as discussed above.

Table 3.7-1 LAWS Electrical Power Requirements

	Survey Mode		High Rep Rate Mode	
Subsystem	Avg. Power (5 Hz) (W)	Peak Power (7.5 Hz) (W)	Avg. Power (10 Hz) (W)	Peak Power (15 Hz) (W)
Optics	127	127	127	127
Laser	1340	1985	2630	3920
Receiver	140	140	140	140
Electrical	80	80	80	80
Digital	22	22	22	22
ADS	23	23	23	23
Thermal	200	200	200	200
Reserve (15%)	290	387	483	677
TOTAL	2222	2964	3705	5189

Power turn-on of LAWS is initiated by the BDU sending an enable signal to the BSR which feeds the Power Conditioner. This provides logic power to the LAWS Controller/Processor to enable a controlled start-up of the instrument. The Laser Power Supply contains on on/off control input and will not be turned on until the other (lower-power) subsystems have completed their confidence routines.

A redundant feed configuration is used for the feed from the BSR to the Power Conditioner, to meet the subsystem reliability requirements. All of the survival power for the LAWS instrument is provided to the Power Conditioner and distributed to the heaters required for thermal control of each subsystem.

The Electrical Subsystem provides the distribution, control and conversion of Platform power to all of the LAWS instrument subsystems. The subsystem consists of the System Power Conditioner and harnesses. The Electrical Subsystem operates upon receipt of input power as specified in the GIIS, and provides filtering for the suppression of transients and load reflections.

The Electrical Subsystem Block Diagram is shown in Figure 3.7-1. The 120 VDC power is provided from the Platform BSRs to the Laser Power Supply and to the System Power Conditioner, which distributes power to the subsystems. It is assumed that the BSRs are provided as GFE from the EOS Program. Redundant busses are provided from the BSRs to the power conditioner, to ensure system reliability.

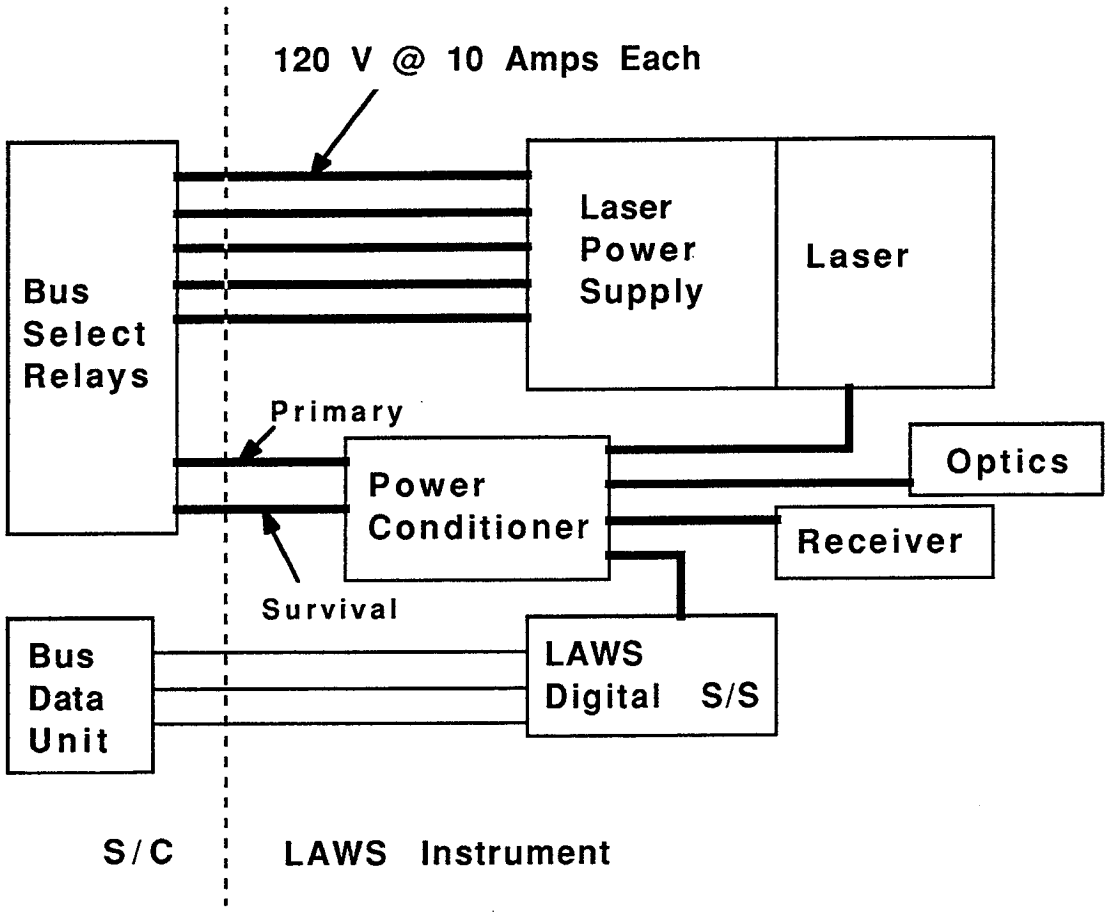

Figure 3.7-1 Electrical Subsystem Block Diagram

3.7.2 Trades and Analyses

The LAWS power requirements were assessed for various mission modes. The laser firing rate varies according to the ground-track position in the orbit. The LAWS power requirements, therefore, vary greatly on an orbital basis. The laser shot rate is expected to be low, with a value approaching zero for ground track positions in the Polar regions and at a maximum in the Tropics, as the ground track position reaches areas of more limited overlap in the equatorial regions. The overall orbit average shot rate depends on the average power available.

As well as varying on a orbital basis the shot rate also may vary with the position of the telescope. For example, using a 1/cos algorithm (based on scan azimuth angle) results in fewer shots being placed at the extremes of the scan where successive scans overlap closely.

The overhead instrument power, i.e. power for everything but the laser, is estimated at <1kW (orbital average). The additional laser power requirements range from nearly zero to 5 kW. The instantaneous power for the LAWS instrument, therefore, is 6 kW, based on these values.

The instantaneous power requirements are driven by the maximum laser pulse repetition rate capability of 20 Hz, with 50 ms between laser pulses.

The system power supply is capable of sustaining a 10 Hz pulse repetition rate of the laser. Survival power is fed to the Power Conditioner from a separate redundant BSR and distributed to subsystem heaters to maintain equipment at temperatures above their survival temperature ranges. The survival (heater) power is provided from the input side of the BSR.

Power will be provided to the LAWS instrument via the EOS Program-provided Portable Platform Simulator (PPS) during ground testing, in accordance with the GIIS. The PPS must be modified to provide the power in excess of the 1200 W capability. A 6 kW maximum power requirement would have to be available for LAWS testing.

An example power profile for one orbit is shown in Figure 3.7-2. Present estimates of the LAWS instrument power are based on the base level of <1kW, to which the laser power profile at the programmed firing rate is added. The maximum instantaneous laser power occurs at 15 Hz, and is estimated to be approximately 5 kW. The power for the laser varies with shot rate from the 5.720 kW at 20 Hz to 287.5W (including contingency) at 1 Hz.

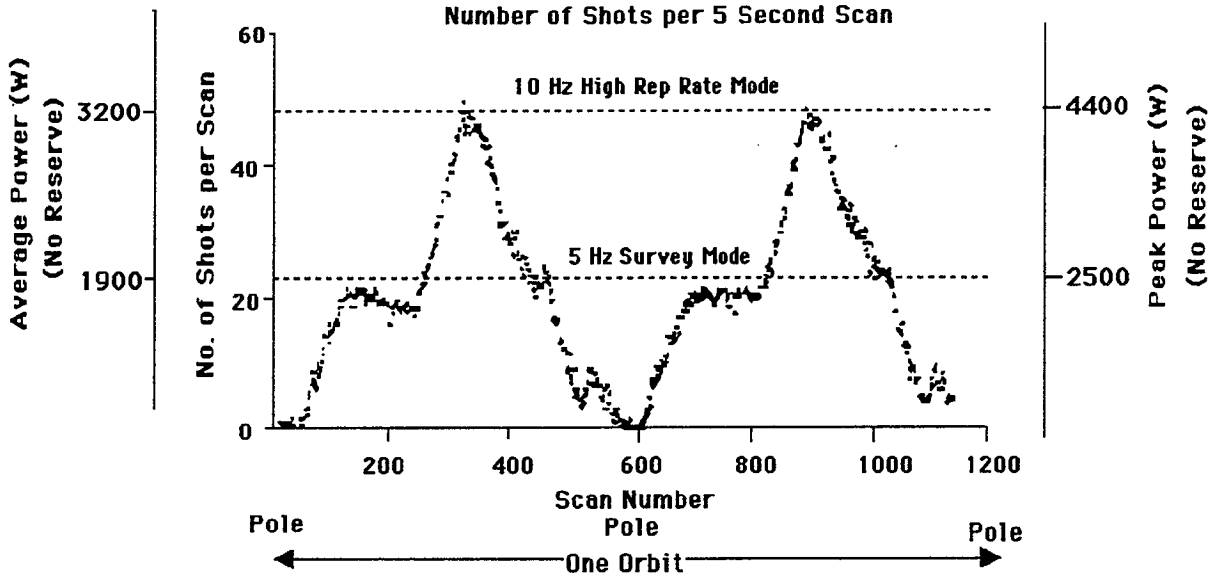

Figure 3.7-2 Power Profile for One Orbit

Several constraints placed on the system power include:

1) the power system must maintain an energy balance over a complete orbit;

2) no charge/discharge cycles of the spacecraft batteries are allowed during the non-eclipse portion of the orbit;

3) the spacecraft thermal rejection capability is 2200 watts;

4) the maximum battery charge rate is C/2 amps based on two 65 amp-hour NiH batteries; and

5) the maximum power available from the spacecraft solar arrays to the LAWS instrument is indicated in the "Bowl Chart" provided by MSFC to the contractors.

The "Bowl Chart" shows that about 4500 watts is available to the instrument from the solar panels while the spacecraft is in full sun. During the winter solstice (or summer solstice depending on whether the orbit has a 6 AM ascending or descending node) the spacecraft is in shadow for a portion of the orbit. This shadow occurs when the satellite is over either the northern or southern polar region. When the spacecraft is in shadow it must use energy from the battery which has been stored during the day, or sunlit portion of the orbit. Thus, there is less than 4500 watts available to the instrument during the sunlit portion of the orbit because of the need to recharge the batteries. The power available during the shadow period is determined by the amount of charge stored in the battery. The sunlit power is always limited by the solar array peak available since rule 2 above prohibits discharge of the battery.

It is clear that there is a trade between the peak power available during the sunlit portion of the orbit (during the solstice, about 100 days) and the amount available during shadow. In the shadow the power comes from the battery and is limited by the amount in the battery which is an average power. There is a limit as to the discharge rate; however, it is high enough so that it is not a practical limit. During the solstice, the shadow period varies from zero to about 23% of an orbit and back to zero over about 100 days. The total orbit period is 1.59 hours. The basic equations governing the power profile are:

$$E_b = \frac{P_d T_d}{\eta_{bl}}$$

$$P_c = \frac{E_b}{T_s \eta_{sb}}$$

$$C = \frac{P_c}{vn}$$

$$R = \frac{C}{c_b} \leq 0.5$$

$$P_s = P_0 - P_c$$

where:

T_d = time in shadow (hr),
T_s = time in sun (1.59 - T_d),
P_0 = peak available during sun with no charging ($\cong$ 4500 watts),
P_d = desired average power in shadow,
E_b = required from battery (watt-hr),
P_c = required to charge battery (w),
P_s = remainder available in sun,
C = charging current (amp),
R = charge rate,
v = voltage per cell (1.22 volts),
n = number of cells (22),
c_b = battery capacity (65 amp-hr),
η_{bl} = efficiency from battery to load, and
η_{sb} = efficiency from solar array to battery.

Using these equations and assumptions, the trade between day and night power use is shown in Figure 3.7-3. This plot shows the available powers for three times during the occultation period, where T_d equals .14 hours, .28 hours and the maximum of .36 hours. The power shown at the left is the peak power available during the sunlit portion and is limited by the available solar array output. The peak rep rate in the sun is shown on the right hand axis and is based on the LAWS instrument power budget. These peak rates correspond to average rates of 1/3 less, based on the 1/cos azimuth-dependent asynchronous scanning. For example, 15 Hz peak would correspond to a 10 Hz average. The bottom axis shows the average power usage in the shadow period from the battery. The top axis shows the corresponding average rep rate in the shadow.

The vertical lines at the end of the .28 and .36 hour lines are due to the maximum charge rate limitation. That is, the maximum charge rate during sunlight has been reached and no more energy can be stored in the battery for nightime use. For the maximum eclipse, .36 hours, the maximum available average power in the shadow is about 1900 watts which is just sufficient to provide a 5 Hz average pulse rate (excluding reserve). At the same time, there is sufficient power available to operate with a maximum rep rate of 10 Hz (about 7 Hz average) during the sunlit portion of the orbit.

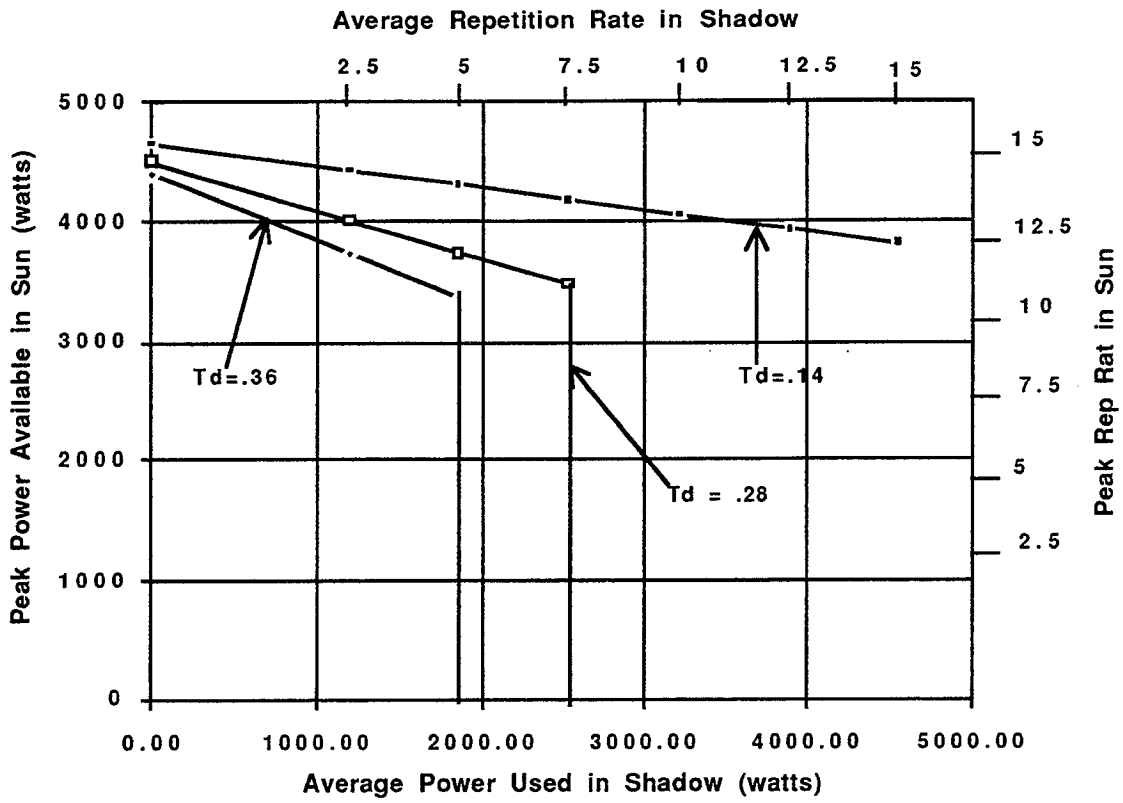

Figure 3.7-3 Day/Night Power Trades

3.7.3 Preliminary Design

The size, weight and power estimates for the Electrical Subsystem components are shown in Table 3.7-2. The estimates for the BSR and BDU were obtained from the GIIS. These components will be supplied by the EOS Program, and the estimates will be updated/revised throughout the LAWS design phase, in accordance with the EOS Program requirements as specified in the GIIS . The size and weight indicated for the BSR are for a single unit; a total of seven BSRs would be required, if each represents a double-pole, double-throw function. The

weight and power associated with the BSRs and the BDU are not included in the LAWS weight or power estimates, since they are provided as GFE.

Table 3.7-2 Electrical Subsystem Estimates

Component	Size (in)	Weight (kg)	Power (W)
Power Conditioner	19 x 8 x9	14.1	80
Harness	in structure	31.0	8
Bus Select Relay (1)	1 x 3 x 2	0.7	N/A
Bus Data Unit	6 x 11 x 7	5.2	N/A

According to the GIIS, the BSR feeds are constrained to 1200 W each (120 volts, 10 amps). A total of five feeds are therefore required to accommodate the 5 kW peak laser power requirement. Another single feed (redundant, or primary and survival feeds) is required for the LAWS power conditioner.

The estimates for the harness power were based on the assumption that requirements are on the order of 1% of the power that is distributed to the subsystem loads, excluding the laser. Due to the unique characteristics of the laser load, the laser power distribution drops are included in the Laser Subsystem power requirements.

3.8 Digital Subsystem

3.8.1 Requirements and Functional Description

The Digital Subsystem includes the Command Processor/Bus Controller and the Doppler Processor. The LAWS Controller/Processor provides the instrument data interface to the EOS Platform, and performs the following functions:

1. Communication with the spacecraft processor for data, command and telemetry
2. Command decoding, interpretation, and distribution to the LAWS instrument subsystems
3. Instrument control functions and the 1553 bus control functions
4. Science data multiplexing, formatting and packetization

5. Telemetry collection and formatting, time code and reference frequency data distribution to the LAWS instrument subsystems

6. Signal processing (quick-look Dopper estimation, range gating, alignment bias, backscatter coefficient and shot management algorithms- optional)

The simplified Digital Subsystem Block Diagram is shown in Figure 3.8-1. The connections shown in the diagram include:

- High-rate instrument science data to the transfer frame generator (TFG) via point-to-point coaxial cable

- Low-rate pre-processed data to the Platform via the Bus Data Unit, BDU, (provided by the EOS Program)

- Command and data transfer among the BDU, Laser, Optical, and Receiver Subsystems, and data mux/packetizer via the MIL-STD-1553B bus:

    - The bus master is a 1750A-type command processor
    - The BDU is master of low-rate processed and ancillary data connections serial digital data

- Time and frequency information; the 1 Hz mark, reference frequency and serial CCSDS epoch information

- Analog passive discrete telemetry (TBD passive temperature sensors)

- Safe mode bi-level discrete from the Platform Command/Telemetry Interface Unit (CTIU)

- Discrete commands

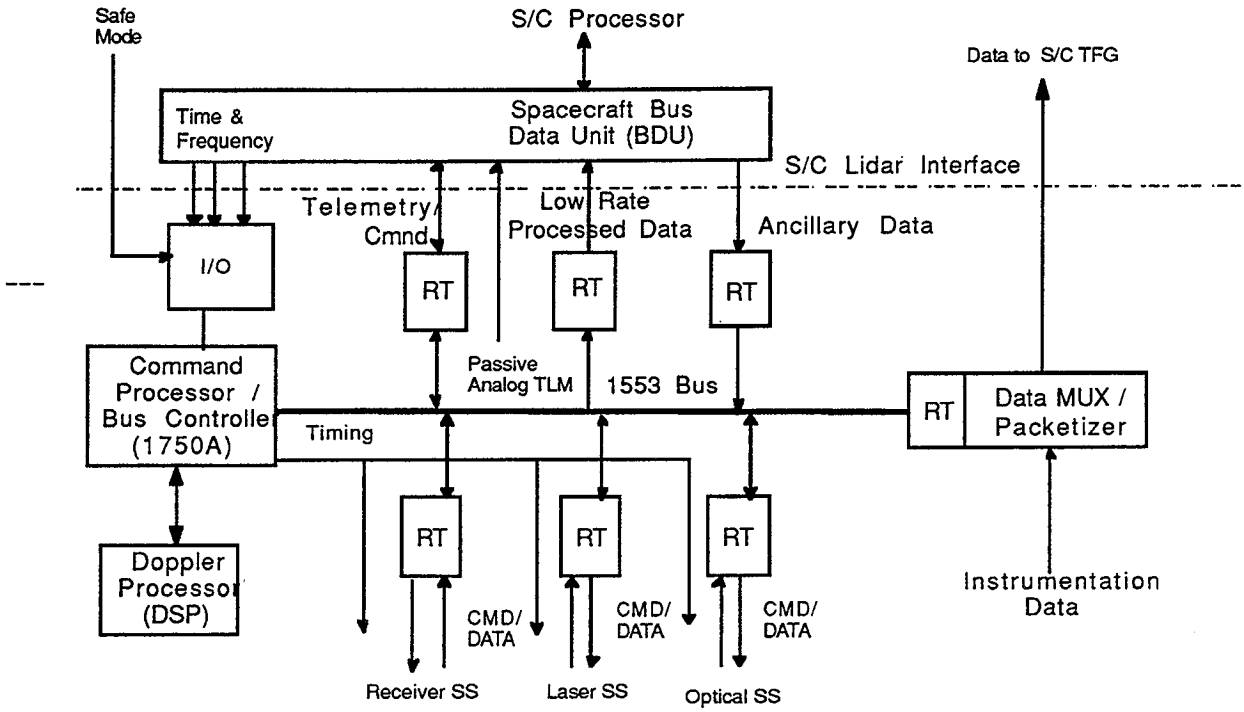

Figure 3.8-1 Digital Subsystem Functional Block Diagram

The types of data transferred over these interfaces include: serial digital telemetry, bi-level discrete telemetry, analog telemetry, serial digital and discrete pulse commands, timing information, frequency reference and ancillary data. The Command Processor/Doppler Processor interface is via a dual-port RAM.

3.8.2 Preliminary Design

Estimates of the memory and software size needed to perform the required Digital Subsystem functions are provided in Table 3.8-1. The power, volume and mass estimates for the Digital Subsystem are provided in Table 3.8-2. The following assumptions were included in the power, volume and mass estimates: use of the 1750A-type processor, a limited application of GE's High-Density Packaging Technology is used for some subassemblies, to decrease system mass and increase reliability. Cross-strapped block redundancy is provided. The Digital Subsystem is packaged in a single shielded enclosure for EMI control.

Table 3.8-1 Digital Subsystem Functions and Memory Size

Function	Memory Size (words)	Duty Cycle (Msec/sec)	Software Size (ADA SLOC)
Initialization/restart	500	-	100
Variables/Parameters	6000		
Bootstrap Loader	2000		
Operating System	8000	15	
Executive	600	10	120
Command Processing	1500	20	300
Telemetry Processing	800	70	160
Instrument Control	2500	50	500
Power Management	1000	10	200
Redundancy Management	200	10	40
Self-Test	2000	100	500
Utility Routines	2000	-	500
Data Transfer/Interface	1000	100	200
Other Processing Functions	2000	100	500
TOTAL	29000	500	3000

Table 3.8-2 Digital Subsystem Estimates

SUB-ASSEMBLY	POWER REQUIREMENT (watts)	VOLUME (5x7 Boards)	MASS (kg)
Command Processor / Bus Controller (1750A Processor)	10	1 Board	0.4
I / O Cards (RT=Remote Terminal Interface)	1.5	1 Board	0.4
Doppler Processor DSP, FFT Chip set, FFT Processor	0.5	0.25	0.1
Data Multipleser / Packetizer	10	1 Board	0.4
Housing / Harness	0	7"x8"x9"	2

TOTALS:	POWER REQMT.	VOLUME	MASS (Kg)
Prime Side:	22.0 Watts	3.25 Boards	1.3 Kg
Redundant Side:	0.0	3.25 Boards	1.3
Housing / Harness	0.0	7"x8"x9"	2.0
	22.0 Watts	7"x8"x9"	4.6 Kg

3.9 Attitude Determination Subsystem

The performance characteristics of the Attitude Determination Subsystem are given in Section 2.3, the System Error Budget section. The subsystem shall ensure that the requirements for uncompensated momentum at the instrument-to-Platform interface specified in the GIIS are met.

The Attitude Determination Subsystem consists of one or more Star Trackers and a Momentum Compensation Assembly. The star tracker hardware is GFE. The Star Tracker(s) is mounted on the instrument side of the Platform-instrument interface. The Momentum Compensation Assembly (MCA) consists of a constant-speed momentum wheel, which is identical to the momentum bias system used on the GE Series 5000 Communications Spacecraft. The MCA contains the Draper 950 in-lb-sec Momentum Wheel Assembly (MWA) and the GE Momentum Wheel Drive Electronics (MWE). The electronics drives the momentum wheel at a speed established by ground command for LAWS. The 950 in-lb-sec momentum capability exceeds the estimated 654 in-lb-sec requirement for LAWS, but includes growth margin, and is the candidate for the present design. The size and weight of the components are:

Momentum Wheel:	
Weight	30 lb.
Dimensions	23 in. dia. x 8 in. high
Momentum Wheel Electronics:	
Weight	6.5 lb
Dimensions	7.2 in. x 7.4 in. x 5.4 in.

4.0 SYSTEM VERIFICATION

The critical LAWS instrument parameters which must be accurately known in order to meet the mission requirements can be divided into two categories:

1) LOS Doppler measurements, which would address the requirements for wind profiles, and

2) Backscatter measurements from LAWS, which would address the mission requirements for aerosol and cloud measurements,

The following sections discuss how the various LAWS parameters, which need to be known to meet the above mission requirements, are measured both on-orbit and during ground test prior to launch.

4.1 On-Orbit Checkout/Verification/Test

The following is a description of the preliminary LAWS on-orbit checkout, test and verification plan. The LAWS on-orbit checkout and verification flow is illustrated in Figure 4.1-1. The required procedures will be initiated upon completion of the LAWS launch phase activities, including: orbit acquisition/trim maneuvers, solar cell deployment, and Platform checkout and test. Additional subsystem-level detail for the major subsystems on-orbit checkout/test is presented in Sections 4.3.1 and 4.3.2, below.

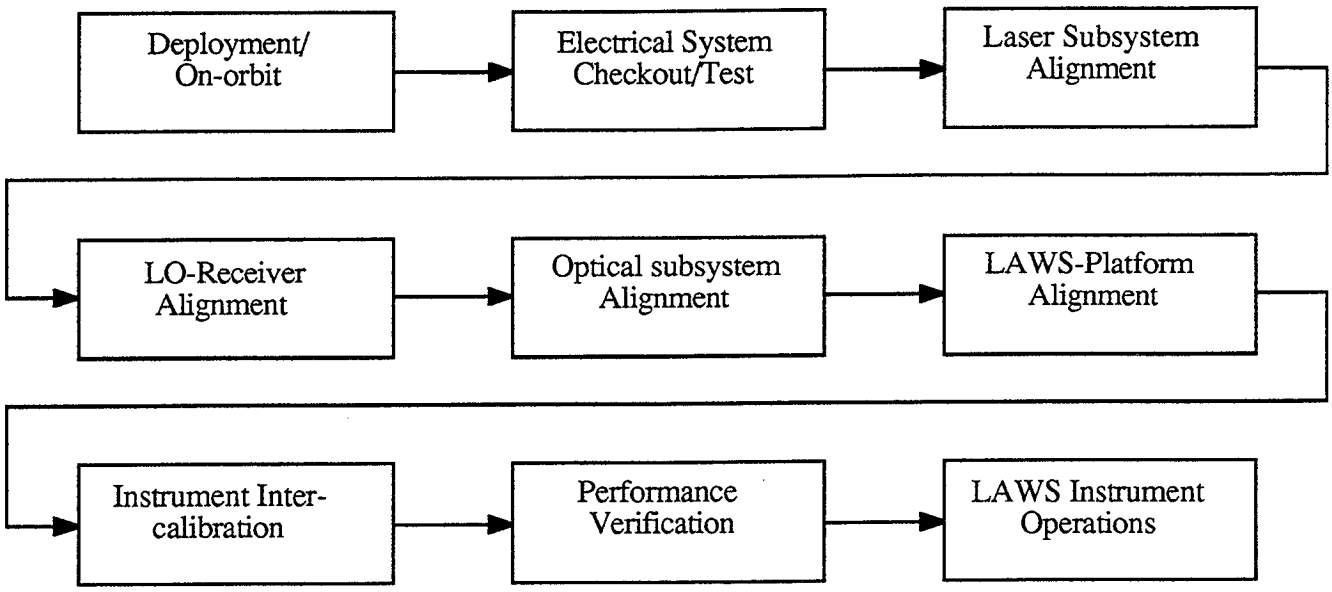

Figure 4.1-1 LAWS On Orbit Checkout/Verification Flow

4.1.1 Instrument Alignment

Laser Subsystem

The Laser Subsystem is the first element in the optical alignment chain since alignment of the Optical and Receiver Subsystems are dependent on the coordinates of the LO and the pulsed laser beams. The baseline on orbit alignment plan for the laser subsystem is based upon the following premises:

1) The structural design of the cw lasers are sufficiently robust to assure that the lasers will operate on the 9.11-μm line after experiencing launch conditions such that no transition discrimination diagnostic is required. Provision is made for minor two-dimensional angular adjustments of the grating angle (using PZT drivers) to maximize output power.

2) The triangular optical bench for mounting the cw lasers, intra-cavity lens, injection optics (Bragg cell, beamsplitters) and the lock loop/frequency offset quad detectors has the required structural rigidity to maintain their spatial and angular alignments within the required tolerances (estimated as 0.25-mm, 50-μr) after experiencing launch conditions. No active alignment control is baselined for these components. (Note: alignment tolerances for these components are an order of magnitude looser than the resonator alignment tolerance).

3) Resonator alignment is accomplished using the graded output coupler, which is housed in a x, y, θ, ϕ mount, and the power oscillator grating, which is housed in a θ, ϕ mount.

The baseline on-orbit initial and periodic checkout/verification process will proceed as follows:

a) Laser Subsystem Power-up.

System power and electrical diagnostics are completed.

b) Initial cw Laser Resonator Alignment

The laser power is peaked via θ, ϕ scans of the cw laser grating mount after which the quad-detector outputs corresponding to this alignment are stored by the alignment servo. The line centering (axial motion) servo loop of the cw laser is also active during this process.

c) Power Oscillator Resonator Alignment

The cw laser radiation (after 40-MHz frequency upconversion using the Bragg cell) injected into the power oscillator cavity and retroreflected radiation from the Littrow grating is sampled by the (power oscillator) incoherent quad detector. While the (power oscillator) grating mount θ, ϕ activators are scanned, the signal level and visibility of the resonance peaks that result from the frequency dither that is superimposed on the injected beam are maximized, after which the quad-detector outputs corresponding to this alignment are stored by the alignment servo. The line centering (axial motion) servo loop of the power oscillator laser is also active during this process.

d) Laser Discharge Test/Evaluation

The laser discharge is fired at a 1-Hz rate and electrical diagnostics to monitor discharge current and voltage are monitored and compared to nominal/pre-launch data.

e) Resonator Alignment Optimization

The optical diagnostic signals from the (power oscillator) incoherent quad detector, used to assess the beam spatial profile, and the frequency content of the optical pulse are monitored by the offset frequency monitor. The x, y position and tilt θ, ϕ of the resonator output coupler are adjusted using the signals from the incoherent quad and the coherent frequency offset detector to optimize the laser for beam shape and single-frequency operation. The alignment servo inputs are updated. The laser is switched to the operational mode after the above alignment steps are completed.

The above procedures are repeated periodically.

LO-Receiver Optical Alignment

The relative alignment of the receiver detector with the LO beam pattern is the primary optical alignment issue in this area. This co-alignment will use the DC currents from the four outer ring elements to center the LO beam onto the detector using the detector selector optics (Risley prism pair) for adjustment. The accuracy of this alignment is TBD μradians.

Optical Subsystem

The Optical Subsystem primary functions are: to provide the appropriate beam expansion for the laser transmitter, scan about the nadir axis, collect the backscattered signal from the atmosphere, center the return signal on the detector, and stabilize this return during the atmospheric dwell time for variations in pointing lag angle or image motion due to vibrations or bearing wobble. Many of the alignment functions of the Optical Subsystem require the laser to be operational for end to end system alignment. The Optical Subsystem alignment flow is as follows.

1) Telescope Focus and Alignment

Initial focus and alignment of the LAWS telescope is an autonomous task for the Optical Subsystem, and is accomplished during the initial checkout and test phase. The telescope is left in a fixed position (not scanning) for focus and alignment of the telescope using the Hartman Wavefront Sensor (HWS). The HWS measures the wavefront tilt and coma caused by telescope misalignment. Wavefront aberrations are determined by sampling wavefront tilt from four widely spaced subapertures on the primary mirror. A laser diode source in the HWS is collimated and injected into the receive beam path toward the primary mirror where the secondary mirror expands the beam, flooding the primary mirror. Four Holographic Optical Elements (HOEs) redirect a small portion of the beam back through the receive path where it is imaged onto a matrix detector. The spacing and symmetry of the spots from the HOEs is indicative of the specific aberrations and therefore the alignment of the telescope. The theoretical analysis of the HOEs optical alignment, verified by the data base generated during subsystem and system-level testing, is used to provide the correction signals to the adjustable secondary mirror actuators. These actuators adjust the secondary for two axes of tilt, focus and decenter. The data from the HWS will be monitored on a continuous basis as a check on the telescope alignment during operational use.

2) Transmit-Receive Alignment

The transmit-receive alignment is monitored by the shot vector sensor on a shot-by-shot basis. This sensor is use to monitor the shot to shot pointing jitter from the laser (specified as <25 μrad rms) and also any bias and offset errors between the laser transmitter and the Optical Subsystem due to launch shifts. As discussed previously the instrument optical bench.will ensure that any launch shift between these subsystems is less than the 250-μrad dynamic range of the shot vector sensor.

3) Receive-Detector Alignment

The receive signal and the detector need to be aligned to 1.5 μrad rms to maintain maximum signal to noise on the heterodyne detector. Active alignment consisting of the Lag Angle Compensator (LAC) and the Image Motion Compensator (IMC) mirrors are used to maintain this alignment tolerance. The LAC compensates for the systematic and deterministic motion due to spacecraft velocity and telescope angular rotation during the dwell of the receive pulse (200μs). The IMC mirror removes the effects of random image motion caused by scan bearing noise, spacecraft jitter and random vibration in the receive optical path occurring during pulse round trip time. Pointing corrections due to these effects are determined from the boresight sensor and the boresight reference which are used to steer the receive beam back to nominal boresight alignment. The alignment of the receive path to the detector requires the laser and the telescope scan assembly to be operational. The shot vector sensor measured the pulse to pulse pointing jitter of the laser due to perturbation in the gas flow and also any pointing offset or bias between the laser transmitter module and the optics module due to launch shifts. This shot pointing vector is provided to the pointing control electronics to provide offset bias signals to the LAC and IMC mirrors. Strong return signals from the surface reflection or clouds are required to have sufficient signal to noise ratio (SNR) in the four outer ring elements of the LAWS detector. Offset adjustments are added to the LAC pointing direction to center the receive diffraction lobe pattern onto these four elements.

4.1.2 Internal Calibration and Performance Verification

Each subsystem of the LAWS instrument will have a series of internal calibration procedures and performance verification tests which will be traceable to calibration and testing conducted during the I&T of LAWS. These internal calibrations and performance verifications tests will use on-board diagnostics sensors and data which have been described in the alignment section.

Laser Subsystem Performance Verification

Internal instrument diagnostics used to monitor the laser total pulse energy (incoherent quad detector or separate, calibrated energy monitor), pulse shape, frequency content (spectral width and chirp) and beam profile (quad detector) will be compared to the pre-launch data obtained during integration and test.

Receiver Subsystem Performance Verification

The log signal channel for high signal conditions must be accurately calibrated (log amplifiers are inherently difficult since they might not be "true" log conversion), and also must be cross-calibrated with the low-signal I&Q channels for accurate backscatter measurements from the atmosphere over the expected dynamic range of interest (Note:ß ranges from 10^{-11}-10^{-6} $m^{-1}sr^{-1}$ for aerosols and clouds, surface reflections may be larger). Figure 4.1-2 illustrates a test concept for cross calibrating the quadrature and log IF channels. The expected return signal dynamic range is covered by a combination of the linear (I,Q) quadrature IF channels and a logarithmic IF channel, which overlap in a given segment of the instrument dynamic range. An electrical test signal with a programmable step attenuator is input into the IF electronics to measure the exact transfer function of the log IF channel at a selected number of input signal levels. Test signal levels in the overlap range are used to cross calibrate the linear and log IF channels. Strong return signals from surface reflection or clouds with known or measured reflectivities are used to create an absolute scale on the signal output.

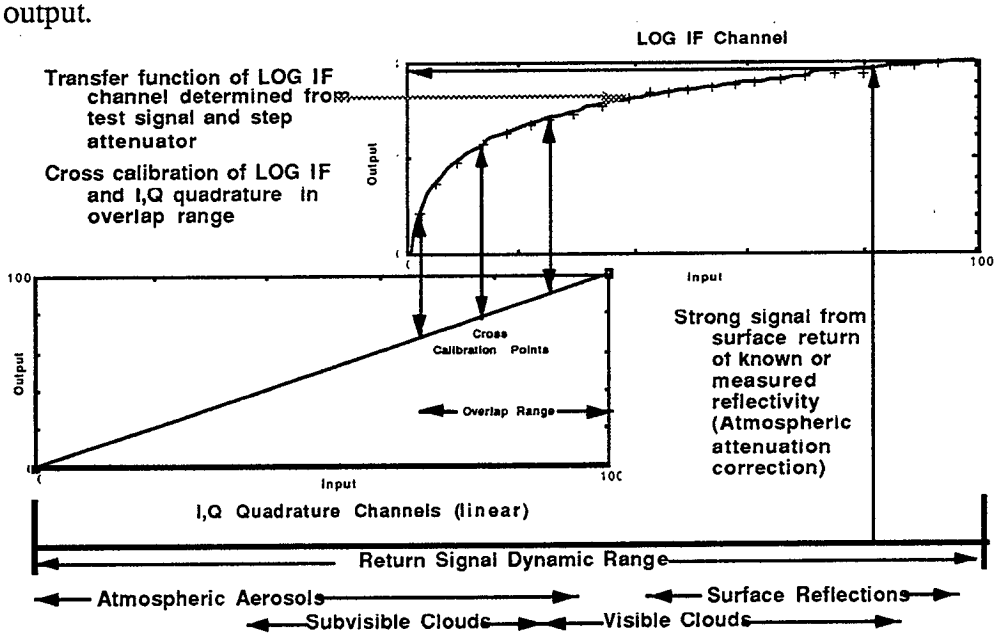

Figure 4.1-2 IF Electronics Intensity Calibration

Optical Subsystem Performance Verification

Verification of the Optical Subsystem performance is primarily accomplished during the alignment phase where the receive signals from strong returns are centered onto the signal detector using the four outer ring elements. Analysis of the shot-to-shot pointing jitter in this end-to-end alignment will be used to verify that the pointing jitter is within the budgeted alignment tolerances. Data from the HWS will be compared to data obtained during integration and testing to verify these functions are within the allocated tolerance budget. The tip-tilt mirror assembly shown in Figure 4.1-3 is used for aligning the LO to the detectors. The hardware consists of a tilt-tip mirror arrangement that is capable of locating the focused LO beam anywhere on the receiver while simultaneously controlling the angle of incidence of the beam. Each of the two mirrors is controllable in two angular degrees of freedom. These four degrees of freedom translate into two positional and two angular degrees of freedom for the outgoing beam. The arrangement is capable of performing the angular alignment as well as shifting from a detector in the receiver to the other back-up detector.

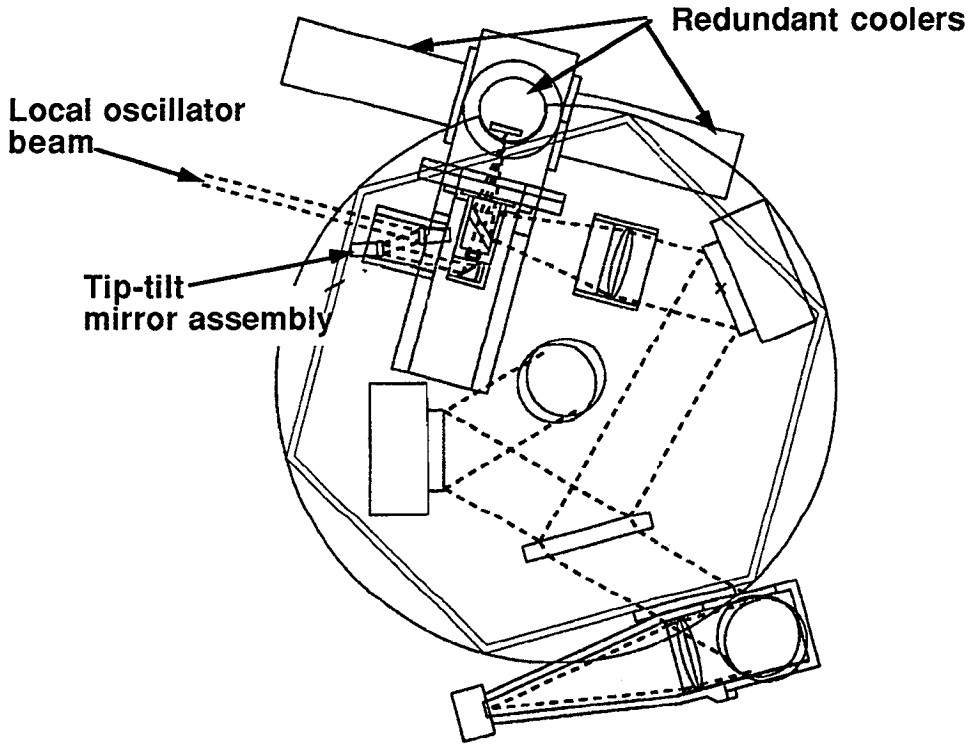

Figure 4.1-3 LO and Received Beam Co-alignment Mechanism

Before science operations and during on-orbit set-up operations, control signals to select the active detector will be provided by a command generated by the LAWS Controller and directed

to the steering mirrors. The command will define an x, y location and incident angle at the receiver focal plane, and the mirrors will direct the beam to this location and angle. Then the selected detector will be turned on, and the signals from the four outer quadrants will be summed and differenced to provide up-down and right-left energy balance error signals. The error signals provide a closed-loop, fine adjustment of the LO image position. The beam translational motion needed to achieve null can be added to the open-loop position command value in the LAWS controller and a refined angle of incidence calculated if later analysis finds this to be necessary. The mirrors will then be locked in the null position and the servo loop turned off until needed for subsequent alignment checks. Since the sensitivity to LO tilt (measured at the LO beam) is relatively low, the fine adjustment of the beam centering will not introduce any appreciable LO beam tilt if the LAWS controller algorithm includes angle of incidence correction as describe above. As measured in object space, the entire effective LO beam width is ~15μrad, and analysis has shown the corresponding allowable LO tilt is ~6μradian (200 μrad. divided by the beam expansion ratio of 33). Corrections for errors as large as an image radius (7.5 μrad.) will be on the order of the tilt tolerance.

The final stage of alignment occurs during calibration operation when ground return signals are being received. Since the received signal alignment is expected to vary slowly (as a function of thermal changes) we plan a slow, integral type of control. Again, the outside elements of the receiver detectors will be employed to produce error signals, but since the LO beam has previously been aligned, the error signals will now be a measure of the decentering of the signal beam. Since ground return signals are expected to be intermittent, the error signals will first be processed for quality (threshold operation) before driving a Kalman filter. The output of the filter will control the off-set of the lag angle compensation mirror in two angular degrees of freedom. The average bias on the mirror is also available to the LAWS controller algorithm for correction of the angle of incidence of the LO beam if further analysis shows this to be necessary.

Backscatter Measurement Verification

Backscatter cross-sections from aerosols and clouds are derived from the estimate of the range gate SNR measured by the LAWS instrument. The SNR for LAWS will depend on some specific instrument design parameters (telescope area, electronic bandwidth, wavelength, transmit and receive optical transmission, range to atmosphere or surface) which should be accurately known or measured and will not change significantly, or will vary slowly over a longer period of time. Other LAWS instrument parameters which need to be monitored on a shot-by-shot basis to determine the end to end detection efficiency are described below.

1. Instrument Heterodyne Mixing Efficiency. The instrument heterodyne mixing efficiency depends upon a number of instrument parameters such as: the target range, telescope focus/alignment, transmit-receive alignment, LO-detector alignment, receiver-detector alignment, intensity/phase of both the transmit beam and the LO in the target plane, scan pointing direction, and the detector heterodyne quantum efficiency (QE) at expected Doppler shift. Diagnostic monitors in the LAWS instrument are used to monitor these functions.

2. Laser Subsystem. Since the SNR from a distributed target (e.g. atmospheric aerosols) is directly proportional to the total energy in the pulse, the total pulse energy is monitored on a pulse-by-pulse basis. The total energy can be monitored using the output from the incoherent quad detector in the resonator servo lock loop, the quad detector from the shot vector sensor or a separate and calibrated energy monitor (location TBD). These measurements are to be monitored on a shot-by-shot basis since it is unlikely that multi-pulse averaging of the LAWS data prior to analysis will occur.

3. Detector/Receiver Subsystem. The SNR is also directly proportional to the detector heterodyne quantum efficiency, however the satellite Doppler shift varies from ±1.2GHz and the heterodyne QE will vary significantly over this bandwidth for backscatter measurements. Ground verification tests will determine the QE as a function of the IF frequency (on-orbit monitoring of I-V characteristics ensures a stable detector). Knowledge of the scan pointing direction and the satellite orbital velocity at the time the laser is fired is required to compute the IF frequency and scale the detector heterodyne QE.

A concept for intensity calibration of the LAWS instrument is shown in Figure 4.1-4 This concept has LAWS operating in a burst mode (20Hz maximum) to place the maximum number of pulses over a designated target region where an instrumented aircraft is located. This airborne measurement comparison would use an aircraft instrumented in a similar manner as the GLOBE or MACAWS missions. These instruments would include both CW and pulsed coherent lidar system to measure backscatter, along with aerosol microphysics instrumentation such as particle counters, and impactors, nephelometers to measure aerosol properties at flight altitudes. Meteorological support equipment (either ground-or airborne-based) will be required to provide temperature, pressure, and moisture parameters to provide atmospheric attenuation corrections for the lidar instruments. Primary cross-calibration of the LAWS instrument would compare the LAWS return signal from the surface reflections with those of the pulsed airborne coherent lidar (either nadir or

at nadir scan angle to simulate LAWS direction) which has been previously calibrated on the ground using a target of known reflectivity. The primary advantage in this airborne measurement inter-comparison concept is calibration of the LAWS instrument in high signal-to-noise conditions, which should minimize the required pulse averaging from LAWS. Additionally, the CW coherent lidar backscatter measurements from the airplane can be used to cross check and verify the LAWS data from the atmosphere at flight altitude where the aerosols are being sampled by the in situ instruments. The pulsed coherent lidar will provide comparison at all levels below the airplane. Calibration uncertainty due to the atmospheric attenuation will be minimized, since each pulsed lidar (LAWS and airborne systems) will essentially view the same target (i.e. surface) through the same atmospheric column.

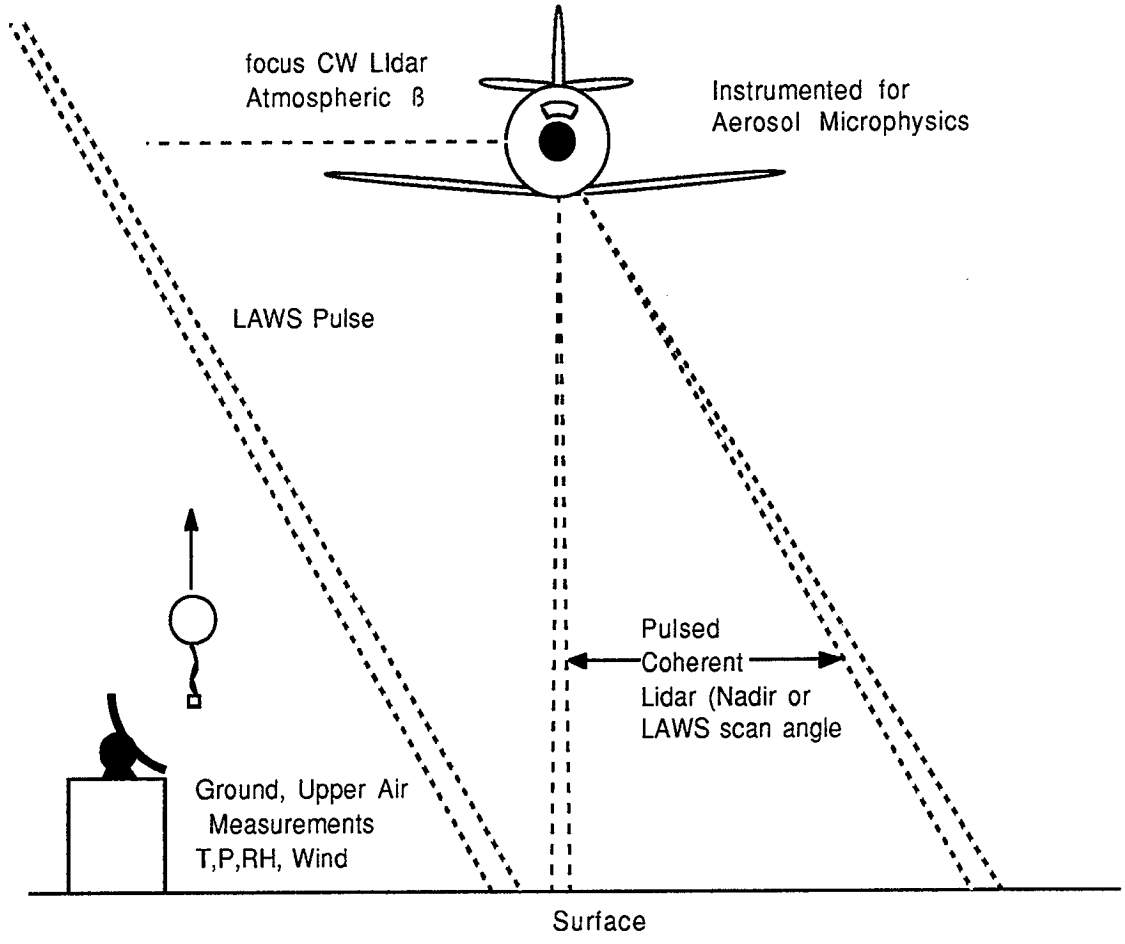

Figure 4.1-4 Concept for LAWS Intensity Calibration

One other possible calibration target for LAWS is an extensive stratiform cloud deck which is viewed by both LAWS and the instrumented aircraft. Spatial and temporal variability of these

cloud types would be issues and would probably require significant pulse averaging to reduce statistical uncertainties. Since the clouds would generally be above most of the water vapor content of the atmosphere, the uncertainty due to the atmospheric attenuation would be reduced significantly.

Unresolved issues in the accuracy of the LAWS backscatter measurements are: the co-location of LAWS and the airborne system, differing sampling time periods (i.e. LAWS overflight of 100 km path would last 13 seconds, airborne system would require 10-15 minutes), and the spatial uniformity of the ground surface or clouds used in the cross-calibration.

Another concept for LAWS backscatter performance verification is shown in Figure 4.1-5. This concept has LAWS operating in a burst mode (20 Hz maximum) to place the maximum number of pulses over a designated target area where a ground-based, pulsed, coherent Doppler lidar is located. The ground-based lidar system would be equipped with a GPS receiver for determining the position and timing coordinates. A target of known reflectivity located in the receiver far field would be used for intensity calibration of the ground-based lidar. Additional ground-based and upper air measurements of the temperature, pressure and moisture profiles in the atmosphere will be required to derive the atmospheric attenuation correction for both the ground-based and LAWS data. The concept here would be to provide a direct ß measurement comparison between the LAWS instrument and the calibrated, ground-based lidar system using natural occurring aerosols. The stratospheric and background aerosol would provide measurements in low-backscatter conditions and might have spatial and temporal uniformity over the time and space scale of this measurement inter-comparison. The primary limitation for this comparison in the low ß regime is that low signal levels require numerous pulses to be averaged from the ground system (~500), and LAWS will not yield this shot density over the region. Direct ß measurement comparison in the low ß regime will most likely use larger vertical integration of the LAWS data (3-5 km). Direct ß comparison in the atmospheric boundary layer (< 5 km) will provide the high ß conditions, but will have high spatial and temporal variability. Clouds could possibly be used in this concept, however, spatial variability and optical thickness of clouds might limit cloud comparison. The primary advantage of this verification concept is the relatively low cost in using existing ground-based operational facilities. This concept would also provide LAWS backscatter calibration on a periodic (e.g. weekly or monthly) basis, depending on weather conditions.

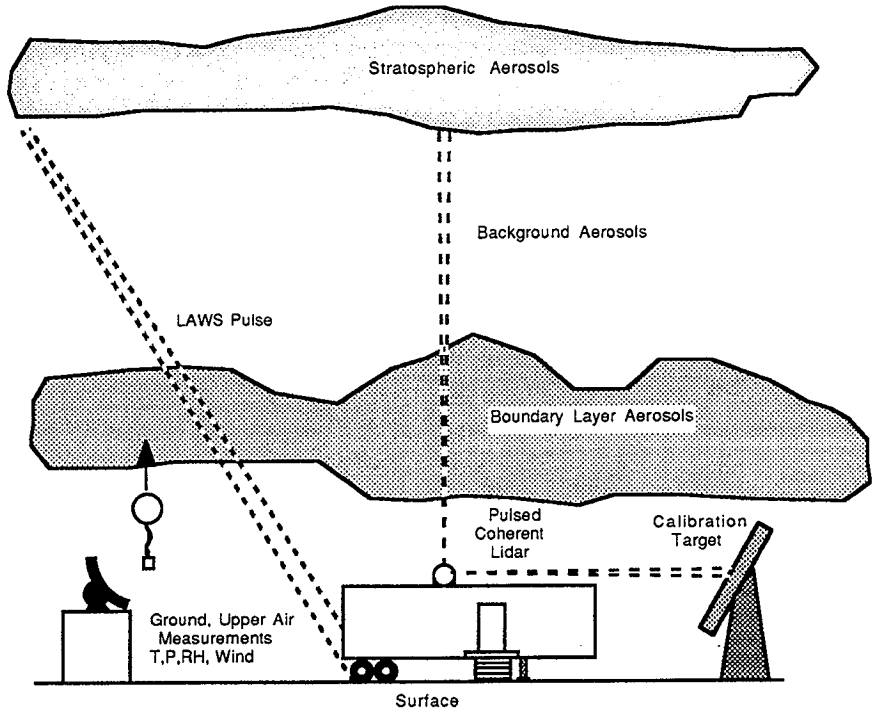

Figure 4.1-5 Concept for LAWS Backscatter Performance Verification

Doppler Measurement Verification

After the LAWS instrument is on orbit and functional, the line-of-sight (LOS) Doppler measurements from the atmosphere must be validated during the initial checkout and test before the instrument is operational.

Figure 4.1-6 schematically illustrates the LAWS Doppler frequency spectrum observed during orbital operation. The Doppler frequency shift detected by the receiver relative to the LO laser frequency is the sum of the LOS satellite Doppler due to spacecraft motion and solid earth rotation, the Doppler shift due to the atmospheric motion along the LOS, and the frequency offset between the pulsed laser output and the LO. Since LAWS is conically scanning to obtain measurements at varying directions for derivation of atmospheric wind vectors, the satellite Doppler shift varies over a ±1.2 GHz frequency range. The baseline design uses a high-bandwidth detector to measure the signal over this frequency band, and utilizes a synthesized RF LO to beat the signal down to the 100 MHz electronics bandwidth. The synthesized RF LO is generated from the knowledge of the satellite orbital velocity (GPS data using Kalman filter for orbital velocity prediction), transceiver pointing direction (scanner encoder data and prediction), and the LO/IO frequency offset fixed by the acousto-optic (AO) modulator in the laser. The signal processor measures the frequency difference between this synthesized RF LO frequency and the

satellite + atmospheric Doppler shift. Post-processing of the LAWS orbit information is conducted using GPS data for detailed orbit analysis, scanner encoder measurements and timing when the laser pulse is fired to determine the actual satellite Doppler shift. The laser frequency offset monitor detector measures the actual frequency offset between the CW LO frequency and the single frequency, TEA pulse frequency. The actual atmospheric LOS Doppler shift can be reduced from the signal processor measured frequency with the accurate knowledge of the satellite Doppler (post-processed), synthesized RF LO shift (knowledge) and the measurement of the laser frequency offset for each pulse.

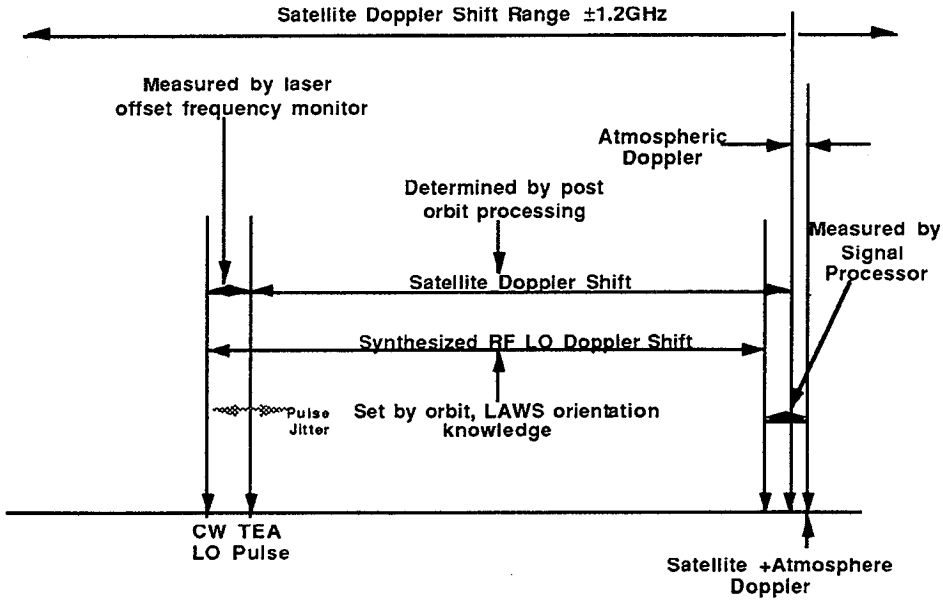

Figure 4.1-6 LAWS Doppler Frequency Spectrum

Validation of the LAWS Doppler data with ground truth measurements will be required before LAWS data is utilized in global numerical models. Figure 4.1-7 conceptually illustrates ground truth LAWS verification test. The concept includes LAWS overflight of a designated measurement inter-comparison region which incorporates: the standard ground and upper air measurement grid, a radar wind profiler network to provide continuous wind profile measurements, and would probably include supplemental or research instruments such as sodar, weather radar or lidar systems to complement the experiment. The radar wind profiler network is designed to provide wind profile data for synoptic and mesoscale research and would be on a grid scale (~200 km) comparable to the LAWS measurement grid (~100 km). The LAWS LOS measurements would be translated into vector winds and compared to the wind profiler data to validate the LAWS measurements. This type of comparison would provide confidence for the

LAWS measurements over the the majority of the Earth, where detailed atmospheric wind measurements are scarce.

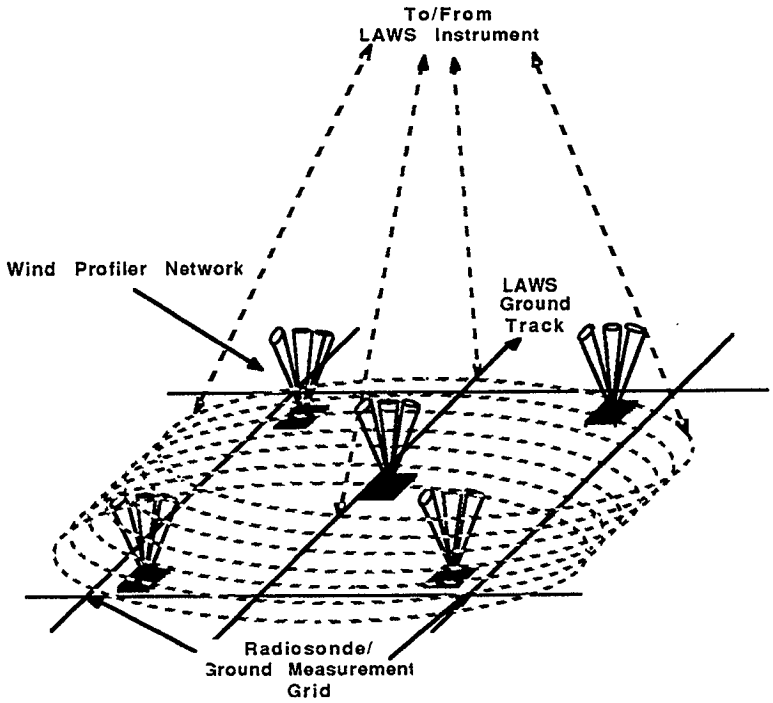

Figure 4.1-7 Concept for LAWS Ground Truth Verification Test

4.1.3 Optical Subsystem

There are eight operations to be performed during the initial On-orbit Check-out procedure. The purpose of these operations is to achieve an operationally adequate level of telescope alignment, to uncage the instrument and to prepare the instrument for science operation.

0 Starting with the launch configuration (telescope caged and all telescope systems unpowered), the eight operations are as follows:

- Thermal Conditioning (including receiver cool-down)
- LO-to-Receiver alignment
- Telescope alignment (align secondary mirror using Hartmann wavefront sensor)
- Boresight alignment of IMC through scan bearing
- Eject aperture cover
- Uncage telescope
- Scan bearing operation and thermal stabilization

- Laser/receiver test using ground returns

Thermal Conditioning

The data needed from this phase of the engineering check-out is the temperature distribution throughout the optical subsystem. The readings from temperature transducers on the primary mirror, secondary mirror, telescope structure, scan bearing and precision optical bench will be multiplexed and telemetered to the ground for engineering analysis. The Receiver coolers and scan bearing heaters will be operated during the check out. The actual readings will be compared with the previously established go-no-go levels. As the on-orbit check-out progresses and the configuration is changed, for example, by ejecting the aperture cover and starting the scan, the temperature monitoring will continue.

LO-to-Receiver alignment

Control signals to select one of the two redundant detectors will be provided by a command generated by the LAWS Controller and directed to the LO steering mirrors. The command will define an x, y location and incident angle at the receiver focal plane, and the mirrors will direct the beam to this location and angle. Then the selected detector will be turned on, and the signals from the four outer quadrants will be summed and differenced to provide up-down and right-left energy balance error signals. The error signals provide a closed-loop, fine adjustment of the LO image position. The mirrors will then be locked in the null position and the LO alignment servo loop turned off until needed for subsequent alignment checks.

Telescope alignment

The secondary mirror alignment will be checked by using the Hartmann Wavefront Sensor (HWS) which measures wavefront tilt, coma and astigmatism. The laser diode source in the HWS will be powered, flooding the PM. The four Holographic Optical Elements (HOEs) redirect a small portion of the beam back through the receive path where it will be imaged onto a matrix detector. The spacing and symmetry of the spots from the HOEs is indicative of specific aberrations and therefore the alignment of the telescope. This data is supplied to the Wavefront Control Electronics which commands the SM actuators to realign the system. During the initial engineering check-out, these signals will also be telemetered to the ground for analysis.

Boresight alignment of IMC through scan bearing

The Image Motion Compensator (IMC) has the primary function of high bandwidth removal of jitter from the receive image bundle. The initial on-orbit check-out will verify that this

closed-loop system is functioning properly. The boresight collimator will be activated and the Boresight Alignment Sensor will provide signals to the Pointing Controller, to drive the IMC mirror in a closed loop. Offsets from the pre-launch null position will be telemetered to the ground for analysis.

Eject aperture cover

At this point, the disposable aperture cover will be ejected. Status transducers will be monitored to verify successful completion of this operation.

Uncage telescope

Immediately following the ejection of the aperture cover, the launch cage clamp on the scan bearing will be uncaged. Status transducers will be monitored to verify successful completion of this operation.

Scan bearing operation and thermal stabilization

As soon as the telescope is uncaged, scan bearing operation will immediately commence. It is important for thermal reasons that the primary mirror should not be continuously illuminated by the Sun. After a period of time needed for thermal equilibrium, the temperature distributions will again be monitored to verify that design conditions are achieved. Azimuth position and velocity signals will also be monitored via telemetry for proper operation and accuracy.

Laser/receiver test using ground returns

The final stage of alignment occurs during calibration operation when ground return signals are being received. Since the received signal alignment is expected to vary slowly (as a function of thermal changes) we plan a slow, integral type of control. Again, the outside elements of the receiver detectors will be employed to produce error signals, but since the LO beam has previously been aligned, the error signals will now be a measure of the decentering of the signal beam. Since ground return signals are expected to be intermittent, the error signals will first be processed for quality (threshold operation) before driving a Kalman filter. The output of the filter will control the off-set of the lag angle compensation mirror in two angular degrees of freedom. The average bias on the mirror is also available to the LAWS controller algorithm for correction of the angle of incidence of the LO beam.

4.1.4 Laser Subsystem

During on-orbit operation, the Laser Subsystem computer interprets outputs of various laser sensors (e.g. lock-loop status, alignment status) and a go/no go signal is transferred to the System computer to indicate whether Laser Subsystem performance is within the operating envelope. This process is updated before each pulse and a positive response is a condition for the System computer to issue a firing command. This same scenario would be retained during checkout with the exception that during the initial phase of the checkout the commands to charge the PFN's and fire the laser would be withheld pending completion of System-wide check-out.

4.1.5 Receiver Subsystem

On-orbit calibration is required to assess the proper operation of the detector and to calibrate the intensity of the backscatter. The MCT detectors will be calibrated on orbit, and the results compared to the pre-launch calibration data. Preliminary calibration requirements and methods are outlined below. The ability to measure the effective heterodyne quantum efficiency, EHQE, is not currently part of our baseline design. We are currently assuming that EHQE remains constant as long as there is no change in the detector I-V characteristic and DC quantum efficiency from pre-launch ground calibrated values.

a. I-V Characteristics Measurement. The measurement of I-V curves is required to monitor the health of the diode. These measurements should be done once per day, and will require the interruption of normal operations for about two minutes. A weakening of the I vs. V characteristics usually indicates that the diode performance is degrading. However, as the I-V characteristics are strongly temperature dependent, operation at the nominal liquid nitrogen temperature must be verified. The operational procedure of I-V calibration will be documented in the appropriate procedure during Phase C/D. The required steps are briefly summarized below.

1. Block the Laser LO by either closing a shutter (location TBD) or by turning off the LO power. Verify the "No LO" condition by monitoring the LO pyro telemetry.

2. Verify that the cold finger temperature is within the allowable range.

3. Vary the bias voltage from 0 to -Vb, where -Vb is the pre-launch value of the bias voltage which was required to draw -1 mAmp of bias current (-Vb = 1 mAmp breakdown voltage).

4. Record and plot the measured bias current vs. the applied bias voltage. Compare the new values to the pre-launch data.

5. Restore LO power and nominal operating bias voltage.

b. DC Quantum Efficiency. The DC quantum efficiency of a diode should not change with time. A loss of DC quantum efficiency indicates degradation of the diode, and is usually accompanied by a weakening of the I-V curve. The DC quantum efficiency can be obtained any time the diode is illuminated by the LO and should be used as an operational diagnostic for detector health. It should be noted that misalignment of the LO or a temperature rise will also result in apparently lower DC quantum efficiency. Therefore, the cold finger temperature should be verified as nominal when monitoring the DC quantum efficiency. If the DC quantum efficiency drops but the I-V curve remains nominal, the problem will probably be alignment which should be correctable. The required steps for monitoring the DC quantum efficiency are summarized below.

1. Measure the total LO power, P_{LO}, on the detector. This is directly measurable by reading the LO power level from the LO pyro and using the pre-launch calibration factor to determine the LO power on the detector. This procedure assumes that neither the alignment has changed, nor have any of the mirror characteristics.

2. Measure the DC bias current, I_b.

3. Calculate the DC quantum efficiency from the relation below, where λ_{LO} is the wavelength of the local oscillator:

$$\eta_{DC} = \frac{I_b}{0.808 P_{LO} \lambda_{LO}}$$

4.2 Ground Test

4.2.1 Optical Subsystem

The optical subsystem ground-test flow is shown in Figure 4.2-1.

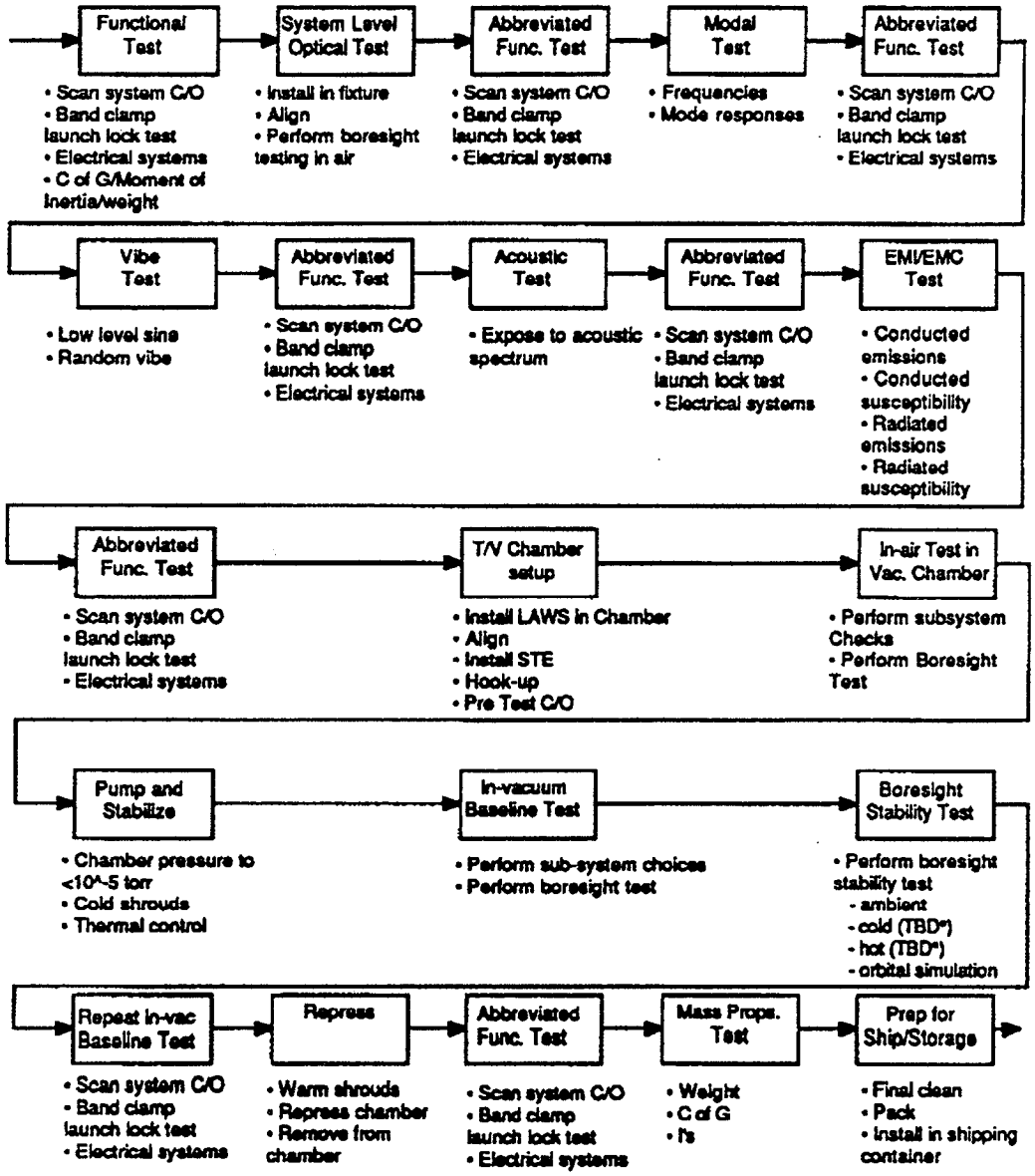

Figure 4.2-1 Optical Subsystem Test Flow

1. FUNCTIONAL TEST

The Optical Subsystem Functional Test will be a complete checkout of the major subsystems that comprise the LAWS telescope assembly. This will include the checkout of the scan system to verify that it is not only operating, but that the command and control interfaces driving it are operating correctly. The band clamp launch lock will be exercised and verified as operational. Electrical systems which include the command and control electronics for the optical systems, will be exercised and verified. Where feasible, operation of the electromechanical subsystems will be checked out. Electrical checkouts including continuity and impedance checks, grounding checks, and power level checks will be carried out.

2. SYSTEM-LEVEL OPTICAL TEST

The system-level optical test will include alignment checks on the system. This will be followed by an in-air boresight measurement to serve as a baseline for the boresight testing to be conducted in vacuum. Other system optical parameters that can be reasonably measured in air will be included in this phase of testing.

3. ABBREVIATED FUNCTIONAL TEST

The abbreviated functional test is designed to provide a health check of the system as it proceeds through the testing. The test will evaluate the functional health of the electrical and mechanical systems, and as feasible, the optical systems. This first abbreviated functional test will serve to establish a baseline for comparison with subsequent abbreviated functional tests so that any degradation in the performance of the system will be detected and properly associated with the particular test producing it.

4. MODAL TEST

Modal testing will be performed to validate and update the structural math models. It will also verify the workmanship of the flight hardware prior to further dynamic testing.

5. ABBREVIATED FUNCTIONAL TEST

Repeat the testing of Test 3 above to verify that the optical subsystem has successfully withstood the previous test.

6. VIBRATION TEST

The vibration testing will consist of low-level sine testing to complement a full random vibration test. These vibration tests will verify the integrity of the flight systems to withstand the rigors of the launch dynamic environment.

7. ABBREVIATED FUNCTIONAL TEST

Repeat the testing of Test 3 above to verify that the optical subsystem has successfully withstood the previous test.

8. ACOUSTIC TEST

The acoustic testing of LAWS will be an additional dynamic test of the system to complete the verification of the flight worthiness of the system.

9. ABBREVIATED FUNCTIONAL TEST

Repeat the testing of Test 3 above to verify that the optical subsystem has successfully withstood the previous test.

10. EMI/EMC TEST

This test will demonstrate the electromagnetic compatibility of the optical subsystem with the spacecraft requirements and will also verify that it will not adversely affect the spacecraft operation. Measurements will include conducted and radiated emissions and susceptibility to such emissions from outside the optical subsystem.

11. ABBREVIATED FUNCTIONAL TEST

Repeat the testing of Test 3 above, to verify that the optical subsystem has successfully withstood the previous test.

12. THERMAL/VACUUM (T/V) CHAMBER SET-UP

The T/V set-up in the chamber will include the normal installation and hook-up of the optical subsystem and special test equipment in the chamber in preparation for the T/V testing. This will include alignment of the optical subsystem to the in-chamber optical measurement systems. Checkout of the subsystem, the special test equipment, and the other chamber equipment used for the test - datalogging, thermal control, and similar test equipment - are also included.

13. IN-AIR TEST IN T/V CHAMBER

The basic subsystem performance testing to be performed under vacuum conditions is first performed in-air. This testing will confirm the readiness of the optical subsystem to be operated in the T/V environment. In addition, it provides a comparison to the T/V performance which may be useful in the current demonstration of the subsystem performance and can be used to benchmark the subsystem should further in-air data be necessary as a check that it has not degraded due to T/V exposure.

14. PUMP AND STABILIZE

The T/V environment is established for the conduct of the in-vacuum testing.

15. IN-VACUUM BASELINE TEST

The optical subsystem performance capabilities under vacuum conditions and room ambient temperature conditions is established. This baseline data will be used as benchmark for subsequent performance evaluations under the varying environmental conditions.

16. BORESIGHT STABILITY TEST

The stability of the boresight and other pertinent performance characteristics are verified under a variety of temperature conditions. There will be runs at both hot (51 degrees C) and cold (10 degrees C) temperature conditions. An orbital simulation (time-varying temperatures) will also be conducted. In each simulation, the temperature levels will be selected to be representative of the design goals for the instrument. Temperature levels include the hot and cold case temperatures and the expected environmental conditions for actual orbit.

17. REPEAT IN-VACUUM BASELINE TEST

This test will verify that the extremes in temperature environments that the hardware has just been exposed to have not adversely affected the instrument performance.

18. REPRESS

At the completion of the chamber testing, chamber shrouds and the optical subsystem will be returned to room ambient temperature conditions. At this point, the chamber will be returned to ambient conditions.

19. ABBREVIATED FUNCTIONAL TEST

Repeat the testing of Test 3 above to verify that the optical subsystem has successfully withstood the previous test.

20. MASS PROPERTIES TEST

As the optical subsystem reaches the end of the test flow, its mass and center-of-gravity are measured to demonstrate conformance to specifications.

21. PREPARATION FOR SHIP/STORAGE

Once the optical subsystem has successfully completed its test flow, it will be cleaned, packed and installed into its shipping container. At this point, it is ready for integration with the instrument and will either be stored until the instrument is ready to accept it or it will be shipped and integrated.

4.2.2 Laser Subsystem

The Laser Subsystem architecture permits the laser to be operated autonomously using the Laser Subsystem computer, which will have a built-in set of self-test routines to simulate the various inputs from the System computer required for various measurement scenarios. These modes of operation will be addressable over the Laser Subsystem Computer - System computer bus.

Ground-test measurements on the laser subsystem include the following:

- A test rig will be constructed that will enable the pulsed and cw local oscillator outputs to be sampled and combined on a HgCdTe photodetector mounted on the rig. Power meters can be substituted for the photodetector for beam power measurements. The rig will be installable whether or not the Laser Subsystem is fully integrated with the instrument. This capability will allow for a full complement of optical diagnostics on the output beams.
- Test points will be incorporated into the gain module for monitoring the discharge I-V characteristic. These points will be made accessible whether or not the laser is integrated with the instrument.

- The high voltage power supply is mounted independently of the Gain module and Truss assemblies and its performance is readily evaluated by monitoring the high-voltage output terminals.
- The Controls and Diagnostics module is mounted independently and incorporates the Laser Subsystem computer and the lock-loop and auto-alignment control electronics and drivers. Signals from feedback sensors, control instructions and drive signals can thus be readily monitored on the interface connector.

A complement of representative measurements based on the above will be developed to quantify the operational status of the Laser Subsystem. This complement of measurements would be repeated at appropriate stages of the qualification testing e.g., before and after temperature and humidity, vacuum, shock and acoustics testing and during electromagnetic compatibility tests.

4.2.3 Receiver Subsystem

Pre-launch calibration of the MCT detectors and the optical alignment is required to assess the proper operation of the detector and to calibrate the intensity of the backscatter. The ground calibration results will be used as a baseline for on orbit health and status monitoring.

The MCT Detector Calibration consists of measuring: the I-V characteristics and the DC quantum efficiency of the diode, and the Effective Heterodyne Quantum Efficiency, EHQE of the detector.

a. I-V Characteristics Measurement. The measurement of I-V curves is required to establish the health of the diode. Prior to launch, the measurements should be done once per day to insure stable diodes have been selected. A weakening of the I vs. V characteristics usually indicates that the diode performance is degrading. However, as the I-V characteristics are strongly temperature dependent, operation at the nominal liquid nitrogen temperature must be verified. The operational procedure of I-V calibration will be documented in the appropriate procedure during Phase C/D. The required steps are briefly summarized below.

1. Block the Laser LO by either inserting a shutter or by turning off the LO power.

2. Verify that the cold finger temperature is within the allowable range.

3. Vary the bias voltage from 0 to -Vb, where -Vb is the value of the bias voltage which was required to draw -1 mAmp of bias current (-Vb = 1 mAmp breakdown voltage).

4. Record and plot the measured bias current vs. the applied bias voltage.

b. DC Quantum Efficiency. The DC quantum efficiency of a diode should not change with time. A loss of DC quantum efficiency indicates degradation of the diode, and is usually accompanied by a weakening of the I-V curve. The procedure for measuring the DC quantum efficiency will be documented in the appropriate procedure during Phase C/D. The required steps are briefly summarized below.

1. Measure the total LO power, P_{LO}, on the detector.

2. Measure the DC bias current, I_b.

3. Calculate the DC quantum efficiency from the relation below, where λ_{LO} is the wavelength of the local oscillator:

$$\eta_{DC} = \frac{I_b}{0.808 P_{LO} \lambda_{LO}}$$

c. Effective Heterodyne Quantum Efficiency, EHQE. The EHQE measures the ability of the detector to respond to the intermediate frequencies created in the mixing process. The EHQE is strongly RF frequency-dependent. Therefore, a good knowledge of EHQE vs. RF frequency from 40 MHz to 2 GHz is required to measure the intensity of the backscatter. This can be achieved using a blackbody source and a single frequency LO. This method of evaluating the EHQE of MCT photodiodes using a blackbody source is documented in "Long-Wave Photodiode Development," D.L. Spears, Project Report NAS-1, prepared for NASA Goddard Space Flight Center, 16 August 1983. Briefly the method is to measure signal-to-noise and evaluate the EHQE using the relation

$$\eta_{EH} = \frac{\left[e^{h\nu_{LO}/kT_{BB}} - 1\right]}{\sqrt{2}t_t} \sqrt{\frac{B_0}{B_{IF}}} \left(\frac{S}{N}\right)_{measured}$$

where:

S/N is the measured voltage signal-to-noise ratio
B_O is the noise bandwidth of the lock-in amplifier
B_{IF} is the intermediate frequency (IF) bandwidth of the RF amplifiers
ν_{LO} is the frequency of the LO laser
t_t is the transmission of the optics, including the chopper factor
T_{BB} is the blackbody temperature
K is Boltzmann's constant, and
h is Planck's constant

The equation parameters and scale factors are defined in detail in the Spear's reference. The LO should be adjusted such that the bias current is maximized, to ensure the optimal photon flux upon the detector.

5.0 SYSTEM PERFORMANCE ANALYSIS

The performance analysis is presented in two parts, the coverage analysis and the line-of-sight, LOS, signal-to-noise ratio, SNR, estimates. Some of the analysis performed in Phase I of the program is summarized here for completeness.

5.1 Coverage

The LAWS instrument will fly in a polar, sun-synchronous 525 km. altitude orbit. The telescope is scanned at an angle of 45 degrees about nadir with a scan rate of 12 RPM. This combination of scan rate and scan angle were chosen after detailed analyses to maximize both coverage and LOS SNR. Increasing the scan angle improves coverage with a reduction in SNR due to the longer range to the atmosphere.

The scan rate has little effect on shot density when defined as the average number of shots in a 100 km x 100 km area (recall the requirement is to have 3 shot pairs or six shots per 100 km x 100 km box). The scan rate does, however, affect the along-track versus cross-track shot resolution. There is some interest in maximizing the along-track resolution since the across-track resolution can be modified by changing the shot repetition rate. Therefore, this is one reason for a high scan rate, or small scan period. Another reason to have a high rotation rate is that the telescope scan bearing prefers a rate greater than or equal to about 8 RPM for smooth operation. Finally, the optical design requires at least a 5 RPM repetition rate for separation of the transmit and receive beams. There are also several reasons for minimizing the rotation rate. These are: 1) to minimize the rotation-induced distortion of the primary mirror; 2) simplification of the lag angle compensation control loop; and 3) to minimize the altitude-dependent variation in the lag angle (the small variation in spacecraft altitude over the orbit is compensated by a slight change in telescope rotation rate). After trading all of these considerations, analysis shows that a 12 RPM scan rate meets all of the requirements and constraints.

The 12 RPM scan rate, 525 km. altitude, and 45° scan angle results in approximately 6 shots per 100 km x 100 km cell for an average repetition rate of 5 Hz. Figure 5.1-1 shows the ground track for the baseline case. The large grid squares are the 100 km x 100 km boxes while the smaller squares along the scan ground track are the shot positions. The laser is firing with a 1/cos azimuth-dependent algorithm with a peak shot rate of 7.5 Hz and an average rate of 5 Hz (Survey mode). It can be seen that, on average about 5 to 6 shots fall in each grid square. The High rep rate mode, nominally 10 Hz average, results in about 12 shots per resolution cell. Figure 5.1-1 also shows that a single scan swath covers about 1100 km. on the ground. Each successive orbital ground track is separated by about 2650 km. This means that to achieve total coverage (no

gaps between orbits) would require a scan angle of 63 degrees which would increase the maximum range from 776 km. (for the 45 degree angle) to 1475 km. This would decrease the LOS SNR by about -5.6 dB from the baseline. In addition, this larger scan angle would reduce the shot density for a given repetition rate.

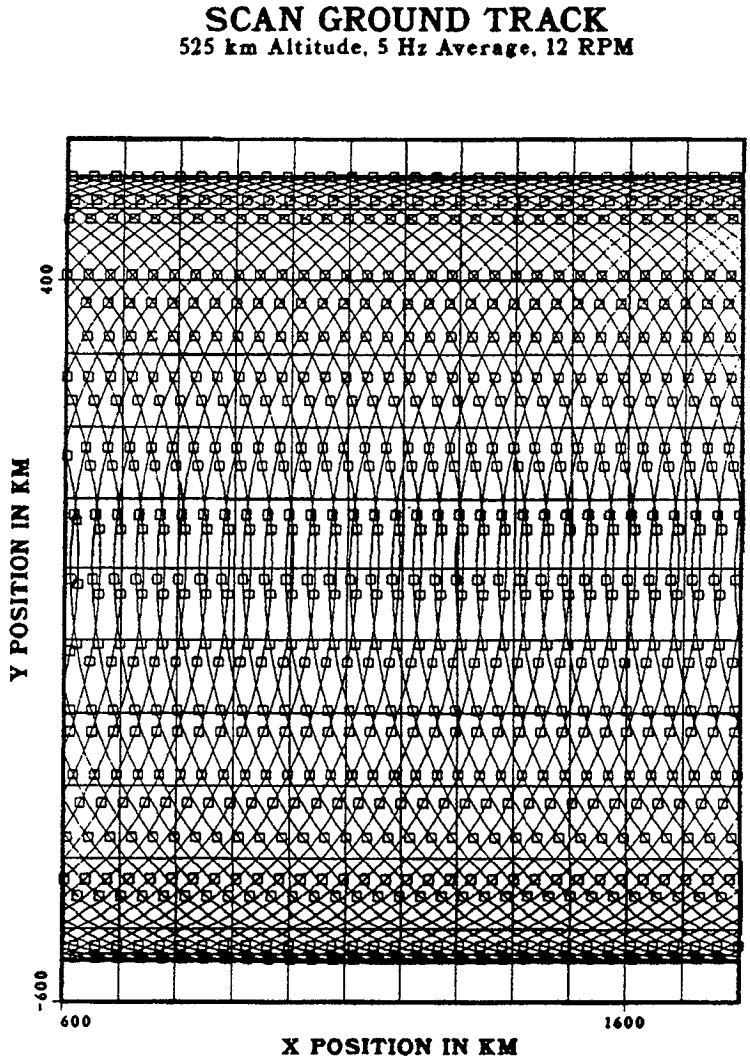

Figure 5.1-1 Scan Ground Track

The 525 km. orbit with the 45 degree scan angle results in a 12 hour average global coverage of about 60%. Increasing the period to 24 hours results in a global coverage of about 75%. This is broken down into roughly the following (for 24 hours):

Tropics: 30 degrees South to 30 North (50% Earth's area) = 65% coverage

Mid-latitudes: 30 to 60 degrees (36% area) = 78% coverage

Polar: 60 to 90 degrees (14% area) = 99% coverage.

5.2 Line-of-Sight SNR Performance

The other measure of system performance is the LOS SNR. This is calculated for a single laser pulse using the average atmospheric and system parameters. The SNR for a single pulse is given by:

$$SNR = \frac{\pi \eta J D^2 \lambda \beta e^{-2\int \alpha(r) dr}}{8hBR^2}$$

where: $\eta = \eta_{qe} \cdot \eta_t \cdot \eta_r \cdot \eta_h$

and η_{qe} = detector quantum efficiency,
η_t, η_r are the transmit and receive optical efficiency,
η_h = heterodyne efficiency,
J = pulse energy (joules),
D = optics diameter (m),
λ = laser wavelength (m),
β = atmospheric backscatter (1/m-sr),
α = atmospheric attenuation (1/m),
h = Planck's constant ($6.63.10^{-34}$ j-s),
B = noise bandwidth (Hz), and
R = slant range (m).

As discussed in section 2.1.1 the SNR is calculated for a pulse energy, J = 17.5 joules (the energy within 10 MHz); and a telescope aperture, D = 1.5 meters. Some of the other terms have been specified by the LAWS Science Team, including the backscatter profile and the representative noise bandwidth. The wavelength is 9.11 μm and the slant range shown above is a maximum of 776 km. Each of the parameters in the SNR equation will be addressed in some detail. This SNR equation assumes that the telescope is focused at infinity and that the atmospheric turbulence is negligible. Both of these conditions are satisfied for the baseline LAWS using the 9.11 μm wavelength.

Backscatter

The LAWS Science Team has provided several baseline backscatter profiles based on data taken in the GLOBE flights, data from the NOAA Lidar and data from the JPL Lidar. This database was used to determine a statistical profile for both continental and maritime aerosols. These statistical profiles were described as log-normal distributions with median and one sigma values specified as a function of altitude, both with and without cirrus present. These profiles were used to generate the mean beta profiles. Figure 5.2-1 is a plot of the mean maritime beta profile without cirrus present and shows a backscatter at 9.11 μm which varies from about 10^{-7} at the surface to a minimum of nearly 10^{-11}.

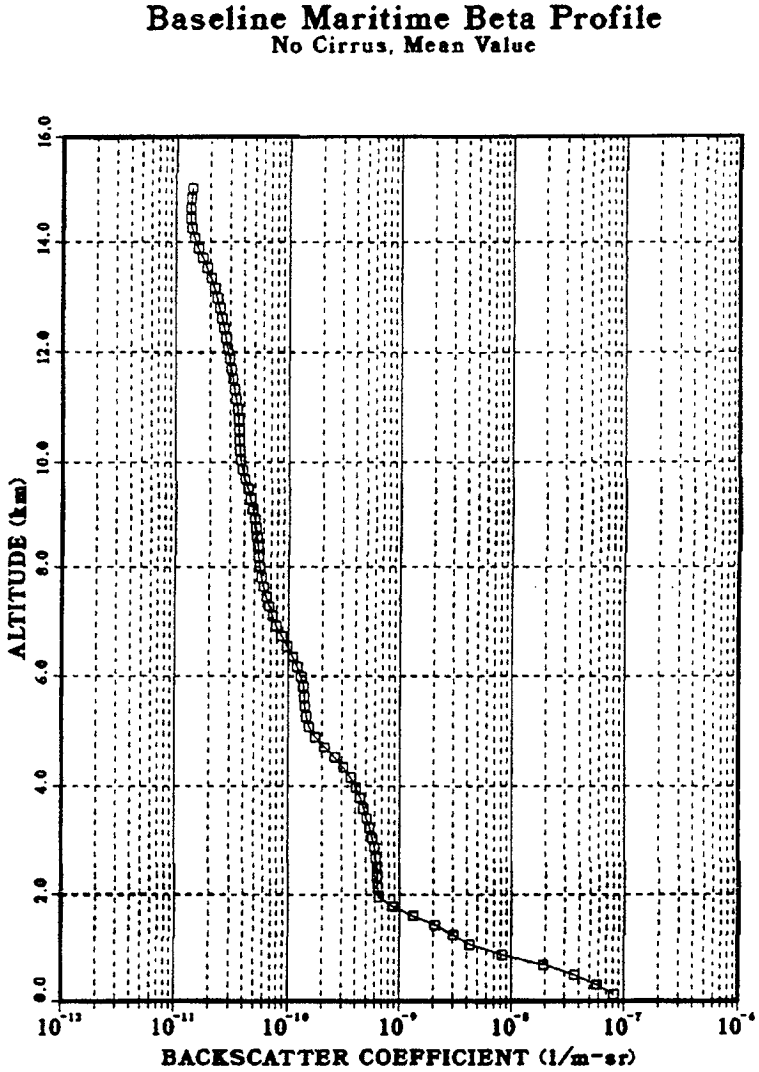

Figure 5.2-1 Baseline Backscatter Profile

The equivalent continental profile shows an enhanced backscatter value near the surface and the cirrus profiles show sharply enhanced values in the mid and upper troposphere. This mean maritime profile without cirrus will be used as the baseline for all the succeeding calculations. For purposes of comparison and simple evaluation of various parameters, a benchmark backscatter value of 10^{-11} was agreed upon by the Science Team.

Noise Bandwidth

The Science Team, after reviewing various Doppler processing algorithms, decided that the wide-band processing window should be ± 25 m/s. This equates to a wideband bandwidth of about 10 MHz for a 9.11 μm system. This has been agreed-upon by the LAWS team to be the noise bandwidth for comparative purposes. The actual wind velocity requirement is 150 m/s.

Atmospheric Attenuation

The FASCODE program has been used to calculate the atmospheric attenuation from the satellite to the surface. Figure 5.2-2 is a plot of the extinction coefficient per km for the tropical atmosphere and the R(20) line of the ^{18}O isotope laser (9.11452 μm). This is equivalent to a one-way transmission of .547 or a two-way transmission of .299. This FASCODE calculation was performed using all 28 molecules available in the code as well as the H_2O continuum and atmospheric aerosols.

System Efficiency

The system efficiency is a product of the transmit and receive optics throughput, the detector quantum efficiency and the heterodyne efficiency. The entire system efficiency used in the SNR calculations was .08. This is broken down into the four items above by the following:

η_{qe} = .40,
η_t = .95,
η_r = .93, and
η_h = .23

The detector quantum efficiency is based on laboratory measurements made at GE on quad detectors at a bandwidth of 1 Ghz. The maximum Doppler shift for the 525 km. orbit is 1.2 Ghz and this estimate, therefore, is a worst case value; that is, for most scan azimuth angles the Doppler shift is less and the resulting detector quantum efficiency higher.

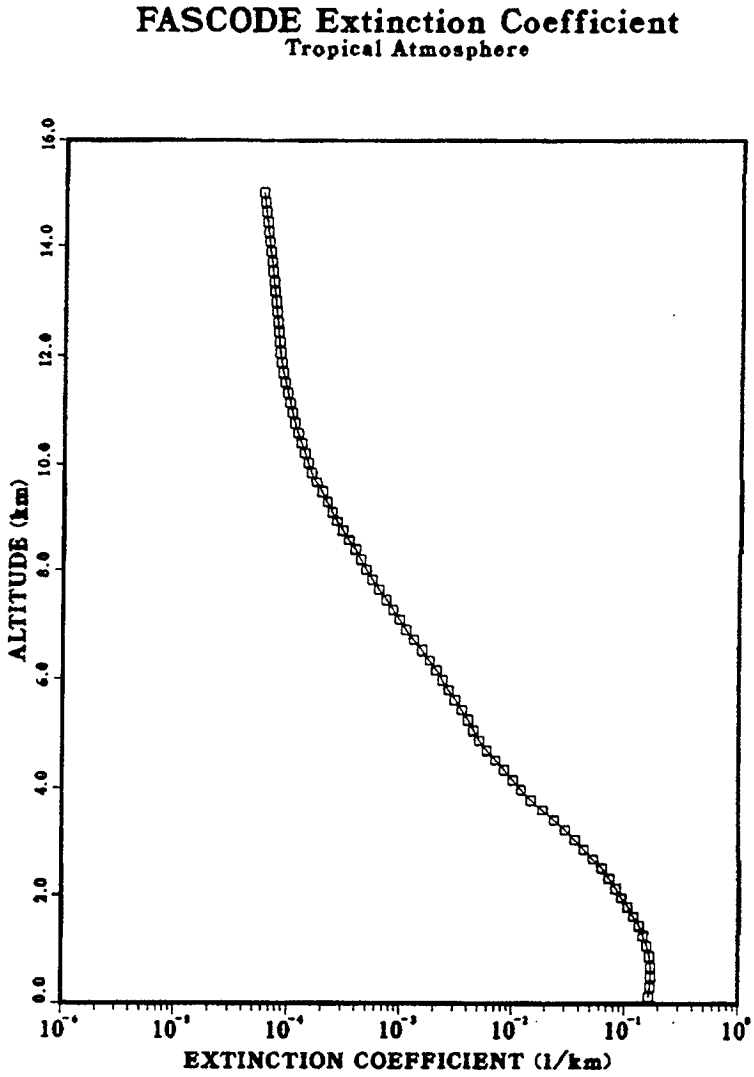

Figure 5.2-2 Baseline Backscatter Profile

The optics transmission is based on an aluminum coating on the primary mirror with a reflectivity of .975, the shot vector sensor beamsplitter with a 98% reflectivity for the transmit energy, and a .999 high-reflectivity surface for all of the remaining, smaller optics. The transmit path has 5 surfaces in addition to the primary mirror and beamsplitter yielding a transmitter throughput of:

$$(.999)^5\ (.98)\ (.975) = .95$$

The receive path has 19 surfaces as well as the primary mirror, the wavefront sensor dichroic beamsplitter (98% for the 9.11 μm radiation) and the mixing optics beam combiner with a 99% throughput for the signal path. This results in a total receive path throughput of:

$$(.999)^{19}\ (.98)\ (.975)\ (.99) = .93$$

The heterodyne efficiency is a measure of the mixing between the LO and signal wavefronts. This includes errors due to aberrations in the optical system (both transmit and receive), laser beam truncation, laser beam tilt and receiver pointing error. Both HDOS and GE have developed (under IR&D funding) extensive modeling tools for evaluation of this efficiency term. Results from these models show good agreement both among themselves and with published data. Some of the results of the HDOS model are presented in Section 3.2. The maximum value for this efficiency term is about .45 when using a Gaussian LO. Extensive modeling at GE and HDOS using wavefronts generated by the STI laser design code and which included the effect of aberrations and other errors mentioned above results in an estimate for the heterodyne efficiency of 0.23.

Signal-to-Noise Ratio

The LOS SNR for the above parameters is presented in Figure 5.2-3. The Figure shows the wideband (10 Mhz) SNR varies from a low of about -14 dB in the upper troposphere to greater than 15 dB at the surface. Another way to present this same data is shown in Figure 5.2-4. Here the SNR is plotted as a function of backscatter over the range of beta values of interest. Note that the atmospheric absorption is not included in this plot so that it is a general result which is independent of position in the atmosphere or the specific atmosphere chosen (there is a very slight range dependence in this plot which is essentially negligible). This plot shows a wideband SNR of roughly -15 dB for the benchmark β value of 10^{-11} $m^{-1}sr^{-1}$.

Analysis by Jon Anderson of the LAWS Science Team ("An Initial Study of the Use of High Performance Signal Processing Algorithms for the LAWS Instrument", Final Report for UAB Contract #SUB89-218) shows that a wideband (10 MHz) SNR of around -10 to -11 dB is required in order to achieve 50% of the velocity errors < 1 m/s. Therefore, referring to Figure 5.2-3, the baseline performance shows that for altitudes up to about 12 km the LAWS instrument will provide velocity errors less than about 1 m/s 50% of the time.

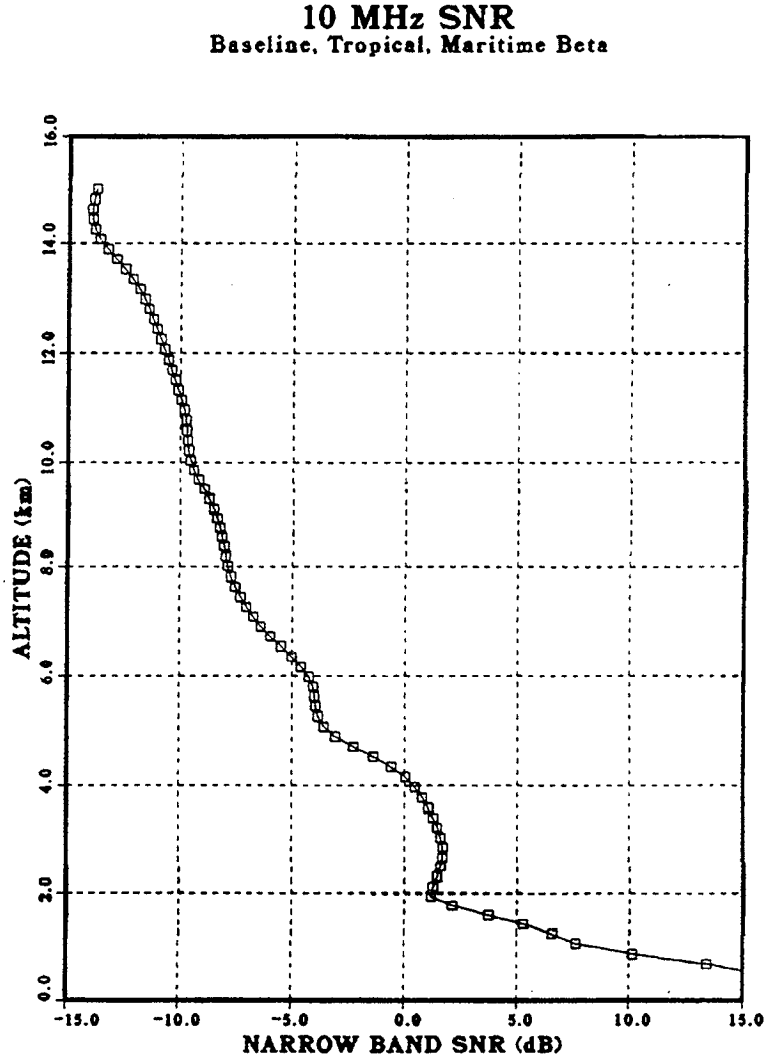

Figure 5.2-3 LOS SNR Estimate

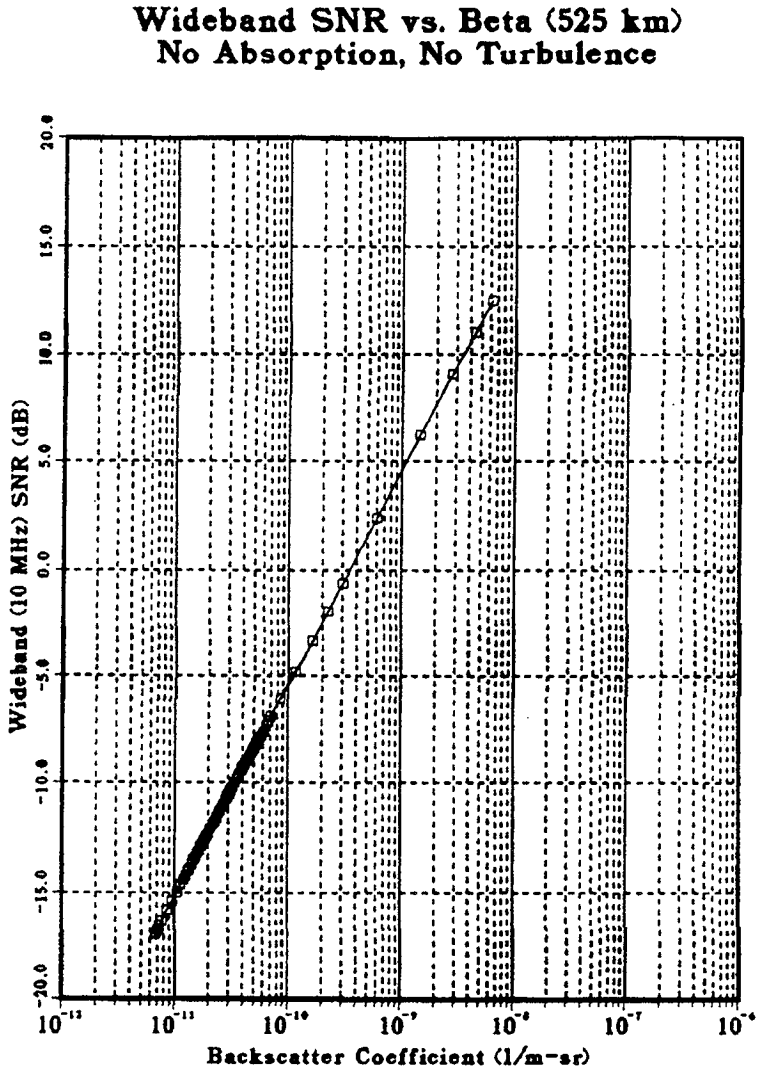

Figure 5.2-4 LOS SNR vs. Backscatter

6.0 LASER BREADBOARD PROGRAM

The LAWS Laser Breadboard program is designed to generate a database to facilitate the optimization of parameter selection, choice of technological approaches and generation of detailed engineering requirements for the flight hardware. It consists of two components: the Performance Laser Breadboard and the Life-test Breadboard respectively, the goals of which are:

Performance Laser Breadboard

The manufacture and test of a full-scale (LAWS parameters) laser transmitter to demonstrate integrated performance and to validate technological approaches.

Life-test Breadboard

The conduct of long-term tests in an existing facility (the STI CO_2 Laser Test-bed or CO_2LT) to address gas life and component reliability issues at the 10^8-shot level and at an elevated pulse repetition rate of 35 Hz.

6.1 Performance Breadboard

Performance Breadboard Laser Requirements

The requirements for the LAWS Laser Breadboard were developed from system wide considerations and are as shown in Table 6.1-1. The Laser Breadboard configuration within the laboratory at STI Optronics is as shown in Figure 6.1-1. A set of Pass/Fail criteria were developed and which are summarized in Figure 6.1-2. A test-plan for laser evaluation tests was generated under a separate cover.

Table 6.1-1 LAWS Laser Breadboard Requirements

REQUIREMENT	MINIMUM (Simultaneous)	GOAL (Single Parameter)
Energy per pulse (useable)	>15 J	20 J
PRF	10 Hz	20 Hz
Beam Quality	1.2x diffraction limited	1.2x diffraction limited
Beam Jitter	0.1 λ/D	0.1 λ/D
Frequency Chirp	< 150 kHz	< 200 kHz
$\eta_{wall\ plug}$	traceable to 5.5%	traceable to 5.5%
$\eta_{intrinsic}$	8.0%	8.0%
Chemical Steady State	at 5 Hz (worst case)	at 10 Hz
Energy Stored	190 J	240 J

NOMINAL OPERATING CONDITIONS:

Gas Pressure	-	0.5 atm ± 20%
Energy Loading	-	160 J/ℓ-atm ± 20%
Laser Gas Mixture	-	3:2:1 $He/N_2/CO_2$
Pumped Discharge Volume	-	5 x 5 x 110 cm^3
Flow Clearing Factor	-	3x (=3 m/sec)
Useful Beam Diameter	-	4.6 cm

Description of the Performance Breadboard Laser

The LAWS Performance Breadboard laser is composed of six major modules as summarized in Figure 6.1-3, which lists the major components of each module. The design approach for each of the modules is presented in the following discussion. Annotated viewgraph packages presented at the Preliminary and Final Design Reviews are available under separate covers.

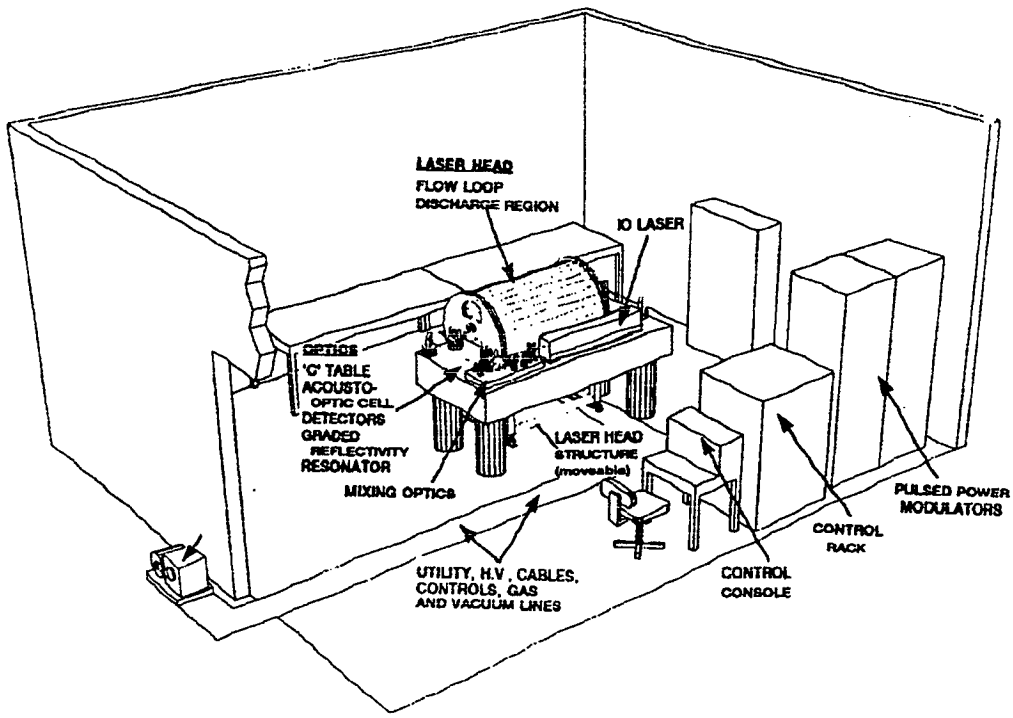

Figure 6.1-1 Laboratory Breadboard Configuration

ITEM	VALUE	COMMENT
CHARACTERISTICS		
Energy	≥15 J	Within FWHM - gain-switched spike
Duration	3 μs ± 0.5	Within FWHM - gain-switched spike
PRF	≥20 Hz	
Wavelength	9.11 μm	
Chirp	<250 kHz	Over FWHM - gain-switched spike
Beam Quality (Strehl)	<1.2 (>0.7)	Beam Quality is times diffraction limited
		Pulse to pulse
Frequency Jitter	<1 MHz	
BEAM CHARACTERISTICS		
Diameter	5 cm ± 0.1	Laser exit to 95% energy contained
Directional Jitter	<25 μr rms	Laser Exit - demagnified by telescope
Far-Field Conversion	>80%	Energy in central lobe
FLOW LOOP		
CHARACTERISTICS		
Clearing Ratio	>3	300 cm/sec flow rate
$\Delta\rho/\rho$	<0.1%	For good beam quality
PULSE POWER		
CHARACTERISTICS		
η Power Supply to PFN	70%	Traceable to >90%
η PFN to Discharge	70%	Traceable to >90%
η Discharge to Laser Output	>7.5%	Intrinsic η - corrected for circular
		aperture, and within FWHM - gain-
		switched spike
η Overall	>3%	Wall-plug efficiency (gain module)
WEIGHT AND VOLUME	N/A	
LIFE	$>10^7$ shots	Per gas fill with external catalyst loop

Figure 6.1-2 Breadboard Pass/Fail Criteria

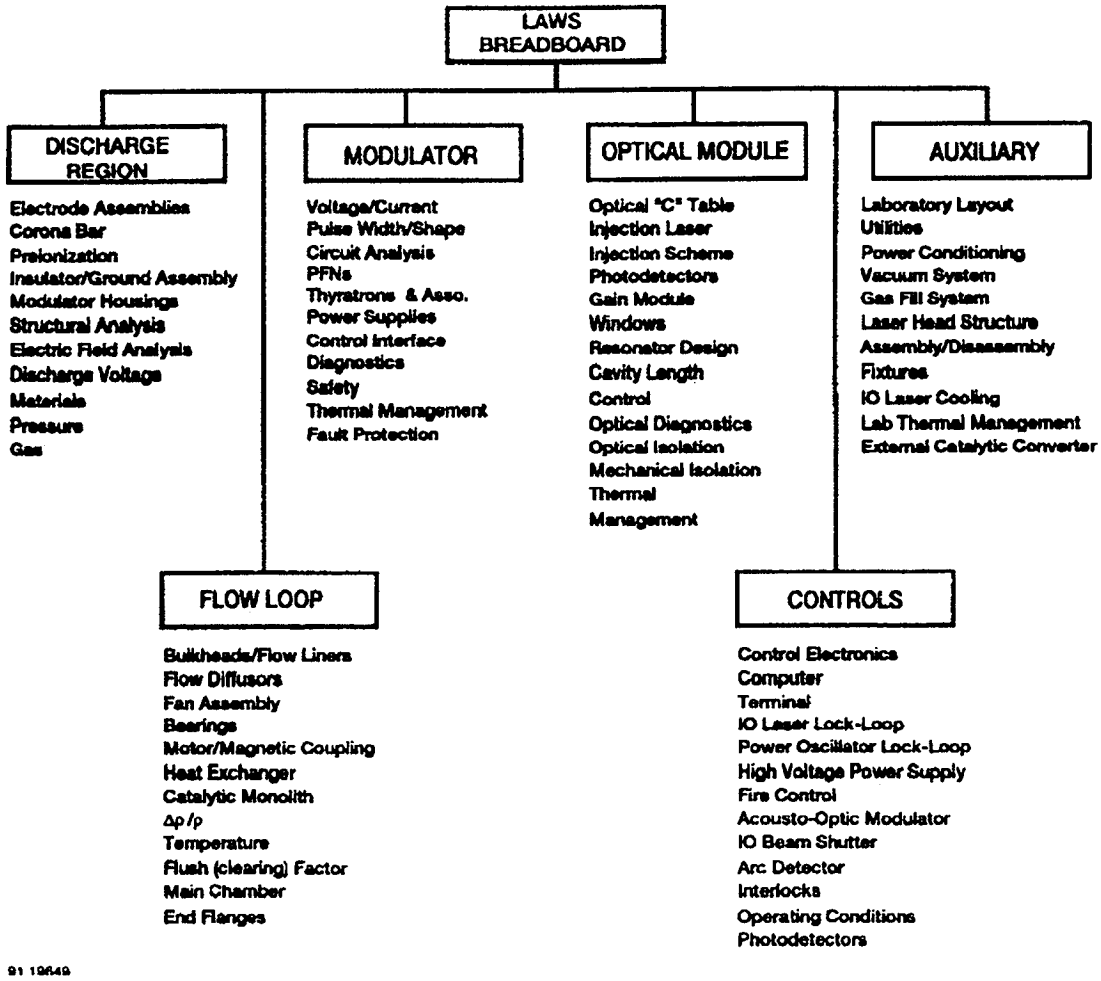

Figure 6.1-3 Performance Breadboard Major Modules

A cross-sectional view of the Performance Breadboard Gain Module design is shown in Figure 6.1-4 and a 3-D view in Figure 6.1-5 and will aid interpretation of the following discussions of the various modules.

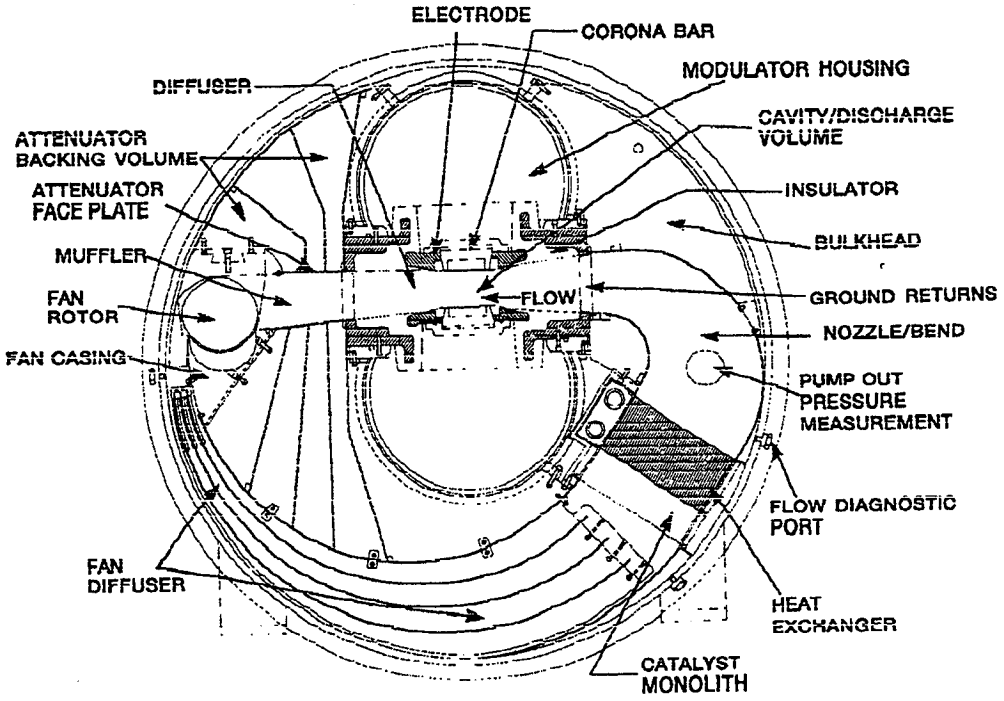

Figure 6.1-4. Design of Gain Module in Cross Section

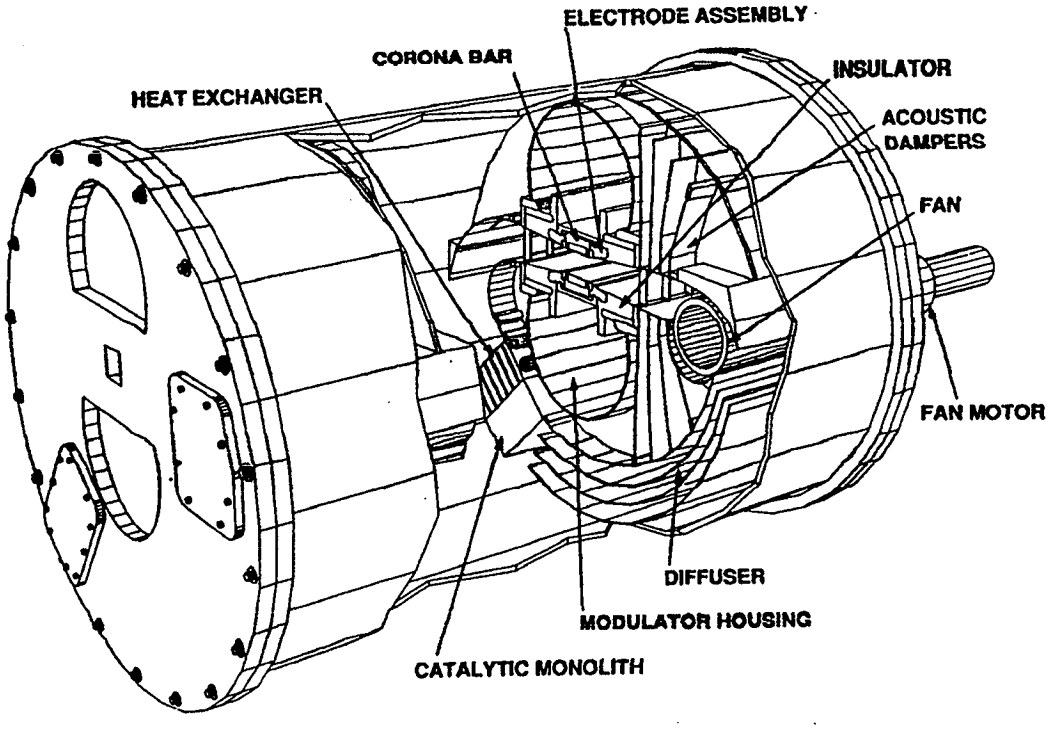

Figure 6.1-5 3-D View of Gain Module

Discharge Region

The discharge region architecture is depicted in Figure 6.1-6. The discharge region is 5 x 5 cm in cross section and 120-cm long, and consists of a flow-compatible insulator/electrode/ground plane assembly. Two 55-cm long electrodes are operated to a maximum 30 kV to ground, but at opposite polarities giving a peak 60 kV between electrodes. Preionization is accomplished using a Barium-Titanate corona bar installed behind the anode screen. Two areas directly above the anode (upper) and below the cathode (lower) are provided within the laser head for the future installation of the compact pulse power. The present breadboard pulse power system (see later discussion) is external to the laser head. The fan provides adequate gas flow at 0.5 atm and 20-Hz PRF to allow a 3 times clearing factor in the discharge region. All internal head construction materials were selected to minimize gas contamination.

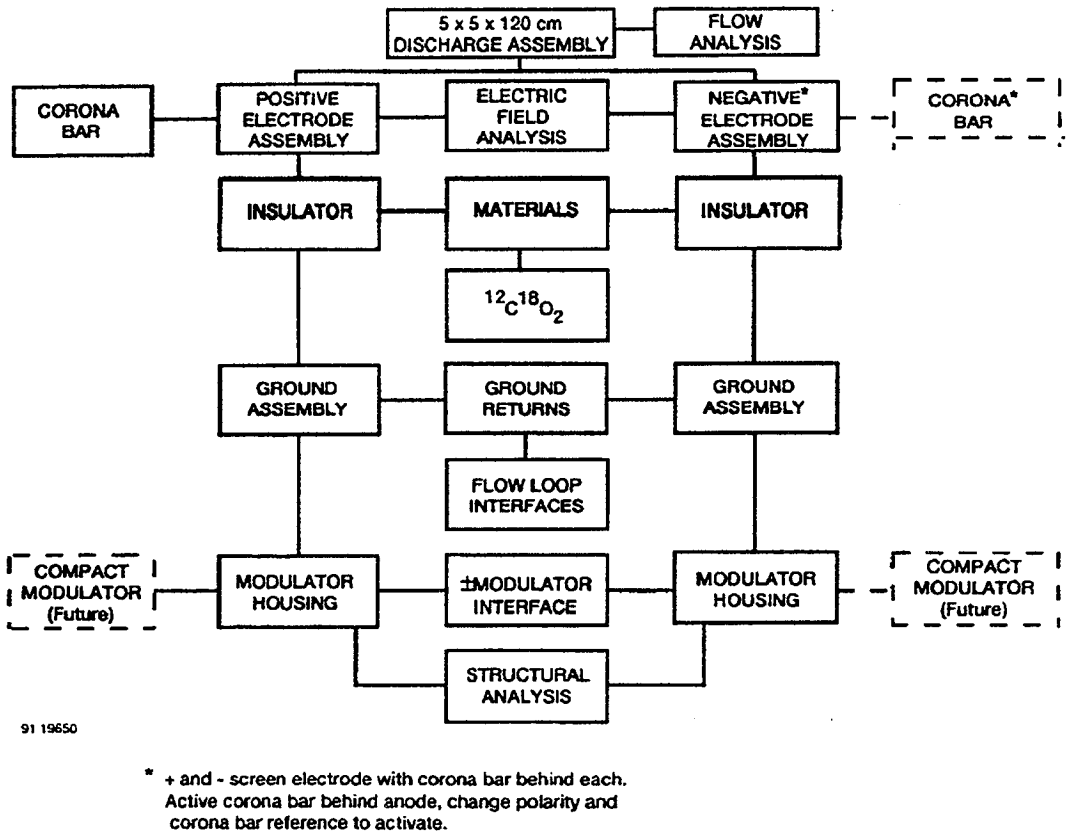

Figure 6.1-6 Discharge Region Architecture

Flow Loop

The flow loop architecture is depicted in Figure 6.1-7. Flow loop construction materials are non-contaminating to ensure long gas lifetimes. The flow loop design is similar to the successful compact flow loop designs used on previous STI Optronics-related laser developments, such as the high pulse energy coherent laser radar amplifier (CORA) for MIT/Lincoln Lab. and the Windvan laser currently incorporated in the NOAA/WPL high pulse energy lidar. A cross-flow (transverse) fan is employed and heat is removed from the gas using an internal fin and tube heat exchanger. Acoustic damping is accomplished using acoustic damper volumes downstream of the discharge region. A 300-cm/sec gas flow rate allows the laser to be operated at 20 Hz. Space for a ceramic catalytic converter monolith is included in the assembly upstream of the heat exchanger. The converter itself is not integrated in the baseline version of the laser. Ports to allow connection of the external catalytic converter used on the CO_2 laser test bed (CO_2LT) are provided.

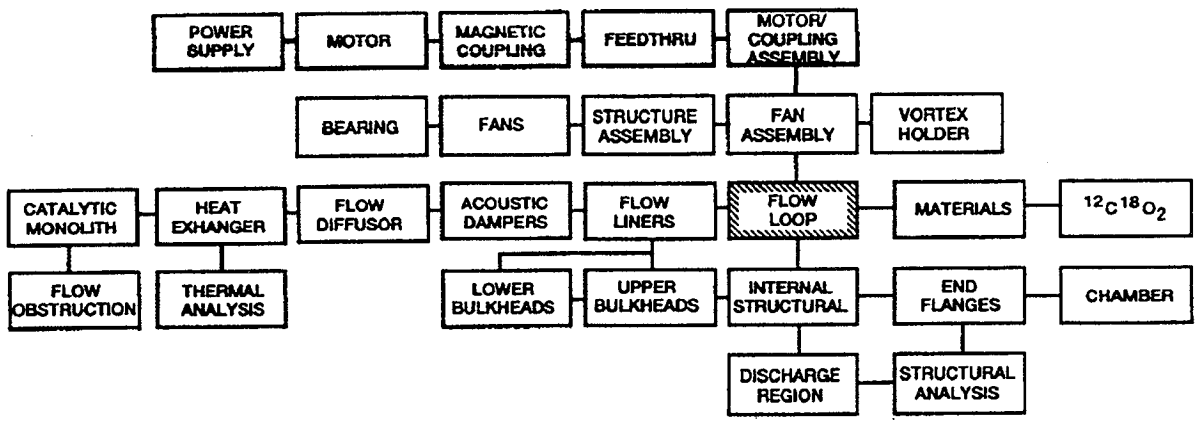

19651

- **3x Flush (clearing) Factor (300 cm/sec)**
- **$\Delta\rho/\rho \leq 0.1\%$**
- **Thermal Management $T_{gas} - T_{coolant} \leq 0.5$ °K**

Figure 6.1-7 Flow Loop Architecture

Pulsed Power

The pulsed power architecture is depicted in Figure 6.1-8. Two air-insulated, 30-kV, 6-ohm, type-'E' PFN's are connected in series via the laser head, and are fired through separate EG&G HY-5 thyratrons. The discharge is initiated by the 60-kV open circuit voltage, and sustained by the 30-kV pulse from the matched impedance PFN's. Two 40- kV, 4000-J/s switching power supplies connected in a bi-polar, master/slave configuration charge the PFNs in less than 50 ms. High-

voltage diode assemblies complete the charge circuit. A dump circuit discharges the capacitors for servicing.

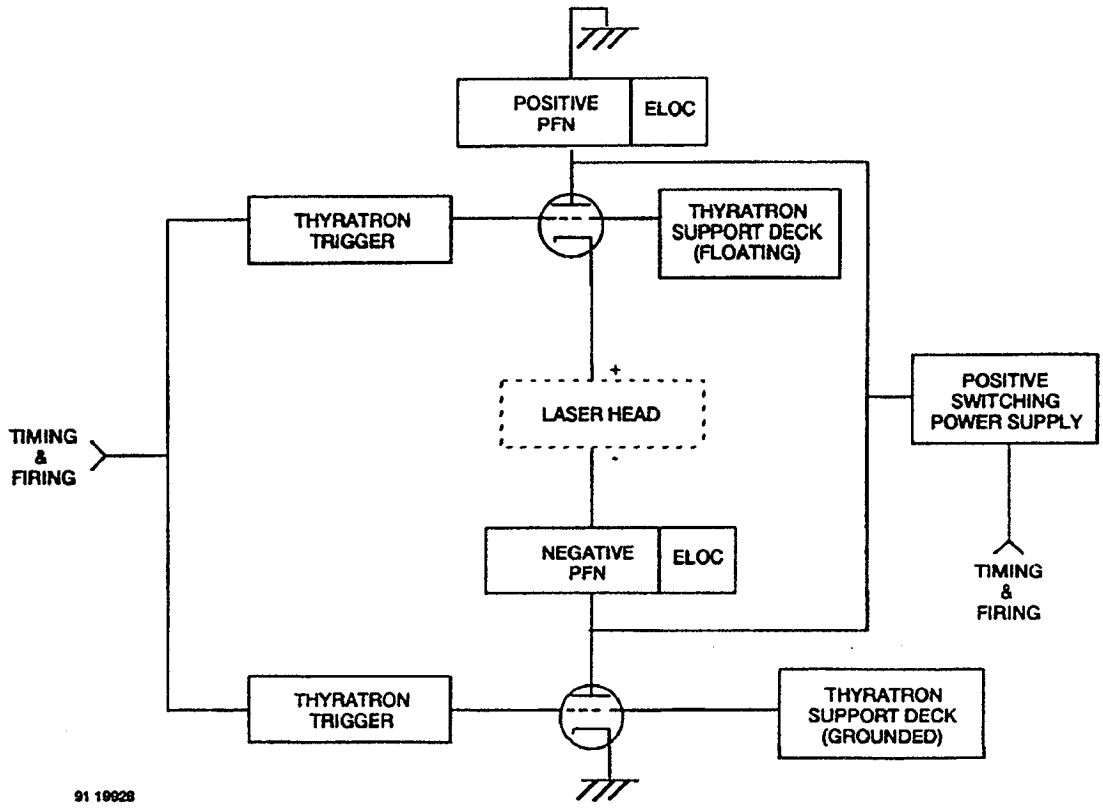

Figure 6.1-8 Pulsed Power Architecture

Figure 6.1-9 is a photograph of the completed pulse power system and Figure 6.1-10 displays oscilloscope traces of the current pulses into a matched dummy load at a full voltage of 35-kV. Two traces are shown since bi-polar excitation is used. Also shown are the traces corresponding to the overlay of 25,000 consecutive pulses. I-V traces obtained under laser load conditions are shown in Figure 6.1-11.

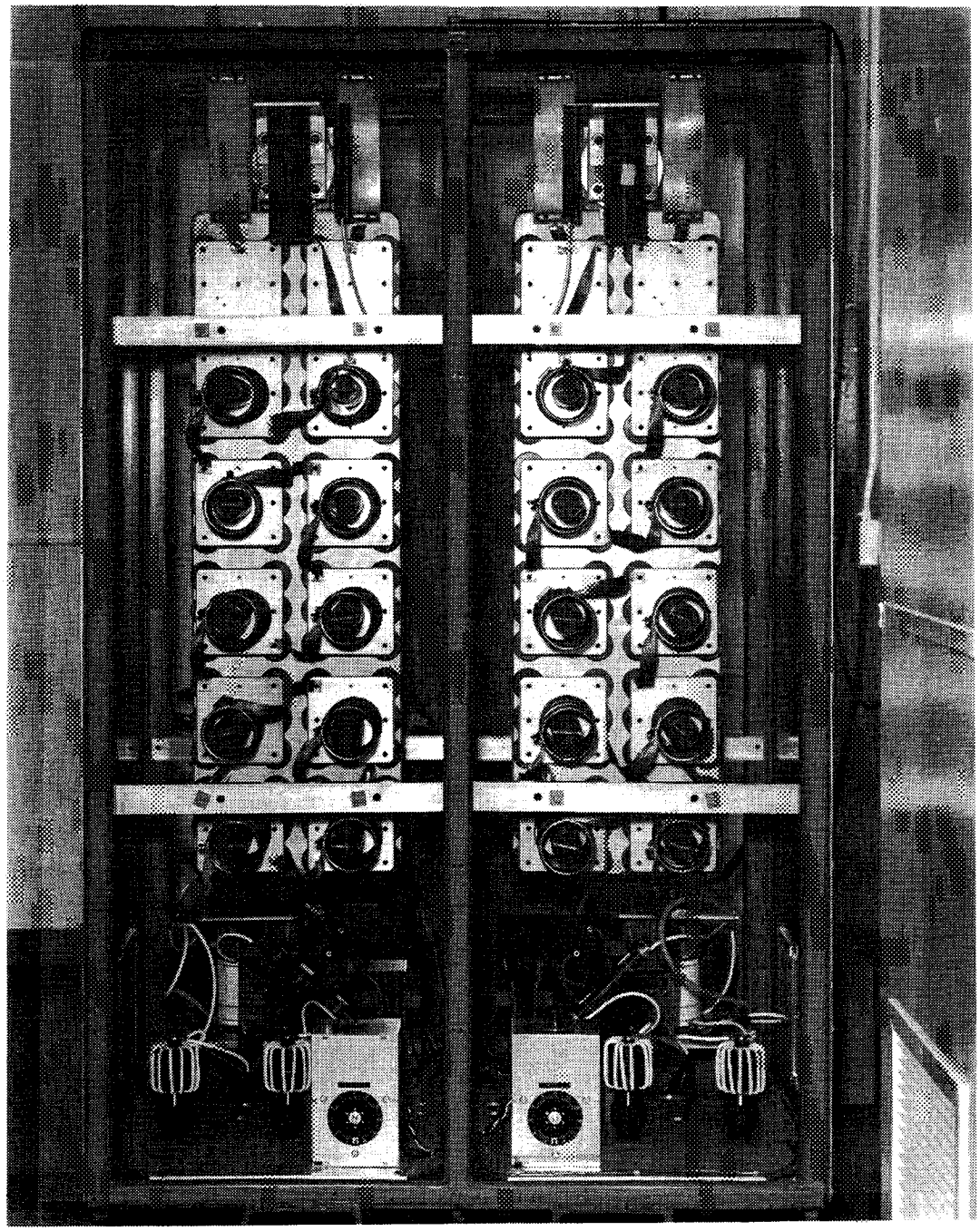

Figure 6.1-9 Photograph of the Pulsed Power System

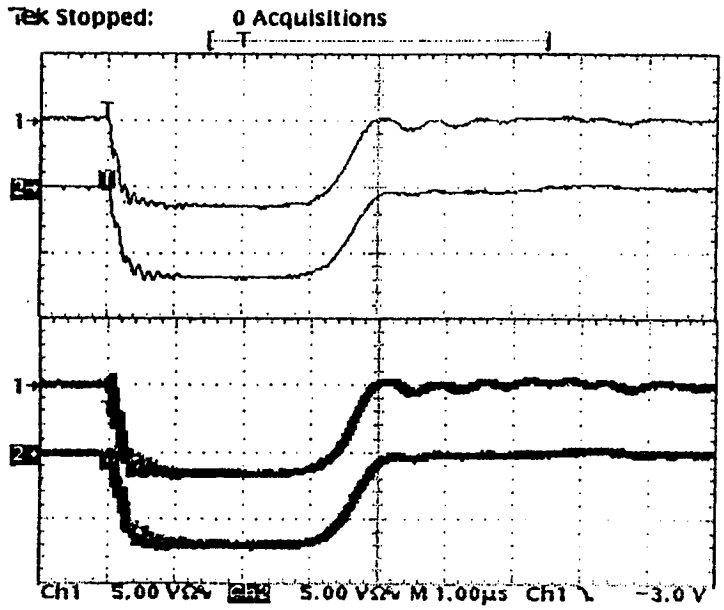

Figure 6.1-10 Current Traces of the High-Voltage Pulse Into a Dummy Load

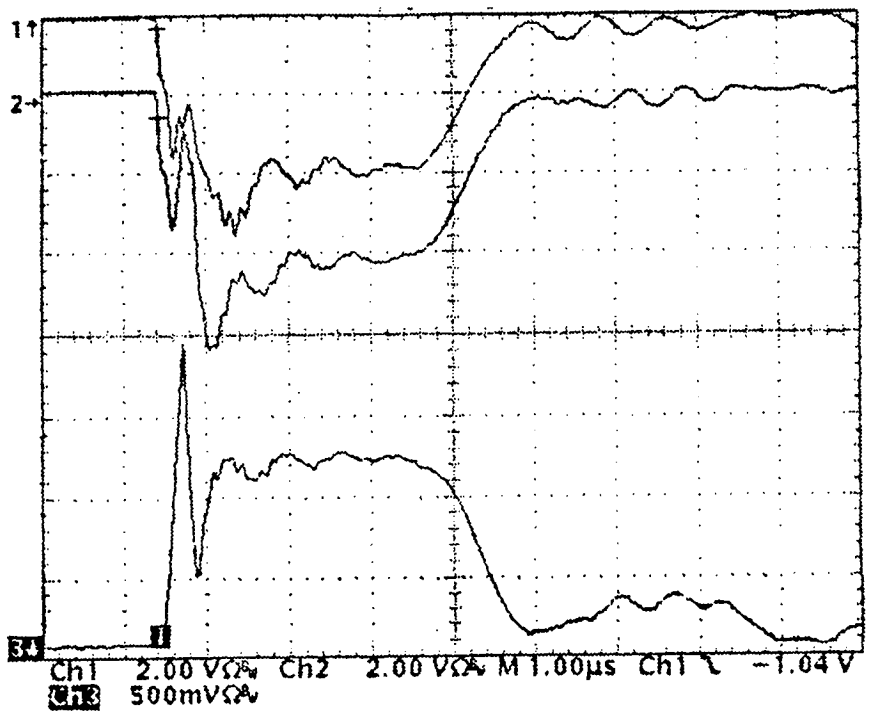

Figure 6.1-11 I-V Traces Obtained Under Laser Load Conditions

Optical

The optical module layout is presented in Figure 6.1-12. The Optical System consists of all the active and passive components necessary to generate the required optical beams. A CW CO_2 injection laser is operated on line center using a hill-climbing servo and the beam is sub-divided into a) a local oscillator beam, and b) an injection beam for the power oscillator. Prior to injection into the cavity, it is propagated through a 30-MHz acousto-optic modulator that upconverts the optical frequency and acts as an optical isolator. Injection is implemented via zeroth order reflection off the grating. The radiation emerging from the power oscillator cavity is monitored by a HgCdTe photodetector, and its output used as feedback to a servo loop that controls the axial position of one of the power oscillator cavity elements (graded reflectivity coupler) to bring the cavity length into resonance with the injected radiation. When all control system requirements are satisfied, the main discharge is fired and the optical pulse emerges. The power oscillator cavity design features an unstable resonator having a magnification of 1.35 with the output coupler being a graded reflectivity zinc selenide lens, chosen for its mode-margin and far-field conversion properties.

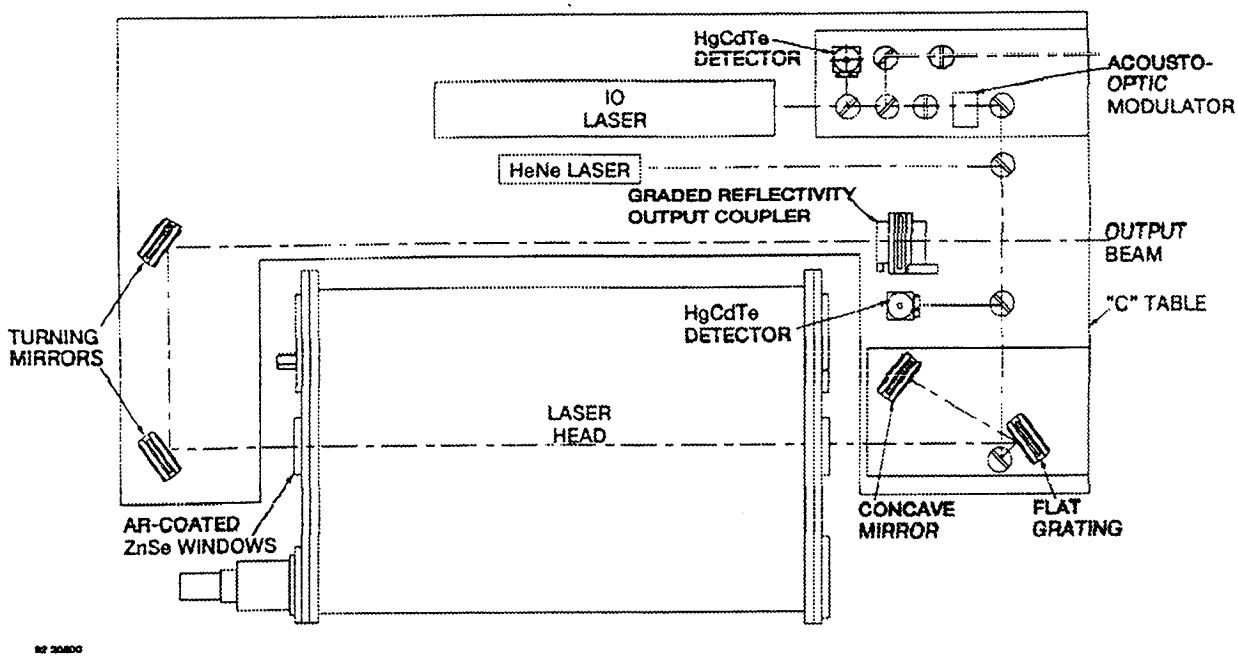

Figure 6.1-12 Optical Module Layout

A close-up photograph of the completed optical module is shown in Figure 6.1-13. The output beam pulse temporal rf diagnostics arrangement is depicted in Figure 6.1-14.

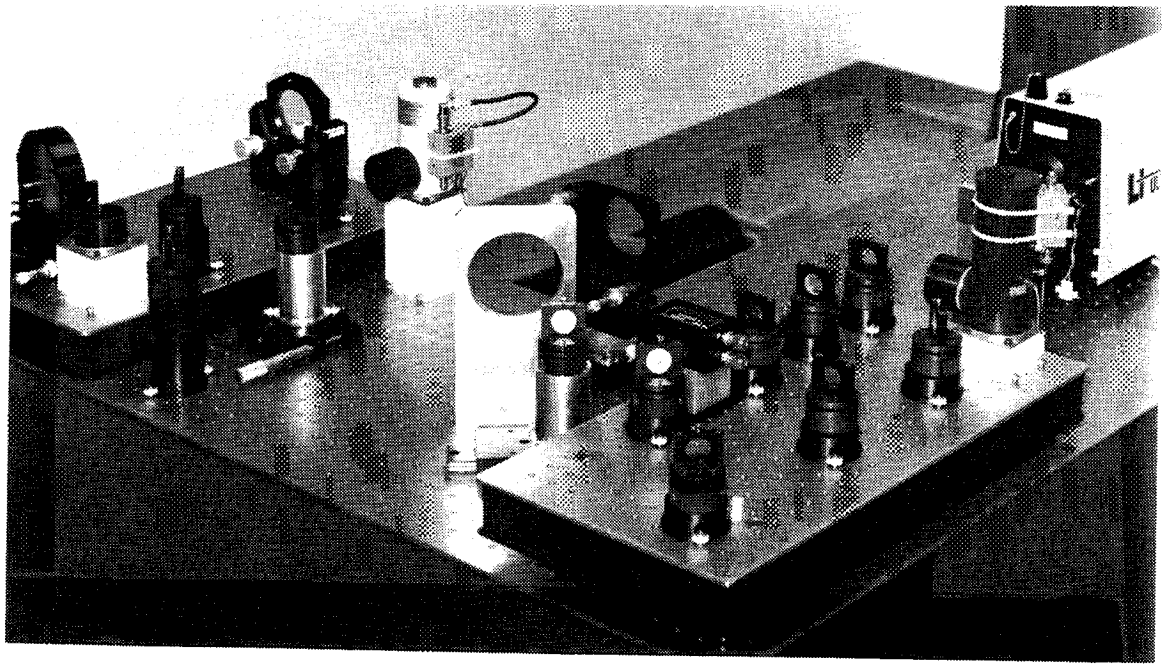

Figure 6.1-13 Photograph of Optical Module

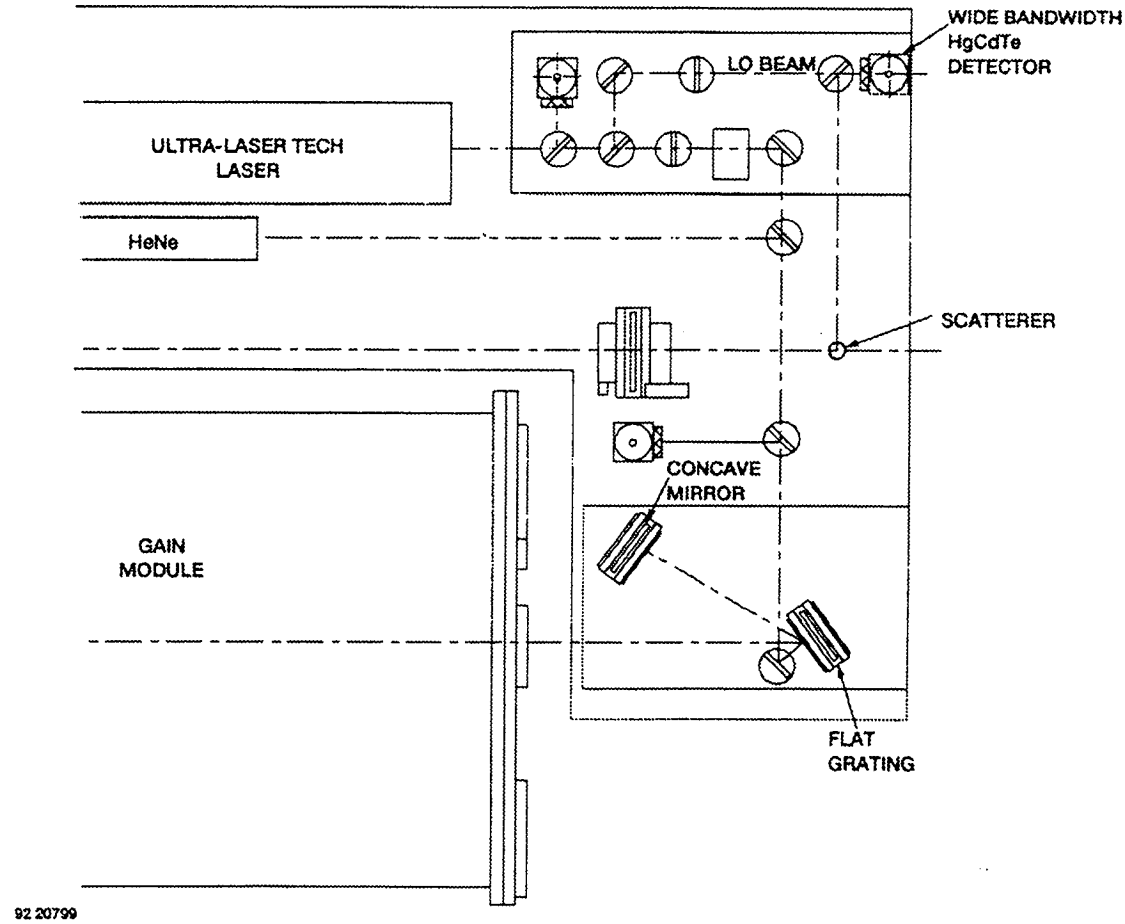

Figure 6.1-14 Pulse Temporal RF Diagnostics Arrangement

Controls

The controls module architecture is depicted in Figure 6.1-15.

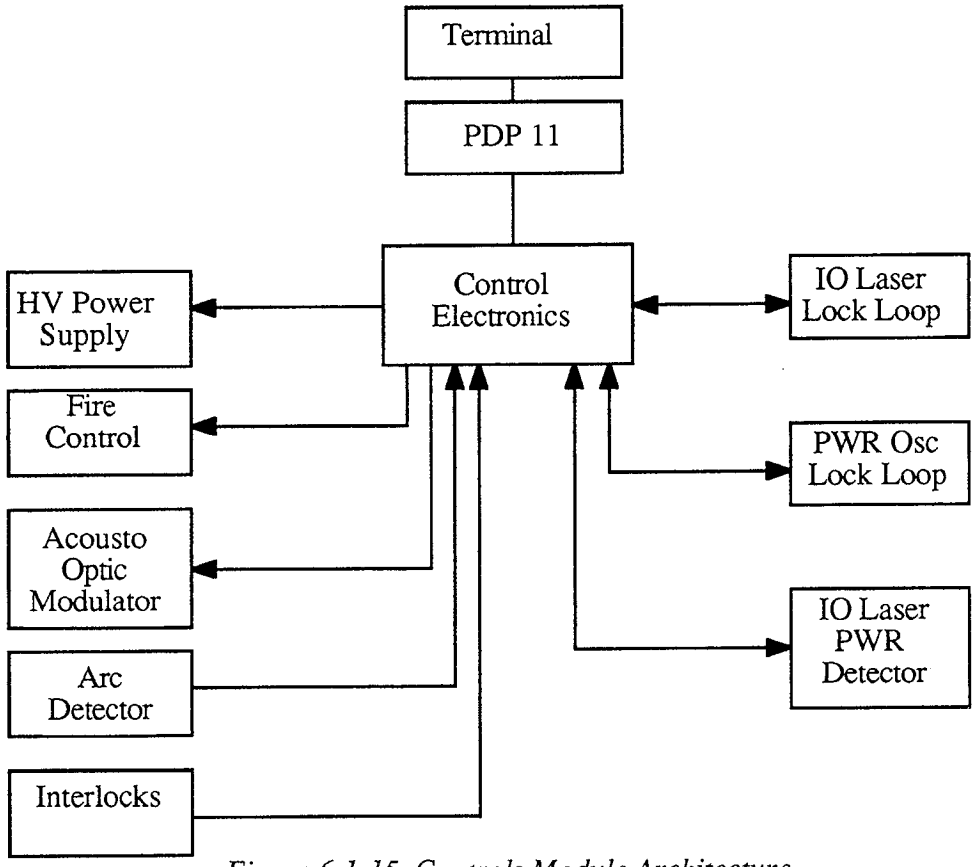

Figure 6.1-15 Controls Module Architecture

The controls module performs all functions to effect the sequencing of laser operation and the gathering of health and status data. All laser functions are controllable via a touch screen terminal (Fluke), which addresses a PDP 11/35 microcomputer. An all-digital approach is used in the control system architecture. Various functions performed by the control system include - servo control of both the injection and power oscillator control loops, monitoring of the power of several detectors, monitoring of interlocks and outputs of arc detectors, enabling of the acousto-optic modulator and high voltage power supply, and fire control of the laser. A photograph of the controls and diagnostics module components (along with other electronics) is shown in Figure 6.1-16.

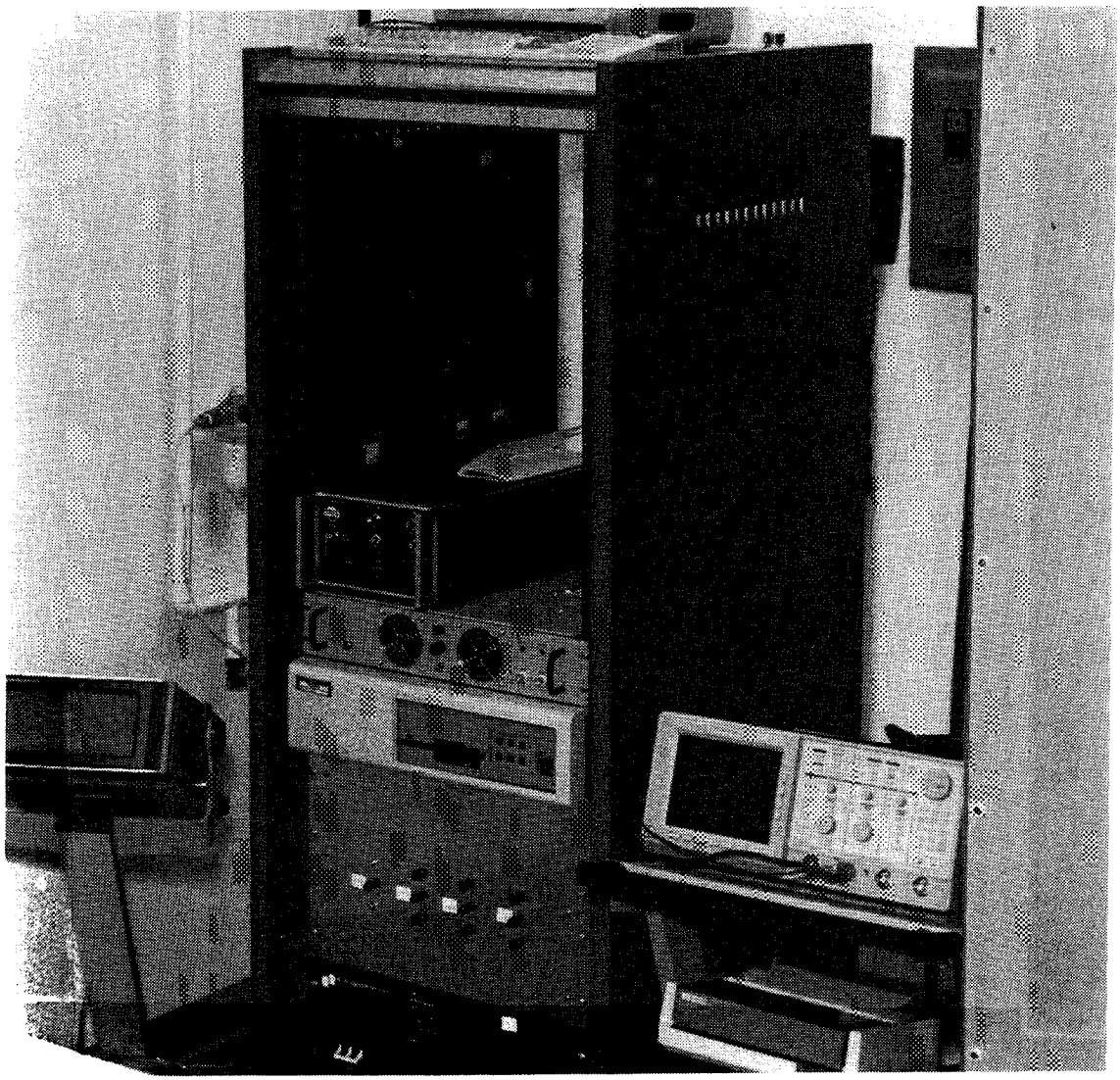

Figure 6.1-16 Photograph of Controls and Diagnostics Module Mounted in 19" Rack

Auxiliary Module

The auxiliary module architecture is summarized in Figure 6.1-17. The auxiliary module includes all support umbilicals.

End and side elevation views of the laser are shown in Figures 6.1-18 and 6.1-19. They show the location of the laser head and its support structure in relation to the optical table and laser optics. The support structure is on wheels to allow easy removal of the laser head from the pocket in the 'C' table for maintenance or modifications. Once the laser head/support table has been located relative to the laser optics, it can be removed and re-installed without re-alignment because of the alignment pins located on the floor. The vacuum line, the coolant hose and the pulse power cable (not shown) are routed from the utility trench under the support table and fed in at one end of the laser head. A 'to scale' plan view of the LAWS laboratory layout is shown in Figure 6.1-20. A photograph of the completed performance breadboard laser is shown in Figure 6.1-21.

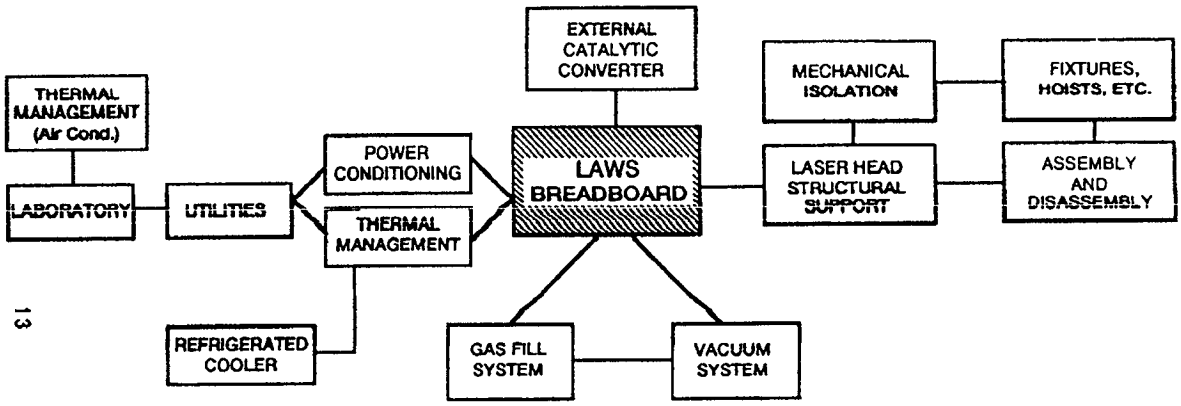

Figure 6.1-17 Auxiliary Module Architecture

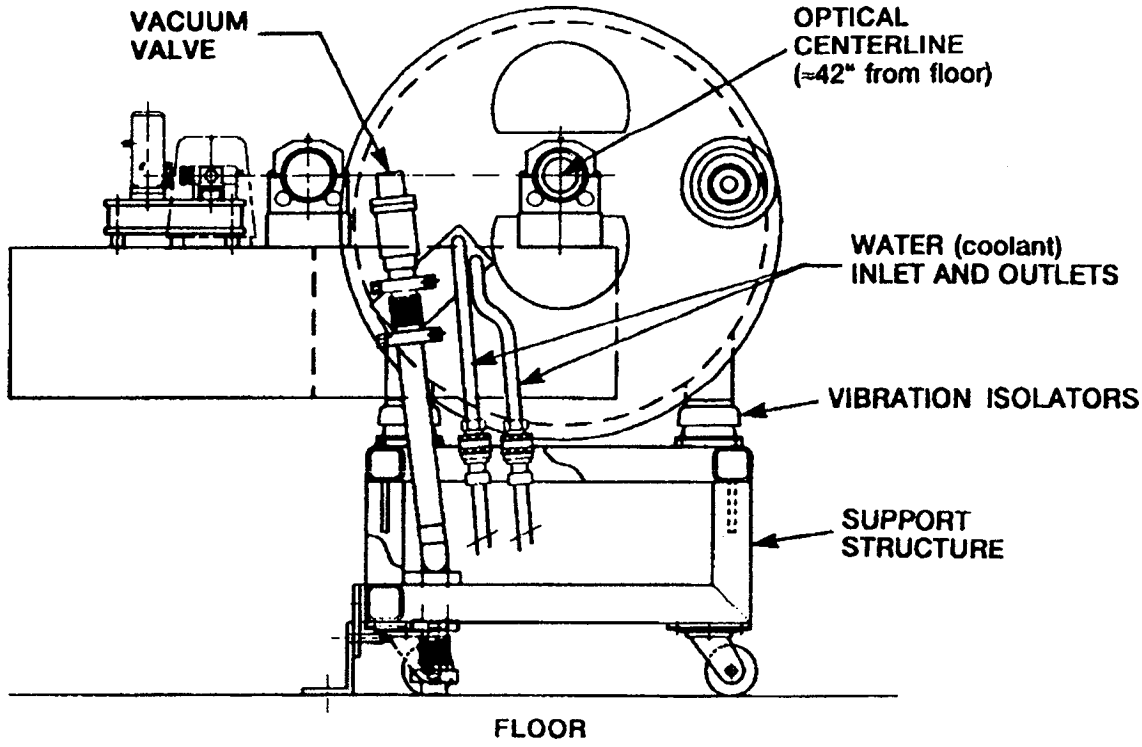

Figure 6.1-18 Laser Breadboard End Elevation

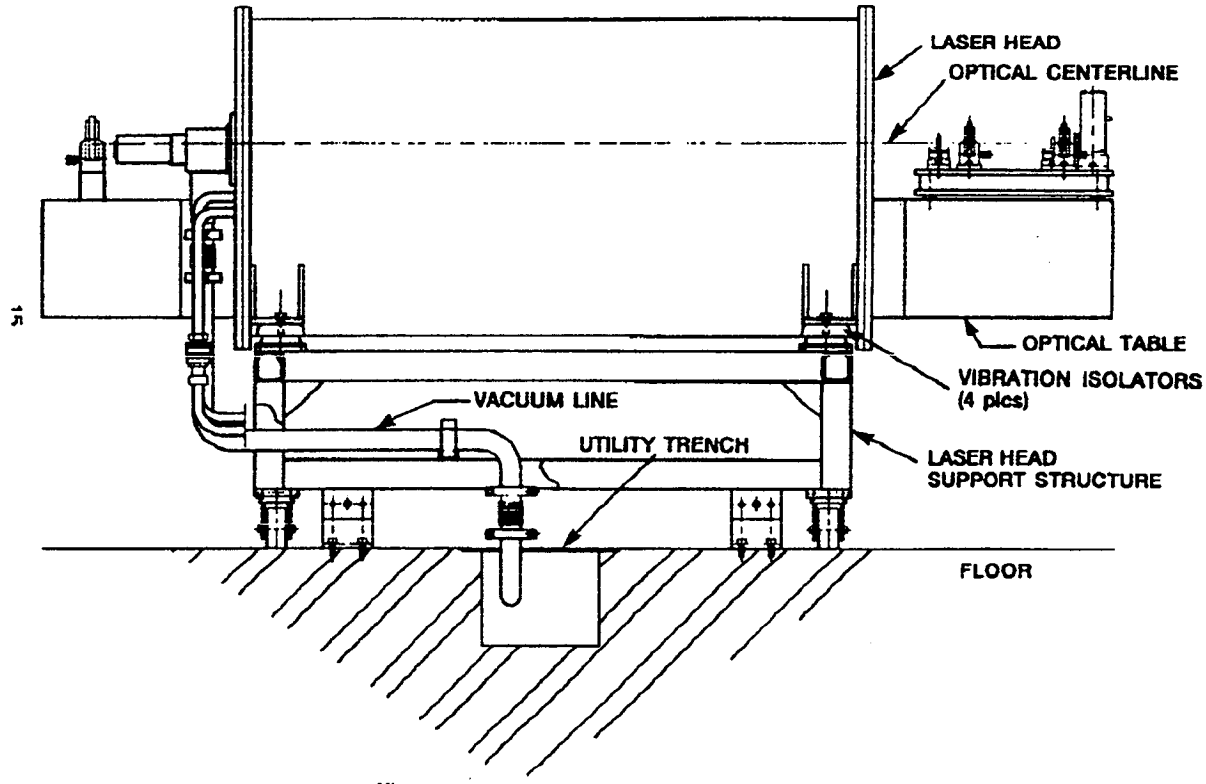

Figure 6.1-19 Laser Breadboard Side Elevation

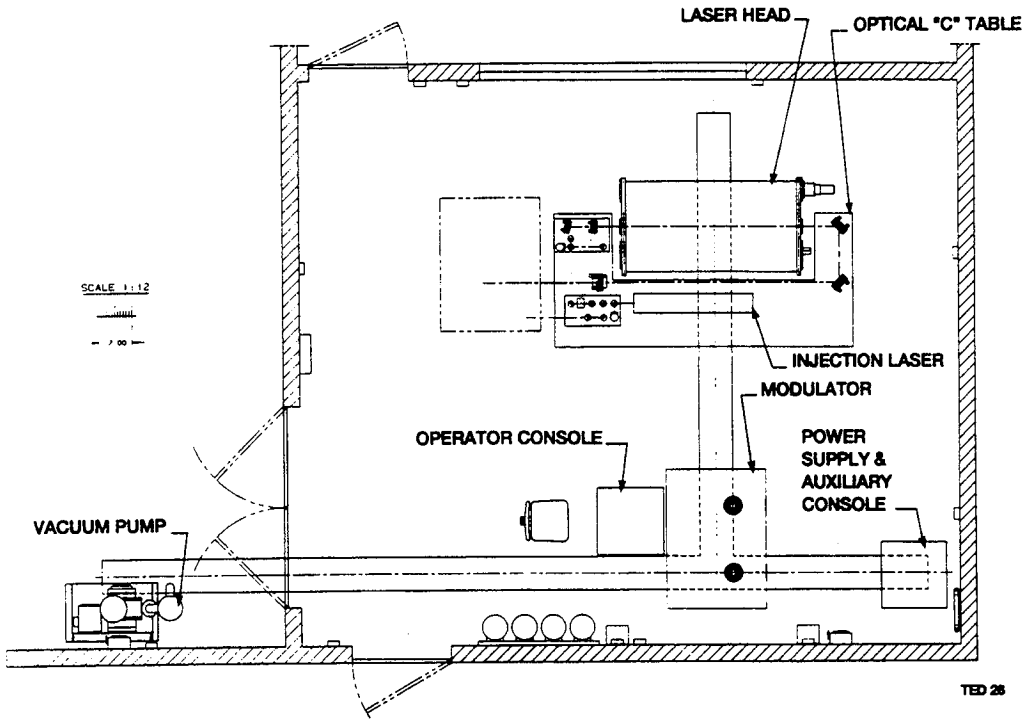

Figure 6.1-20 LAWS Laboratory Layout

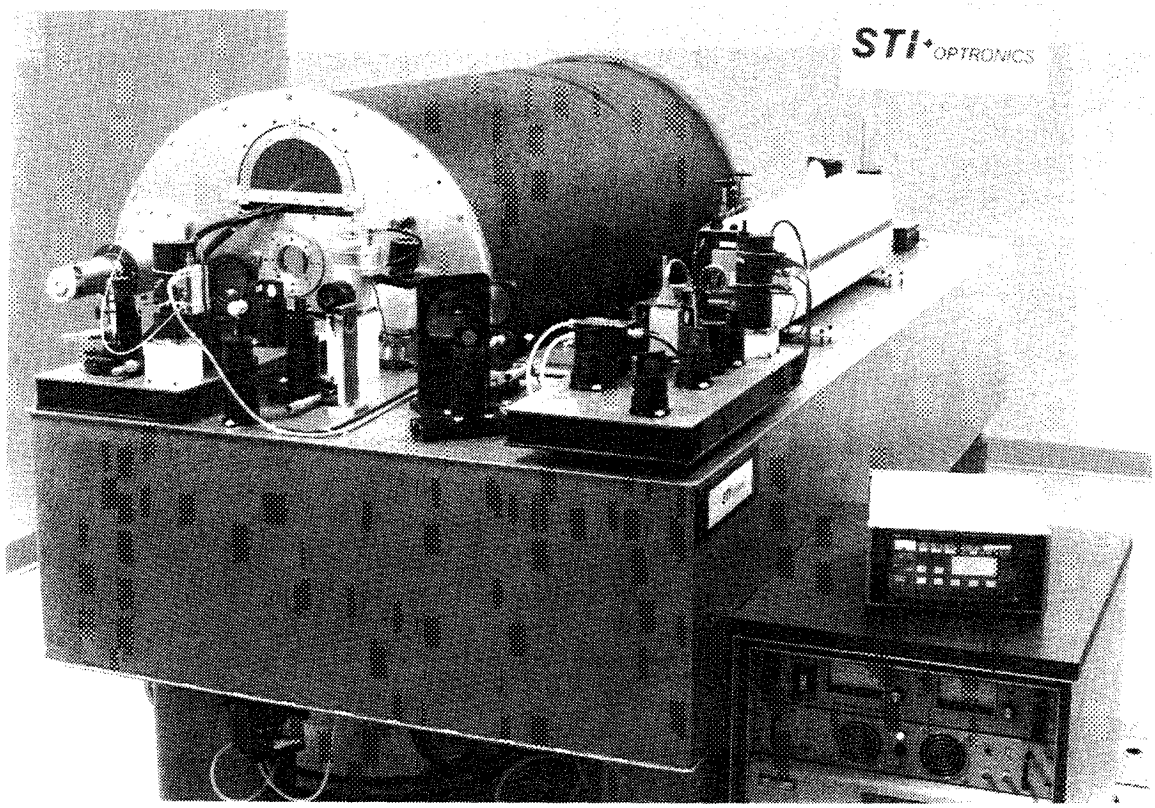

Figure 6.1-21 Perspective Photograph of Performance Breadboard Laser

Breadboard Laser Status and Performance

The integration of the laser is complete and preliminary performance results have been obtained. The following discussion summarizes the operational status of the individual laser modules and concludes with the results of measurements conducted on the output pulse. During laser shakedown, modifications were made to some of the technical approaches relative to the baseline design and these are noted for each of the modules affected. Areas where additional effort will be required to maximize the performance of the laser are also identified.

Gain Module

A nominal energy loading of 140 J/l-atm has been achieved at 200 cavity pressure (equivalent to a total stored electrical energy of 140 J) at pulse repetition frequencies of up to 5 Hz. While higher loadings at higher pressure were also demonstrated, the discharges were not stable for every shot under these conditions. Our current assessment is that additional (coupled) flow-loop configuration

and pulse forming network output pulse optimization is required to reach the goal of 160 J/l-atm at a 380 torr pressure and a 20 Hz PRF.

The inactive catalyst monolith was not installed since the results of the life-test phase of this effort (Section 6.2) yielded strong evidence that an intra-flow-loop catalyst bed is not required for long-life operation since gas self-catalysis was shown to be adequate.

The observed width of the laser discharge is larger than the design value (7 cm vs 5.2 cm) and there is no immediate solution for this short of redesign and manufacture of another electrode. The increased width represents a volume of excited laser gas from which there is no optical extraction, with the consequent degradation of laser efficiency.

Pulse Power Module

The pulse power system was tested into a dummy load over the full parameter envelope (voltage and prf). Measured I-V traces agree with simulated profiles. Testing over the full parameter envelope into a laser load has been limited by discharge instabilities at the higher loadings as described previously. Modifications to the pulse power system were implemented during laser shakedown to adjust the balance between capacitance and inductance in the PFN in an attempt to optimize the laser load impedance match at the required voltage. Since the impedance and sustaining voltage are gas-mix dependent, more such iterations are required to determine the optimum laser operating point.

Optical Module

The power oscillator resonator was implemented per design and is fully operational.

Optical components for the baseline resonator were designed for operation at 9.1 μm (assuming use of the rare isotope gas mixture). The components are significantly lossier at 10.6 μm, the wavelength at which all of the extraction tests conducted to date have been conducted. For example, the transmission loss of the gain windows is 2% (each) greater at 10.6 μm, and grating loss per reflection is 3% greater (the graded coupler reflectivity profile variation has not been measured). Therefore, it is to be expected that the energy extraction performance observed to date is less than would result for a laser utilizing a set of optics optimized for a 10.6-μm wavelength. The gain module window(s), diffraction grating spectral profiles and computed reflectivity profiles of the graded coupler at several wavelengths are shown in Figures 6.1-22, 6.1-23 and 6.1-24, respectively. Note that in the calculation for the latter figure, the optical coating was optimized for a wavelength of 9.85 μm, and the curve is only included here to illustrate that a significant plateau in the reflectivity profile (>10%) at the outer radii exists for wavelengths displaced from the design value.

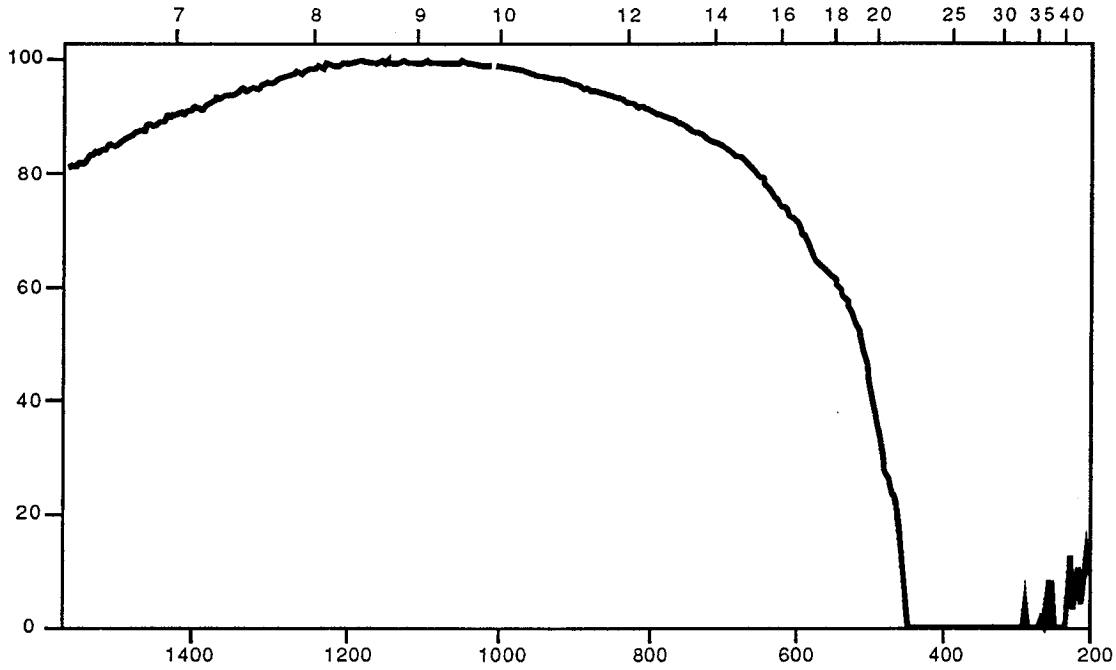

Figure 6.1-22 Gain Module Window Transmission

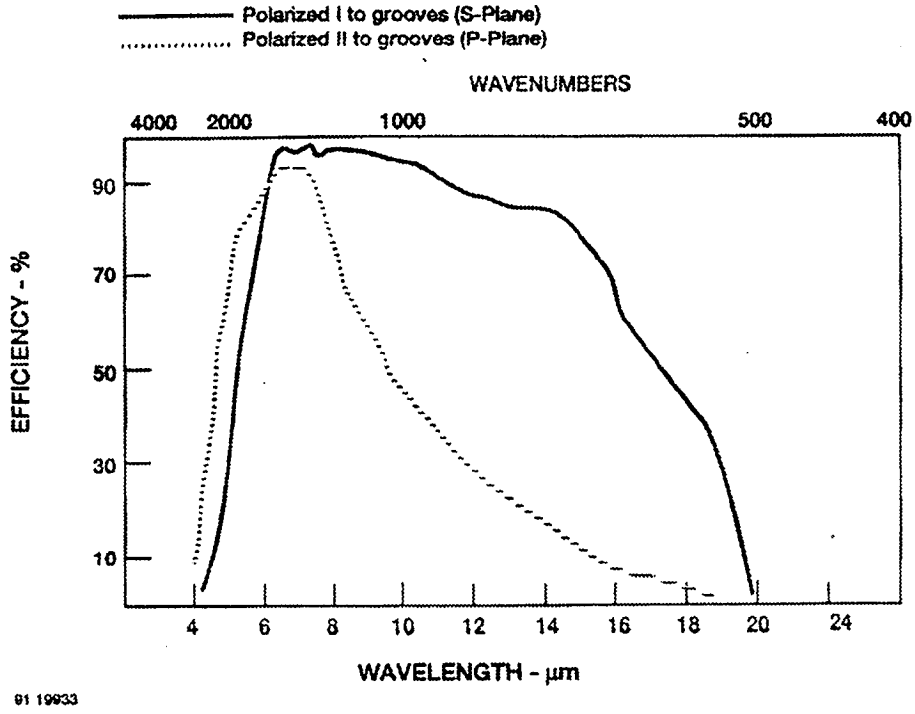

Figure 6.1-23 Grating Efficiency

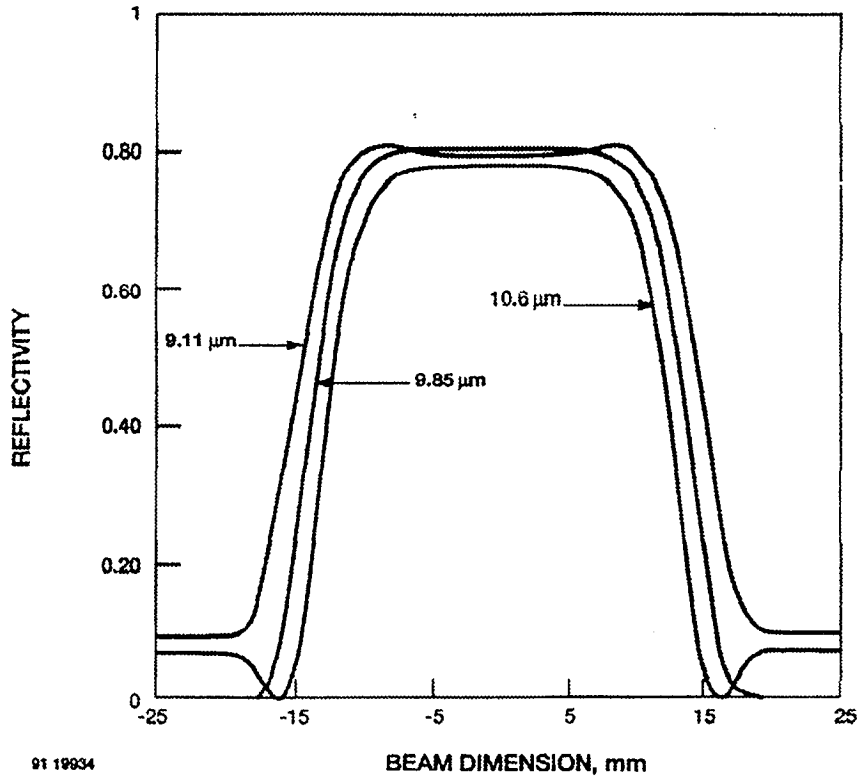

Figure 6.1-24 Graded Coupler Reflectivity

Control and Diagnostics Module

The Control and Diagnostics module is fully operational. Optical feedback (at a frequency of 60 MHz) through the acousto-optic modulator is currently impacting the performance of the laser diagnostics photodetection system. The cause has been identified as leakage of RF drive power onto the acousto-optic crystal during the nominal RF input off condition, a factory fault. A fix has been identified but has not been implemented (shorting of the RF driver's VCO source output using an RF switch).

Full-up Laser Performance

Preliminary measurements of the primary pulse parameters have been conducted (pulse energy, transverse beam profile and pulse power spectral density) at pulse repetition rates of up to 5 Hz. A summary of the results obtained for each of these parameters is now given.

Pulse Energy

The measured pulse energy for the laser in the baseline configuration (injected via a grating, outcoupled via the graded coupler and tuned to a wavelength of 10.6 μm) is 6 J. The pulse energy is measured using a wide-aperture Molectron energy meter, a thermopile-based device. The pulse

energy is currently being limited by the gain module coating, grating efficiency and graded coupler reflectivity losses referred to earlier due to operation at the 10.6-μm wavelength vs the design wavelength at 9.11 μm. There is also evidence that the grating loss is significantly higher than manufacturer specification, at least for the configuration (angular arrangement) in which it is being used. This evidence is based on measurement of the pulse energy when the grating is replaced by a concave mirror of 30 m radius of curvature (vs the optimum 40 m). The >15 J reading obtained exceeds the 15 J goal for the Performance Breadboard. Currently when operating in this configuration the laser is not being injected, so that it oscillates simultaneously on many longitudinal modes. Single-tranverse-mode operation was observed, however. Typically the sum of the energies in all the longitudinal modes transforms into a single longitudinal mode during injection. On delivery of a custom beamsplitter, currently on order, it will be possible to repeat this measurement using an optimum resonator arrangement under injection conditions. When both the grating and output coupler were substituted by a set of stable resonator optics the observed pulse energy increased to >22 J. However, this energy includes the contribution of several transverse modes.

With the diffraction grating included in the configuration, it would be possible to operate the laser at wavelengths <9.5 μm, which would partially overcome the wavelength dependent cavity losses referred to earlier. However, for the abundant CO_2 isotope, the optical gain for this band is considerably reduced . The reverse is true for the rare isotope and in addition the peak gain values are higher. Thus high pulse energies can not be expected for the abundant isotope gas mixture at a wavelength <9.5 μm. Laser operation using the rare isotope gas has been deferred pending optimization of the laser because of the high cost of the gas.

Transverse Beam Profile

There is qualitative agreement between the modeled transverse beam intensity profile (Figure 6.1-25) and the features of a burn pattern obtained 1' downstream of the laser output coupler (Figure 6.1-26). In the latter figure, the high intensity annulus is the lighter region encircling the central core, the lighter shade being the result of bleaching of the heat sensitive paper.

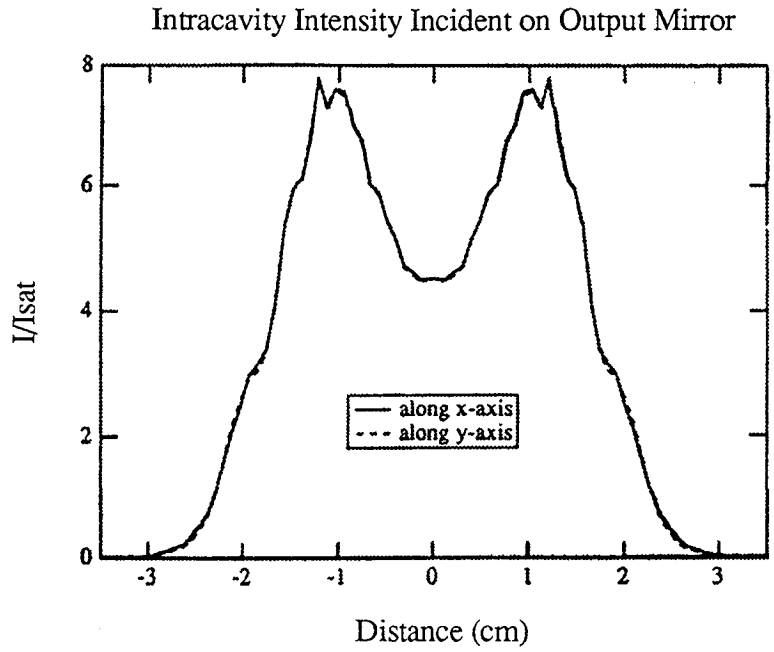

Figure 6.1-25 Effect of Electrodes on Mode Intensity Profile

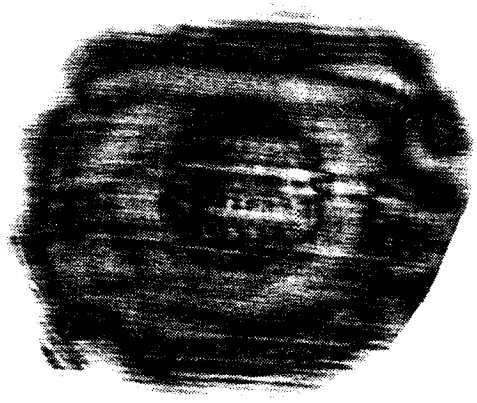

Figure 6.1-26 Laser Burn Pattern

Pulse Power Spectral Density (chirp)

The optical pulse temporal energy profile is shown in Figure 6.1-27 and is the output of a gold-doped germanium photodetector operated in the energy detection mode.

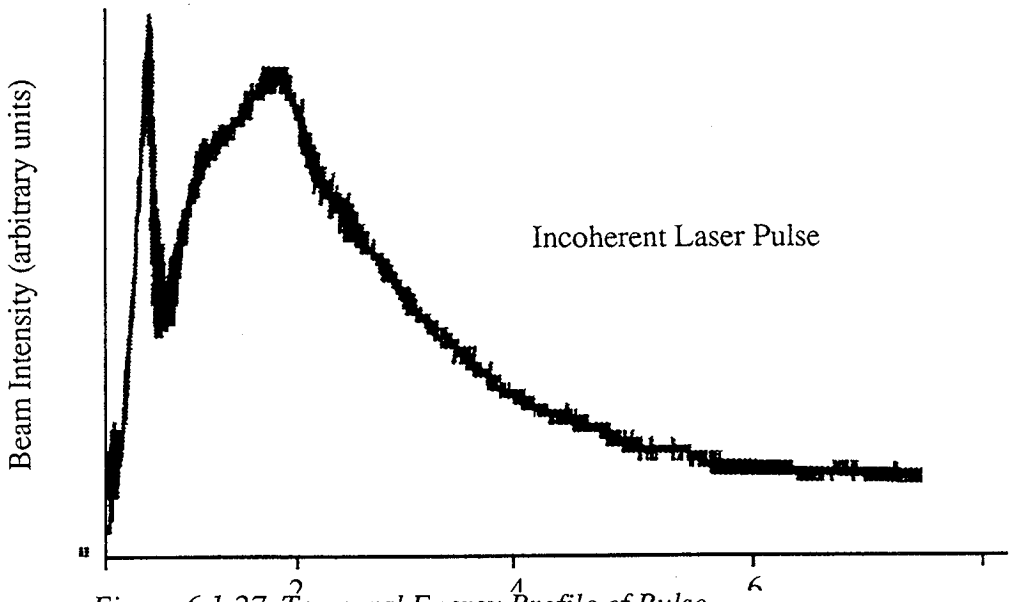

Figure 6.1-27 Temporal Energy Profile of Pulse

The counterpart heterodyne signal is shown in Figure 6.1-28 and is the output of a mercury cadmium telluride germanium photodetector operated in the heterodyne mode.

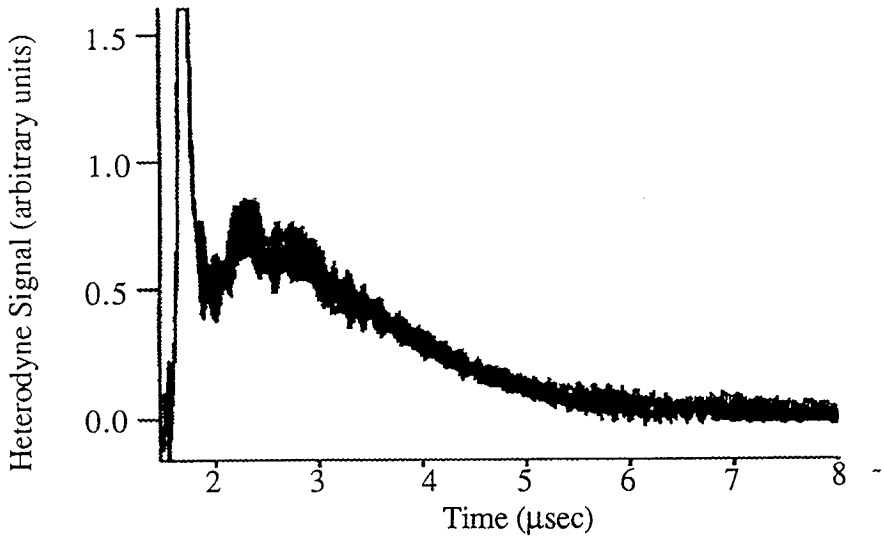

Figure 6.1-28 Heterodyne Output of Pulse

The signal appears at a frequency of 60 MHz (double the 30 MHz acousto-optic IF), since the displayed beat is due to photomixing of the local oscillator beam derived from the injection laser and leakage of the power output pulse back through the acousto-optic modulator where it is upconverted in frequency by an additional 30 MHz. The wide-band power spectral density of the heterodyne pulse, shown in Figure 6.1.28, is shown in Figure 6.1.29, and an expanded version centered at 60 MHz is shown in Figure 6.1.30. The energy is concentrated within a bandwidth of

approximately 0.5 MHz indicating that the frequency chirp does not contribute substantially to the overall spectral width since the transform limit of the pulse (= inverse of the pulse duration) is of similar magnitude.

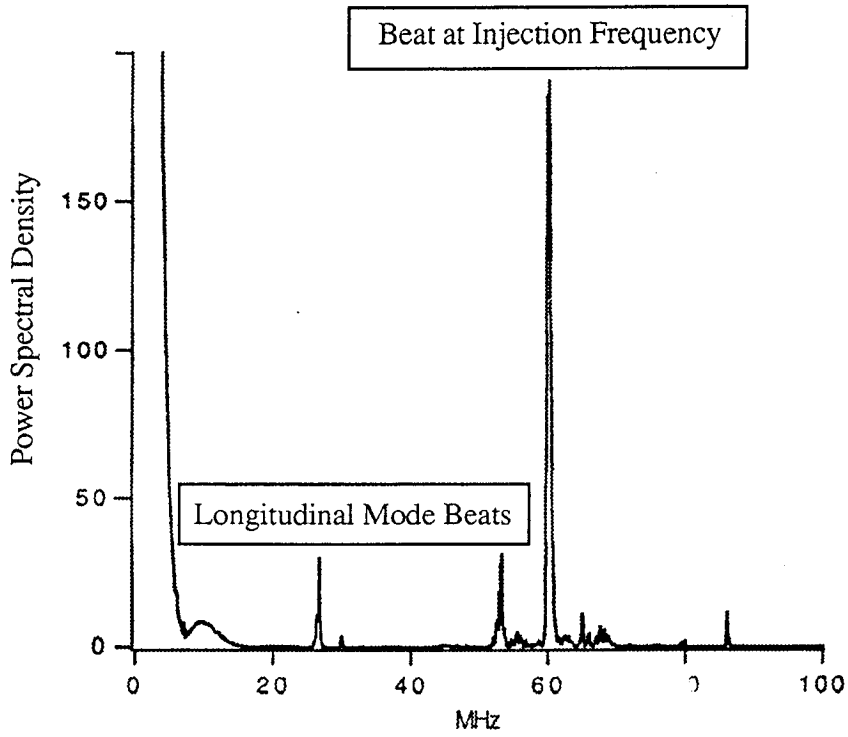

Figure 6.1-29 Power Spectral Density of Pulse

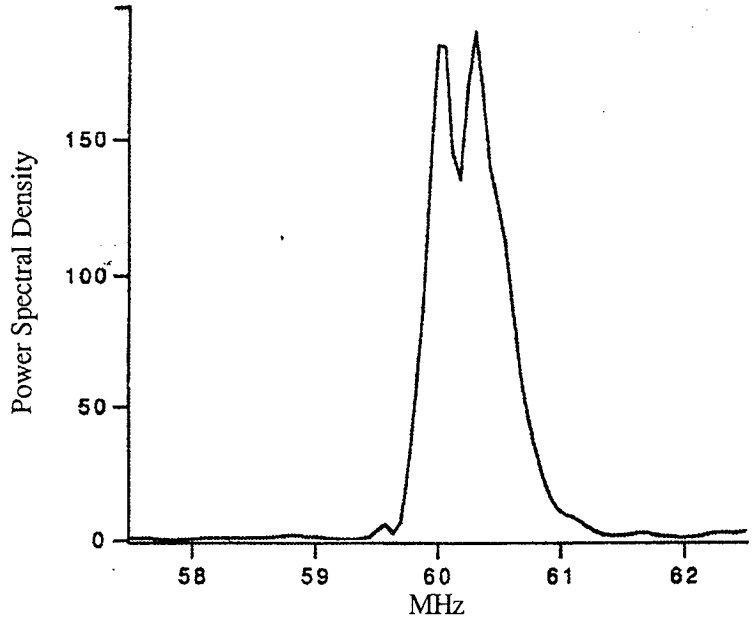

Figure 6.1-30 Power Spectral Density of Pulse Around 60 MHz

6.2 Life-test Program

DESCRIPTION OF THE TEST AND DIAGNOSTIC SET-UP

The goals of the life-testing program include the evaluation of system life and reliability issues by performing long duration (large shot number) tests culminating in 10^8 shot duration runs using the STI Optronics-owned CO_2 Laser Testbed (CO_2LT). The CO_2LT is essentially a clone of the NOAA Windvan gain module manufactured by STI Optronics about a decade ago. It was fitted with an external catalyst loop to facilitate extended duration runs to investigate the laser chemistry at large shot number. Catalyst obtained from two sources (Langley Research Center and UOP Plc.) were used during the investigation. Both abundant and rare-isotope $^{12}C^{18}O_2$ gas were used. Previously, GE Astro-Space and STI Optronics-funded IR&D efforts had established the baseline chemistry at the one million shot level, provided for installation of complete CO_2LT diagnostics, and validated gas chemistry models. Prior to initiation of tests under the current program (late September 1991), internally-funded modifications to the CO_2LT flow ducting and shell were completed. The resulting increase in flow efficiency and uniformity has decreased the power required to drive the fans and increased the clearing of the flow from the discharge volume. The combined effect of these modifications increased the reliability of operation at a 35-Hz pulse repetition frequency (PRF). Modifications to eliminate dead volumes, plastics and virtual leaks

were also done to the shell of CO_2LT to improve vacuum integrity. A photograph of the CO_2LT device with diagnostic systems in place is shown in Figure 6.2-1. The diagnostic systems in place include the following:

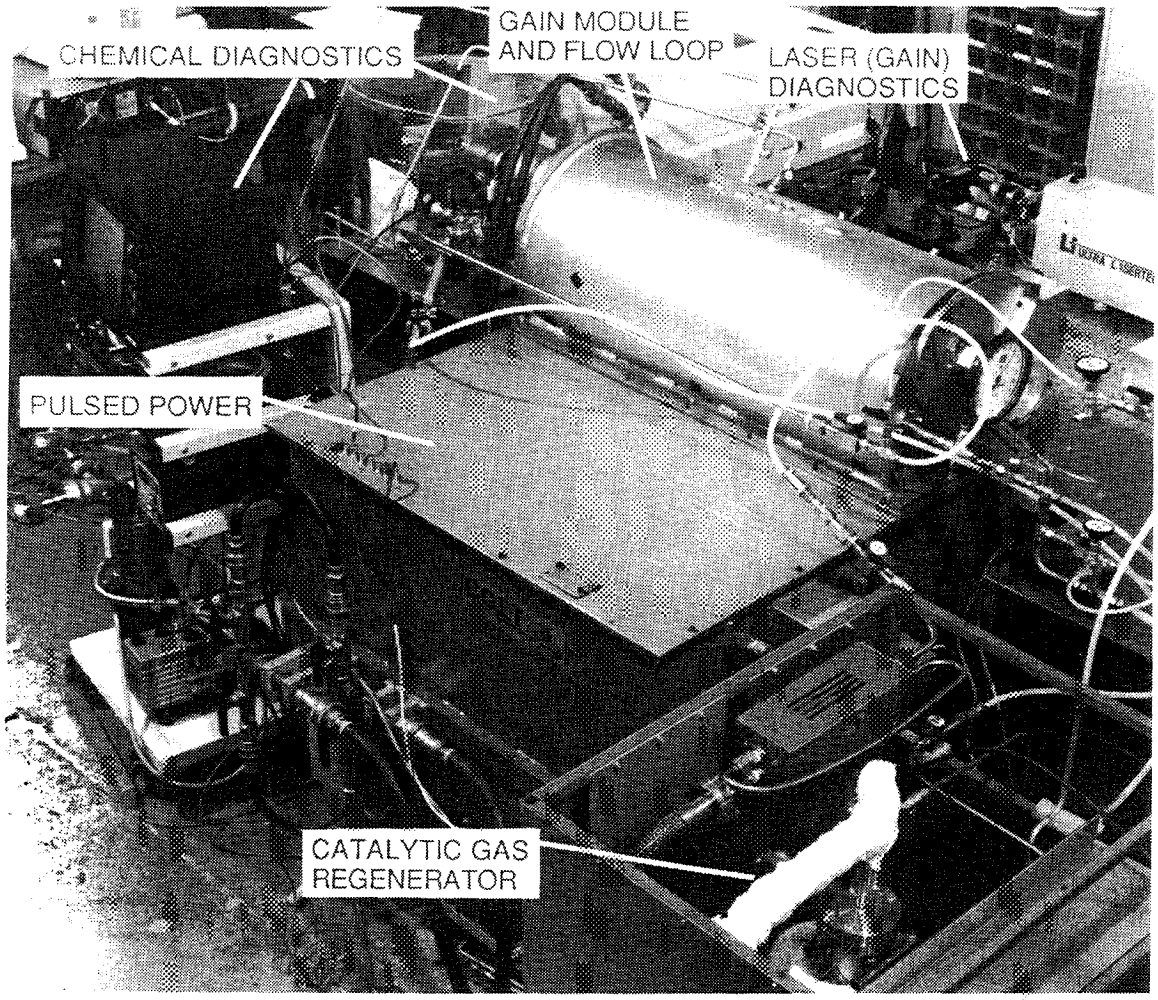

Figure 6.2-1. LAWS Life Test Bed

- A mass spectrometer used to periodically analyze a sample of the gas drawn from the laser cavity. This proved particularly useful in assessing the O_2 level in the gas mixture formed by dissociation of CO_2, and also in assessing the relative abundances of the various CO_2 isotopes during nominal rare isotope runs.
- A Nicolet Fourier Transform Infrared Spectrometer capable of performing *in-situ* laser cavity spectral analyses of the gas, since the sampling optical beam traverses a path along the length of the laser at a station located in the flow loop. This proved particularly useful in assessment of infrared active molecules, specifically CO, since its

mass peak coincides with N_2 and makes the mass spectrometer reading ambiguous during abundant CO_2 isotope runs. The FTIR output was calibrated against the indications for a gas mixture introduced into the laser prior to the runs which included a known quantity of CO.

- A laser medium gain measurement set-up capable of *in-situ* monitoring of the single-pass gain along the axis of the gain module. It consists of an Ultralasertech CW laser beam that is propagated down the axis of the gain module and directed onto an infrared detector, where the increase in laser power during discharge excitation is measured.
- Measurement of discharge I-V curves to establish the laser discharge energy loading

The diagnostic set-up is depicted in Figure 6.2-2.

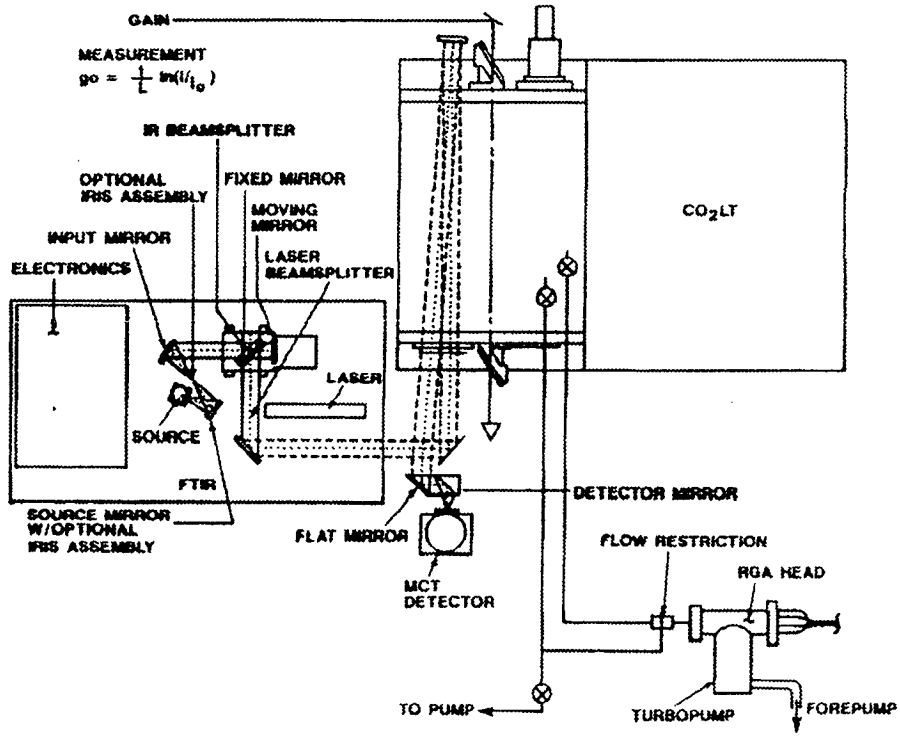

Figure 6.2-2 CO_2LT Gas Life Diagnostic Setup

LIFE-TEST PROGRAM RESULTS

The life-test program undertaken subdivides into three phases:

1) A preliminary experimental phase to condition the system for extended duration runs.
2) A nominal 10^8 shot run using abundant isotope CO_2, during which 1.1×10^8 shots were actually achieved.

3) A nominal 10^8 shot run using rare isotope $^{12}C^{18}O_2$, during which 0.55 x 10^8 shots were actually achieved.

The following discussion is subdivided accordingly. None of these phases involved optical energy extraction since the goal of these tests was limited to investigation of gas and component life. It is recommended that future life testing incorporate optical extraction so that all aspects of laser operation can be assessed simultaneously.

Preliminary Experimental Phase

The preliminary experimental phase of the effort extended from September 1991 through March 1992 and consisted of several short duration life runs at the 10^6 through 10^7 shot level and constituted a shakedown for the longer duration 10^8 shot level tests. This phase of the effort was conducted exclusively using abundant isotope CO_2 gas and the catalyst provided to us courtesy of NASA/Langley Research Center (Contact: Billy T. Upchurch). Four hundred gm of catalyst was loaded onto four monoliths of 400 cell density Corning Cordierite 9475 (3.0-in. diameter, 3.0-in. thick discs) and stacked vertically in an aluminum cylinder catalyst cell and loosely packed with glass wool. The catalyst cell was inserted in the laser flow system (external to the gain module flow loop) and surrounded by heating tape such that its temperature could be varied during the testing. The catalyst cell could also be totally flow isolated from the laser head. The composition of the catalyst was not known to us.

A total of two 10^7 shot and two 10^6 shot runs were completed during this phase. These runs served primarily to highlight several shortcomings within the gain module.

The first concerns operation at the highest possible pulse repetition rate. The goal was to operate at a PRF in excess of 50 Hz at the nominal 28-kV PFN charge voltage (corresponding to a 70 J/(liter-atm) energy loading at 300-torr cavity pressure) to minimize the time to accumulate a given number of shots. However, operation at this rate proved marginal and led to frequent arcing and system shutdown by the automated arc detection/shutdown system. This led to the decision to reduce the PRF to 35 Hz, at which rate stable operation was achieved. We hasten to add that even this reduced PRF is well in excess of the baseline LAWS laser PRF, and thus does not represent any inherent limitation of CO_2 laser systems for on-orbit use, but merely an extension of the time to acquire a given number of shots during life testing. With the benefit of the knowledge regarding gas mixtures, discharge loading, etc., gained as a result of the extended life tests to be described later, it was possible to obtain stable operation at 50 Hz over the several hours sample period near the end of this test program. However, an increase in the flow margin would be desirable for future tests. Marginal flow properties contributes to a non-uniform discharge which in turn

translates to a higher equilibrium O_2 level and, consequently, increased proneness to arcing. Upgrades to the flow loop were not possible within the time and funding constraints of the current program. We recommend that the fan within the gain module be modified prior to future tests to increase the flow margin. The current fan is an off-the-shelf aluminum construction cross-flow design consisting of two sections to span the length of the laser and mechanically coupled in the center of the laser. The revised design would be of single section stainless steel construction with the blades brazed to the support bulkheads. This would afford higher rigidity at higher rotational speeds and also eliminate the "dead volume" in the center due to the mechanical coupling. Since the fan is balanced using reverse rotation of the blades prior to insertion into the laser and, hence, at atmospheric pressure, the increased rigidity would also minimize the change in balance that currently occurs under laser pressure head conditions.

The second shortcoming that came to light during the first 10^7 shot run was a deposit that formed on the cathode. Subsequent analysis showed that this film had a high silicon content, and we concluded that its source was the silicon-loaded epoxy insulator in which the electrodes were embedded. Prior to the second 10^7 shot run, the silicon-based epoxy was removed and replaced with an alumina-filled epoxy. During the second 10^7 shot run, there was no external evidence of a film forming on the electrode. On examining the electrodes at the end of the run, however, a light film was observed. Analysis of this film showed a preponderance of zinc and copper, probably in the form of oxides, and negligible amounts of aluminum. Thus, the epoxy contribution to the film was now minimal and we ascribed the source as sputtering of the brass electrodes. Given that the film did not markedly affect the qualities of the laser discharge, that a resistive film on the electrodes is sometimes considered advantageous for discharge stability, and coupled with the reality that upgrades to the electrodes were not possible within the time and funding constraints of the current program, we decided to proceed without any further modifications to the discharge region. However, additional effort on electrode material compatibility is clearly recommended. For example, we have previously found that the Pt coating of electrodes is a rugged solution for the highly corrosive environments of long-life, high-repetition-rate, high-energy excimer lasers.

Early during the effort we experienced a corona bar failure. This represents the first such corona bar failure since early designs were being evaluated. After several 10^7 shot runs with a substitute corona bar, we experienced extensive arcing due to the sagging of its unsupported ends and shortly thereafter it shorted during use after an attempt to straighten it broke the ceramic epoxy bond around one of the ceramic blocks, thus effecting a corona bar short. We consider the sagging an engineering issue which has been solved by additional strengthening of the corona bar using a strong-back plate. Another substitute corona bar performed flawlessly throughout the long-life runs to be described, during which tests close to 2×10^8 shots were accumulated. Flawless

performance of these corona bars (provided by STI Optronics) has been experienced by NOAA and GE Astro-Space in CO_2 lasers, and also by us in high-repetition-rate, high-energy excimer lasers.

On the more mundane level, we also experienced an air leak in a flow sampling line coupling and the failure of a vacuum valve.

This phase of the effort, during which in excess of 30 million shots were accumulated, demonstrated also that window deposits were not being formed and that unexpected species were not being formed at higher than a 10-ppm level. Specifically, ozone and nitrogen oxide formation was negligible. The quantitative data obtained during this phase was superseded by the data obtained during the longer life runs, and since, for the most part, it was taken during a program of resolution of system problems it is not summarized here.

10^8 Shot Abundant Isotope Run

After completion of the preparation and modifications to the CO_2LT described above, a long duration (100 million shot goal) run was attempted during April 1992 using a gas fill containing the abundant CO_2 isotope. The purpose of this test was to further qualify the performance of the device and measurement methods before initiation of tests using the rare isotope CO_2 gas mixtures. A research-grade fill of gas ($He:N_2:CO_2$ = 76.7%:13.3%:10%), premixed by the supplier, was introduced into the laser flow loop to a pressure of 300 torr. This mixture had previously been determined to yield a stable discharge in the CO_2LT at the 35-Hz pulse repetition rate. It is not the baseline LAWS laser mix (3:2:1), since the available pulse power system was not capable of supplying the higher voltage required. The external catalyst bed was reduced by a CO:He mixture prior to the run and was switched on in the flow loop at the initiation of the run and nominally left on during the run except for specific experiments. The temperature of the unheated catalyst bed reached an equilibrium value of about 39 °C during continuous operation. During the early part of the run, frequent (several times daily) diagnostic data runs were conducted. The frequency of these runs were reduced to one or two daily during the latter two thirds of the run. Some of these tests required that the laser be shut-off for various reasons, e.g., sensitivity of instruments to electrical noise. So that the condition of the gas would not change during these measurement periods, the catalyst bed was switched out. Use of the mass spectrometer to monitor gas composition involved sampling of the gas in the cavity and the draining of the sampling line to ensure that a representative volume of gas was being sampled. Over time, this led to a loss of gas that was periodically replenished. The rate of loss decreased substantially when the frequency of the sampling was decreased. Over the duration of the run the total quantity of the gas replenished

amounted to 87 torr (vs the 300 torr initial pressure). The run was kept going overnights and weekends. An arc detector built into the laser acted as a sentinel over the operation and was programmed to shut down the discharge if three successive discharges resulted in arcs, in which case the laser was restarted at the earliest opportunity (e.g., the first thing in the morning or during the day, whenever that it became apparent to any one of four people that it had shut down). A electrical power glitch, as happens frequently in the Seattle area because of power line interaction with trees during breezy conditions, would also shut down the laser discharge. After such shutdowns, the catalyst bed remained switched into the system. Several times, the shutdowns were due to system faults which had to be corrected and these will be described later. None of the resulting repairs required opening up the gain module and hence loss of the gas sample.

The main diagnostics were, respectively, the Fourier Transform Infrared (FTIR) spectrometer output, the optical gain measurement on the P(20) transition (both *in-situ* measurements) and the mass spectrometer output, which required the drawing of a gas sample. The FTIR spectrum (absorbance) of the initial gas mix is shown in Figure 6.2-3. Notably absent are the CO fundamental (2100 cm^{-1}) and overtone (4200 cm^{-1}) bands, which are very evident in the spectrum of the gas sample after 104 million shots, Figure 6.2-4. There is also no evidence in the spectrum at the end of the run of any build-up of undesirable contaminants, specifically ozone and the nitrogen oxides. The FTIR spectra proved very useful in that they provided an accurate measure of the CO concentration. The overtone spectrum was used for this assessment since the band strength is linear with concentration at small absorbance while the band strength of the fundamental is not. The FTIR CO spectrum was calibrated by introducing a known concentration of CO into a laser mix prior to and after the run. After background subtraction, the CO overtone spectrum is shown in Figure 6.2-5. CO concentrations were derived after integration over this spectrum. For the abundant isotope gas mix the CO concentration could not be assessed from the mass spectrometer output because of the overlap of the CO^+ and N_2^+ peaks. A typical optical gain profile throughout the laser pulse is shown in Figure 6.2-6 and was used as a surrogate measure of the "lasing" potential of the gas mix, a measure that is not contaminated by resonator fine-tuning uncertainties. The initial positive step in the trace is due to the switching in of the CW CO_2 beam by an acousto-optic modulator and is a measure of the input beam intensity, and is followed by the exponentially decaying optical gain profile, due to the discharge and finally the negative going step when the acousto-optic modulator is deactivated. Trace amplitude within the gain profile is ratioed to the amplitude of the step to yield the gain. A typical mass spectrometer profile is shown in Figure 6.2-7 and was used primarily for assessment of the level of oxygen, e.g., oxygen production rates, and the relative abundances of the CO_2 isotopes (rare isotope run). It proved very useful in

assessing catalyst effectiveness by observing the rate of oxygen clean-up during discharge shutdown periods with the catalyst loop switched in.

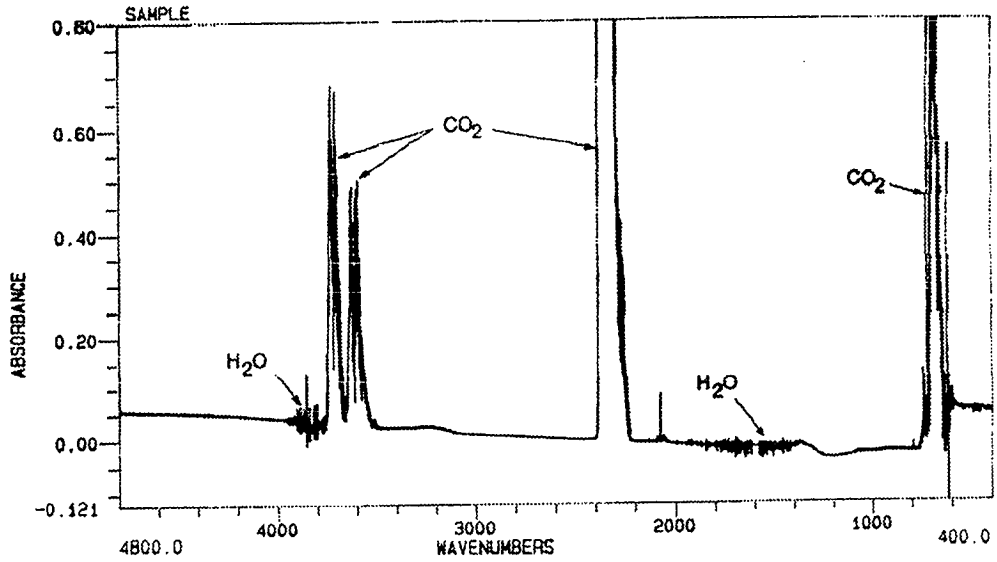

Figure 6.2-3. FTIR Spectrum of Starting Gas Mix

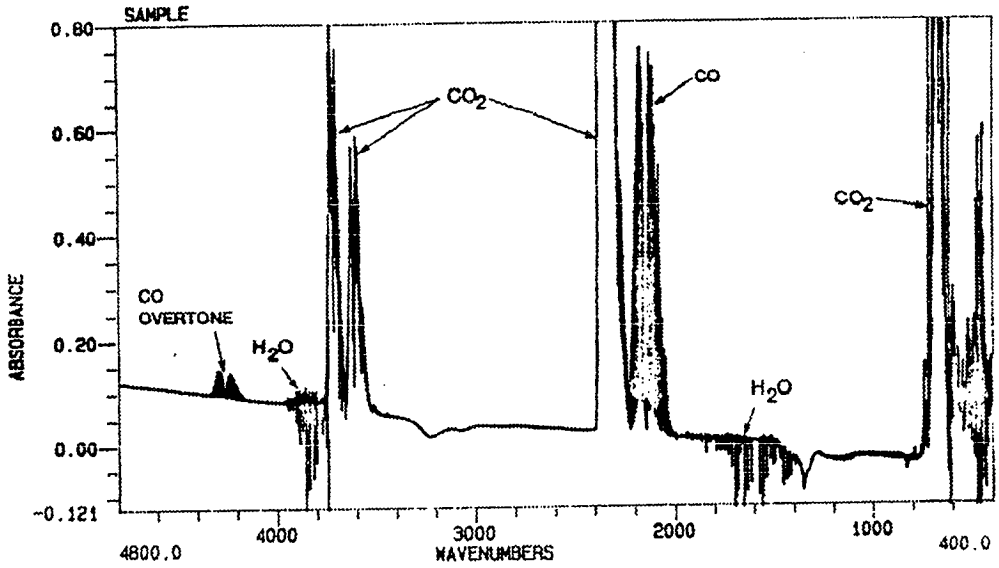

Figure 6.2-4. FTIR Spectrum of Gas After 104-Million Shots

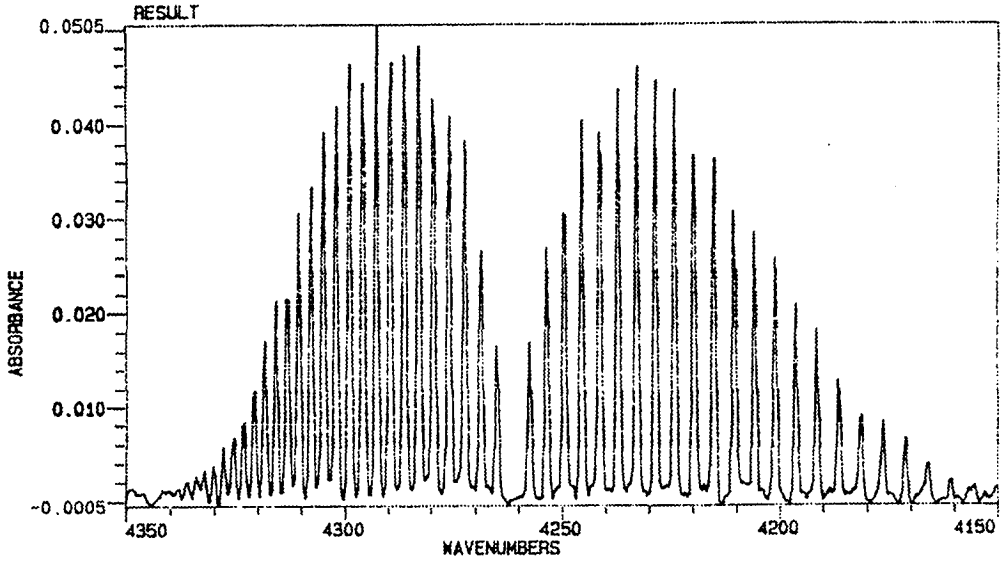

Figure 6.2-5. FTIR Spectrum of CO Overtone After 104-Million Shots

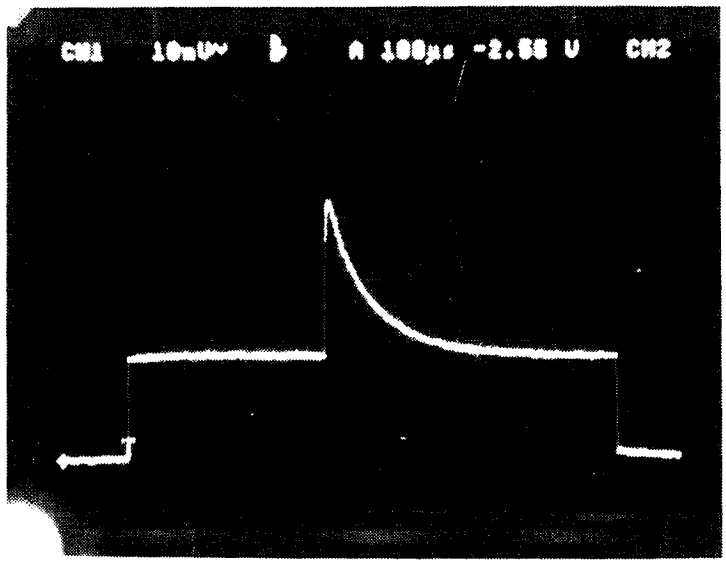

Figure 6.2-6. Example Oscilloscope Trace Used for Optical Gain Measurement

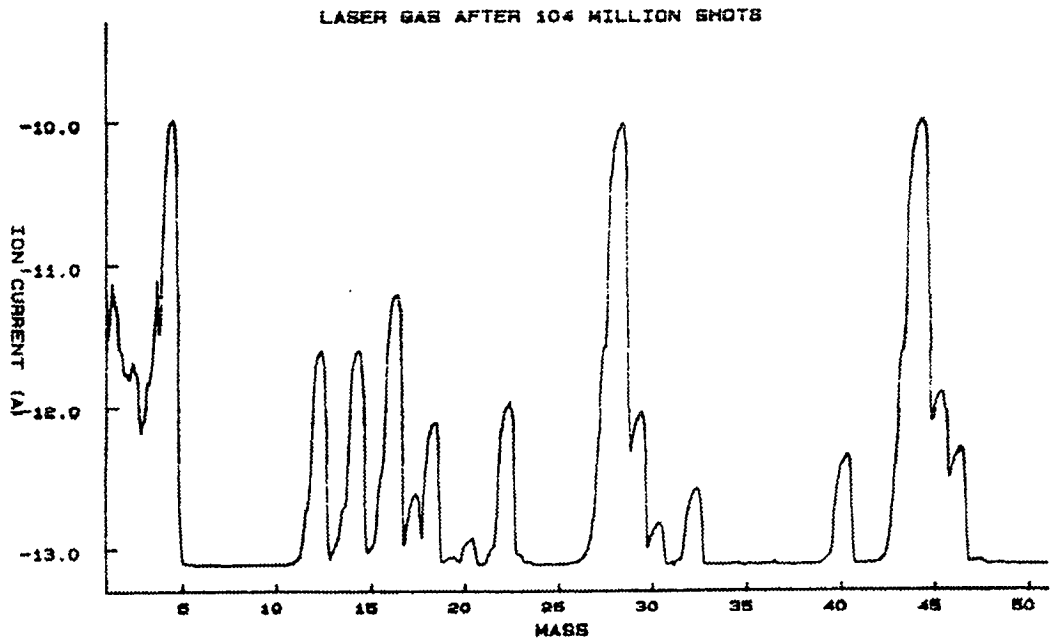

Figure 6.2-7. Example of Mass Spectrometer Output (Abundant Isotope Run After 104-Million Shots

A plot of the relative optical gain and CO concentration throughout the 10^8 shot run are shown in Figure 6.2-8. Annotations for significant events are appended. (Note that the optical gain is normalized by the initial gain and the CO concentration by an early value of the CO concentration and not the initial value, since this was zero). A general observation is the expected anti-correlation between the optical gain and the CO concentration. The optical gain was maintained in excess of approximately 80% of the initial gain throughout the run. The early part of the run (1 - 5 million shots) displays a precipitous drop in the gain, and an attendant increase in the CO level. Arcing of the discharge became very frequent at this time and the decision was made to heat the catalyst. This resulted in an immediate reversal of the deterioration - a dramatic increase in the gain and decrease of the CO level. At this time we believed that the primary reason for this reversal was a significant increase in the catalyst activity with temperature, even though regardless of temperature, the catalyst appeared to be equally effective in removing the CO/O_2 with the laser discharge off. After about 20 million and up to about 65 million shots, the optical gain and CO levels achieved a kind of equilibrium. During this time a few adjustments were made to the catalyst temperature as noted in Figure 6.2.8 whenever discharge arcing appeared to be getting out of hand. At about the 70-million-shot level, we experienced two failures in rapid succession. A failure in the insulation of a cable connecting the switchable DC high-voltage supply was followed by a failure of both a PFN

capacitor and the inverting transformer incorporated in CO_2LT. We suspect that the short in the transformer was related to the capacitor short. Perturbations to the gain and CO levels that occurred around this time were probably due to precursors to these failures. All of the components that failed were external to the gain module and fixes were implemented without disturbing the gas fill. After restart, the gain and CO levels approached their "equilibrium" level. Late in the run at around the 85-million-shot level, the catalyst was cooled on two occasions in an attempt to evaluate its efficiency vs temperature. Discharge performance degraded with the consequent arcing, gain decrease and increase in the CO level. These trends were reversed on reheating. After one of the diagnostic runs, the catalyst loop was inadvertently left disconnected for a 24-hour period during which extremely stable operation of the discharge was observed. That the CO/O_2 levels could be maintained without the use of a catalyst for 10-million-shots led us to the conclusion that the dominant catalytic process occurring was gas self-catalysis (or homogeneous catalysis), and that the apparent variation of catalytic efficiency with catalyst temperature was due to the temperature dependence of the water retaining properties of the (in-homogeneous) catalyst. We intentionally repeated this experiment with similar results about 101-million shots into the run. It is well known to us and others (e.g., Willetts et.al.[1]) that adding a few percent of hydrogen to the gas mixture contributes immeasurably to the life of the gas mixture. For example, this has been standard procedure for the NOAA Windvan laser since it was delivered about ten years ago. In this particular run, since hydrogen was not included in the original mix, we believe that the laser was sufficiently contaminated with water at the start of the run that the required hydrogen concentration developed naturally. We believe also that CO plays a major role in the catalytic process. As a follow up to this run, we embarked on another long-life (10^7 shot) run using a fresh gas mix, including a few percent each of H_2 and CO, and depending solely on self-catalysis; this run is described later. During the latter part of the 10^8 shot run, beyond about 90-million shots, the optical gain remained relatively stable while the CO concentration increased about 50% from its "equilibrium" level during the run. Just prior to the voluntary termination of the run at around 110-million shots, the gas mix was "perturbed" by first the addition of 7.5 torr of CO_2, and further by the addition of 3 torr of O_2 to evaluate the response of the system to these stimuli. The calibrated CO concentration (percent of gas mix pressure), and derived from the FTIR, during the 10^8 shot run is shown in Figure 6.2-9. Also shown in the figure are the residual level of CO after a 20 min. clean-up with the catalyst in the loop and discharge off, and the incremental amount of CO removed, respectively. The relative oxygen level derived from the mass spectrometer (mass 32) output during the run is shown in Figure 6.2-10. Time histories of the relative concentrations of some other relevant mass peaks (mass 44 = CO_2^+, mass 28 = $N_2^+ + CO^+$) are shown in Figure 6.2-11. The results of an experiment to assess the effect of temperature on catalyst performance

conducted over an eight-hour period during the 10^8 shot run are summarized in Figure 6.2-12. The left-most plot shows the optical gain and CO (FTIR) concentration dependence as the temperature is decreased. The gain is seen to decrease as the CO level builds up at the lower temperatures, since the increasing CO level represents a decrease in the amount of CO_2. The right-most plot displays the mass spectrometer derived concentrations for three mass peaks, viz. mass 28 = $N_2^+ + CO^+$, mass 32 = O_2^+ and mass 44 = CO_2^+. As the temperature decreases, the O_2 concentration increases and the CO_2 concentration decreases. The small increase in the mass 28 peak data is due to the build-up of CO.

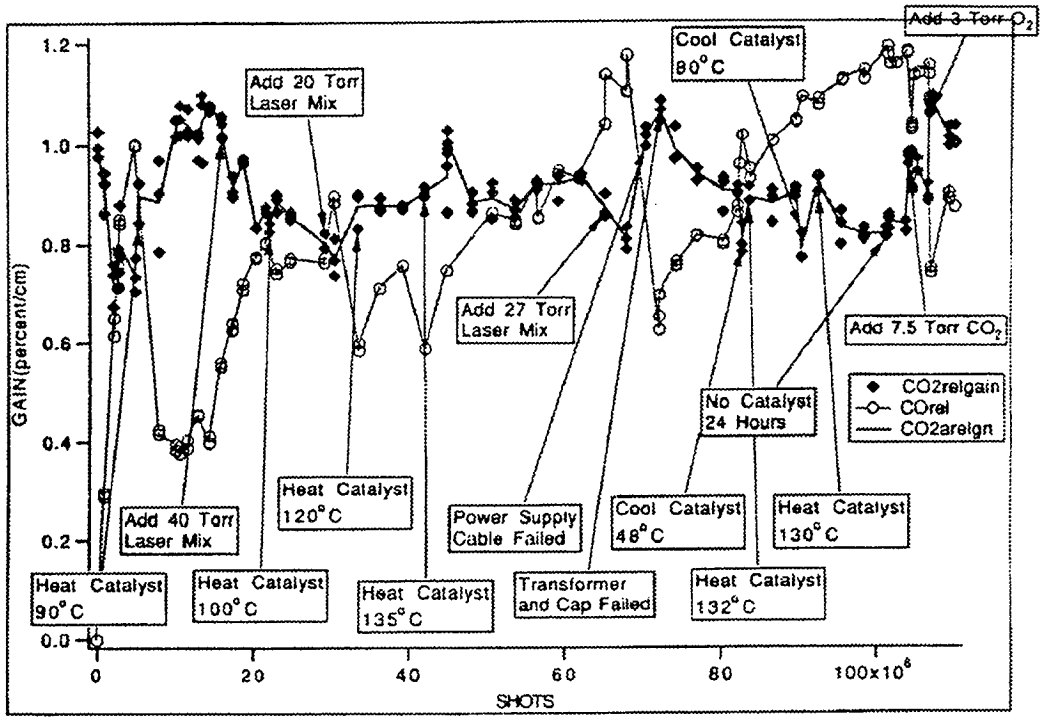

Figure 6.2-8 Plot of Optical Gain and CO Concentration During 10^8 Shot Run

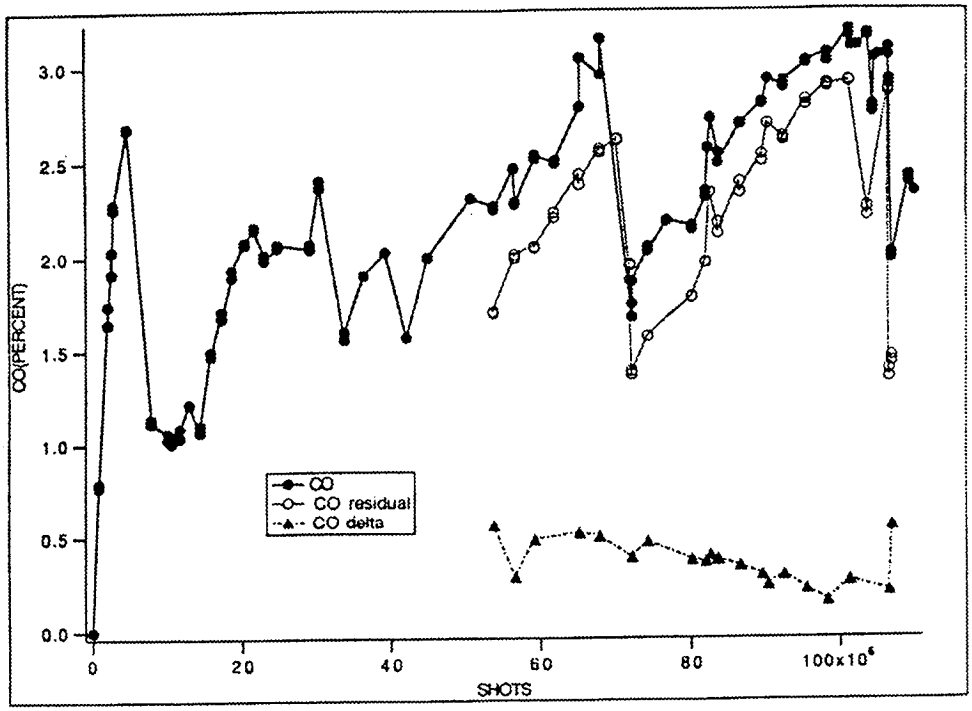

Figure 6.2-9. Calibrated CO Concentration from FTIR Spectra During 10^8 Shot Run

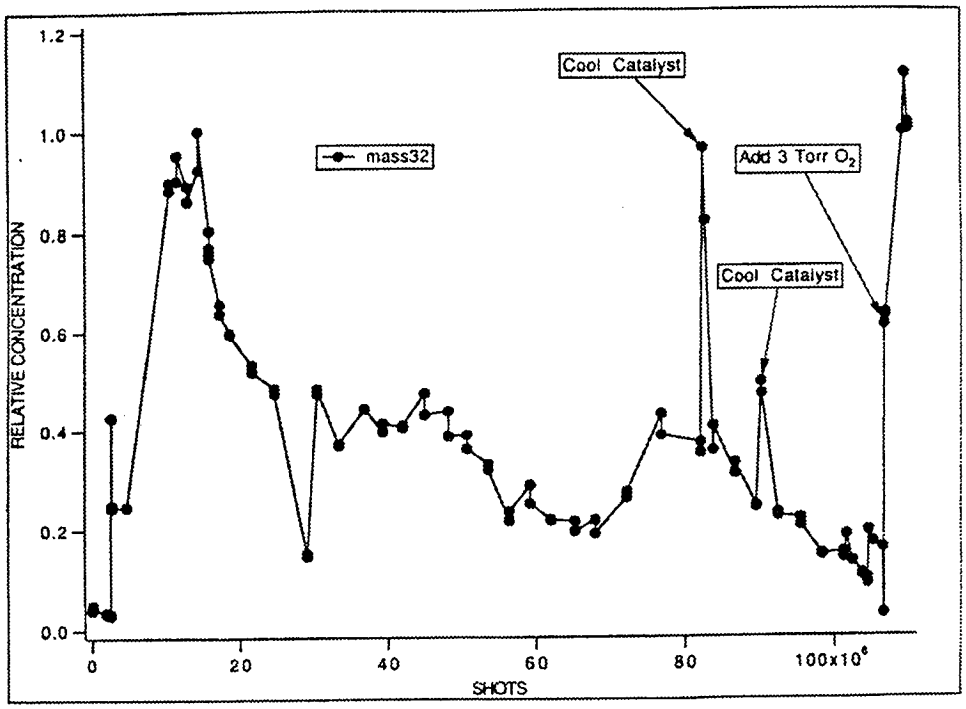

Figure 6.2-10 Relative Oxygen Concentration From Mass Spectrometer During 10^8 Shot Run

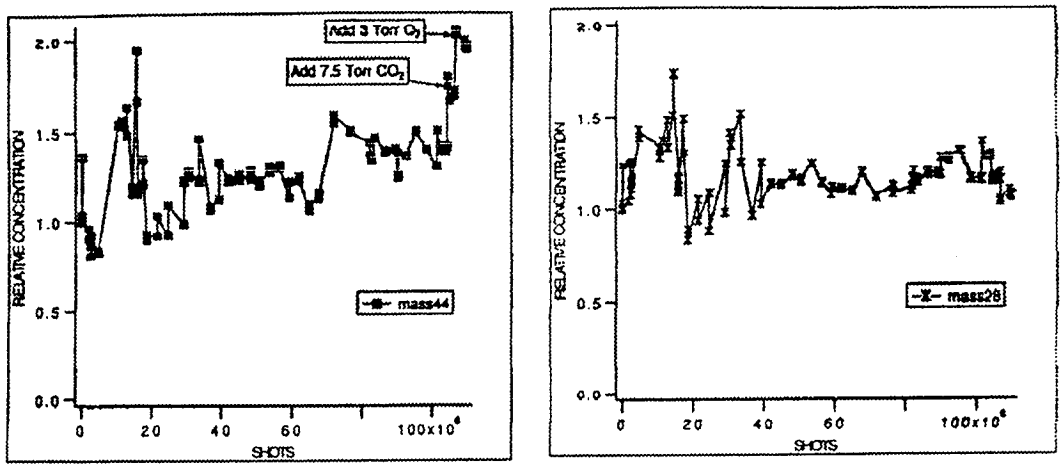

Figure 6.2-11. Mass Spectrometer Data of CO_2 and N_2+CO During 10^8 Shot Run

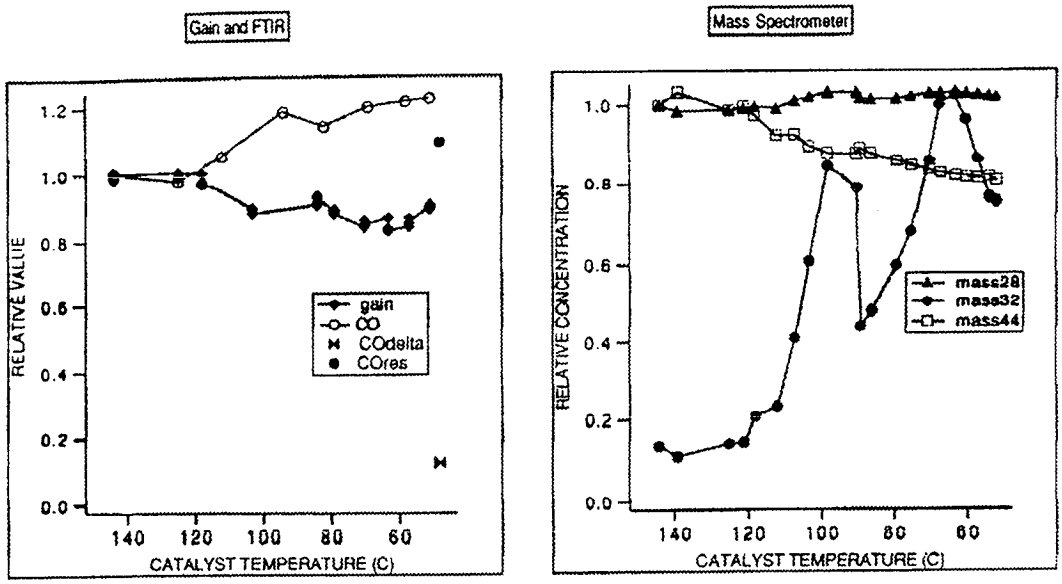

Figure 6.2-12. Gain, FTIR, and Mass Spectrometer Data During an Experiment Assess the Impact on Laser Operation of Cooling the Catalyst

Because of the significance of the self-catalysis action observed during the 10^8 run to the LAWS program (discussed later), a 10^7 run was attempted using self-catalysis from run start-up. An initial attempt at establishing a stable discharge run using the standard laser gas mix ended after about 25,000 shots, since at least the initial self-catalysis action of the standard mix could not prevent runaway O_2 formation and, thus, severe discharge arcing. This failure initiated experimentation with addition to the standard gas mix of small percentages of either/and H_2, CO. Attempts using either of the additives failed while a run using both succeeded. It was not possible within the

timeframe of this study to establish the relevant kinetics involved and the optimum start mix and this is left to a follow-on effort. The data gathered during this run are summarized in Figure 6.2-13. The optical gain exceeded 90% of the initial gain throughout the run and no undue build-up of CO and O_2 was observed other than for a rise to an equilibrium level early in the run. The run was terminated voluntarily at the 10-million shot mark. It was interrupted at the 5-million shot level by a shorted charging cable, but this failure did not require access to the gain module interior and loss of the gas mix.

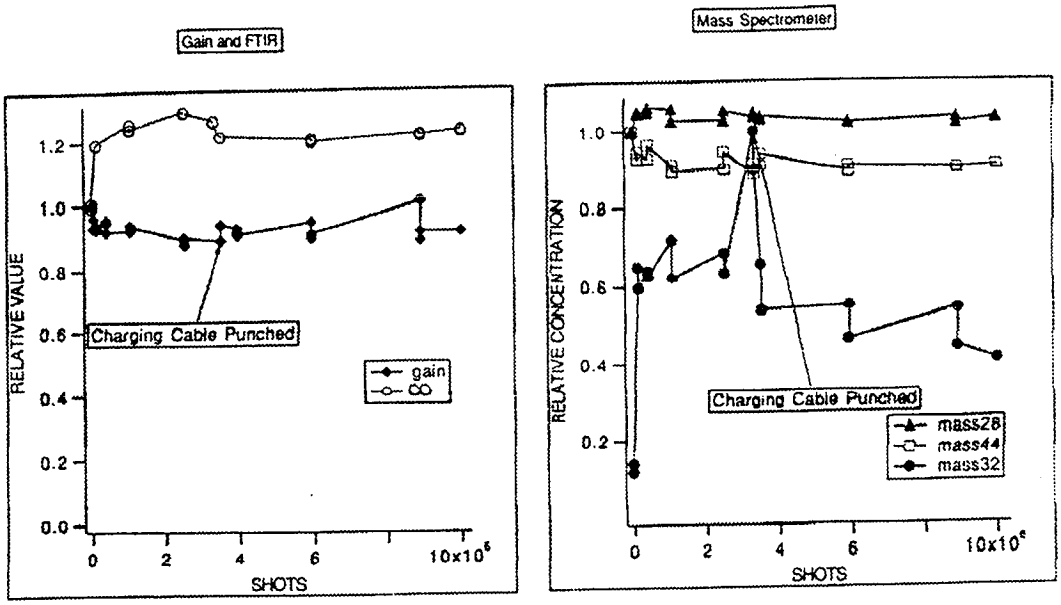

Figure 6.2-13. Optical Gain, FTIR (CO) and Mass Spectrometer Data Obtained During 10^7 Shot Run Using Gas Self Catalysis

To our knowledge, the 10^8 shot run reported here is the first report of such a long-duration closed-cycle operation of a significant scale CO_2 laser. The significance to the LAWS Program of the data obtained can be summarized as follows:

- Current designs of laser head components (corona bars, electrodes and insulators) demonstrated promising reliability and resiliency.
- No build-up of impurities other than CO and O_2 was observed.
- Demonstration of gas self-catalysis during a long-duration run allows consideration of a laser without a catalyst monolith in the flow loop. This simplifies flow-loop design, reduces fan power requirements, eliminates catalyst monolith launch integrity concerns and decreases risk in general.

10^8 Shot Rare Isotope Run

For the rare isotope run, the NASA/Langley Research Center (LaRC) catalyst in the external catalyst bed was replaced with the UOP Plc catalyst. This change involved replacement of the monolith cylinders by ones having having similar geometry. The only reason for this substitution was to gain experience using another catalyst. An attempt was made to passivate the catalyst by circulating several flushes drawn from the available 10 liters of rare isotope oxygen ($^{18}O_2$) over the heated catalyst. Using the indications of the mass spectrometer it became readily apparent that the required degree of passivation would not be achievable using only the available gas. Since an additional supply would not be forthcoming for six weeks, the decision was made to sideline the catalyst until additional $^{18}O_2$ became available and to proceed with the run depending on gas self-catalysis (homogeneous catalysis) for O_2 removal. Passivation of the laser head consisted of short duration (25,000 shot) runs using the standard laser mix with rare isotope $^{12}C^{18}O_2$ substituted for the abundant version used during previous runs. Three flush/discharge cycles appeared to provide adequate passivation. An Ultralasertech laser having a rare-isotope ($^{12}C^{18}O_2$) gain tube was substituted for the existing laser in the optical gain measurement set-up.

The long duration rare isotope runs consisted of one 10^7 shot run followed by a 5.5 x 10^7 shot run. Sufficient $^{18}O_2$ to $^{16}O_2$ scrambling had occurred after 10^7 shots during the first run to justify a restart with a fresh gas fill. Therefore, the 10^7 shot run served as an additional passivation run. Scrambling was also observed during the ensuing 5.5 x 10^7 shot run, however, it was considerably less than that observed during the 10^7 shot run. This observation provides strong evidence that adequate passivation of the laser for rare-isotope should be possible. The run was voluntarily terminated at 5.5 x 10^7 shots because of the degree of scrambling that had occurred. The optimum way to continue would have been to restart the run using a fresh gas fill to verify that improved passivation could be achieved, but time and funding constraints precluded the conduct of additional runs.

These long duration runs were established using a few percent of H_2 as the only additive to the standard (rare isotope) gas mix. The optical gain data for these runs are summarized in Figure 6.2-14. It is observed that the drop in the optical gain to approximately 75% of the initial gain during the first run was relatively rapid (a few hundred thousand shots). During the second run, the gain held above this 75% value for >3.5 x 10^7 shots. This loss of gain is primarily due to the scrambling of the $C^{18}O_2$ to $C^{16}O^{18}O$ and $C^{16}O_2$. Mass spectrometer data for the 5.5 x 10^7 shot run is displayed in Figure 6.2-15. Displayed are the time histories of the mass 30 ($C^{18}O^+$), mass 44 ($C^{16}O_2^+$), mass 46 ($C^{16}O^{18}O^+$), and mass 48 ($C^{18}O_2^+$) relative concentrations. The isotopic carbon monoxide ($C^{18}O$) concentration (formed totally by dissociative action) is seen to plateau

after about 10-million shots and remain relatively constant. The $C^{18}O_2$ concentration decreases slowly as expected, accompanied by slow increases in the $C^{16}O^{18}O$ and $C^{16}O_2$ concentrations. The growth in $C^{16}O^{18}O$ is faster than that of $C^{16}O_2$ as expected since ^{18}O is the most abundant oxygen atom present. At 40-million shots into the run, the system chemistry response to the addition of 2 torr of $^{18}O_2$ was evaluated. Re-formation of $C^{18}O$ to $C^{18}O_2$ is evident with a reversion to the "quasi-equilibrium" $C^{18}O$ level within about 10-million shots.

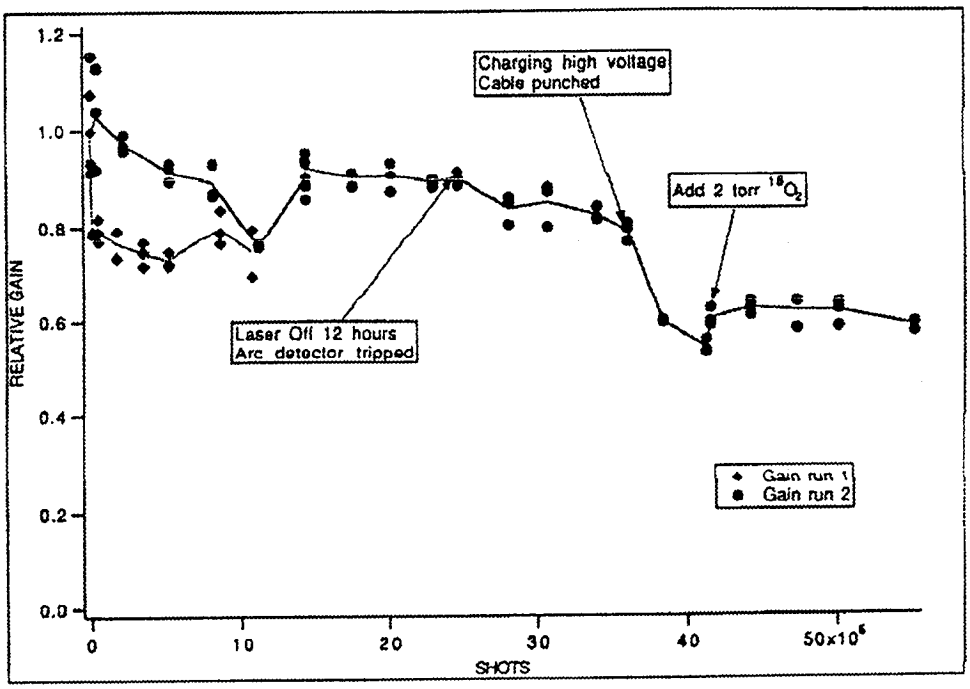

Figure 6.2-14. $C^{18}O_2$ Optical Gain Data During 55-Million-Shot Run

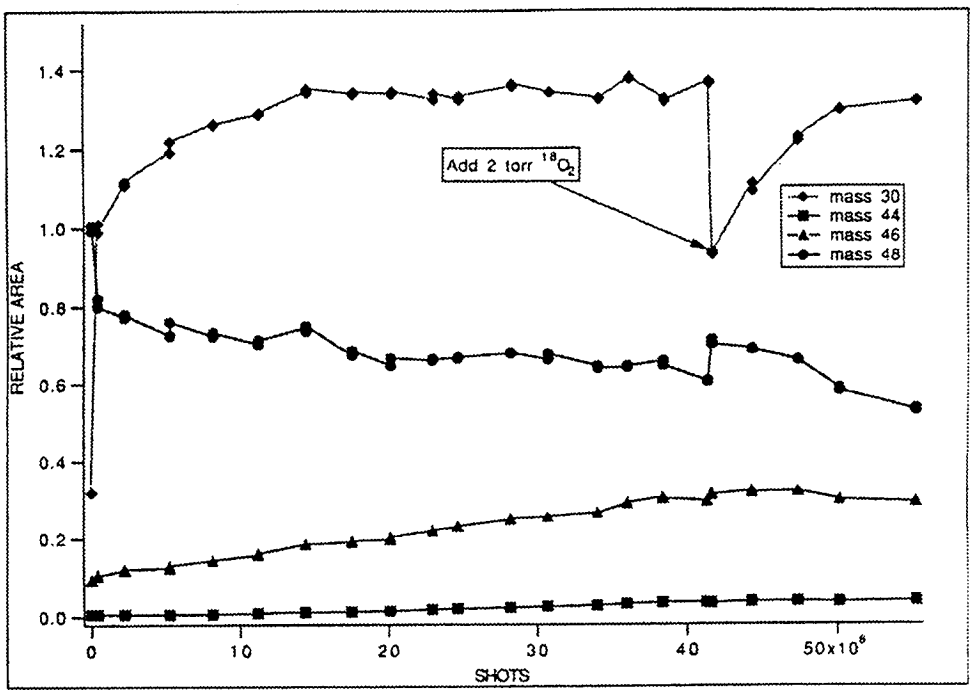

Figure 6.2-15. Mass Spectra Data Obtained During 55-Million-Shot Rare Isotope Run

To meet the time constraints of the program, the rare isotope runs were undertaken with no preparation of the interior of the gain module other than for the passivation with $^{18}O_2$ described earlier. The gain module was not opened and cleaned prior to these runs so as not to compromise its vacuum integrity. In light of the fact that it was known that an oxidized layer had formed on the electrodes during previous runs, including the abundant isotope 10^8 shot run, it is highly encouraging that such positive results were obtained after only partial passivation of the system. However, prior to any future long duration rare isotope runs, we would propose to carefully clean the head and passivate it extensively with $^{18}O_2$. We conclude that the isotope scrambling issue is a manageable one for the LAWS program. The 55-million-shot run reported here is to our knowledge the longest duration run for a repetitively pulsed CO_2 laser using the same gas mix and employing gas self-catalysis or homogeneous catalysis.

Reference

1. D.V. Willetts and M.R. Harris, "Homogeneous Catalysis for CO_2 Lasers" Proceedings of Coherent Laser Radar: Technology and Applications (Snowmass, CO), July 8-12, 1991.

APPENDIX A

Preliminary LAWS Instrument Drawings

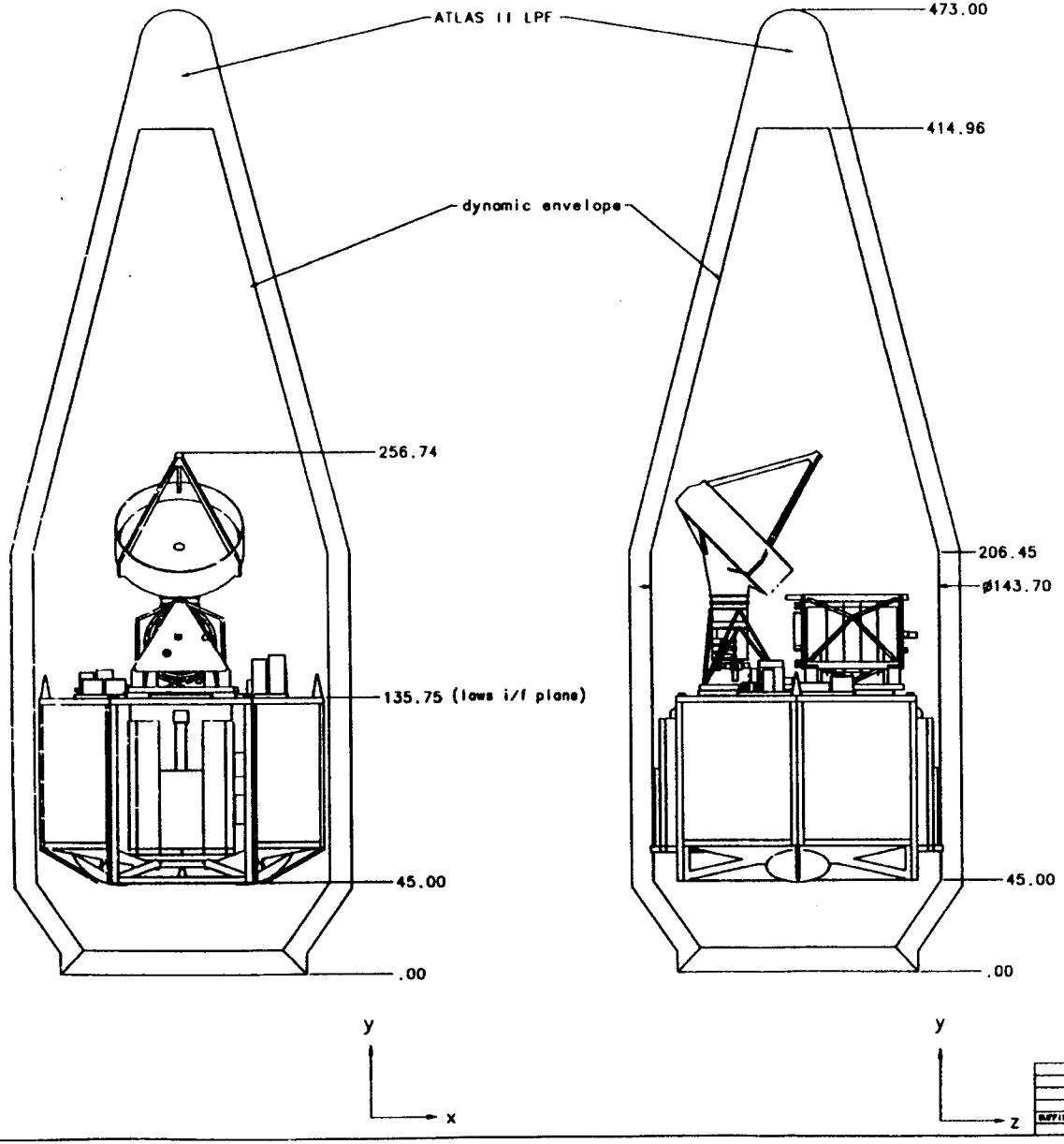

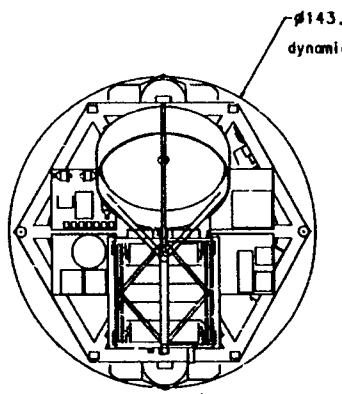

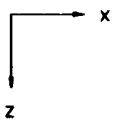

CE Astro Space

laws

launch config

lawsg1

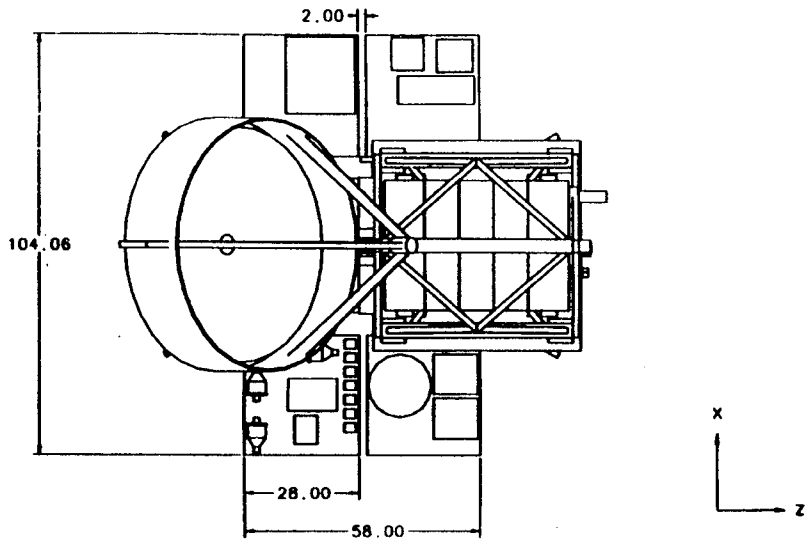

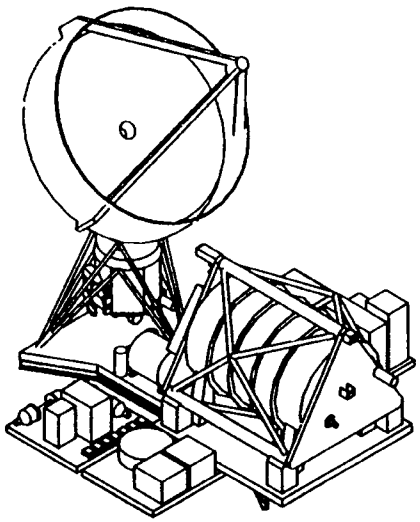

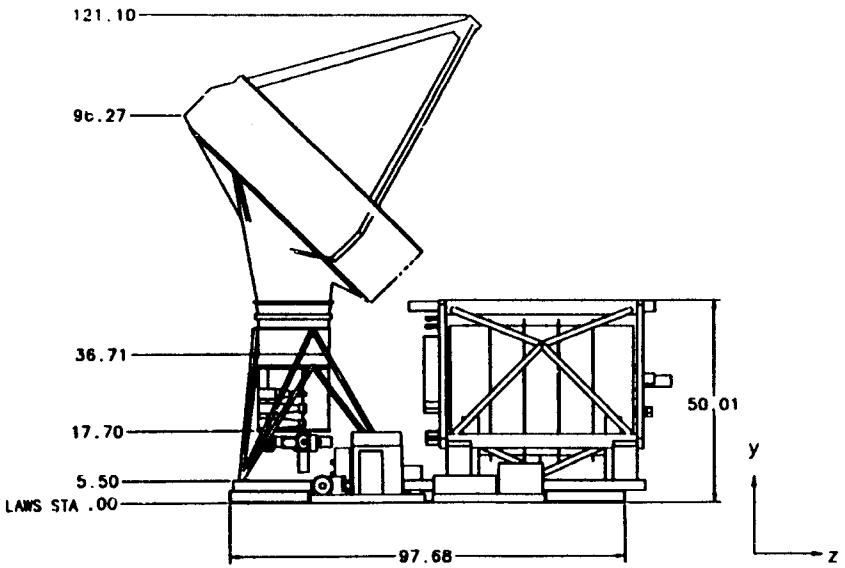

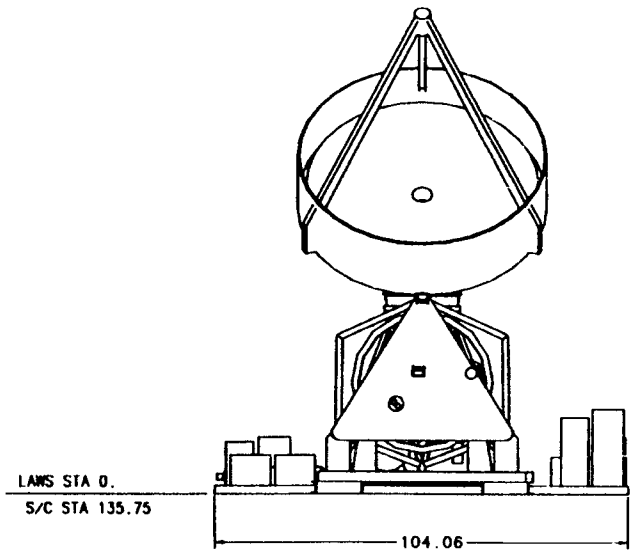

CE Astro Space

LAWS PAYLOAD

lawsg2

cold plate layout

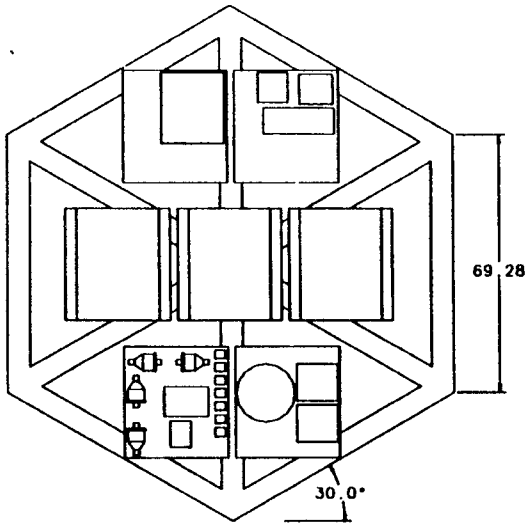

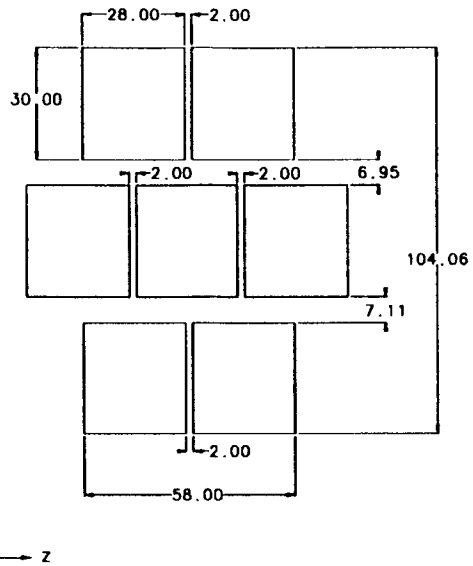

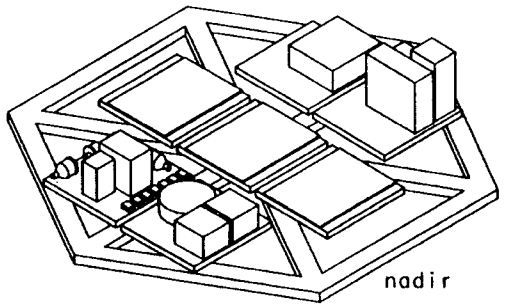

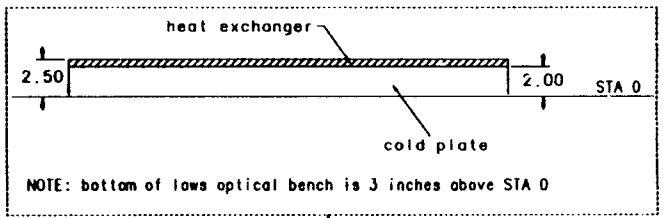

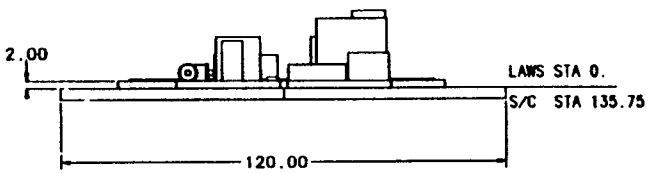

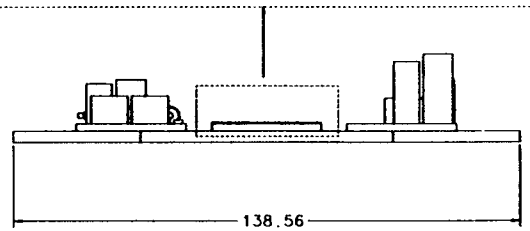

GE Astro Space

laws interface components

lawsg3

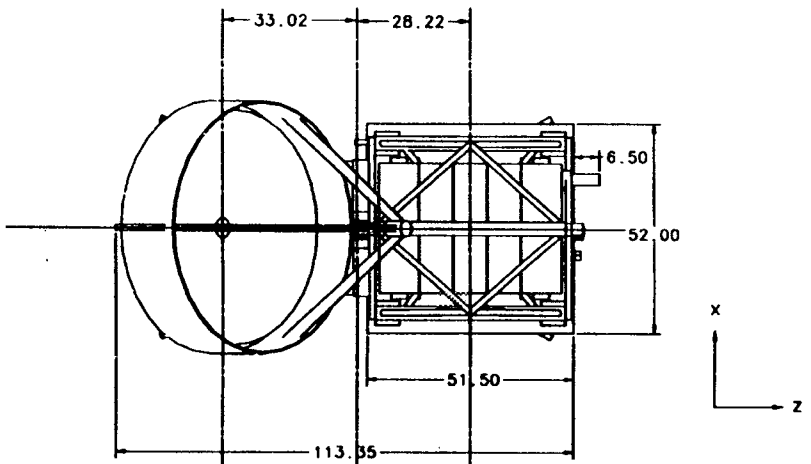

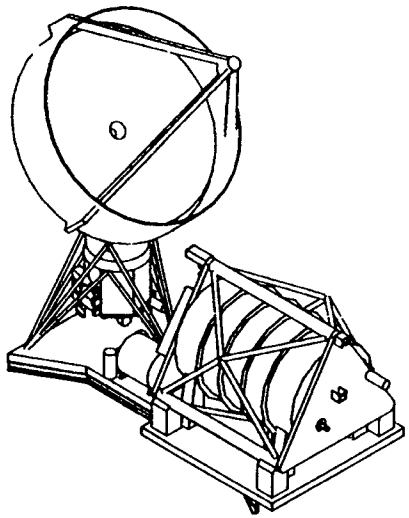

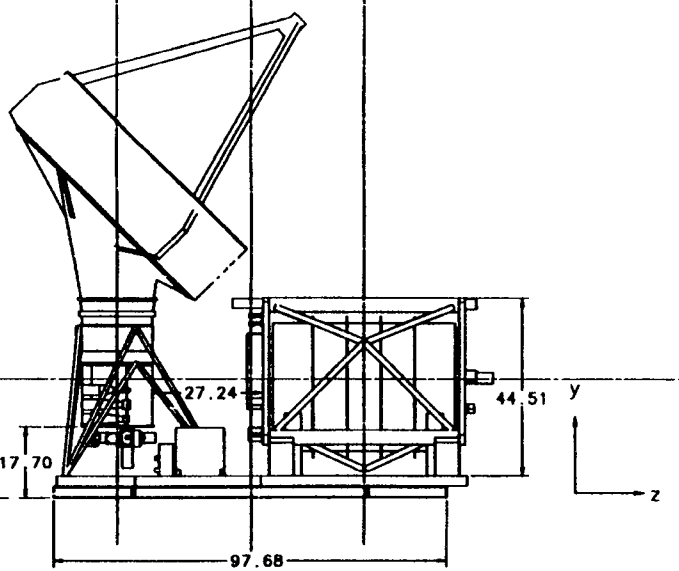

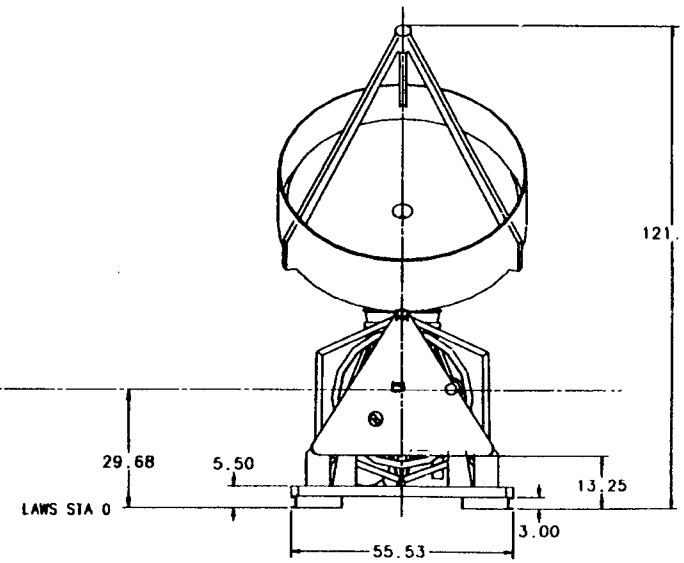

GE Astro Space

laws optical bench comps

lawsg4

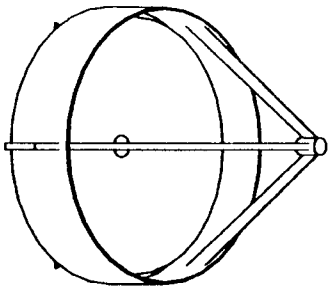

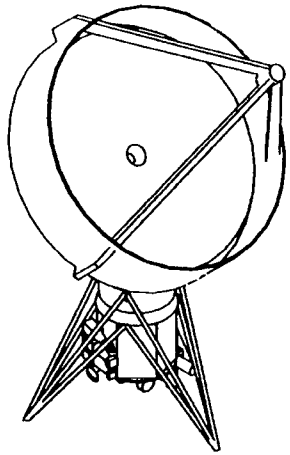

nadir

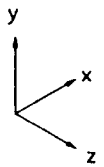

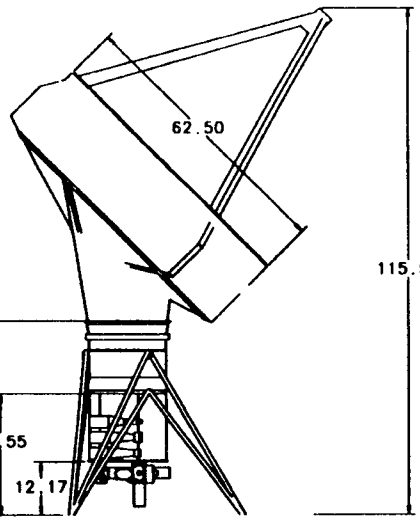

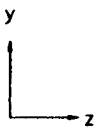

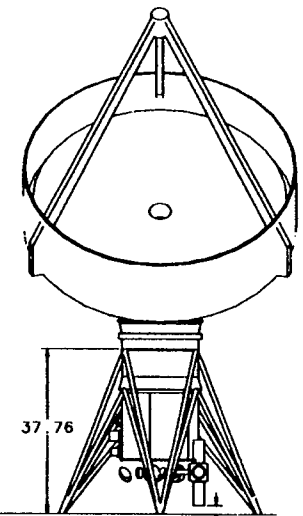

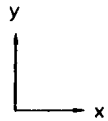

GE Astro Space

laws telescope

lawsg5

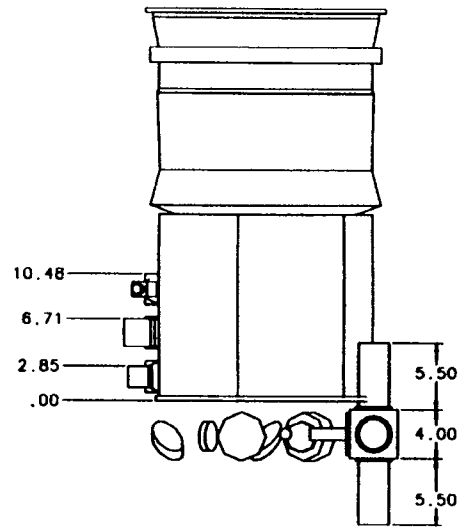

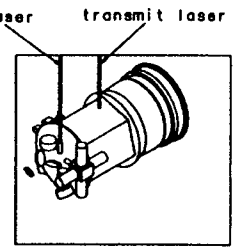

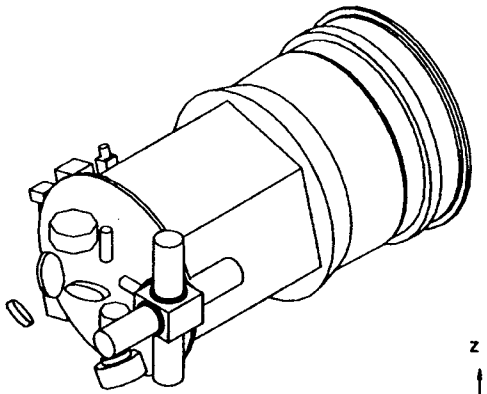

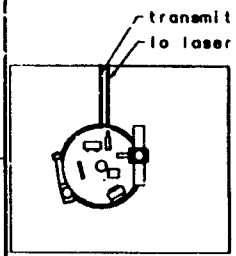

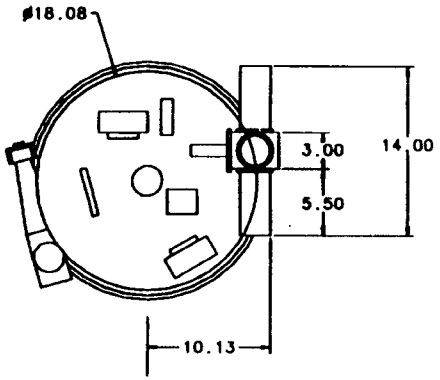

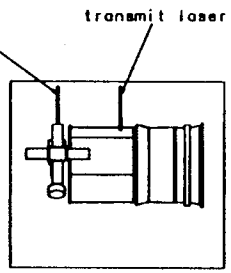

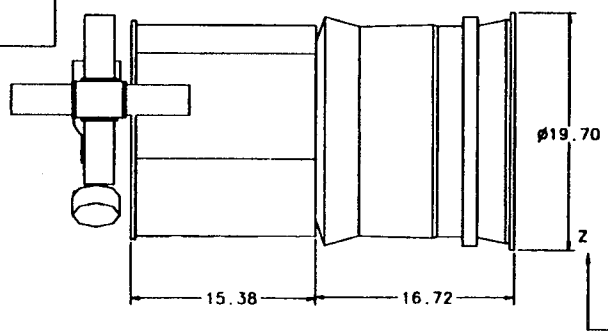

NOTE
small boxed pictures show laser beams into telescope

GE Astro Space
laws telescope
optical bench
lawsg5b

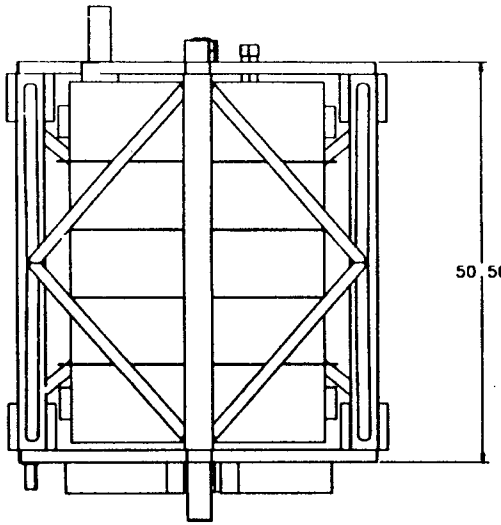

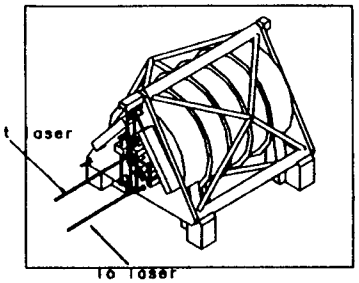

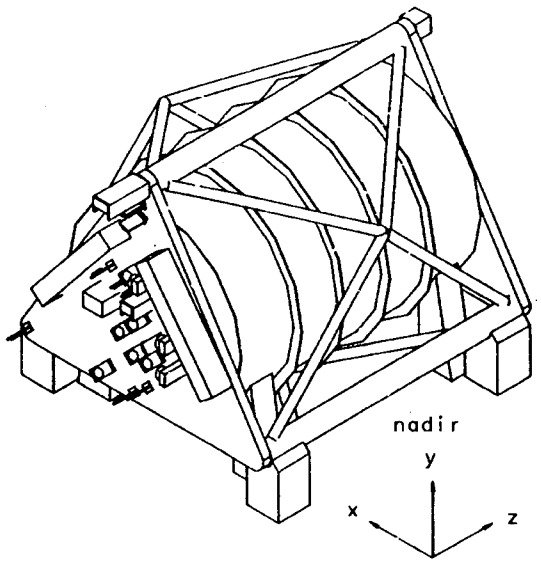

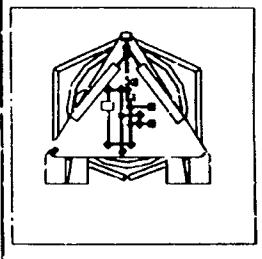

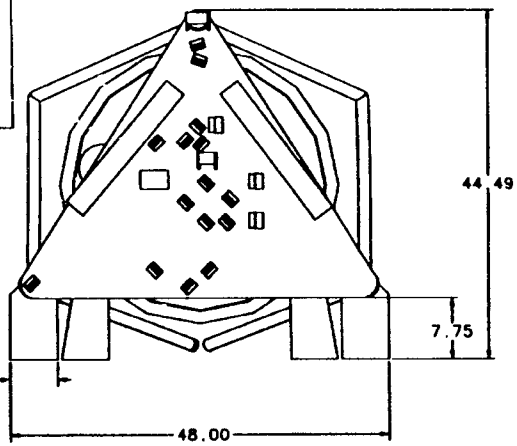

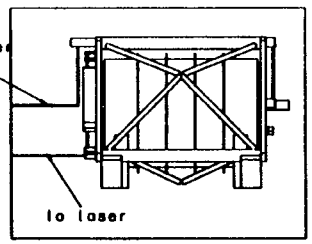

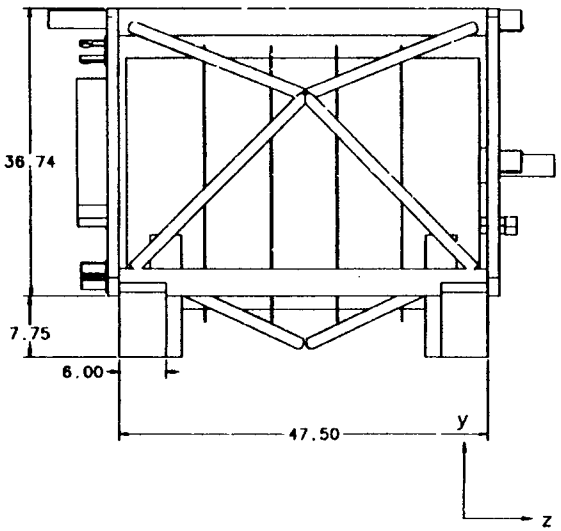

GE Astro Space

laws laser

lawsg6

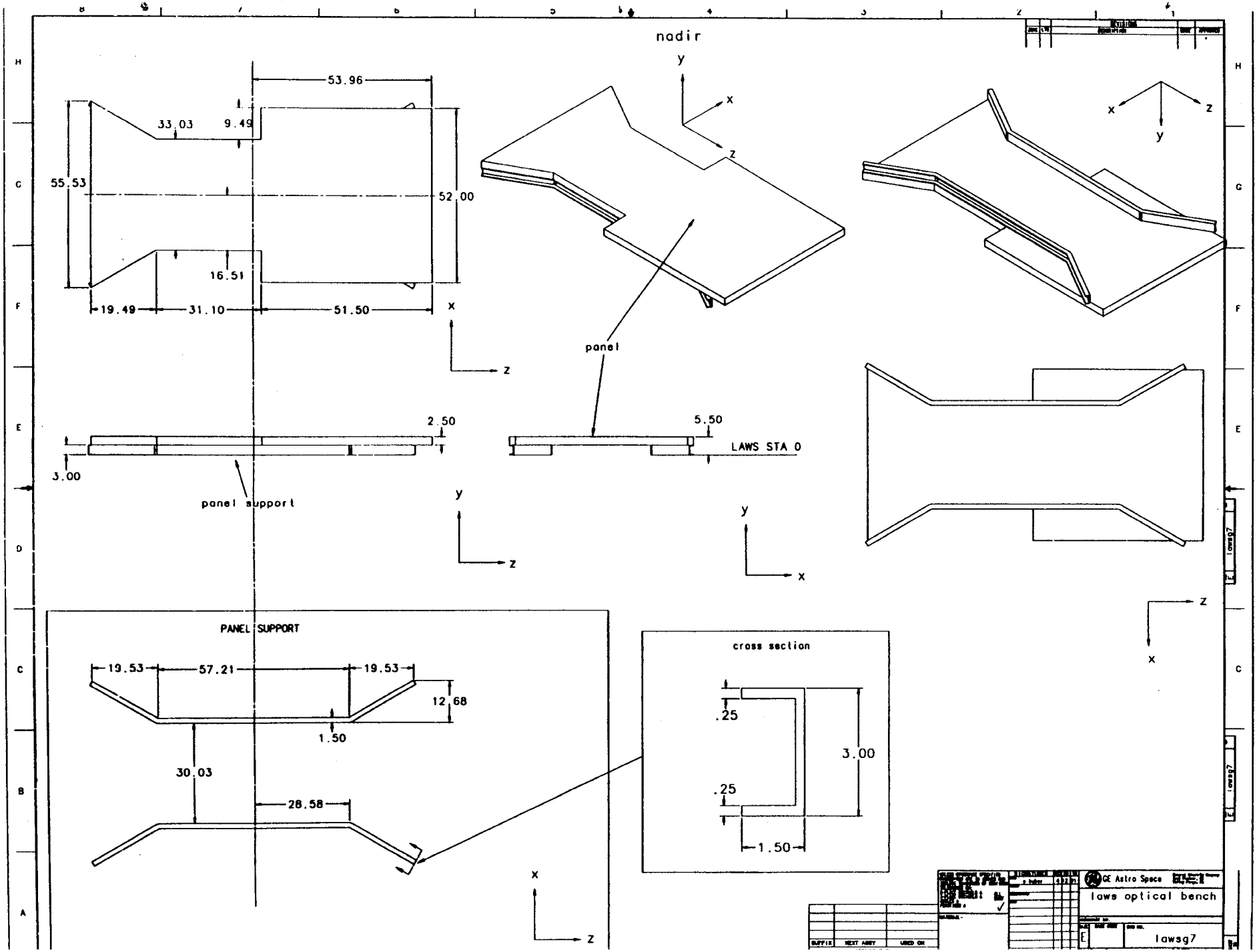
nadir
53.96
33.03
9.49
55.53
52.00
16.51
19.49
31.10
51.50
x
z
y
panel
2.50
3.00
panel support
5.50
LAWS STA 0
PANEL SUPPORT
19.53
57.21
19.53
12.68
1.50
30.03
28.58
cross section
.25
3.00
.25
1.50
GE Astro Space
laws optical bench
lawsg7